University of Camerino

SCHOOL OF ADVANCED STUDIES

Chemical and Pharmaceutical Sciences and Biotechnologies Area

Ph.D. Curriculum in Chemical Science

XXXIV Cycle

Doctoral Thesis

Investigation of Interfacial and Transport properties of LIBs/NIBs anodes and commercial SOFCs

Ph.D. Candidate

Antunes Staffolani

Supervisor

Prof. Francesco Nobili

Academic year 2018/19-2021/22

"No! I tried to settle bets with my own soul
Bless my lips for the first time before you don't
Gripping to the last touch of your hand I grow to loathe
Hope that you remember just how far I'll go
I'll spend the rest of my life wishing I'm enough"

Abstract

In this thesis work, two types of electrochemical energy systems (EESs) have been studied, i.e.: electrochemical energy storage by Li-/Na-ion batteries, and electrochemical energy conversion by Solid Oxide Fuel Cells. Energy production worldwide is moving toward renewable energy sources to decrease the greenhouse gases emissions. In this context, electrochemical energy systems will be in the very next future the key enablers for the production and storage of green energy. Furthermore, Li-ion batteries will play the main role for the transport electrification. To achieve this goal, several aspects of EESs needs to be studied and optimized, considering both performances and sustainability. Speaking of Li-ion batteries, graphite is the state-of-the-art anode material. However, it must be partially or totally replaced because of its low specific capacity (372 mAh g^{-1}) as well as its introduction into the critical raw materials list of the European Union. SnO_2 is a potential candidate because of its high theoretical capacity (1484 mAh g^{-1}), environmentally friendliness, and at the moment is not considered a critical raw material by the European Union. However, it suffers of cycling instability due to the structural rearrangements upon cycling, and large voltage hysteresis. In this regard, three different nanocomposite anodes based on SnO_2 have been synthesized and characterized in terms of both performance and interfacial and transport properties. The effect of an active/inactive matrix, as well as the morphology of SnO_2 has been deeply studied. As a result, the studied SnO_2-based anodes can offer promising and tailored performances in terms of energy density, energy efficiency, and rate capability according to the end user application. Speaking of Na-ion batteries, a Fe_3O_4-based anode was studied as a sustainable high-power anode material. In this regard, the material was structurally, morphologically, and electrochemically characterized. A deep electrochemical characterization in terms of interfacial and transport properties has been carried out by means of cyclic voltammetry at different scan rates, potentiostatic electrochemical impedance spectroscopy, and ex-situ Raman spectroscopy. The last section is focused on electrochemical energy conversion by Solid Oxide Fuel Cells. In this regard, a new technique, based on electrochemical impedance spectroscopy and the study of the distribution of relaxation times, has been proposed for assessing the state-of-health of the SOFC under real operating conditions. Firstly, an extended experimental campaign has been pursued to build a meaningful equivalent circuit model. Subsequently, an *a priori* known stress agent was applied to validate the obtained electrochemical model.

Preface

The following doctoral thesis reports the results obtained during three years of the PhD course in Chemical Sciences at the University of Camerino (Italy), under the supervision of Prof. Francesco Nobili. Part of the research work reported in this thesis is the subject of the following scientific publications and conference proceedings.

Scientific Publications:

- G. Carbonari, F. Maroni, S. Gabrielli, **A. Staffolani**, R. Tossici, A. Palmieri, F. Nobili, *Synthesis and Characterization of Vanillin-Templated Fe_2O_3 Nanoparticles as a Sustainable Anode Material for Li-Ion Batteries,* ChemElectrochem (**2019**) Vol. 6, 1915-1920, https://doi.org/10.1002/celc.201900189
- A. Baldinelli, **A. Staffolani**, G. Bidini, L. Barelli, F. Nobili, *An extensive model for renewable energy electrochemical storage with Solid Oxide Cells based on a comprehensive analysis of impedance deconvolution,* Journal of Energy Storage (**2021**) Vol. 33, 102052, https://doi.org/10.1016/j.est.2020.102052
- H. Darjazi, **A. Staffolani**, L. Sbrascini, L. Bottoni, R. Tossici, F. Nobili, *Sustainable Anodes for Lithium- and Sodium-Ion Batteries Based on Coffee Ground-Derived Hard Carbon and Green Binders,* Energies (**2020**) Vol. 13, 6216, https://doi.org/10.3390/en13236216
- **A. Staffolani**, A. Baldinelli, L. Barelli, G. Bidini, F. Nobili, *Early-Stage Detection of Solid Oxide Cells Anode Degradation by Operando Impedance Analysis,* Processes (**2021**) Vol. 9, 848, https://doi.org/10.3390/pr9050848
- **A. Staffolani**, H. Darjazi, G. Carbonari, F. Maroni, S. Gabrielli, F. Nobili, *Fe_3O_4/Graphene Composite Anode Material for Fast-Charging Li-Ion Batteries,* molecules (**2021**) Vol. 26, 4316, http://doi.org/10.3390/molecules26144316
- **A. Staffolani**, L. Sbrascini, L. Bottoni, H. Darjazi, S.J. Rezvani, M. Minicucci, F. Nobili, Synthesis and characterization of a high-capacity anode material for Na-ion batteries based on Fe_3O_4 and reduced graphene oxide, **currently under review**

Conference proceedings:

- **A. Staffolani**, G. Carbonari, F. Maroni, H. Darjazi, F. Nobili. *Synthesis and Characterization of TiO_2@SnO2 Nanocomposite as Viable Anode for Lithium-Ion Batteries,* Advanced Batteries for Automobile Applications, Ulm, Germany, 6-9/10/2019. **Poster**
- **A. Staffolani**, H. Darjazi, R. Tossici, F. Nobili. *Synthesis and characterization of high-performance and stability SnO_2/C composite anode for Li-ion batteries,* Advanced Batteries for Automobile Applications, Ulm, Germany, 6-9/10/2019. **Poster**
- A. Baldinelli, L. Barelli, G. Bidini, F. Nobili, **A. Staffolani**. *Monitoring of Solid Oxide Fuel Cell Performance Through Deconvolution of Electrochemical Impedance Spectra,* Enerchem 2, University of Padova, Italy, 12-14/02/2020. **Poster**
- **A. Staffolani**, *An Extensive Model for Solid Oxide Fuel Cells Based on Impedance Time-Based Deconvolution,* Bridging two centuries of electrochemical energy storage and conversion in honor of Prof. Roberto Marassi, 4-5/02/2021, **Oral communication – Invited speaker**
- **A. Staffolani**, H. Darjazi, L. Sbrascini, Luca Bottoni, Roberto Tossici, Francesco Nobili, *Fast Charging Anode for LIBs and NIBs Based on Fe_3O_4/rGO: Synthesis and Characterization,* IWES 2021, GISEL, 24-26/02/2021, **Oral communication – Accepted speaker**
- **A. Staffolani**, F. Nobili, L. Sbrascini, H. Darjazi, L. Bottoni, *Synthesis and Characterization of Fe_3O_4/rGO as Anode Material for Na-ion Batteries*, XIII INSTM CONFERENCE, 23-26/01/2022, **Oral communication – Accepted speaker**

Award

- "IWES2021 Lecture award", **IWES 2021**, 24-26/02/2021

Table of contents

Figures index

Tables index

1. Introduction

Nowadays, the climate change is posing a real threat to mankind, environment and all the living things. Indeed, several drastic phenomena are already occurring such as the increase of +0.5°C/decade of the average sea surface temperature in Europe (shown in **Figure 1-1**) (1; 2; 3; 4), land degradation and desert expansion (5), melting of permafrost and sea ice loss (6), and extreme weather conditions (7). This shift is mainly due to global warming induced by two factors i.e., greenhouse gases (GHGs) emissions, especially CO_2 (around 90%) and methane (8), and large-scale weather changes.

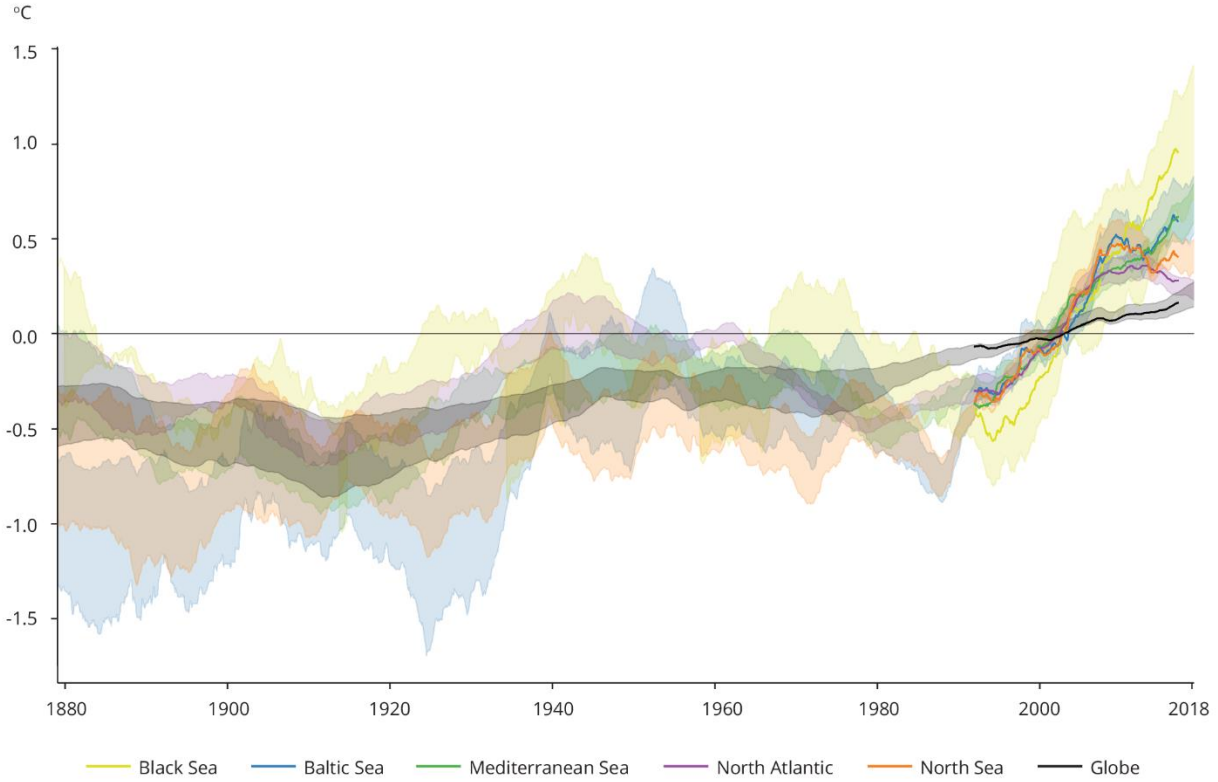

Figure 1-1. Average sea surface temperature anomaly in different European seas (1870 to 2018), taken from the European Environment Agency (EEA) website

As shown in **Figure 1-2**, ≈ 70 % of GHGs are introduced in the atmosphere by burning fossil fuels (coal, oil, and natural gas) and its derivatives (diesel, gasoline, and low molecular weight organic compounds) for production of electrical energy and transport, respectively. Smaller percentages of emissions are given by agriculture, manufacturing, and domestic heating systems. Furthermore, as forecasted by the peak oil proposed by the geologist and geophysicist Marion King Hubbert, fossil fuels are a finite source and due to expire in the next decades. Indeed, right now the peak is expected to be centered between 2019 and 2040, depending on global economy

and how states and institutions will respond to global warming (9). For these reasons, energy production worldwide is moving toward renewable energy sources such as solar, wind, hydro, tidal, and geothermal energy. However, due to the fitful nature of these energy sources, energy storage systems (ESS) are required to have a continuous supply of it. ESSs can be classified according to their storage mechanism or their application considering their rated energy density and power (10; 11):

- **Mechanical Energy Storage Systems**:
    - Pumped hydroelectric (potential energy storage).
    - Compressed air (potential energy storage).
    - Flywheel (kinetic energy storage).
- **Electrochemical Energy Storage Systems:**
    - Secondary batteries.
    - Ultracapacitors.
    - Redox-flow batteries.
    - Hydrogen & Fuel cells (hydrogen as energy vector to fuel cells).
    - Superconducting magnetic energy storage.

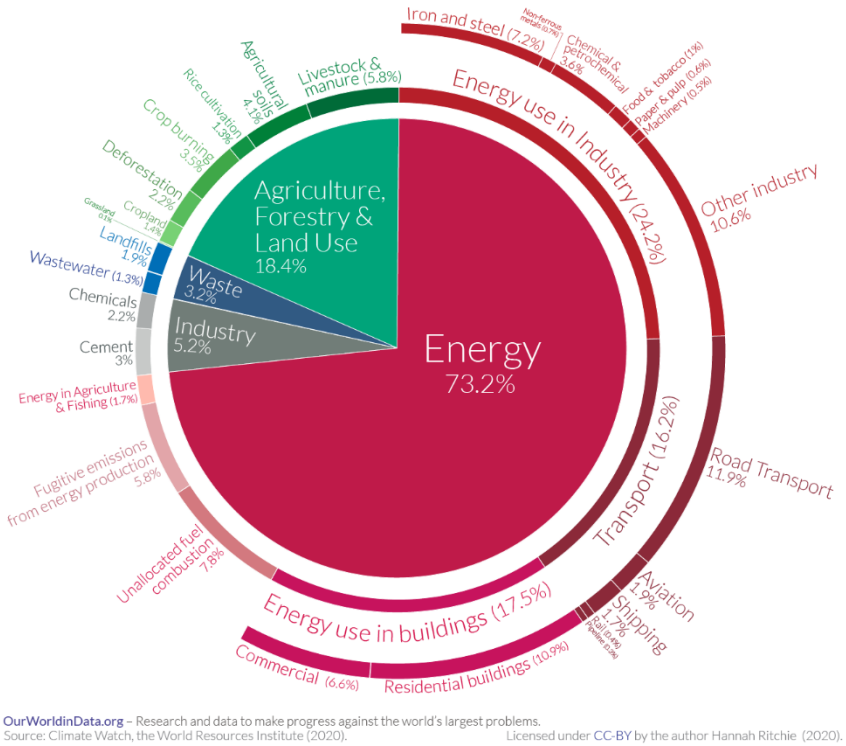

Figure 1-2. Total contribution of global greenhouse gases emission divided by sector. Image taken from Our World Data website.

A Ragone plot comprising all the mentioned ESSs is shown in **Figure 1-3**.

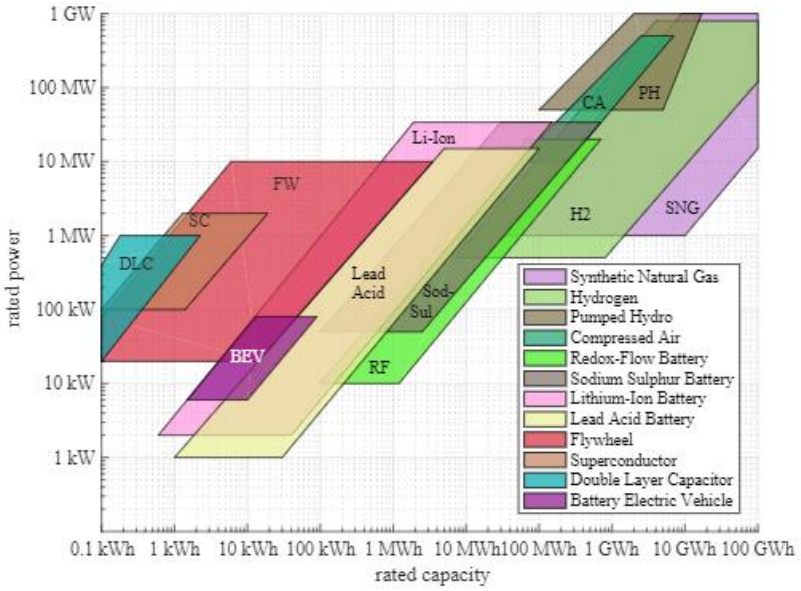

Figure 1-3. Ragone plot of both mechanical and electrochemical ESSs (11)

In this regard, Li-ion batteries (LIBs) are nowadays the market leader for battery-based energy storage systems thanks to their high-energy density, efficiency, cycle life (especially LFP-based batteries) and flexible designs ranging from few Wh up to several kWh in large modules (12). Indeed, LIBs experienced a massive market growth thanks to their application in portable electronic devices such as laptops, smartphones, and even radio-controlled toys. Furthermore, they are considered the ESS of choice for low- or zero-emission vehicles such as hybrid electric vehicles (HEVs), plug-in hybrid electric vehicles (PHEVs), battery electric vehicles (BEVs), and even as support for the upcoming fuel cell electric vehicles (FCEVs) (13; 14). However, their use in both transport and ESSs market sectors still needs improvement in several aspects such as safety, energy density, efficiency, cycle life and charging speed (ΔSOC = 80 % in 15 min for transport) (14). Indeed, the BEVs market share was only about 2 % in 2020 because of low mileage per charge, safety issues and charging rate limit. To overcome these drawbacks and ensure a large electrification of road transport, all the components of LIBs must be optimized in terms of both performance, sustainability, and recyclability.

On the other hand, fuel cells (FCs) are a promising technology for harvesting energy from green fuels such as hydrogen, giving as by-product only water and heat. Indeed, FCs can offer a higher energy density compared to LIBs and an easy scalability of the implant (15). Moreover, in the last decade, car makers are developing FCEVs as an alternative clean transport to BEVs (16). However, as in the case of LIBs, this technology is not mature yet for large-scale energy

production and road transport, limiting its use only as backup energy source in buildings. Several issues need to be addressed for its commercialization such as raw material cost, and hydrogen storage and supply (15).

1.1 Electrochemical energy storage systems

Electrochemical energy storage systems (EESSs) are those devices able to store and release electrical energy thanks to bulk redox reactions (secondary batteries family) or surface charge storage reactions (capacitors family). As shown in **Figure 1-3**, secondary batteries have an intermediate power density due to the high internal resistance which is too high for delivering high-power pulses without risking any performance failure. Anyway, thanks to their higher energy density compared to capacitors and supercapacitors, they are the perfect choice for energy demanding applications. The cell chemistry dictates several properties of secondary batteries such as nominal voltage, power density, energy density, shelf-life, and cycle life. In **Figure 1-4**, a Ragone plot comparing different secondary batteries chemistries is shown.

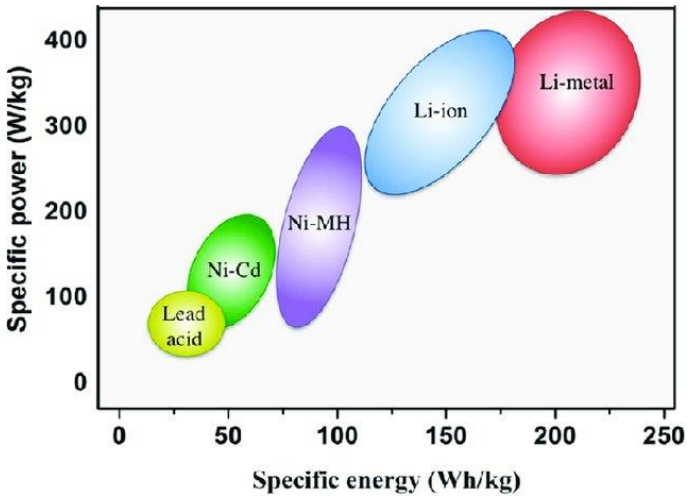

Figure 1-4. Ragone plot specific for secondary batteries (17)

As we can see, LIBs and the upcoming Li-metal batteries (LMBs) offer higher energy and power densities compared to other accumulators such as lead-acid or Ni-MH.

1.1.1 Lithium-ion batteries

Lithium is the lightest metal of the periodic table (6.941 a.m.u.) and has one of the lowest standard redox potentials i.e., -3.04 V vs SHE. Furthermore, it has a theoretical gravimetric capacity of 3860 mAh g^{-1}, making it an attractive anode. Indeed, in the 1970s, the first Li primary cells comprising a lithium metal anode were commercialized for small applications such as watches, and medical

implants. In the same years, the reversible reaction of several inorganic compounds with alkali metal was shown. This type of reaction, later known as intercalation reaction, was fundamental for the development of Li-ion batteries (18). Specifically, Prof. S. M. Whittingam discovered that some metal chalcogenides, especially sulfides, were able to act as host for alkali metal ion, giving intercalated compounds. In 1976, after getting hired by Exxon, he improved his innovation building the first prototype of rechargeable lithium battery with lithium metal as anode material, $LiClO_4$ in 1,3-dioxolane as electrolyte, and titanium disulfide as cathode material (19). However, this prototype was never commercialized because of the safety issues and operational faults. Later it was found that this fail was related to the electrodes materials. Indeed, on the cathode side, TiS_2 is air and moisture sensitive by which can release hydrogen sulfide. On the anode side, lithium reacted with the electrolyte during every charging step, giving loss of active lithium, Li dendrite growth, and in the worst case short-circuit with thermal runaway. Therefore, research activities pointed toward the substitution of lithium metal with safer lithium-containing compounds. Fundamental studies on lithium host were pursued by Murphy et al (20) using rutile TiO_2, and Scrosati et al (21) using Li_xWO_2 and TiS_2 as anode and cathode material, respectively. This system was called "lithium rocking chair batteries", in which lithium ions reversibly intercalate between the cathode and the anode materials. During 1974-1976, J. O. Besenhard discovered the reversible intercalation of lithium ions into graphite and carbonaceous materials and suggested it for Li storage applications (22). In particular, graphite is able to intercalate Li ions with low volume change and potential close to the Li redox couple, making it an attractive candidate for such application. To overcome the higher potential of graphite compared to lithium metal, cathode materials based on metal oxides, having higher oxidation potential were investigated (23; 24). Indeed, thanks to the more pronounced ionic character of the "M-O" bonds compared to the "M-S" bonds, researchers were able to increase the potential window of the first Li-based batteries. Goodenough et al. (25) proposed $LiCoO_2$ as high-energy cathode material which can act as donor of Li^+ ions, and thus, allowed the use of several kinds of Li-free materials as anodes. In 1985, A. Yoshino and his co-workers filed a patent in which a new cell design implying an $LiCoO_2$ as cathode and an insertion carbon anode was developed. In this document, for the first time the term "Lithium-ion battery" appeared, and since then the expression started to be used worldwide.

After this research and development, the first Lithium-ion batteries were commercialized by Sony Corporation in 1991.

Nowadays, the basic design of Lithium-ion batteries relies in the same technology developed three decades ago (**Figure 1-5**). The anode, cathode, electrolyte, separator, and current collectors are the main components of a LIB. The anode is the electrode at lower potential where the reduction takes place when charging the cell. The cathode is the electrode at higher potential in which the oxidation reaction occurs during charging. The two electrodes are connected by an external electrical circuit to ensure the flow of electrons from the cathode to the anode when charging, and back when discharging. The electrolyte is the component needed to guarantee the flow of the ionic current and the charge balance between the electrodes. Since the active materials are essentially powders, they are attached to a rigid and conductive support called current collector (Cu for anodes and Al for cathodes).

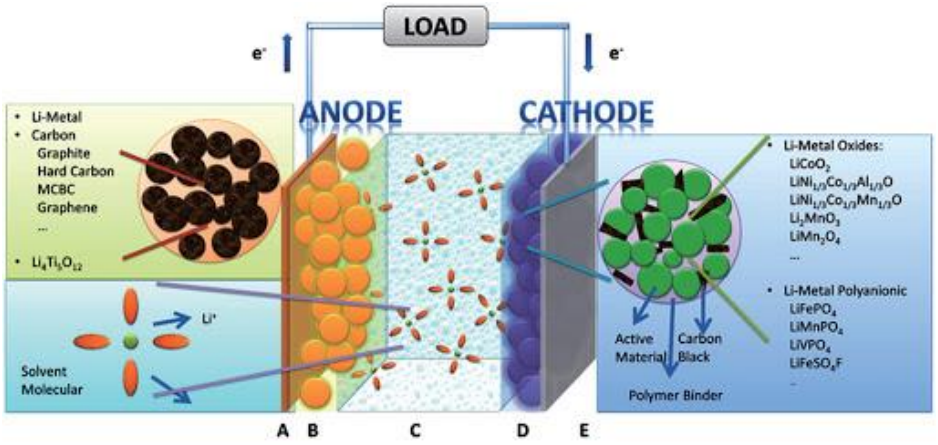

Figure 1-5. Schematic of a Li-ion battery

To do that, a polymeric binder is used which can ensure the adhesion of the electrode powders while maintaining a certain degree of flexibility and processability of the electrode films. At last, the separator is used to physically separate the two electrodes to avoid any event of short circuit. Usually, it is a microporous polymeric film (polyethylene, polypropylene, or a co-polymer of them) interposed between the electrodes which allows the liquid electrolyte permeation thanks to its pores.

The reaction mechanism of a state-of-the-art LIB made with graphite as anode and $LiCoO_2$ as cathode can be summarized with the set of **Equations 1-6**.

Charge:

Cathode $LiCoO_2 \rightarrow Li_{1-x}CoO_2 + xLi^+ + xe^-$ **Eq. 1**

Anode $6C_{(graphite)} + xLi^+ + xe^- \rightarrow Li_xC_6$ **Eq. 2**

Overall $LiCoO_2 + 6C_{(graphite)} \rightarrow Li_{1-x}CoO_2 + Li_xC_6$ **Eq. 3**

Discharge:

Cathode $Li_{1-x}CoO_2 + xLi^+ + xe^- \rightarrow LiCoO_2$ **Eq. 4**

Anode $Li_xC_6 \rightarrow 6C_{(graphite)} + xLi^+ + xe^-$ **Eq. 5**

Overall $Li_{1-x}CoO_2 + Li_xC_6 \rightarrow LiCoO_2 + 6C_{(graphite)}$ **Eq. 6**

During the charge, the Co^{3+} in $LiCoO_2$ gets oxidized, releasing Li^+ ions which migrate to the anode thanks to the electrolyte. At the same time, the electrons flow from the cathode toward the anode thanks to the external electrical circuit. At last, the graphite anode is reduced along with the insertion of Li^+ ions into its crystal structure.

The electrolyte at the solid-liquid interface on the anode side will undergo a series of electrochemical decomposition reactions, forming a passivation layer which will prevent any further decomposition reaction. Some lithium is lost during this process causing a low coulombic efficiency in the first charge/discharge cycle. This layer is called solid electrolyte interphase (SEI) and it is of paramount importance for the cycle life of the battery. It can conduct Li^+ ions but not electrons, thus avoiding any further reduction reaction of the electrolyte and is not permeable by the solvent molecule. However, under some circumstances e.g., cell ageing, unproper cycling conditions, the SEI layer can break, and consequently further lithium is lost in the next charge for a new SEI formation. This will lead to a continuous loss of cyclable lithium and thus capacity fading of the cell, along with the increase of the internal resistance due to the increasing thickness of the passivation layer. Furthermore, the exposure of graphite to the electrolyte can cause the Li^+-solvent co-intercalation, graphene interlayer expansion and at last pulverization of the electrode (26).

In sections 1.1.1.1, 1.1.1.2, and 1.1.1.3, an overview of the three major components of LIBs i.e., anode, cathode, and electrolyte are reported.

1.1.1.1 Anode materials

In this section, an overview of different anode materials based on their elemental composition as well as their reaction mechanism is reported.

After the discovery of the reversible intercalation of Li^+ ions into carbonaceous material, graphite became the main anode material of LIBs. This success relies on the low inherent cost of carbon-based materials, the well-known and reversible intercalation reaction, and the formation of the protective passivation film (SEI). However, its relatively low specific gravimetric capacity of 372 mAh g^{-1} cannot satisfy the requirements of high-energy density batteries for transport electrification. Several materials have been studied considering their sustainability, cost, safety, and performance. They can be divided in three classes according to their reaction mechanism i.e., intercalation/de-intercalation, conversion/oxidation, and alloying/de-alloying. All of them have advantages and disadvantages to consider prior their commercial application in real batteries. In **Table 1**, advantages and drawbacks of these three classes are reported.

Table 1. Advantages and drawbacks of anode materials based on reaction mechanism

	Advantages	**Drawbacks**
Insertion/de-insertion	• Stability • Low or negligible volume expansion • Reversibility	• Low specific capacity (ranging from 100 up to 400 mAh g^{-1})
Conversion/oxidation	• High specific capacity (ranging from 500 up to 1000 mAh g^{-1}) • Economically and environmentally sustainable	• Voltage hysteresis • Structural change
Alloying/de-alloying	• Highest specific capacities (ranging from 700 up to 4000 mAh g^{-1})	• High volume expansion • Instability

Insertion/de-insertion materials are usually characterized by an extremely reversible intercalation reaction accompanied by a low or negligible volume change. They are mainly carbon-based or titanium-based materials. The formers are characterized by higher specific capacity (from 200 up

to 400 mAh g^{-1}) and lower working potential, while the latter are characterized by high working potential (around 1.5 V) and low specific capacities. However, since their crystal structure can accommodate a relatively low amount of Li, in both cases the specific capacities are too low for high-energy density applications.

A relatively new reaction concept is the conversion reaction (**Equation 7**), in which a transition metal oxide, phosphide, nitride, or sulfide is reduced with Li^+ to give metal nanoparticles and the corresponding lithium compound (27).

$$M_aY_x + xnLi^+ + xne^- \rightarrow aM^0 + xLi_nY \qquad \textbf{Eq. 7}$$

They can offer a higher specific capacity than insertion materials (ranging from 500 up to 1000 mAh g^{-1}) thanks to the large quantity of exchanged lithium. However, their application is hindered because of the instability driven by the intrinsic structural change of the conversion reaction. Furthermore, the voltage profile of conversion-based materials is characterized by a large voltage hysteresis which lowers the charge/discharge energy efficiency.

Alloying/de-alloying materials can store a large amount of Li compared to the other two classes. Metals and semimetals of groups IV and V can electrochemically form alloys with lithium or, in some cases, other alkali metal (**Equation 8**).

$$M + xLi^+ + xe^- \rightarrow Li_xM \qquad \textbf{Eq. 8}$$

The reaction can be classified in two categories depending on whether a crystal structure change take place or not:

- Solid-solution reaction.
- Addition reaction.

Formation of Li alloys with crystalline Si, Sn, Al, and Sb, in which a crystal structure change takes place, are considered solid-solution reactions. Electrochemical alloying of Li with Mg and amorphous-Si are considered addition reactions. The specific capacities of these materials are very high (ranging from 700 up to 4000 mAh g^{-1}) thanks to their low atomic weight and amount of alloyed Li. However, the alloying reaction is commonly accompanied by a drastic volume change V_f > 200 % which inevitably leads to loss of electrical contact and pulverization of the electrode.

Carbon-based materials.

After the introduction of graphite as a replacement of lithium metal in the very first lithium-ion battery, carbonaceous materials have served as anode materials for several year. Thanks to their low cost, ability to form a "protective" passivating film (SEI), and corrosion resistance to HF, they have been the anode of choice for the last two decades. Some other advantages can be their remarkable electronic conductivity and possible preparation from biowaste materials (28; 29; 30). Carbon based materials belongs to the intercalation reaction family and are mainly divided into two categories according to their crystallinity degree and carbon atom stacking (**Figure 1-6**):

- Ordered carbon characterized by long-range order.
- Disordered carbon characterized by no long-range order and thus, no crystallinity.

Ordered carbon. The former comprehends graphite, single or few layers graphene, and carbon nanotubes. Graphite is quite famous in the battery community and is the state-of-the-art anode material. It can store Li^+ ions through stages, reaching a maximum stoichiometry of LiC_6 and a theoretical specific capacity of 372 mAh g^{-1}. Graphite is characterized by a layered structure made of sp^2-hybridized carbon sheets (31). Thanks to the delocalization of π electrons it possesses a high electronic conductivity along the plane, useful to build up the electronic conduction pathway in the electrode. The graphene layers are held together thanks to Van der Waals interactions, giving an interlayer distance of 3.35 Å in which ions can be intercalated (32).

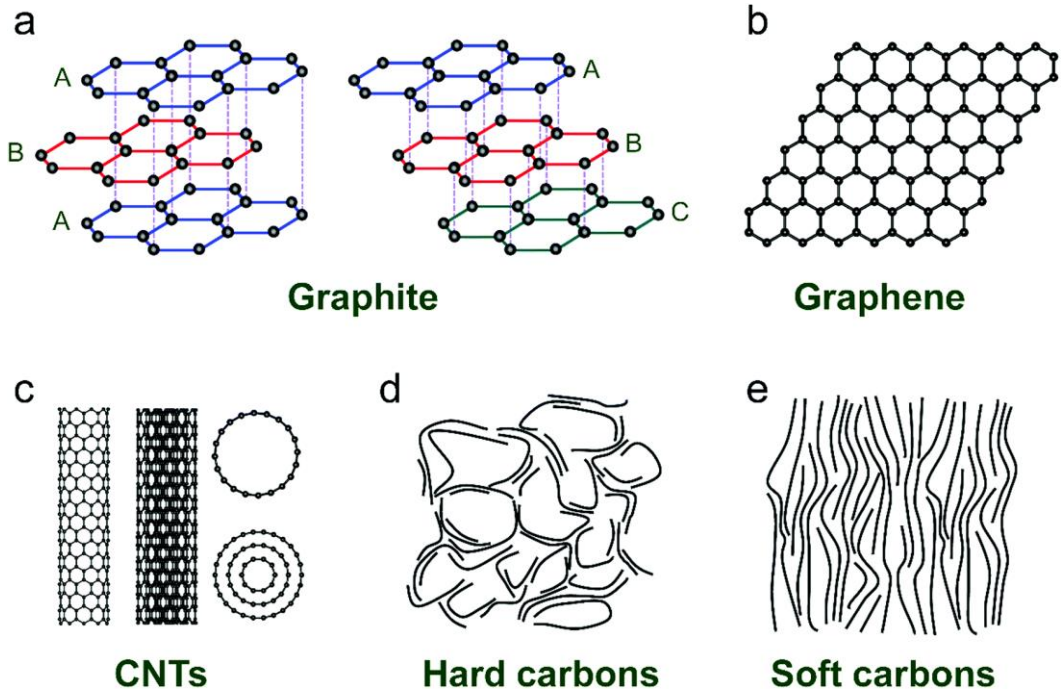

Figure 1-6. Typical structure of a) graphite AB and ABC, b) graphene monolayer, c) single- and multi-walled carbon nanotube, d) non-graphitizable hard carbon, and e) graphitizable soft carbon. Image taken from (32)

Li^+ intercalation into graphite occurs via a mechanism known as "staging" (**Figure 1-7**). This is a stepwise process in which Li^+ is intercalated in distant layers, leaving a certain gap *n* of unoccupied layers. As the intercalation proceeds, the number of unoccupied layers decreases until reaching the stoichiometry of LiC_6 (33). The stages are named after the number *n* of unoccupied layers between intercalated layers. The staging mechanism results in the observation of plateaus in the galvanostatic profiles, due to the formation of the two-phases region, and sharp peaks in potential-controlled techniques (33).

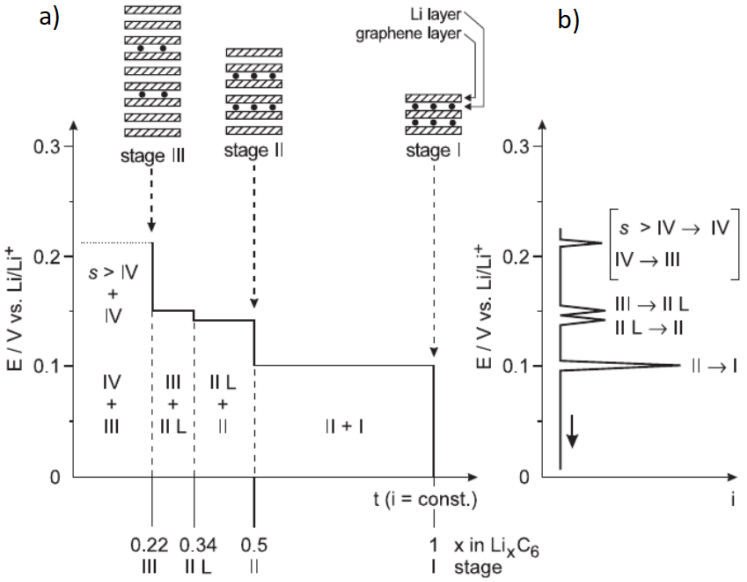

Figure 1-7. Electrochemical observation of the staging mechanism of graphite from a) galvanostatic profiles and b) linear sweep voltammetry. Image taken from (33).

Ball milling can easily break the C-C bond, leading to the formation of defect and amorphization around the particle edges. High number of defects can improve the specific capacities with the drawback of a larger voltage hysteresis.

Specific new forms of graphite other than from petroleum coke have been developed with improved specific capacities and especially rate capability such as the mesocarbon microbeads graphite (MCMB graphite) or microcarbon fiber (MCF) (34; 35).

The term graphene refers to the single or few layer of sp^2-hybridized carbon. After its isolation in 2004 (36), graphene caught the attention of both academy and industry thanks to its remarkable properties such as reliable thermal conductivity (37), good electrical conductivity (38) and superior mechanical properties (39). In **Table 2**, a summary of the outstanding properties of graphene is reported.

Table 2. Summary of mechanical, electronic, and thermal properties of graphene

Tensile strength / GPa (40)	**Young's modulus / GPa** (40)	**Electronic conductivity / S m^{-1}** (41)	**Charge mobility / cm^2 V^{-1} s^{-1}** (41)	**Thermal conductivity / W m^{-1} K^{-1}** (42)
125	1100	1 x 10^8	2 x 10^5	≈ 4000

However, its application as anode material for battery application is still under investigation (43). Indeed, although it possesses a high theoretical specific capacity of 744 mAh g^{-1}, due to the ability to store Li^+ ions on both side of single layers (stoichiometry of Li_2C_6), graphene layers tend to quickly restack together forming amorphous carbon and, at long last, graphite, losing all the properties related to it. Furthermore, the material suffers of a high irreversible capacity in the first cycle, and a large voltage hysteresis hinders its practical use in batteries as anode material (43; 44). However, thanks to its remarkable electronic and mechanical properties, graphene is a promising containment matrix for composite materials, able to withstand the stressed caused by alloying and conversion materials. Furthermore, it may increase the electronic conductivity of the whole electrode. For these reasons, graphene has been already used as an additive for the synthesis of high-performance nanocomposites with Si (45), Sn (46), and transition metal oxides (TMOs) (47; 48; 49). Graphene synthesis can be divided in two groups, i.e.: bottom-up synthesis and top-down exfoliation of graphite. Bottom-up approach is usually achieved with epitaxial-growth with structure defined precursor or with chemical vapour deposition (CVD) (36; 50; 51). With this routes, high quality, purity, and defect-free graphene can be obtained. However, the expensive reagents and equipment coupled to limited scalability restrict the use of this type of graphene only for fundamental research and niche applications (43). The most common top-down approach is the Hummer's method (52). It consists in the oxidation of graphite to graphite oxide in a strong oxidant environment. In this way, the interlayer distance between graphene planes increases, weakening the Van Der Waals forces and eventually separating them via sonication. Once graphene oxide (GO) is obtained, the sp^2 carbon network can be restored via chemical, thermal or electrochemical reduction (53). With this method, large quantities of graphene can be produced, however, the product is rich in defects and functional groups.

Carbon nanotubes (CNTs) were discovered in 1991 and consist of one-dimensional carbon nanostructures (54). At first sight, the structure recall one of a cylinder with one or more walls,

obtained by wrapping a single or few layer graphene, respectively. Up to now, CNTs are mainly used in the synthesis of nanocomposite to ensure a continuous and efficient conducting pathway in the electrode (55).

Disordered carbon. Different from the previous case, ordered carbon does not present long-range order in planes or along the stacking direction. It can be described as sp^2-hybridized carbon networks randomly positioned and partially crosslinked with sp^3-hybridized carbon. The degree of crosslinking and graphitization possibility subdivide the class of disordered carbon into two other subclasses i.e., hard carbon and soft carbon. In the former case, the crosslinking degree is so high that even at high temperature (3000° C) there is no movement of the sp^2 carbon domain and thus, no possibility to obtain graphite. This type of carbon is usually produced by thermal decomposition under inert atmosphere of organic precursors such as sucrose or glucose, or even from bio-waste. During pyrolysis, at relatively low temperature (250-500° C) there is the main mass loss assigned to the removal of heteroatoms (as O, S, N, etc.) as volatile product (as CO, CO_2, NO_2, SO_2, etc.). At temperature higher than 700° C the material can be considered carbonized; however, some functionalities and heteroatoms still persist and must be removed at higher temperatures (>1000° C) (32). This class of carbon can deliver a specific capacity ranging from 200 up to 800 mAh g^{-1} depending on the precursor material, pre-treatment conditions, pyrolysis temperature and environment (N_2, Ar or even under vacuum) (56). Furthermore, can be used as anode in sodium-ion batteries (NIBs) and potassium-ion batteries (KIBs) (56), and even as containment matrix for Si anode (57; 58). In the case of soft carbon or graphitizing carbons, the graphite structure develops continuously upon thermal treatment thanks to the lower degree of crosslinking and thus, relatively higher mobility of sp^2 carbon domains. They can be prepared from pyrolytic compounds rich of aromatic functionalities such as pitch, petroleum coke, etc. Heat-treatment below the graphitization temperature will lead to turbostratic disordered carbon in which lithium cannot be readily accommodated and thus, low specific capacities are observed.

Titanium-based materials

Another important class of materials belonging to the insertion reaction family are the titanium-based materials. In the last years they became quite important thanks to their properties such as biocompatibility, natural abundance, readiness to bulk production, and long cycle life (59; 60). They can be divided into two classes i.e., the polymorph TiO_2 and the spinel $Li_4Ti_5O_{12}$ (LTO), shown in **Figure 1-8**.

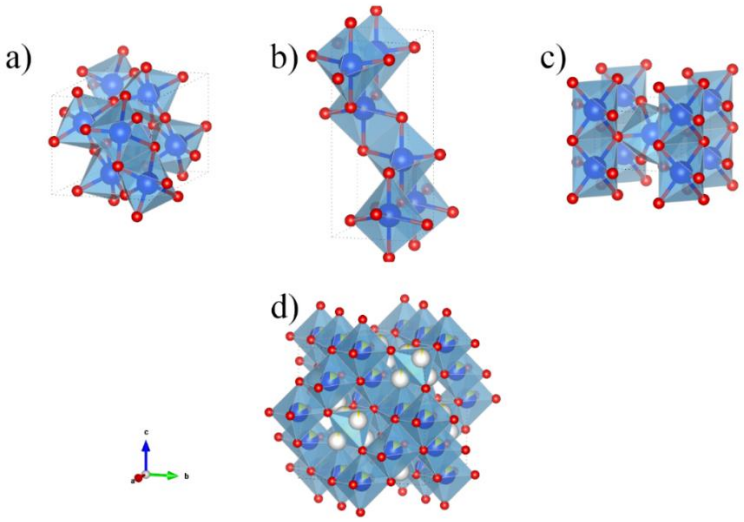

Figure 1-8. Crystal structure of a) brookite TiO_2, b) anatase TiO_2, c) rutile TiO_2 and d) spinel $Li_4Ti_5O_{12}$

In both materials, the intercalation reaction takes place at a relatively high working potential of E > 1.5 V vs Li^+/Li. This can lead to significant improvements in terms of safety by eliminating the risk of lithium plating and dendrite formation. Furthermore, the SEI is not formed at such high potential, which means that there is a negligible irreversible specific capacity in the first cycle and thus, no loss of cyclable lithium. However, they need to be coupled with high-voltage cathodes to have an energy density competitive with other LIB chemistries.

TiO_2 polymorphs. TiO_2 is a promising anode material thank to its biocompatibility, cost, and readiness to bulk production. Indeed, it has been targeted as possible anode material for LIBs in HEV (61). It has a theoretical specific capacity similar to graphite of 330 mAh g^{-1}, corresponding to 1 mole of Li per mole of TiO_2. However, such value has never been reached experimentally, with the limitation for micro-sized TiO_2 at ≈ 170 mAh g^{-1}, corresponding to 0.5 mole of Li per TiO_2 (62). To improve the electrochemical properties of TiO_2, the effect of different crystal structures was tested along with different particle sizes and specific surface areas (63; 64; 65). TiO_2 has eight known crystal structures i.e., brookite, anatase, rutile, TiO_2-R, TiO_2-B, TiO_2-H, TiO_2-II, and TiO_2-III. Among them, rutile, anatase, and TiO_2-B are the most studied TiO_2-based anodes in the LIBs research field. Rutile has a crystal structure with tetragonal symmetry and space group $P4_2/mnm$ with TiO_6 octahedra sharing edges in the c-axis direction. Only a small amount of Li can be inserted in rutile-TiO_2 (≈ 0.1 mole of Li per mole of Ti), due to the Li diffusion into rutile, which is favorable only along the c axis channels and hindered in the ab planes (66). TiO_2-B crystal structure belongs to the monoclinic family with a space group *C2m.* TiO_2-B can store Li without

any volume change thanks to its "open" crystal structure. Furthermore, a pseudocapacitive behavior has been reported, which can be translated in higher diffusion rate and higher rate capability (61). Anatase, as rutile, has a tetragonal structure with a space group $I4_1/amd$. Anatase is the preferred crystal structure for LIBs application since it can exceed the stoichiometry of $Li_{0.5}TiO_2$ ($Q \geq 170$ mAh g^{-1}). Furthermore, the intercalation reaction is accompanied with a small volume change of 4 %, thanks to the simultaneous increase and decrease of the b-axis and c-axis lattice parameter, respectively (67).

Reducing the particle size of anatase TiO_2 is an effective way to enhance its electrochemical properties, improving the specific capacity and the rate performances (66). As the particle size decreases, the surface area increases and the diffusion path is shortened, improving the diffusion of Li^+ ions and electrolyte access. Indeed, in (64), a comparison study of anatase TiO_2 from micro- to nanoparticles evidenced how using smaller particles greatly enhance the specific capacity and rate capability (68). It has been proven that particles with Ø $\leq$ 7 nm can be fully transformed in Li_1TiO_2, and thus reaching the maximum theoretical specific capacity (64).

Spinel $Li_4Ti_5O_{12}$. Another important Ti-based material for LIBs is the spinel $Li_4Ti_5O_{12}$ (LTO), also known as "zero-strain material" for its negligible volume change during (de-)insertion reaction and outstanding stability upon cycling. Its working potential is close to the one of TiO_2, with a value of ≈ 1.55 V vs Li^+/Li, which can be translated in no SEI formation and no Li plating/dendrite. The only disadvantage is the relatively low specific capacity of 175 mAh g^{-1}. Despite its drawbacks, LTO-based cells are already produced by EnerDel and Toshiba group for its HEV battery modules thanks to its power capability, safety, and reliability (69). LTO crystallizes in a spinel structure with a $Fd\bar{3}m$ and a cubic symmetry (70). The oxygen ions occupy the 32e sites. Lithium ions are in the tetrahedral 8a sites and ⅛ of octahedral 16d sites, while the remaining ⅝ sites are occupied by the tetravalent Ti^{4+} ions. The tetrahedral 8b and 48f sites along with the octahedral 16c sites are unoccupied and available for insertion reaction (71). The insertion of Li^+ ions into LTO is summarized in **Equation 9**.

$$Li_4Ti_5O_{12(spinel)} + 3Li^+ + 3e^- \rightarrow Li_7Ti_5O_{12(rock-salt)} \qquad \textbf{Eq. 9}$$

During the insertion reaction, the tetravalent Ti^{4+} ions are reduced to Ti^{3+} and there is the topotactic transition from a spinel structure to a rock-salt one. The insertion reaction can be

electrochemically observed as a long plateau at 1.55 V vs Li^+/Li in galvanostatic profiles and as a sharp peak in potential-controlled techniques, due to the two-phases transition.

As already mentioned, LTO has many advantages such as safety, negligible volume change, reliability, and improved stability. However, since Ti is present at its highest oxidation state of 4+, LTO possesses a relatively low electronic conductivity which hinders the practical specific capacity to values ranging from 140 up to 160 mAh g^{-1}. As for the polymorph TiO_2, several strategies have been implemented to improve its electrochemical properties i.e., reduction of particle size to nanometer range (72), ion lattice doping (73; 74; 75), and surface coating (76; 77). For instance, the partial substitution of Li^+ in the tetrahedral 8a sites with the Zn^{2+} ions or the partial substitution of Ti^{4+} with V^{5+} in the octahedral 16d sites, can lead to a mixture of Ti^{4+}/Ti^{3+} as charge compensation, and thus increase the local electrons concentration (73; 74; 75). With the synthesis of nanostructured LTO, the Li^+ diffusivity as well as the electronic conductivity are almost unaltered. However, thanks to a larger surface area, and thus a larger electrode/electrolyte contact area, the kinetics of the insertion reaction can be improved (78; 79). At last, surface coating with conductive materials such as conductive carbon (76) or conducting polymers (77) can greatly improve the electrochemical properties of LTO in terms of capacity retention, rate capability, and specific capacity.

Conversion anodes

Anode materials based on the conversion reaction are a relatively new concept respect to other two families of (de-)intercalation and (de-)alloying materials. Indeed, they were discovered only in 2000 by Prof. Tarascon group (80), which reported the very first reversible storage of Li in nanosized TMOs anode. This late discovery was due to the fact that TMOs and sulfides were discarded due to the lack of presence of vacancies, and thus for their inability of intercalating lithium. However, these phases started to be taken into consideration after being proven their ability to store Li with specific capacities up to three times of carbon materials. Since then, binary compounds M-X, with X = O, F, N, P, S, and even H have been studied as alternative anode materials (27). The key factor, which ensure the reversibility of the conversion reaction, is that upon full lithiation there is the formation of the metal nanoparticles possessing large specific surface area. Therefore, when the polarization is reversed (discharge of the full cell) they are quite active towards the decomposition of the Li_nX matrix in which they are embedded. The working potential of conversion anode materials strongly depends on both M and X species, and thus the

ionicity of the M-X bond (81) (**Figure 1-9**). Indeed, by changing the anion, the working potential can be tailored for specific applications.

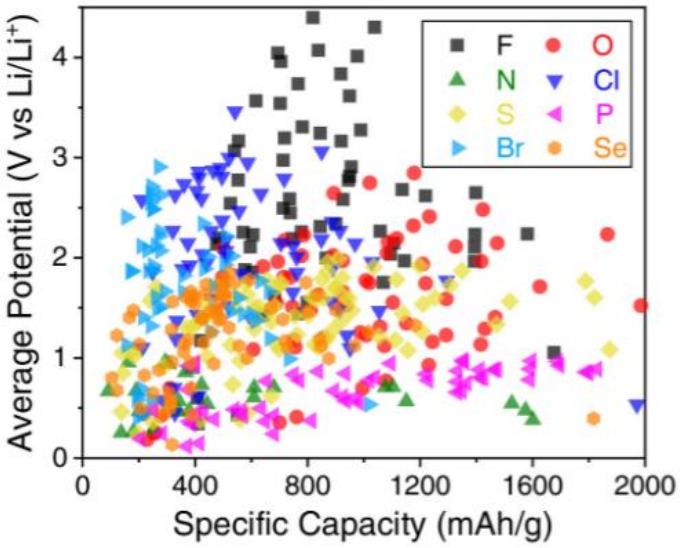

Figure 1-9. Working potential (V vs Li^+/Li) as a function of the anion used in conversion materials. Image taken from (81).

As clearly depicted in **Figure 1-9**, compounds containing halides have working potential higher than 2 V vs Li+/Li and, therefore, are mainly studied as cathode materials for Li metal batteries (82). Oxides and sulfides work at an intermediate potential, while nitrides and phosphide commonly react at rather low potentials.

Their "electrochemical fingerprint" is characterized by sloping lines in the galvanostatic profiles, with a length equivalent to the amount of Li stored, and broad peaks in potential controlled techniques. In some cases, very large capacities can be obtained with metals able to electrochemically form alloys with Li such as In, Sn, Ge, Pb, Sb, and Bi (83; 84; 85). In that case, a higher amount of Li is stored, and the average working voltage is lower than conventional conversion materials. Despite their appealing properties, their practical use in commercial cells is still hindered because of the poor capacity retention, due to the volume and structural change during charge/discharge, and thus pulverization of the electrode along with loss of electrical contact. Furthermore, the conversion and oxidation reaction are accompanied by a large voltage hysteresis which lower the energy efficiency of the charge/discharge cycle.

Iron Oxide anodes. Iron oxide-based electrodes are attractive candidates because of their cost, earth crust abundancy, and biocompatibility (86). Their specific capacities range from 744 mAh g^{-1} for FeO (87) up to 1007 mAh g^{-1} for Fe_2O_3 (88). In addition, thanks to their high density, the obtained volumetric capacities are much higher than that of graphite (88). Thanks to their

properties, several researchers focused their efforts on the study of novel and sustainable iron oxide-based batteries (27). As an example, in (89) Prof. Edström proposed a novel, green, and fluorine-free LIB based on iron oxide anode coupled to an $LiFePO_4$ (LFP) cathode.
However, as other conversion materials, issues such as poor capacity retention, and high voltage hysteresis must be addressed. The former is usually addressed by (i) employing nanostructured materials (90; 91; 92), to have free space for the structural change, or (ii) by synthesizing nanocomposite with active or inactive matrices able to withstand the volume changes upon cycling. The latter is mainly addressed by tailoring the cycling parameters of the electrode and pre-lithiation (89; 93).

Tin oxide anodes. Tin oxide-based electrodes are attractive candidates thanks to the extra capacity given by the alloying reaction of Li with tin metal (94). Furthermore, since the potential of the alloying reaction is at ≈ 0.2 V vs Li^+/Li, the resulting average working potential is lower than "pure" conversion materials, which means higher energy density in full cell setup (94). The overall reaction mechanism is summarized in **Equations 10-11**.

$$SnO_2 + 4Li^+ + 4e^- \rightarrow Sn^0 + 2Li_2O \quad (conversion\ reaction, partially\ reversible) \quad \textbf{Eq. 10}$$

$$Sn^0 + 4.4Li^+ + 4.4e^- \leftrightarrow Li_{4.4}Sn \quad (Alloying\ reaction, fully\ reversible) \quad \textbf{Eq. 11}$$

SnO_2 possess a theoretical specific capacity of 1494 mAh g^{-1} which is the result of the sum given by the conversion reaction (711 mAh g^{-1}) and the alloying reaction (783 mAh g^{-1}). However, the practical specific capacity does not reach the theoretical one because the conversion reaction is only partially reversible (95). This behavior can be attributed to several reasons i.e., (i) formation of large metal particles which hinder the kinetic of the conversion reaction and isolate itself from the Li_2O matrix (95), and (ii) larger energy barrier for the oxidation reaction compared to other transition metal oxides (95). This is mainly due to the larger atomic radius and lower temperature of recrystallization of Sn (T = 224 K) compared to other TMs (86). This will inevitably lead to coarsening and migration of Sn^0 particles towards the surface of the electrode. For these reasons, the synthesis of nanostructured SnO_2, along with caging it in active or inactive matrices, is of paramount importance to maintain a close contact between Sn and Li_2O and avoid Sn particle coarsening. Furthermore, when Sn performs the alloying reaction there is a volume expansion of ≈ 300 % which must be considered.

Alloying anodes

The study of metals and semimetals able to electrochemically form alloys with Li and other alkali metal was conducted parallel to the discovery of intercalation materials in the 70s. Indeed, the first trial to substitute Li metal was done by employing a Li-Al alloy (96), which solved the dendrite issue, but as discussed earlier, alloying electrodes suffer of large volume expansion, and thus poor capacity retention. Three cluster of elements can form alloys with Li i.e., alkali earth metals, transition metals, and p-block metals and metalloids. In **Figure 1-10**, a periodic table with highlighted the elements able to form alloys with Li is shown.

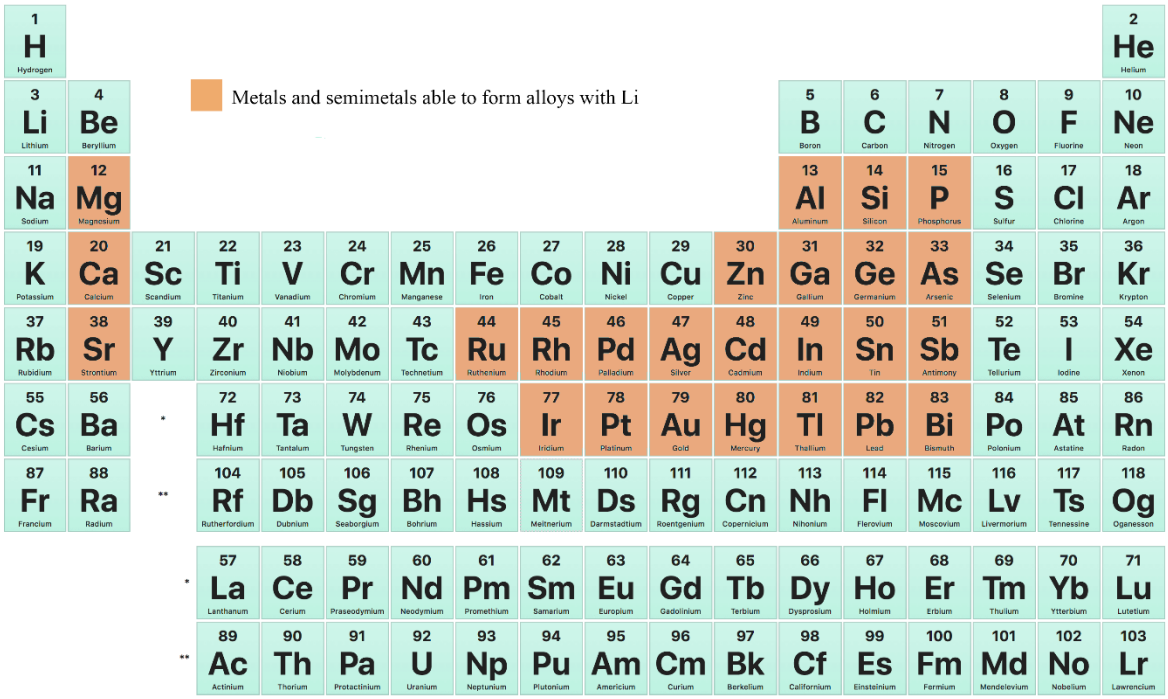

Figure 1-10. Periodic table with highlighted the elements able to electrochemically form alloys with lithium

The study of the alloying reaction of Li with alkali earth metal has received poor attention, probably due to the intrinsic poor kinetic of the reaction and the air sensitivity of the materials. Among them, Mg has been the most studied, especially as component in alloys with Si (97; 98). Between transition metals, only Zn and Ag seems to be viable options. In the other cases, high cost and toxicity hindered their practical use and study (98). On the p-block, the carbon group and the pnictogens brought a lot of interest and, in some cases (Si and Sn), they have been used in commercial LIBs. Indeed, a Sn-based anode was included in the "Nexelion" battery commercialized by Sony in 2005 (99), while silicon has been appointed as the anode material of

choice for the upcoming LIBs generations 3a and 3b, as mixture with graphite or nanocomposite with carbon, respectively (100).

Common attractive features of alloying materials are the low working potential in the range of 0.2 – 1 V vs Li^+/Li, which overcome the penalty given by Ti-based and conversion materials, and the large specific capacities ranging from 700 up 3579 mAh g^{-1} (given by Si forming the phase $Li_{15}Si_4$). However, the alloying reaction is always accompanied by a large volume expansion which can lead to loss of electrical contact because of the particle detachment, and pulverization of the electrode. Several strategies have been implemented to overcome this issue by acting not only on the anode materials itself, but also optimizing other cell components such as the electrolyte, the binder, and the current collector. In the former case, nanostructured materials can offer free space to accommodate the volume expansion (101). Other common ways are the use of nanocomposite with active or inactive matrices able to withstand the volume stresses (102) or employing alloys with active or inactive metals (98). Specific reductive additives such as VC and FEC have been implemented in the electrolyte to build a more robust SEI (103). The PVdF binder is being substituted by green water-processable polymer with improved mechanical properties such as Na-carboxymethyl cellulose and polyacrylic acid (104; 105). At last, nanostructured current collector have been proven to partially release the stresses given by the volume expansion (106).

1.1.1.2 Cathode materials

The cathode material is the positive electrode in which the oxidation reaction takes place during charge. Commonly it acts as Li^+ sources, so that Li-free anode materials can be used on the other side. Cathode materials should satisfy the following requirements (107):

- High working potential to maximize the energy density of the full cell.
- Stable structure to ensure the reversibility of the (de-)insertion reaction.
- Chemical stability and compatibility with the electrolyte at high potential.
- Reasonable electronic and ionic conductivity to improve the rate performance and lower the energy barrier of the insertion reaction, respectively.
- Low cost, nontoxic, and environmentally friendly.

The most used cathode materials are oxides of lithium with transition metals, and their reaction pathway belongs to the family of the intercalation reaction. Only for the next generations of LIBs

(gen. 4 and 5 (108)) conversion cathode materials such as S_8, O_2, FeF_3 will be implemented. However, their practical use is still hindered by the poor reversibility of the conversion reaction (109).

The insertion cathode materials can be divided into three classes according to their crystal structure, and thus Li diffusion pathway i.e., (i) olivine compounds with a 1-D Li-diffusion pathway, (ii) layered oxides with a 2-D Li-diffusion pathway, and (iii) spinel oxides with a 3-D Li-diffusion pathway (97; 107). In **Figure 1-11**, the three classes of insertion cathode materials are shown.

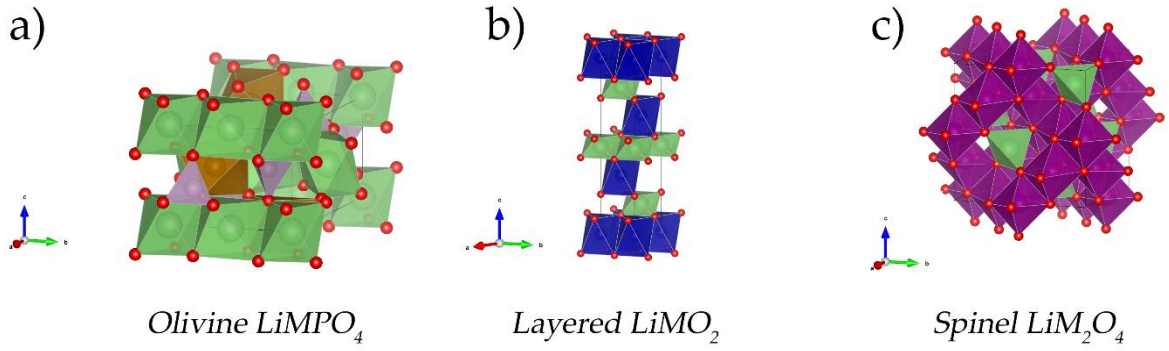

Figure 1-11. Crystal structure of a) olivine $LiMPO_4$, b) layered $LiMO_2$, and c) spinel LiM_2O_4

Layered oxides. The layered oxide with the general formula of $LiMO_2$, with M = Co, Ni, Mn, or a combination of them, are the most used cathode materials in commercial LIBs. They crystallize with a trigonal structure as α-$NaFeO_2$ with a space group *R3m* in which Li and M atoms are located at the octahedral sites of alternating layers with ABCABC as stacking sequence. This structure is also known as O3-type according to Delmas nomenclature (110), in which Li^+ ions are inserted in octahedral sites. The first studied material belonging to this class was $LiCoO_2$ proposed by J. Goodenough et al (25). It was commercialized by Sony in 1991, and since then is still used in LIBs for portable electronics. The theoretical specific capacity of $LiCoO_2$ is 274 mAh g^{-1}, calculated as the extraction of 1 mole of Li. However, extracting more than 0.5 mole of Li from $LiCoO_2$ will result in an irreversible structural change from trigonal to monoclinic, and thus the practical specific capacity is limited in the range of 130 – 150 mAh g^{-1}. Nowadays, $LiCoO_2$ is being substituted by other layered oxides because of the low specific capacity, cost, the toxicity of Co, and its limited sources (mainly presents in area subjected to geopolitical risks) (107). Dahn et al (111) proposed as an alternative $LiNiO_2$, which is isostructural of $LiCoO_2$ having as advantages

higher volumetric and specific capacities, and raw material cost. However, its practical use has been impeded by the tendency of nickel to migrate to the Li sites. To overcome these issues, as well as lowering the Co content, the combination of Co, Ni, and/or Mn has been investigated. Several compounds with the general formula of $LiNi_yM_{1-y-x}Co_xO_2$ (NMC) have been studied, reporting improved structural stability and lower costs due to the lower content of Co.

Spinel oxides. Compared to layered oxides, spinel oxides represent a safer, and cheaper alternative. The first material proposed in literature was $LiMn_2O_4$ (LMO) by Thackeray et al. (112). It possesses a cubic structure with a space group $Fd\bar{3}m$ in which Mn and Li occupy the octahedral 16d and the tetrahedral 8a sites, respectively. Oxygen ions are placed in the 32a site. The main issue of this material is the capacity fading upon cycling. This phenomenon is due to two causes i.e., (i) Mn^{2+} dissolution, and (ii) Jahn-Teller effect. In the first case, the disproportionation of Mn^{3+} will lead to the formation of Mn^{2+} and Mn^{4+}. The former is soluble in the electrolyte, and thus there is the loss of the redox center and capacity. In the second case, when the concentration of Mn^{3+} (d4) increases, the crystal symmetry changes from cubic to tetragonal, which will inevitably lead to poor electrochemical performances. Another important spinel oxide cathode is $LiNi_{0.5}Mn_{1.5}O_4$ (LNMO). Its average working potential is 4.8 V vs Li^+/Li thanks to the partial substitution of Mn with Ni^{2+} (113). Furthermore, it possesses a specific capacity of 147 mAh g^{-1}, making it an attractive cathode material for the next generation batteries (100). This material can crystallize into two different crystal structure according to the annealing temperature i.e., the face-centered cubic phase with space group $Fd\bar{3}m$ also called disordered phase, and the primitive cubic with space group $P4_332$ known as ordered phase (114). Despite the appealing properties, issues such as surface instability given by Li-rich and Li-poor domains, Mn^{2+} dissolution, and electrode/electrolyte interphase instability must be overcome to reach commercialization.

Olivine phosphates. Olivine phosphates cathode materials were firstly proposed by Goodenough et al. in 1997 (115). Among them, triphylite $LiFePO_4$ has attracted particular attention thank to its properties such as safety, stability upon cycling, low raw material cost, and good thermal and chemical stability. It crystallizes with an orthorhombic structure with space group Pnma, in which both Li and Fe ions occupy the octahedral sites, P occupies the tetrahedral site, and O ions are in hexagonal close-packed arrangement. The theoretical specific capacity is 170 mAh g^{-1}, corresponding to the extraction of 1 mole of Li per formula unit. The insertion/extraction reaction

is characterized by a flat plateau at ≈ 3.4 V vs Li^+/Li, indicating a two-phases region reaction. The principal issues of this material are the rather low working potential compared to other cathode classes, the poor electronic conductivity, and the limited Li^+ ions diffusion. For these reasons, LFP-batteries have been commercialized mainly for stationary storage in which the power demand is low and the energy efficiency as well as safety are the priorities.

Phosphates with higher working potential have been thorough studied. In particular, the partial or complete substitution of Fe with Mn can increase the working potential up to 4.1 V vs Li^+/Li, while the complete substitution of Fe with Co can increase the working potential as high as 4.8 V vs Li^+/Li (116).

1.1.1.3 Electrolyte

The electrolyte is an essential component in every electrochemical device and is the medium which allows the flow of the ionic current between the electrodes. Several battery properties rely on the electrolyte such as the working temperature, charge and discharge cut-off voltage, rate capability etc. A good electrolyte must satisfy the following requirements:

- High ionic conductivity ($\sigma_{Li} > 10^{-4}$ S cm^{-1}) to minimize the internal resistance in the widest temperature range.
- Low electronic conductivity ($\sigma_e < 10^{-10}$ S cm^{-1}) to avoid short-circuit between the electrodes.
- Low viscosity.
- Chemically stability and lack of reactivity towards the other cell components.
- Wide voltage range, larger than the anode and cathode working potentials.
- Cheapness, acceptable safety characteristic and environmental benignity.

The electrolyte can be either liquid, solid, or a hybrid. Liquid electrolytes are constituted by two components i.e. the Li salt and the solvent. The Li salt provide the charge carriers needed for the ionic current flow, while the solvent must be able to dissolve high amount of salt while having a low viscosity and a wide working temperature range. The most used electrolyte in LIBs is a solution of $LiPF_6$ dissolved in a mixture of carbonate solvents. Despite the issues connected with the use of $LiPF_6$, it is the most used Li salt because of a compromise between electrochemical properties and safety. The other candidates such as $LiAsF_6$, $LiClO_4$, and $LiBF_4$ cannot be used because of their toxicity, fire hazard, and poor passivation properties, respectively (117). The solvent choice is restricted to polar organic aprotic solvent, since water cannot be used due to

large cell potential and acidic protons can lead to H_2 formation. In particular, polar solvents based on ethers, esters, and alkyl carbonate are the most used in battery applications. Their anodic stability is ethers < esters < carbonates (118). Furthermore, ethers and esters cannot be used with carbon anode due to their poor passivation properties. For these reasons, the most used solvents are a mixture of alkyl carbonate (**Figure 1-12**), able to ensure a low viscosity, a high conductivity, and a wide working temperature range.

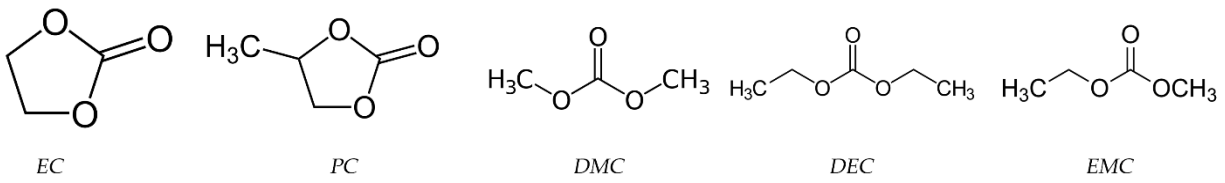

Figure 1-12. Structure of the main carbonate-based solvent used in LIBs

Ethylene carbonate is the most used solvent thanks to its high dielectric constant (≈ 89) higher than that of water (≈ 79). Its use in LIBs electrolytes was established in 1990 by Dahn et al., which reported the electrochemical behavior of a mixture of EC and PC with graphitic anodes (119). Thanks to its high passivation ability, the EC-derived SEI was able to block any further solvent decomposition and co-intercalation of PC into graphite, which can lead to its exfoliation and electrode pulverization. However, EC is solid at room temperature and must be mixed with other alkyl carbonate-based solvents. Nowadays, common electrolyte solutions include $LiPF_6$ as Li salt in a binary mixture of EC with DMC, DEC, or EMC. Ternary mixtures are often used in batteries working at low temperature. Furthermore, additives (from 2 % up to 10 % by weight) such as vinylene carbonate (VC) or flurorethylene carbonate (FEC), which gets reduced before the SEI formation, can be used for the buildup of a more flexible SEI (120).

1.1.2 Sodium-ion batteries

In 2018, 70 % of LIBs produced worldwide were used in EVs application. By forecasting the transport electrification market growth, 25 % of the Li reservoir will be depleted by 2025 (121). Furthermore, the recycling rate of Li from spent batteries is still rather low (≈ 1 %) (122). For these reasons, an alternative battery technology based on cheaper, sustainable, and more abundant elements is needed.

Sodium is the 4th most abundant element worldwide with unlimited resources everywhere, even seawater and salts deposit can be taken into consideration as reservoirs. In **Table 3**, a comparison of Li and Na properties is reported.

Table 3. Comparison of Li and Na properties

Characteristic	**Lithium**	**Sodium**
Cation radii	0.7 Å	1 Å
Carbonate-based cost	5000 $ ton^{-1}	150 $ ton^{-1}
Capacity	3829 mAh g^{-1}	1165 mAh g^{-1}
Voltage vs SHE	-3.04	-2.71
Availability	Limited places: Chile, Australia, Argentina and China	Everywhere. Sea water can be a possible source

Thanks to the availability of Na, its similar chemical properties to Li as well as its cheaper price, Na-based batteries have attracted considerable attention as potential alternative energy storage to LIBs (123).

The research of Na-based batteries started in the same period as LIBs. Indeed, the first reversible intercalation of sodium in layered TiS_2 was reported in 1980 (124), right after the work of Whittingam et al. with Li metal. In the same period, Braconnier et al. (125) proposed the layered Na_xCoO_2 as cathode material. However, the rapid development of LIBs eclipsed further development of NIBs in that period of time. Prior to commercialization of the first LIBs by Sony, few US and Japanese companies proposed a Na battery which employed a Na-Pb alloy and Na_xCoO_2, as anode and cathode, respectively (126; 127). However, the nominal voltage (E < 3 V) was lower than that of carbon // $LiCoO_2$ (3.7 V), and thus it didn't attract much attention. The chemistry of Li and Na are quite similar, apart from the standard reduction potential (-3.04 V vs SHE for Li and -2.71 V vs SHE for Na) and the larger ionic radii (0.7 Å vs 1 Å for Li and Na, respectively). These differences will inevitably lead to lower energy densities and rate performances of NIBs compared to LIBs. Despite these drawbacks, Na-based batteries can offer

some advantages over LIBs such as cheaper raw material costs (150 $ ton^{-1} for $NaCO_3$ vs. 15000 $ ton^{-1} for $LiCO_3$/ LME 30/08/2021), and Al current collector can be used in both anode and cathode, and thus lower the electrode production cost. Most of the research work for NIBs is based on the transposition of the acquired knowledge on LIBs in the alternative energy storage system. In the following sections, a description of the materials as well as the difference with LIBs counterpart is given.

1.1.2.1 Anode materials

As in the case of Li metal, use of Na metal is hindered by safety issues such as dendrite formation, which can lead to short-circuit in prolonged cycling. In this regard, several materials which can act as host for Na^+ have been developed and tested (128; 129). Their classification follows the same rules applied to Li anodes materials i.e., insertion anodes, conversion anodes, and alloying anodes.

Carbon based materials

While graphite is the state-of-the-art anode material in LIBs, its electrochemical properties with Na are rather poor. In fact, when sodium is intercalated into graphite, poor specific capacities of 30-50 mAh g^{-1} are observed (130; 131). Computational studies suggest that the formation of highly sodiated graphite compounds such as NaC_6 or NaC_8 is thermodynamically not favorable (132). However, as demonstrated by Adelhelm et al., the reversible co-intercalation of Na and diglyme can be used to improve the specific capacity up to 100 mAh g^{-1} (133). Despite the high reversibility of the co-intercalation reaction, the specific capacities obtained are too low for practical applications. In this regard, the storage of Na^+ ions into disordered carbon has shown promising results, with specific capacities higher than that of graphite. Indeed, in 2000 Dahn et al. demonstrated that hard carbon obtained by the pyrolysis of glucose can achieve specific capacities as high as 300 mAh g^{-1} (134). Since then, several hard carbons produced from different and sustainable sources such as biowaste have been studied (135; 32).

Titanium based materials

As for LIBs, Ti-based materials have been thoroughly studied as anode candidates in NIBs. The sodiation reaction mechanism of anatase TiO_2 is strongly different from the lithiation. At first, a

metastable sodium titanate phase is formed, which is then converted as Ti^0, sodium superoxide, and an amorphous titanate phase (136). The maximum content of Na per formula unit is 0.69. However, the reversible content which can be extracted is only about 0.41.

The reversible intercalation of Na^+ ions in LTO has been demonstrated (137). The material was able to deliver a specific capacity of 145 mAh g^{-1} with an average potential of 1 V vs Na^+/Na. In this case, the intercalation reaction occurs through a three-phase reaction according to **Equation 12**.

$$2Li_4Ti_5O_{12} + 6Na^+ + 6e^- \rightarrow Li_7Ti_5O_{12} + Na_6LiTi_5O_{12} \qquad \textbf{Eq. 12}$$

As a result of the large ionic radii, Na^+ ions tend to occupy the octahedral 16c sites, leading to a phase separation giving the two rock-salt phases $Li_7Ti_5O_{12}$ and $Na_6LiTi_5O_{12}$ (137).

Another important Ti-based material for NIBs is $Na_2Ti_3O_7$, which can store up to 2 mole of Na per unit formula at the average potential of 0.3 V vs Na^+/Na (138).

Conversion materials

As for LIBs, transition metal oxides, sulfides, and phosphides have been thoroughly studied as potential anode candidates. They follow the same reaction mechanism, in which the transition metal is reduced and there is the formation of Na_2O matrix. However, they suffer from the same issues as in LIBs i.e., large voltage hysteresis, and the structural change which can lead to the electrode pulverization. In addition, in some cases the conversion reaction does not go to completion because of the formation of a dense Na_2O layer, which acts as a transport barrier; hence, specific capacities lower than the theoretical ones are observed (139). The strategy to overcome these issues rely on the use of nanostructured materials, nanocomposite materials, and surface coatings (129; 140).

Alloying materials

Metal and semi-metals of the carbon and pnictogens group can electrochemically form binary Na_xA compounds via the alloying reaction. These alloys are quite attractive as potential anode materials thanks to their relatively low working potential compared to Ti-based and conversion materials, as well as their high specific capacity. Even if c-Si has been appointed as the next gen anode material for LIBs, it cannot accommodate Na^+ ions into its structure (123). Computational

studies proved that a-Si can accommodate 0.76 Na^+ ions per mole of Si with a resulting specific capacity of 725 mAh g^{-1} (141); however, this value has never been reached experimentally. For these reasons, Sn and Sb have been appointed as the alloying anode materials of choice for sodium-ion batteries. Sn has a promising theoretical capacity of 847 mAh g^{-1} which correspond to the stoichiometry of $Na_{15}Sn_4$. The reaction mechanism occurs via a series of two-phase reaction steps: β-Sn, $NaSn_2$, a-$Na_{1.2}Sn$, $Na_{5-x}Sn_2$, and $Na_{15}Sn_4$ (142). In addition, micrometric Sn particles have shown a highly reversible sodiation when glyme-based electrolytes are used, maintaining specific capacity of 800 mAh g^{-1} for 50 cycles (143). Sb can deliver a specific capacity of 660 mAh g^{-1} based on the stoichimetry of Na_3Sb. The reaction mechanism involves the amorphization of c-Sb upon sodiation, in which an amorphous $Na_{1.7}Sb$ appears as intermediate phase. At the end of the reduction, a crystalline Na_3Sb phase is formed (144). However, the large ionic radii of Na^+ can lead to volume expansions higher than the one encountered on the Li counterpart. As a result, several morphologies as well as containment active/inactive matrices have been studied to improve the structural stability of the electrodes.

1.1.2.2 Cathode materials

Thanks to the similar chemistry of Li and Na, comparable Na counterparts of LIBs cathode materials have been studied in Na cells. Therefore, in the last decade several cathode materials have been proposed as potential candidates for practical applications (145); they can be divided in layered oxides, polyanionic compounds, prussian blue analogs, and organic compounds. Several improvements are still needed in terms of structural stability, kinetic of Na insertion/extraction, and electronic conductivity as well as ionic conductivity (146).

Layered oxides

Layered oxides with the general formula of Na_xMO_2 (with M = transition metal) have been proposed by Braconnier et al. in 1982 (125). Their unique construction provides short Na diffusion path which can be beneficial for cycling stability and rate performances. As for LIBs, their structure can be divided in two groups (110): (i) O*n* types in which the alkali ions are located in an octahedral environment, whereas (ii) in P*n* types are in a prismatic environment. The number *n* indicates the number of transition metal layer per each unit cell. In **Figure 1-13**, the crystal structures of O3/P3 and O2/P2 types is shown (147). The sodium extraction from O3 type leads

to the formation of the corresponding P3 type, the same process occurs for the P2 type. However, the variation from the O3/P3 system to O2/P2 system and *vice versa* is not possible without breaking the M-O bonds (148; 149). The first studied material, Na_xCoO_2, can be synthesized in the three configurations O3, P2, and P3 depending on the amount of Na present in the structure. The P2-$Na_{0.7}CoO_2$ seems to be the best performing in terms of specific capacity (149).

Several O3-type materials such as $NaCrO_2$ and $NaFeO_2$ can intercalate Na^+ ions, even if they are electrochemically inactive with Li. However, as in the case of LIBs, extracting more than 0.5 Na mole per formula unit will results in irreversible structural change.

In addition, binary metal oxide systems have been studied as well to improve the structural stability and the Na insertion/extraction kinetic (145).

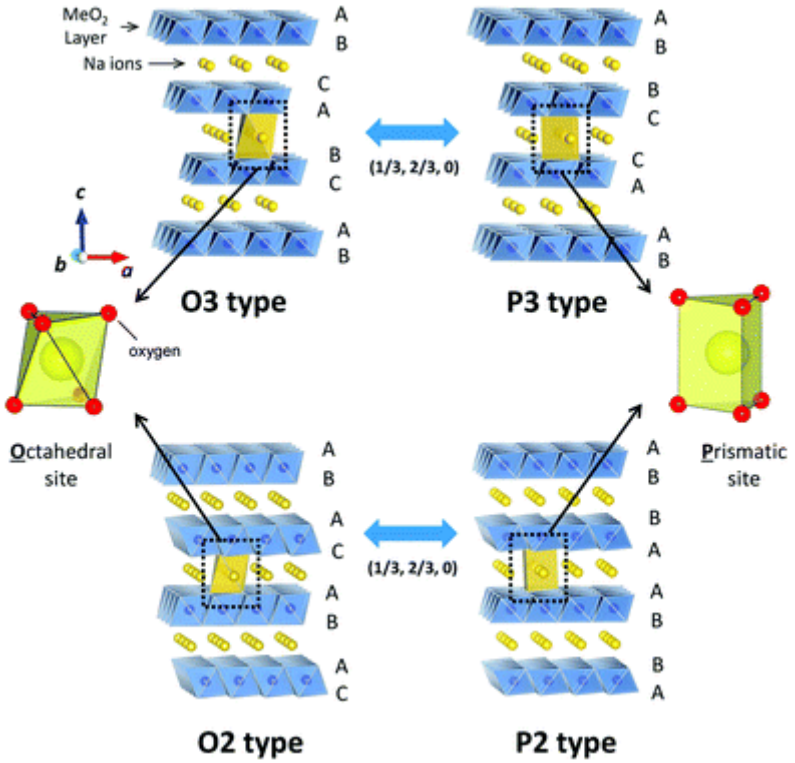

Figure 1-13. Crystal structures of layered Na_xMO_2 oxides and phase transitions between insertion and extraction of Na+ ions. Image taken from (147).

Polyanionic compounds

Polyanionic compounds refers to the family of cathode materials in which the anion can be generalized as $(XO_m)^{n-}$, with X = P, S, As, W, and other (150; 151). Among them, phosphates, NASICON (Na Super Ionic CONductor) phosphates, pyrophosphates, and fluorophosphates have attracted particular interest as potential cathode materials. The sodium counterpart of LFP, $NaFePO_4$ have been extensively studied in literature (152; 153). It can exist with two different

crystal structure i.e., (i) maricite $NaFePO_4$ which is electrochemically inactive, and (ii) triphylite $NaFePO_4$ which is active towards sodium insertion/extraction. However, the latter cannot be synthesized and must be obtained with the electrochemical delithiation LFP (154). In addition, the extraction mechanism is different compared to the lithium counterpart, with the formation of an intermediate phase $Na_{\approx 0.7}FePO_4$.

The NASICON type cathode materials have attracted particular interest thanks to their remarkable Na^+ conductivity, relatively high working potential, and thermal stability. They are characterized by the general formula $Na_3M_2(XO)_3$, in which X = Si^{4+}, P^{5+}, S^{6+}, Mo^{6+}, As^{5+} (150; 151). Among them, $Na_3V_2(PO_4)_3$ (NVP) has shown promising properties for practical applications (155). Moreover, thanks to the V^{3+} ions, it can act as both anode and cathode material. When employed as cathode material, two Na^+ ions can be extracted at about 3.4 V vs Na^+/Na with the oxidation of V^{3+} to V^{4+}. When employed as anode, one Na^+ ion can be inserted at about 1.6 V vs Na^+/Na with the reduction of V^{3+} to V^{2+}. Thanks to these features, symmetric cell employing NVP as both anode and cathode can be assembled.

1.1.2.3 Electrolyte

Analogous to LIBs, a good electrolyte for NIBs should display a high ionic conductivity, a low electronic conductivity, a large electrochemical window, chemical compatibility with other cell components, and at last thermal stability. Liquid electrolytes for both Li and Na share almost the same "recipe" thanks to the transposition of the scientific work done with Li. In fact, as early as 1980, electrolytes comprising $NaClO_4$, $NaPF_6$, or NaI dissolved in PC were already studied (156). However, some differences between the two systems are present. The solvent PC can be used in NIBs since there is no co-intercalation of it into hard carbon. In addition, the additive VC seems to be detrimental for the performance of a Na cell (157). The most used electrolyte in literature studies is 1 M $NaClO_4$ in PC, with few reports with $NaPF_6$ and other solvents (158). The formulation 1 M $NaPF_6$ in glyme solvent has attracted the interest of the scientific community since it allows the reversible sodiation of Sn without the need of nanostructured electrode nor nanocomposite formulation (143).

1.2 Electrochemical energy conversion systems

The term electrochemical energy conversion systems (EECS) comprehends all the devices which can convert electrical energy into chemical energy and *vice versa*. It includes systems able to generate electrical current from different sources such small molecule fuels and/or light radiation, or systems able to use electrical energy for producing small molecules which can be used as energy sources in other processes. The most studied technologies with commercial application in this regard are:

- Fuel cells (gas-to-power conversion).
- Electrolyzers (power-to-gas conversion).
- Photoelectrochemical cells (light-to-power conversion).

However, advanced systems such as the electrochemical reduction of CO_2 (159), electromethanogenesis (160), and electrohydrogenesis (161) attracted the attention of the scientific community in the last years for their ability to produce fuels such as H_2, CH_4, and HCOOH by a green process.

1.2.1 Fuel cells

Fuel cells have attracted a lot of attention from both the scientific community and the industrial market thanks to their high fuel-to-power efficiency. Indeed, since they are not subjected to the Carnot cycle, efficiencies as high as 40-50 % for energy conversion can be achieved. As shown in **Figure 1-3**, FCs offer higher-energy densities compared to Li-ion batteries at the expense of a lower rated power density. They have potential for various applications such as portable power, stationary electricity generation, and vehicle propulsion (162; 163). Several types of fuel cells exist, and their classification is based on the type of the ionic conductor (electrolyte) i.e., proton exchange membrane fuel cells (PEMFCs), direct methanol fuel cells (DMFCs), alkaline fuel cells (AFCs), phosphoric acid fuel cells (PAFCs), molten carbonate fuel cells (MCFCs), solid oxide fuel cells (SOFC), and protonic SOFCs. As shown in **Figure 1-14**, as the ionic conductor changes, the conducted ions, the electrode catalysts as well as the working temperature are different.

In addition, as the working temperature increases, the rated power increases, and fuels other than H_2 can be used (164). In the following section, an overview on SOFCs is given.

1.2.2 Solid Oxide Fuel cells

Two types of SOFC exist based on the electrolyte used i.e., SOFC in which the electrolyte is an oxygen-ion conductor (normally called SOFCs), and the relatively new protonic-SOFC in which the electrolyte is a H^+ ions conductor (H-SOFCs). In this thesis, the focus will be on SOFC in which the electrolyte is an O^{2-} ions conductor.

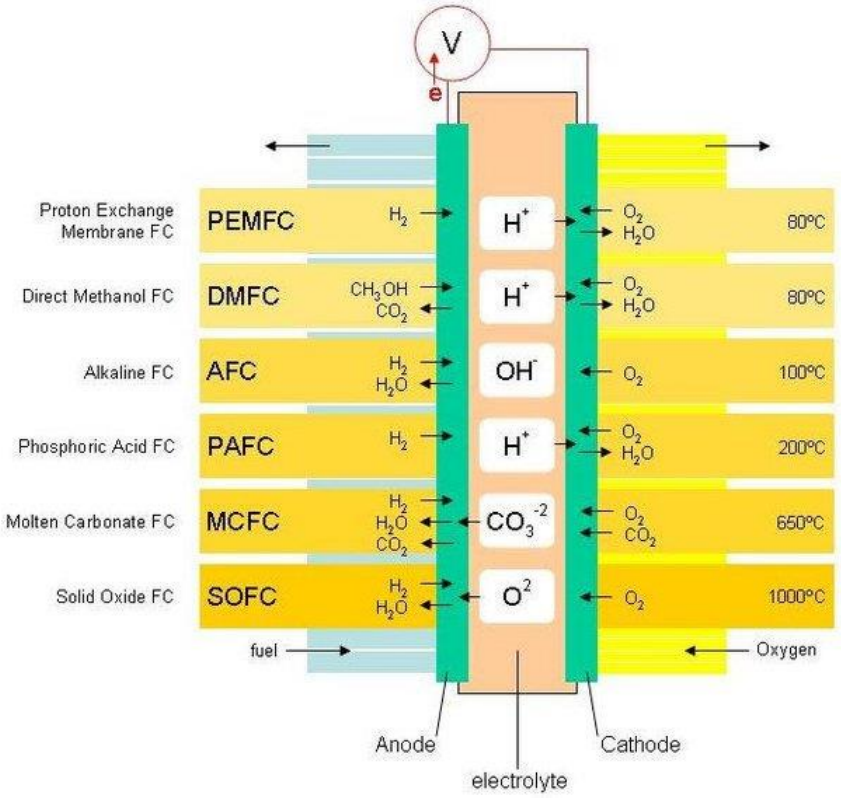

Figure 1-14. Different types of fuel cells classified according to the type of ionic conductor used.

Reduction of O_2 to O^{2-} ions occurs at the cathode side, in which a $La_{1-x}Sr_xMO_3$ (with M = Mn, Fe, and/or Co) catalyst is present. The O^{2-} ions are conducted by the electrolyte to the cermet anode in which the oxidation of the fuel (H_2) as well as the formation of the "combustion" product (H_2O in the case of H_2 is used as fuel) occurs. The electrolyte consists of a ZrO_2 doped with 8 % Y to stabilize the crystal structure (8-YSZ). The anode consists of Ni metal catalyst sintered with the 8-YSZ powder, also called cermet anode for having a metal embedded in a ceramic matrix. SOFCs have several advantages respect to the other classes of FCs (165): higher electric efficiency, and flexible designs for low- and high-power application (ranging from 1kW up to 1MW). Furthermore, they support the reversible operation (fuel cell + electrolyzer), which is interesting for coupling this technology with renewable energy production plants (166). At last, the heat involved during operation can be used for cogeneration (167). However, under real operation the

temperature and load variations (168), as well as fuels containing impurities (169) can pose serious threats for the cell life, involving side reactions and loss of performances. These problems could be more pronounced when the cell is used as electrolyzer or in reversible mode (reversible solid oxide cells, rSOCs) (170; 171). In this regard, the SOFCs lifetime can be increased by optimizing the cell materials and operating parameters. In the former case, the scientific community is focused on the development of materials with improved electrochemical properties, gas diffusion and porosity, as well as chemical and thermomechanical resistance. In the latter case, researchers are focused on diagnostic systems as well as optimized operating conditions to avoid irreversible damages on the cell. In this thesis work, the focus is on the characterization of polarization losses by means of electrochemical impedance spectroscopy and its use as diagnostic tool for the early detection of degradation phenomena. Further details will be given in section 4.

References

1. *Longer and more frequent marine heatwaves over the past century.* **E. C. J. Oliver, M. G. Donat, M. T. Burrows, P. J. Moore, D. A. Smale, L. V. Alexander, J. A. Benthuysen, M. Feng, A. S. Gupta, A. J. Hobday, N. J. Holbrook, S. E. Perkins-Kirkpatrick, H. A. Scannell, S. C. Straub, T. Wernberg.** 1324, 2018, Nature Communications, Vol. 9.

2. *An Ensemble Dta Set of Sea Surface Temperature Change from 1850: The Met Office Hadley Centre HadSST.4.0.0.0 Data Set.* **J. J. Kennedy, N. A. Rayner,C. P. Atkinson, R. E. Killick.** 14, 2019, Journal of Geophysical Research: Atmospheres, Vol. 124, p. 7719-7763.

3. *Extended Reconstructed Sea Surface Temperature, Version 5 (ERSSTv5): Upgrades, Validations, and Intercomparisons.* **B. Huang, P W. Thorne, V. F. Banzon, T. Boyer, G. Chepurin, J. H. Lawrimore, M. J. Menne, T. M. Smith, R. S. Vose, and H.-M. Zhang.** 20, 2017, Journal fo Climate, Vol. 30, p. 8179-8205.

4. *Vulnerability of coastal ecosystems to changes in harmful algal bloom distribution in response to climate change: projections based on model analysis.* **P. M Glibert, J Icarus Allen, Y. Artioli, A. Beusen, L. Bouwman, J. Harle, R. Holmes, J. Holt.** 12, 2014, Global Change Biology, Vol. 20, p. 3845-58.

5. **[P.R. Shukla, J. Skea, E. C. Buendia, V. M.-Delmotte, H.-O. Pörtner, D. C. Roberts, P. Zhai, R. Slade, S. Connors, R. van Diemen, M. Ferrat, E. Haughey, S. Luz, S. Neogi, M. Pathak, J. Petzold, J. P. Pereira, P. Vyas, E. Huntley, K. Kissick, M. Belkacemi,.** *IPCC, 2019: Climate Change and Land: an IPCC special report on climate change, desertification, land degradation, sustainable land management, food security, and greenhouse gas fluxes in terrestrial ecosystems .* s.l. : Intergovernmental Panel on Climate Change, 2019. p. 6-7.

6. —. *IPCC, 2019: Climate Change and Land: an IPCC special report on climate change, desertification, land degradation, sustainable land management, food security, and greenhouse gas fluxes in terrestrial ecosystems.* s.l. : Intergovernmental Panel on Climate Change, 2019. p. 16.

7. **Wuebbles, D. J., et al.** *Climate Science Special Report: Fourth National Climate Assessment.* Washington DC : U.S. Global Change Research Program, 2017.

8. **Peters, J.G.J. Olivier and J.A.H.W.** *Trends in Global CO2 and Total Greenhouse Gas Emission.* The Hague : PBL Netherlands Environmental Assessment Agency, 2019.

9. **Robert L. Hirsch, Roger Bezdek, Robert Wendling.** *PEAKING OF WORLD OIL PRODUCTION: IMPACTS, MITIGATION, & RISK MANAGEMENT.* s.l. : US Department Of Energy, 2005.

10. **G.B. Gharehpetian, S. Mohammad Mousavi Agah.** *Distributed Generation Systems. Design, Operation and Grid Integration.* s.l. : Butterworth-Einemann, 2017. p. 335-337. Vol. Ch. 7.

11. **Steber, David.** *Integration of Decentralized Battery Energy Storage Systems into the German Electrical Power System.* 208.

12. *Lithium batteries: Status, prospects and future.* **Bruno Scrosati, Jürgen Garche.** 9, s.l. : Journal of Power Sources, 2010, Vol. 195, p. 2419-2430.

13. *Technology generation of lithium batteries in leading countries.* **Fernando Moreno-Brieva, Carlos Merino-Moreno.** s.l. : Environmental Science and Pollution Research , 2021, Vol. 28, p. 28367-28380.

14. *Electric Vehicles Batteries: Requirements and Challenges.* **Jie Deng, Chulheung Bae, Adam Denlinger, Theodore Miller.** 3, s.l. : Joule, 2020, Vol. 4, p. 511-515.

15. *New Perspectives on Fuel Cell Technology: A Brief Review.* **Norazlianie Sazali, Wan Norharyati Wan Salleh,,Ahmad Shahir Jamaludin, Mohd Nizar Mhd Razali.** 5, s.l. : Membranes, Vol. 10, p. 99.

16. *The development of fuel cell electric vehicles – A review.* **M. Muthukumar, N. Rengarajan, B. Velliyangiri, M. A. Omprakas, C. B. Rohit, U. Kartheek Raja.** s.l. : materials today: Proceedings , 2021, Vol. 45, p. 1181-1187.

17. *Recent Advancements in Li-Ion Conductors for All-Solid-State Li-Ion Batteries.* **Y. Meesala, A. Jena, H. Chang, R.-S. Liu.** 12, s.l. : ACS Energy Letters, 2017, Vol. 2, p. 2734–2751.

18. *Issues and challenges facing rechargeable lithium batteries.* **J. M. Tarascon, M. Armand.** s.l. : Nature , 2001, Vol. 414, p. 359–367.

19. *Electrical Energy Storage and Intercalation Chemistry.* **Whittingham, M. S.** 4244, s.l. : Science, Vol. 192, p. 1126-1127.

20. *Topochemical reactions of rutile related structure with lithium.* **D.W. Murphy, F.J. Di Salvo, J. N. Carides, J. V. Waszczak.** 12, s.l. : Materials Research Bulletin, 1978, Vol. 13, p. 1395-1402.

21. *A Cyclable Lithium Organic Electrolyte Cell Based on Two Intercalation Electrodes.* **M. Lazzari, B. Scrosati.** 3, s.l. : Journal of The Electrochemical Society, 1980, Vol. 127, p. 773-774.

22. *The electrochemical preparation and properties of ionic alkali metal-and NR4-graphite intercalation compounds in organic electrolytes.* **Besenhard, J. O.** 2, s.l. : Carbon, 1976, Vol. 14, p. 111-115.

23. *The discharge reaction mechanism of the MoO3 electrode in organic electrolytes.* **J. O. Besenhard, R. Schöllhorn.** 3, s.l. : Journal of Power SOurces, 1976-977, Vol. 1, p. 267-276.

24. *Topotactic redox reactions and ion exchange of layered MoO3 bronzes.* **R. Schöllhorn, R. Kuhlmann, J. O. Besenhard.** 1, s.l. : Materials Research Bulletin, 1976, Vol. 11, p. 83-90.

25. *LixCoO2 (0<x<-1): A new cathode material for batteries of high energy density.* **K. Mizushima, P.C. Jones, P.J. Wiseman, J.B. Goodenough.** 6, s.l. : Materials Research Bulletin, 1980, Vol. 15, p. 783-789.

26. *The state of understanding of the lithium-ion-battery graphite solid electrolyte interphase (SEI) and its relationship to formation cycling.* **Seong Jin An, Jianlin Li, Claus Daniel, Debasish Mohanty, Shrinkan Nagpure, David L. Wood III.** s.l. : Carbon, 2016, Vol. 105, p. 52-76.

27. *Beyond intercalation-based Li-ion batteries: The state of the art and challenges of electrode materials reacting through conversion reactions.* **Jordi Cabana, Laure Monconduit , Dominique Larcher , and M. Rosa Palacín.** 35, s.l. : Advanced Materials, 2010, Vol. 22, p. 170-192.

28. *Mechanisms for Lithium Insertion in Cabonaceous Materials.* **J. R. Dahn, Tao Zheng, Yinghu Liu, J. S. Xue.** 5236, s.l. : Science, 1995, Vol. 270, p. 590-593.

29. *Negative Electrodes for Lithium- and Sodium-Ion Batteries Obtained by Heat-Treatment of Petroleum Cokes below 1000°C.* **R. Alcantara, J. M. Jimenez Mateos, J. L. Tirado.** s.l. : Journal of The Electrochemical Society, 2002, Vol. 149, p. A201.

30. *The "falling cards model" for the structure of microporous carbons.* **J. R. Dahn, W. Xing, Y. Gao.** 6, s.l. : Carbon, 1997, Vol. 35, p. 825-830.

31. *Graphene: Tri and tri again.* **Yacoby, Amir.** s.l. : Nature Physics, 2011, Vol. 7, p. 925-926.

32. *Carbon materials for ion-intercalation involved rechargeable battery technologies.* **Gang Wang, Minghao Yu and Xinliang Feng.** s.l. : Chemical Society Reviews, 2021, Vol. 50, p. 2388-2443.

33. *Insertion Electrode Materials for Rechargeable Lithium Batteries.* **Martin Winter, Jürgen O. Besenhard, Michael E. Spahr, Petr Novak.** 10, s.l. : Advanced Materials, 1998, Vol. 10, p. 725-763.

34. *The Influence of the Graphitic Structure on the Electrochemical Characteristics for the Anode of Secondary Lithium Batteries.* **K. Tatsumi, N. Iwashita, H. Sakaebe, H. Shioyama, S. Higuchi, A. Mabuchi, H. Fujimoto.** s.l. : Journal of The Electrochemical Society, 1995, Vol. 142, p. 716.

35. *Characterisation of mesocarbon microbeads (MCMB) as active electrode material in lithium and sodium cells.* **R. Alcántara, F. J. Fernández Madrigal, P. Lavela, J. L. Tirado, J. M. Jiménez Mateos, C. Gómez de Salazar, R. Stoyanova, E.Zhecheva.** 7, s.l. : Carbon, 2000, Vol. 38, p. 1031-1041.

36. *Electric Field Effect in Atomically Thin Carbon Films.* **K. S. Novoselov, A. K. Geim, S. V. Morozov, D. Jiang, Y. Zhang, S. V. Dubonos, I. V. Grigorieva, A. A. Firsov.** 5696, s.l. : Science, 2004, Vol. 306, p. 666-669.

37. *Superior Thermal Conductivity of Single-Layer Graphene.* **Alexander A. Balandin, Suchismita Ghosh, Wenzhong Bao, Irene Calizo, Desalegne Teweldebrhan† Feng Miao, and Chun Ning Lau.** 3, s.l. : Nano Letters, 2008, Vol. 8, p. 902-907.

38. *Electrical conductivity of compacts of graphene, multi-wall carbon nanotubes, carbon black, and graphite powder.* **Bernardo Marinho, Marcos Ghislandi, Evgeniy Tkalya, Cor E. Koning, Gijsbertus de With.** s.l. : Powder Technology, 2012, Vol. 221, p. 351-358.

39. *Mechanical properties of graphene and graphene-based nanocomposites.* **Dimitrios G. Papageorgiou, Ian A.Kinloch, Robert J.Young.** s.l. : Progress in Material Science, 2017, Vol. 90, p. 75-127.

40. *Measurement of the Elastic Properties and Intrinsic Strength of Monolayer Graphene.* **Changgu Lee, Xiaoding Wei, Jeffrey W. Kysar, James Hone.** 5887, s.l. : Science, 2008, Vol. 321, p. 385-388.

41. *Ultrahigh electron mobility in suspended graphene.* **K.I.Bolotin, K. J. Sikes, Z. Jianga, M. Klima, G. Fudenberg, J. Hone, P. Kim, H. L. Stormer.** 9-10, s.l. : Solid State Communications, 2008, Vol. 146, p. 351-355.

42. *Electronic and Thermal Properties of Graphene and Recent Advances in Graphene Based Electronics Applications.* **Mingyu Sang, Jongwoon Shin, Kiho Kim, Ki Jun Yu.** s.l. : nanomaterials, 2019, Vol. 9(3).

43. *The role of graphene for electrochemical energy storage.* **Rinaldo Raccichini, Alberto Varzi, Stefano Passerini, Bruno Scrosati.** s.l. : Nature materials, 2015, Vol. 14, p. 271-279.

44. *Can the performance of graphene nanosheets for lithium storage in Li-ion batteris be predicted?* **Oscar A. Vargas C., Alvaro Caballero, Julian Morales.** 6, s.l. : Nanoscale, 2012, Vol. 4, p. 2083-2092.

45. *Graphene/silicon nanocomposite anode with enhanced electrochemical stability for lithium-ion battery applications.* **F. Maroni, R. Raccichini, A. Birrozzi, G. Carbonari, R. Tossici, F. Croce, R. Marassi, F. Nobili.** s.l. : Journal of Power Sources, 2014, Vol. 269, p. 873-882.

46. *Enhanced stability of SnSb/graphene anode through alternative binder and electrolyte additiive for lithium ion batteries application.* **Agnese Birrozzi, Fabio Maroni, Rinaldo Raccichini, Roberto Tossici, Roberto Marassi, Francesco Nobili.** s.l. : Journal of Power Sources, 2015, Vol. 294, p. 248-253.

47. *Sandwich-structured graphene hollow spheres limited Mn2SnO4/SnO2 heterostructures as anode materials for high-performance lithium-ion batteries.* **Hua Zhuang, Mingrui Han, Wencheng Ma, Yanghao Ou, Yong Jiang, Wenrong Li, Xiaoyu Liu, Bing Zhao, Jiujun Zhang.** s.l. : Journal of Colloid and Interface Science, 2021, Vol. 586, p. 1-10.

48. *SnO2/NiFe2O4/graphene nanocomposites as anode materials for lithium ion batteries.* **Honglong Shen, Xifeng Xia, Shuai Yan, Xinyan Jiao, Dongping Sun, Wu Lei, Qingli Hao.** s.l. : Journal of Alloys and Compounds, 2021, Vol. 853, p. 157017.

49. *Janus Graphene Oxide Sheets with Fe3O4 Nanoparticles and Polydopamine as Anodes for Lithium-Ion Batteries.* **Jiwon Jand, Seok Hyun Song, Hyeri Kim, Junsoo Moon, Hyungju Ahn, Kyoung-II Jo, Joona Bang, Hyungsub Kim, Jaseung Koo.** 12, s.l. : Applied Materials & Interfaces, 2021, Vol. 13, p. 14786-14795.

50. *A roadmap for graphene.* **K. S. Novoselov, V. I. Fal'ko, L. Colombo, P. R. Gellert, M. G. Schwab, K. Kim.** s.l. : Nature, 2012, Vol. 490, p. 192-200.

51. **Jamie H. Warner, Franziska schäffel, Alicja Bachmatiuk, Mark H. Rümmeli.** Graphene: Fundamentals and emergent applications. 2013, Vol. Chapter 4.

52. *Preparation of Graphitic Oxide.* **William S. Hummers Jr, Richard E. Offerman.** 6, s.l. : Journal of The American Chemical Society, 1958, Vol. 80, p. 1339.

53. *The chemistry of graphene oxide.* **Daniel R. Dreyer, Sungjin Park, Christopher W. Bielawski, Rodney S. Ruoff.** 1, s.l. : Chemical Society Reviews, 2010, Vol. 39, p. 228-240.

54. *Helical microtubules of graphitic carbon.* **Lijima, Sumio.** s.l. : Nature, 1991, Vol. 354, p. 56-58.

55. *Carbon nanotubes in Li-ion batteries: A review.* **Poonam Sehrawat, C. Julien, S. S: Isalm.** s.l. : Material Science and Engineering: B, 2016, Vol. 213, p. 12-40.

56. *Recent progress in biomass-derived carbon materials used for secondary batteries.* **Yun Chen, Xiaolin Guo, Anmin Liu, Haiding Zhu, Tingli Ma.** 12, s.l. : Sustainable Energy & Fuels, 2021, Vol. 5, p. 3017-3038.

57. *Energy Storage Materials from Nature through Nanotechnology: A Sustainable Roude from Reed Plants to a Silicon Anode for Lithium-Ion Batteries.* **Jun Liu, Peter Kopold, Peter A. van Aken, Joachim Maier, Yan Yu.** 33, s.l. : Angewandte Chemie International Edition, 2015, Vol. 54, p. 9632-9636.

58. *3D Porous Silicon/N-Doped Carbon Composite Derived from Bamboo Charcoal as High-Performance Anode Material for Lithium-Ion Batteries.* **Congcong Zhang, Xin Cai, Wenyan Chen, Siyuan Yang, Donghui Xu, Yueping Fang, and Xiaoyuan Yu.** 8, s.l. : ACS Sustainable Chemistry & Engineering, 2018, Vol. 6, p. 9930-9939.

59. *Ti-based compounds as anode materials for Li-ion batteries.* **Guan-Nan Zhu, Yong-Gang Wang, Yong-Yao Xia.** 5, s.l. : Energy & Environmental Science, 2012, Vol. 5, p. 6652-6667.

60. *Nanostructures and lithium electrochemical reactivity of lithium titanites and titanium oxides: A review.* **Zhenguo Yang, Daiwon Choi, Sebastien Kerisit, kevin M. Rosso, Donghai Wang, Jason Zhang, Gordon Graff, Jun Liu.** 5, s.l. : Journal of Power Sources, 2009, Vol. 192, p. 588-598.

61. *Is TiO2(B) the Future of Titanium-Based Battery Materials?* **Dr. Marcus Fehse, Edgar Ventosa.** 5, s.l. : ChemPlusChem, 2015, Vol. 80, p. 785-795.

62. *Investigation of different binding agents for nanocrystalline anatase TiO2 anodes and its application in a novel, green lithium-ion battery.* **Arianna Moretti, Guk-Tae Kim, Dominic Bresser, katrin Renger, Elie Paillard, Roberto Marassi, Martin Winter, Stefano Passerini.** s.l. : Journal of Power Sources, 2013, Vol. 221, p. 419-426.

63. *Electrochemical lithium reactivity with nanotextured anatase-type TiO2.* **Guillaume Sudant, Emmanuel Baudrin, Dominique Larcher, Jean-Marie Tarascon.** 12, s.l. : Journal of Materials Chemistry, 2005, Vol. 15, p. 1263-1269.

64. *Large Impact of Particles Size on Insertion Reactions. A Case for Anatase LixTiO2.* **Marnix Wagemaker, Wouter J. H. Borghols, Fokko M. Mulder.** 14, s.l. : Journal of The American Chemical Society, 2007, Vol. 129, p. 4323-4327.

65. *The Influece of Size on Phase Morphology and Li-Ion Mobility in nanosized Lithiated Anatase TiO2.* **Marnix Wagemaker, Wouter J. H. Borghols, Ernst R. H. van Eck, Arno P. M. Kentgens, Gordon J. Kearley, Fokko M. Mulder.** 7, s.l. : Chamistry - A European Journal, 2007, Vol. 13, p. 2023-2028.

66. *Current Advances in TiO2-Based Nanostructure Electrodes for High Performance Lithium Ion Batteries.* **Mahmoud Madian, Alexander Eychmüller, Lars Giebeler.** 7, s.l. : Batteries, 2018, Vol. 4.

67. *Multiple Li Positions inside Oxygen Octahedra in Lithiated TiO2 Anatase.* **Marnix Wagemaker, Gordon J. Kearley, Ad A. van Well, Hannu Mutka, Fokko M. Mulder.** 3, s.l. : Journal of American Chemical Society, 2003, Vol. 125, p. 840-848.

68. *Particle size dependence of the lithium storage and high rate performance of nanocrystalline anatase TiO2 electrode.* **Chunhai Jiang, Mingdeng Wei, Zhimei Qi, Tesuichi Kudo, Itaru Honma, Haoshen Zhou.** 1, s.l. : Journal of Power Sources, 2007, Vol. 166, p. 239-243.

69. *High-power and long-life lithium-ion batteries using lithium titanium oxide anode for automotive and stationary power applications.* **Norio Takami, Hiroki Inagaki, Yoshinao Tatebayashi, Hidesato Saruwatari, Keizoh Honda, Shun Egusa.** s.l. : Journal of Power Sources, 2012, Vol. 244, p. 469-475.

70. *Size Effects in the Li4+xTi5O12 Spinel.* **W. J. Borghols, M. Wagemaker, U. Lafont, E. M. Kelder, F. M. Mulder.** 49, s.l. : Journal of The American Chemical Society, 2009, Vol. 131, p. 17786-17792.

71. *Cation ordering and order-disorder phase transition Co-substituted Li4Ti5O12 spinels.* **N. Jovic, B. Antic, A. Kremenovic, A. Spasojevic-de Bire, V. Spasojevic.** 1, s.l. : physica status solidi (a), 2003, Vol. 198, p. 18-28.

72. *Scaling up "Nano" Li4Ti5O12 for High-Power Lithium-Ion Anodes Using Large Scale Flame Spray Pyrolysis.* **Agnese Birrozzi, Mark Copley, Jan Von Zamory, Marta Pasqualini, Silvia Calcaterra, Francesco Nobili, Andrea Di Cicco, Hanna Rajantie, Martha Briceno, Edward Bilbé.** s.l. : Journal of The Electrochemical Society, 2015, Vol. 162, p. A2331.

73. *Preparation and effects of W-doping on electrochemical properties of spinel Li4Ti5O12 as anode material for lithium ion battery.* **Xin-long Zhang, Guo-rong Hu, Zhong-dong Peng.** s.l. : Journal of Central South University, 2013, Vol. 20, p. 1151-1155.

74. *Improving the high rate performance of Li4Ti5O12 through divalent zinc substitution.* **Ting-Feng Yi, Haiping Liu, Yan-Rong Zhu, Li-Juan Jiang, Ying Xie, Rong-Sun Zhu.** s.l. : Journal of Power Sources, 2012, Vol. 215, p. 258-265.

75. *High rate capability and long-term cyclability of Li4Ti4.9V0.1O12 as anode material in lithium ion battery.* **Zijia Yu, Xianfa Zhang, Guiling Yang, Jing Liu, Jiawei Wang, Rongshun Wang, Jinping Zhang.** 24, s.l. : Electrochimica Acta, 2011, Vol. 56, p. 8611-8617.

76. *Li4Ti5O12/C composite electrode material synthesized involving conductive carbon precursor for Li-ion battery.* **Liuxiang Yang, Lijun Gao.** 1-2, s.l. : Journal of Alloys and Compounds, 2009, Vol. 485, p. 93-97.

77. *PEDOT coated Li4Ti5O12 nanorods: Soft chemistry approach synthesis and their lithium storage properties.* **Xiaoyan Wang, Laifa Shen, Hongsen Li, Jie Wang, Hui Dou, Xiaogang Zhang.** s.l. : Electrochimica Acta, 2014, Vol. 129, p. 283-289.

78. *Mesoporous Li4Ti5O12 Hollow Spheres with Enhanced Lithium Storage Capability.* **Le Yu, Hao Bin Wu, Xiong Wen (david) Lou.** 16, s.l. : Advanced Materials, 2013, Vol. 25, p. 2296-2300.

79. *Lithium Storage in Li4Ti5O12 Spinel: The Full Static Picture from Electron Microscopy.* **Xia Lu, Liang Zhao, Xiaoqing He, Ruijuan Xiao, Lin Gu, Yong-Sheng Hu, Hong Li, Zhaoxiang Wang, Xiaofeng Duan,Liquan Chen,Joachim Maier,Yuichi Ikuhara.** 24, s.l. : Advanced Materials, 2012, Vol. 24, p. 3233-3238.

80. *nano-sized transition-metal oxides as negative-electrode materials for lithium-ion batteries.* **P. Poizot, S. Laurelle, S. Grugeon, L. Dupont, J-M. Tarascon.** 2000 : Nature, Vol. 407, p. 496-499.

81. *Thermodynamic analysis of high energy density conversion type cathode materials for Na- and K-ion batteries.* **Yongheum Lee, Sang-Ok Kim, Hyung-Seok Kim, Seungho Yu.** 7, s.l. : Internation journal of Energy Research, 2020, Vol. 44, p. 6068-6077.

82. *Li-free Cathode Materials for High Energy Density Lithium Batteries.* **Liping Wang, 1Liping Wang, Zhenrui Wu, Jian Zou, Peng Gao, Xiaobin Niu, Hong Li, Liquan Chen.** 9, s.l. : Joule, 2019, Vol. 3, p. 2086-2102.

83. *Alloy negative electrodes for lithium batteries formed in-situ from oxides.* **Huggins, R. A.** s.l. : Ionics, 1997, Vol. 3, p. 245-255.

84. *Electrochemical behavior of Ge and GeX2 (X = O, S) glasses: Improved reversibility of the reaction of Li with Ge in a sulfide medium.* **Youngsik Kima, Haesuk Hwang, Katherine Lawler,Steve W. Martin, Jaephil Cho.** 15, s.l. : Electrochimica Acta, 2008, Vol. 53, p. 5058-5064.

85. *Electrochemical reduction of nano-SiO2 in hard carbon as anode material for lithium ion batteries.* **Bingkun Guo, Jie Shu, Zhaoxiang Wang, Hong Yang, Lihong Shi, Yinong Liu, Liquan Chen.** 12, s.l. : Electrochemistry Communications, 2008, Vol. 10, p. 1876-1878.

86. **N. N. Greenwood, A. Earnshaw.** *Chemistry of the Elements.* s.l. : Butterworth-Heinemann, 1997. 9780750633659.

87. *FeO/C anode materials of high capacity and cycle stability for lithium-ion batteries synthesized by carbothermal reduction.* **Mingxia Gao, Pei Zhou, Peng Wang, Junhua Wang, Chu Liang, Jialei Zhang, Yongfeng Liu.** s.l. : Journal of Alloyis and Compounds, 20113, Vol. 565, p. 97-103.

88. *α-Fe2O3 nanoplates with superior electrochemical performance for lithium-ion batteries.* **Li Xiu, Yuhui Tian, Tiefeng Liu, Henan Li, Jingxia Qiu, Sheng Li, Huaming Li, Shouqi Yuan, Shanqing Zhang.** 2, s.l. : Green Energy & Environment, 2018, Vol. 3, p. 156-162.

89. *Iron-Based Electrodes Meet Water-Based Preparation, Fluorine-Free Electrolyte and Binder: A Chance for More Sustainable Lithium-Ion Batteries?* **Mario Valvo, Anti Liivat, Henrik Eriksson, Cheuk-Wai Tai, Kristina Edström.** 11, s.l. : ChemSusChem, 2017, Vol. 10, p. 2431-2448.

90. *Iron Oxide Nanosheets and Nanoparticles Synthesized by a Facile Single-Step Coprecipitation Method for Lithium-Ion Batteries.* **Mao-Sung Wu, Yang-Hui Ou and Ya-Ping Lin.** s.l. : Journal of The Electrochemical Society, 2011, Vol. 158, p. A231.

91. *Novel iron oxide nanotube arrays as high-performance anodes for lithium ion batteries.* **Yuan Zhong, Huiqing Fan, Ling Changa, Haibo Shao, Jianming Wang, Jianqing Zhang, Chu-nan Cao.** s.l. : Journal of Power Sources, 2015, Vol. 296, p. 255-260.

92. *Unveiling multi-channelled 3D porous iron oxide nanostructures with exalted capacity towards high-performance Li-ion battery applications.* **D.Narsimulu, Goli Nagaraju, S. Chandra Sekhar, Bhimanaboina Ramulu,Sk. Khaja Hussain,Jae Su Yu.** s.l. : Journal of Alloys and Compounds, 2020, Vol. 846, p. 156385.

93. *Revisiting the energy efficiency and (potential) full-cell performance of lithium-ion batteries employing conversion/alloying-type negative electrodes.* **Jakob Asenbauer, Alberto Varzi, Stefano Passerini, Dominc Bresser.** s.l. : Journal of Power Sources, 2020, Vol. 473, p. 228583.

94. *Tin oxide-based anodes for both lithium-ion and sodium-ion batteries.* **Kebede, mesfin A.** s.l. : Current Opinion in Electrochemistry, 2020, Vol. 21, p. 182-187.

95. *Dramatically enhanced reversibility of Li2Oin SnO2-based electrodes: the effect of nanostructure on high initial reversible capacity.* **Renzong Hu, Dongchang Chen, Gordon Waller, Yunpeng Ouyang, Yu Chen, Bote Zhao, Ben Rainwater, Chenghao Yang, Min Zhu, Meilin Liu.** s.l. : Energy & Environmental Science, 2016, Vol. 9, p. 595-603.

96. *Lithium-Aluminum Electrode.* **B. M. L. Rao, R. W. Francis, H. A. Christopher.** s.l. : Journal of The Electrochemical Society, 1977, Vol. 124, p. 1490.

97. **Gholam-Abbas Nazri, Gianfranco Pistoia.** *Lithium Batteries: Science and Technology.* s.l. : Springer, 2003. 978-0-387-92675-9.

98. *Alloy Negative Electrodes for Li-Ion Batteries.* **M. N. Obrovac, V. L. Chevrier.** s.l. : Chemical Reviews, 2014, Vol. 114, p. 11444-11502.

99. **Sony.** SONY's NEW NEXELION HYBRID LITHIUM ION BATTERIES TO HAVE THIRTY-PERCENT MORE CAPACITY THAN CONVENTIONAL OFFERING. [Online] 2004. https://www.sony.com/en/SonyInfo/News/Press/200502/05-006E/.

100. **Meeus, Marcel.** *Overview of Battery Cell Technologies.* s.l. : European Commission, 2018.

101. *Hierarchical nanostructured silicon-based anodes for lithium-ion battery: Processing and performance.* **M.Jana, Tianxiang Ning, Raj N. Singh.** s.l. : Material Science and Engineering: B, 2018, Vol. 232-235, p. 61-67.

102. *Recent advances in the Si-based nanocomposite materials as high capacity anode materials for lithium ion batteries.* **Hansu Kim, Eung-Ju Lee, Yang-Kook Sun.** 6, s.l. : materialstoday, 2014, Vol. 17, p. 285-297.

103. *Electrolyte additives for lithium ion battery electrodes: progress and perspectives.* **Atetegeb Meazah Haregewoin, Aselefech Sorsa Wotango,Bing-Joe Hwang.** 6, s.l. : Energy & Environmental Science, 2016, Vol. 9, p. 1955-1988.

104. *Towards efficient binders for silicon based lithium-ion battery anodes.* **Yajun Yang, Shuxing Wu, Yaping Zhang, Canbin Liu, Xiujuan Wei, Dong Luo, Zhan Lin.** s.l. : Chemical Engineering Journal, 2021, Vol. 406, p. 126807.

105. *Alternative binders for sustainable electrochemical energy storage – the transition to aqueous electrode processing and bio-derived polymers.* **Dominic Bresser, Daniel Buchholz, Arianna Moretti, Alberto Varzi, Stefano Passerini.** 11, s.l. : Energy & Environmental Science, 2018, Vol. 11, p. 3096-3127.

106. *Review of the Design of Current Collectors for Improving the Battery Performance in Lithium-Ion and Post-Lithium-Ion Batteries.* **Mitsuru Yamada, Tatsuya Watanabe,Takao Gunji, Jianfei Wu,Futoshi Matsumoto.** 2, s.l. : electrochem, 2020, Vol. 1, p. 124-159.

107. *A reflection on lithium-ion battery cathode chemistry.* **Manthiram, Arumugam.** 1550, s.l. : Nature communications, 2020, Vol. 11.

108. **Europe, Batteries.** *Strategic Research Agenda for batteries 2020.* 2020.

109. *Conversion cathodes for rechargeable lithium and lithium-ion batteries.* **Feixiang Wu, Gleb Yushin.** 2, s.l. : Energy & Environmental Science, 2017, Vol. 10, p. 435-459.

110. *Structural classification and properties of the layered oxides.* **C. Delmas, C. Fouassier, P. Hagenmuller.** s.l. : Physica, 1980, Vol. 99B, p. 82-85.

111. *Rechargeable LiNiO2/Carbon Cells.* **J. R. Dahn, U. von Sacken, M. W. Juzkow, H. Al-Janaby.** s.l. : Journal of The Electrochemical Society, 1991, Vol. 138, p. 2207.

112. *Electrochemical extraction of lithium from LiMn2O4.* **M. M. Thackeray, P. J. Johnson, L.A. de Picciotto, P.G. Bruce, J. B Goodenough.** 2, s.l. : Materials Research Bulletin, 1984, Vol. 19, p. 179-187.

113. *Increased Cycling Performance of Li-Ion Batteries by Phosphoric Acid Modified LiNi0.5Mn1.5O4 Cathodes in the Presence of LiBOB.* **Maheeka Yapa Abeywardana, Nina Laszczynski, Matthias Kuenzel, Dominic Bresser, Stefano Passerini, Brett Lucht.** Article ID 8636540, s.l. : International Journal of Electrochemistry, 2019, Vol. 2019.

114. *Developing high-voltage spinel LiNI0.5Mn1.5O4 cathodes for high-energy-density lithium-ion batteries: current achievements and future prospects.* **Gemeng Liang, Vanessa K. Peterson, Khay Wai See, Zaiping Guo, Wei Kong Pang.** 31, s.l. : Journal of Materials Chemistry A, 2020, Vol. 8, p. 15373-15398.

115. *Phospho-olivines as Positive-electrode Materials for Rechargeable Lithium Batteries.* **A. K. Padhi, K. S. Nanjudaswamy, J. B. Goodenough.** s.l. : Journal of The Electrochemical Society, 1997, Vol. 144, p. 1188-1194.

116. *Understanding and development of olivine LiCoPO4 cathode materials for lithium-ion batteries.* **Min Zhang, Nuria Garcia-Araez, Andrew L. Hector.** 30, s.l. : Journal of Materials Chemistry A, 2018, Vol. 6, p. 14483-14517.

117. *Design of electrolyte solutions for Li and Li-ion batteries: a review.* **Doron Aurbach, Yosef Talyosef, Boris Markovsky, Elena Markevich, Ella Zinigrad, Liraz Asraf, Joseph, S. Gnanaraj, Hyeong-Jin Kim.** 2-3, s.l. : Electrochimica Acta, 2004, Vol. 50, p. 247-254.

118. **T. Richard Jow, kang Xu, Oleg Borodin, Makoto Ue.** *Electrolytes for Lithium and Lithium-Ion Batteries.* s.l. : Springer, 2014.

119. *Studies of Lithium Intercalation into Carbons Using Nonaqueous Electrochemical Cells.* **Rosamaria Fong, ulrich von Sacken, J. R. Dahn.** 7, s.l. : Journal of The Electrochemical Society, 1990, Vol. 137, p. 2009-2013.

120. *Electrolyte additives for lithium ion battery electrodes: progress and perspectives.* **Atetegeb Meazah Haregewoin, Aselefech Sorsa Wotango, Bing-Joe Hwang.** 6, s.l. : Energy & Environmental Science, 2016, Vol. 9, p. 1955-1988.

121. *Lithium availability and future production outlooks.* **Hanna Vikström, Simon Davidsson, Mikael Höök.** s.l. : Applied Energy, 2013, Vol. 110, p. 252-266.

122. *The future of lithium avaiability for electric vehicle batteries.* **Jamie Speirs, Marcello Contestabile, Yassine Houari, Robert Gross.** s.l. : Renewable and Sustainable Energy Reviews, 2014, Vol. 35, p. 183-193.

123. *State-of-the-Art Electrode materials for Sodium-Ion Batteries.* **Alain Mauger, Christian M. Julien.** 16, s.l. : materials, 2020, Vol. 13, p. 3453.

124. *Ambient Temperature Cycling of an Na - TiS2 Cell.* **Gerald H. Newman, Lawrence P. Klemann.** s.l. : Journal of the Electrochemical Society, 1980, Vol. 127, p. 2097.

125. *A new variety of LiCoO2 with unusual oxygen packing obtained by exchange reaction.* **Claude Delmas, Jean-Jacques Braconnier, Paul Hagenmuller.** 1, s.l. : Materials Research Bulletin, 1982, Vol. 17, p. 117-123.

126. **Shacklette, L W, Toth, J E e Elsenbaumer, R L.** *Conjugated polymer as substrate for the plating of alkali metal in a nonaqueous secondary battery. US 4695521* United States, 22 09 1987.

127. **Kazunori Fujita, Shigeoki Nishimura, Hiroyuki Sugimoto, Shinpei Matsuda, Noboru Ebato, Atsuko Tohyama.** *Secondary battery. EP0198484A2* 1986.

128. *Prospects in anode materials for sodium ion batteries - A review.* **Tahira Perveen, Muhammad Siddiq, Nadia Shahzad, Rida Ihsan, Abrar Ahmad, Muhammad Imran Shahzad.** s.l. : Renewable and Sustainable Energy Reviews, 2020, Vol. 119, p. 109549.

129. *Beyond Insertion for Na-Ion Batteries: Nanostructured Alloying and Conversion Anode Materials.* **Huang Zhang, Ivana Hasa, Stefano Passerini.** 17, s.l. : Advanced Energy Materials, 2018, Vol. 8, p. 1702582.

130. *Room-temperature sodium-ion batteries: Improving the rate capability of carbon anode materials by templating strategies.* **Sebastian Wenzel, Takeshi Hara, Jürgen Janek, Philipp Adelhelm.** 9, s.l. : Energy & Environmental Sceince, 2011, Vol. 4, p. 3342-3345.

131. *Na-ion batteries, recent advances and present challenges to become low cost energy storage systems.* **Verónica Palomares, Paula Serras, Irune Villaluenga,Karina B. Hueso, Javier Carretero-González, Teófilo Rojo.** 3, s.l. : Energy & Environmental Science, 2012, Vol. 5, p. 5884-5901.

132. *First-principles study of alkali metal-graphite intercalation compounds.* **Kunihiro Nobuhara, Hideki Nakayama, Masafumi Nose, Shinji Nakanishi, Hideki Iba.** s.l. : Journal of Power Sources, 2013, Vol. 243, p. 585-587.

133. *Use of Graphite as a Highly Reversible Electrode with Superior Cycle Life for Sodium-Ion Batteries by Making Use of Co-Intercalation Phenomena.* **Birte Jache, Philipp Adelhelm.** 38, s.l. : Angewandte Chemie International Edition, 2014, Vol. 53, p. 10169-10173.

134. *High Capacity Anode Materials for Rechargeable Sodium-Ion Batteries.* **D. A. Stevens, J. R. dahn.** s.l. : Journal of The Electrochemical Society, 2000, Vol. 147, p. 1271.

135. *Recent progress in plant-derived hard carbon anode materials for sodium-ion batteries: a review.* **Peng Yu, Wei Tang, Fang-Fang Wu, Chun Zhang, Hua-Yun Luo, Hui Liu, Zhi-Guo Wang.** s.l. : Rare Metals, 2020, Vol. 39, p. 1019-1033.

136. *Unfolding the Mechanism of Sodium Insertion in Anatase TiO2 Nanoparticles.* **Liming Wu, Dominic Bresser, Daniel Buchholz, Guinevere A. Giffin, Claudia Ramirez Castro, Anders Ochel, Stefano Passerini.** 2, s.l. : Advanced Energy Materials, 2014, Vol. 5, p. 1401142.

137. *Direct atomic-scale confirmation of three-phase storage mechanism in Li4Ti5O12 anodes for room-temperature sodium-ion batteries.* **Yang Sun, Liang Zhao, Huilin Pan, Xia Lu, Lin Gu, Yong-Sheng Hu, Hong Li, Michel Armand, Yuichi Ikuhara, Liquan Chen, Xuejie Huang.** 1870, s.l. : Nature Communications, 2013, Vol. 4.

138. *Na2Ti3O7: Lowest Voltage Ever Reported Oxide Insertion Electrode for Sodium Ion Batteries.* **Premkumar Senguttuvan, Gwenaëlle Rousse, Vincent Seznec, Jean-Marie Tarascon, M.Rosa Palacín.** 18, s.l. : Chemistry of Materials, 2011, Vol. 23, p. 4109-4111.

139. *Difference in Electrochemical Mechanism of SnO2 Conversion in Lithium-Ion and Sodium-Ion Batteries: Combined in Operando and Ex Situ XAS Investigations.* **Ditty Dixon, Marta Ávila, Helmut Ehrenberg, Aiswarya Bhaskar.** 6, s.l. : ACS Omega, 2019, Vol. 4, p. 9731-9738.

140. *Conversion-Alloying Anode Materials for Sodium Ion Batteries.* **Libin Fang, Naoufal Bahlawane,Wenping Sun,Hongge Pan,Ben Bin Xu,Mi Yan,Yinzhu Jiang.** s.l. : Small, 2021, p. 2101137.

141. *Atom-Level Understanding of the Sodiation Process in Silicon Anode Material.* **Sung Chul Jung, Dae Soo Jung, Jang Wook Choi, Young-Kyu Han.** 7, s.l. : The Journal of Physical Chemistry Letters, 2014, Vol. 5, p. 1283-1288.

142. *Investigating Sodium Storage Mechanisms in Tin Anodes: A Combined Pair Distribution Function Analysis, Density Functional Theory, and Solid-State NMR Approach.* **Joshua M. Stratford, Martin Mayo, Phoebe K. Allan, Oliver Pecher, Olaf J. Borkiewicz, Kamila M. Wiaderek, Karena W. Chapman, Chris J. Pickard, Andrew J. Morris, Clare P. Grey.** 21, s.l. : Journal fo The American Chemical Society, 2017, Vol. 139, p. 7273-7286.

143. *Highly Reversible Sodiation of Tin in Glyme Electrolytes: The Critical Role of the Solid Electrolyte Interphase and Its Formation Mechanism.* **Bingsheng Qin, Alexander Schiele, Zenonas Jusys, Alessandro Mariani, Thomas Diemant, Xu Liu, Torsten Brezesinski, R. Jürgen Behm, Alberto Varzi, Stefano Passerini.** 3, s.l. : ACS Applied Materials & Interfaces, 2019, Vol. 12, p. 3697-3708.

144. *Tracking Sodium-Antimonide Phase Transformations in Sodium-Ion Anodes: Insights from Operando Pair Distribution Function Analysis and Solid-State NMR Spectroscopy.* **Phoebe K. Allan, John M. Griffin, Ali Darwiche, Olaf J. Borkiewicz, Kamila M. Wiaderek, Karena W. Chapman, Andrew J. Morris, Peter J. Chupas, Laure Monconduit, Clare P. Grey.** 7, s.l. : Journal of The American Electrochemical Society, 2016, Vol. 138, p. 2352-2365.

145. *Recent progress of emerging cathode materials for sodium ion batteries.* **Jun Xiao, Xiao Li, Kaikai Tang, Dandan Wang, Mengqi Long, Hong Gao, Weihua Chen, Chuntai Liu, Hao Liu, Guoxiu Wang.** 10, s.l. : Materials Chemistry Frontiers, 2021, Vol. 5, p. 3735-3764.

146. *Toward high energy density cathode materials for sodium-ion batteries: investigating the beneficial effect of aluminum doping on the P2-type structure.* **Ivana Hasa, Stefano Passerini, Jousef Hassoun.** 9, s.l. : Journal of materials Chemistry A, 2017, Vol. 5, p. 4467-4477.

147. *Research Development on Sodium-Ion Batteries.* **Naoaki Yabuuchi, Kei Kubota, Mouad Dahbi, Shinichi Komaba.** 23, s.l. : Chemical Reviews, 2014, Vol. 114, p. 11636-11682.

148. *Advances and challenges of sodium ion batteries as post lithium ion batteries.* **Monica Sawicki, Leon L. Shaw.** 65, s.l. : RSC Advances, 2015, Vol. 5, p. 53129-53154.

149. *Sodium and sodium-ion energy storage batteries.* **Brian. L. Ellis, F. Nazar.** 4, s.l. : Current Opinion in Solid State and Material Science, 2012, Vol. 16, p. 168-177.

150. *Constructing micro-nano Na3V2(PO4)3/C architecture for practical high-loading electrode fabrication as superior-rate and ultralong-life sodium ion battery cathode.* **Junfeng Yang, Dongdong Li, Xusheng Wang, Xinxiang Zhang, Jian Xu, Jitao Chen.** s.l. : Energy Storage materials, 2020, Vol. 24, p. 694-699.

151. *A Novel NASICON-Type Na4MnCr(PO4)3 Demonstrating the Energy Density Record of Phosphate Cathodes for Sodium-Ion Batteries.* **Jian Zhang, Yongchang Liu, Xudong Zhao, Lunhua He, Hui Liu, Yuzhu Song, Shengdong Sun, Qiang Li, Xianran Xing, Jun Chen.** 11, s.l. : Avenced Materials, 2020, Vol. 32, p. 1906348.

152. *Sodium-Ion Battery based on an Electrochemically Converted NaFePO4 Cathode and Nanostructured Tin–Carbon Anode.* **Ivana Hasa, Jusef Hassoun, Yang-Kook Sun, Bruno Scrosati.** 10, s.l. : ChemPhysChem, 2014, Vol. 15, p. 2152-2155.

153. *Reversible NaFePO4 electrode for sodium secondary batteries.* **Seung-Min Oh, Seung-Taek Myung, Jusef Hassoun, Bruno Scrosati, Yang-Kook Sun.** s.l. : Electrochemistry Communications, 2012, Vol. 22, p. 149-152.

154. *Sodium-Ion Battery based on an Electrochemically Converted NaFePO4 Cathode and Nanostructured Tin–Carbon Anode.* **Ivana Hasa, Jusef Hassoun, Yang-Kook Sun, Bruno Scrosati.** 10, s.l. : ChemPhysChem, 2014, Vol. 15, p. 2152-2155.

155. *Highly Reversible Na Storage in Na3V2(PO4)3 by Optimizing Nanostructure and Rational Surface Engineering.* **Yu Jiang, Xuefeng Zhou, Dongjun Li, Xiaolong Cheng, Fanfan Liu, Yan Yu.** 16, s.l. : Advanced Energy Materials, 2018, Vol. 8, p. 1800068.

156. *Comportement electrochimique des phases NaxCoO2.* **Jean-Jacques Braconnier, Claude Delmas, Claude Fouassier, Paul Hagenmuller.** 12, s.l. : Materials Research Bulletin, 1980, Vol. 15, p. 1797-1804.

157. *Fluorinated Ethylene Carbonate as Electrolyte Additive for Rechargeable Na Batteries.* **Shinichi Komaba, Toru Ishikawa, Naoaki Yabuuchi, Wataru Murata, Atsushi Ito, Yasuhiko Ohsawa.** 11, s.l. : ACS Applied Materials & Interfaces, 2011, Vol. 3, p. 4165-4168.

158. *In search of an optimized electrolyte for Na-ion batteries.* **Alexandre Ponrouch, Elena Marchante, Matthieu Courty, Jean-Marie Tarascon, M. Rosa Palacín.** 9, s.l. : Energy & Environmental Science, 2012, Vol. 5, p. 8572-8583.

159. *Progress and Perspectives of Electrochemical CO2 Reduction on Copper in Aqueous Electrolyte.* **Stephanie Nitopi, Erlend Bertheussen, Soren B. Scott, Xinyan Liu, Albert K. Engstfeld, Sebastian Horch, Brian Seger, Ifan E. L. Stephens, Karen Chan, Christopher hahn, Jens K. Nørskov, Thomas F. Jaramillo, Ib Chorkendorff.** 12, s.l. : Chemical Reviews, 2019, Vol. 119, p. 7610-7672.

160. *On the Edge of Research and Technological Application: A Critical Review of Electromethanogenesis.* **Ramiro Blasco-Gómez, Pau Batlle-Vilanova, Marianna Villano, Maria Dolors Balaguer, Jesús Colprim, Sebastià Puig.** 4, s.l. : Internation Journal of Molecular Sciences, 2017, Vol. 18, p. 874.

161. *Microbial electrohydrogenesis cell and dark fermentation integrated system enhances biohydrogen production from lignocellulosic agricultural wastes: Substrate pretreatment towards optimization.* **Fabrice Ndayisenga, Zhisheng Yu, Jianzhong Zheng, Bobo Wang, Hongxia Liang, Irfan Ali Phulpoto, Telesphore Habiyakare, Dandan Zhou.** s.l. : Renewable and Sustainable Energy Reviews, 2021, Vol. 145, p. 111078.

162. *Economic prospects and policy framework for hydrogen as fuel in the transport sector.* **Amela Ajanovic, Reinhard Haas.** s.l. : Energy Policy, 2018, Vol. 123, p. 280-288.

163. *Analysis of the control strategies for fuel saving in the hydrogen fuel cell vehicles.* **Yakup Hames, Kemal Kaya, Ertugrul Baltacioglu,Arzu Turksoy.** 23, s.l. : Internation Journal of Hydrogen Energy, 2018, Vol. 43, p. 10810-10821.

164. *New Perspectives on Fuel Cell Technology: A Brief Review.* **Norazlianie Sazali, Wan Norharyati Wan Salleh, Ahmad Shahir Jamaludin, Mohd Nizar Mhd Razali.** 5, s.l. : Membranes, 2020, Vol. 10, p. 99.

165. *Progress in renewable power exploitation: reversible solid oxide cells-flywheel hybrid storage systems to enhance flexibility in micro-grids management.* **A. Baldinelli, L. Barelli, G. Bidini.** s.l. : Journal of Energy Storage, 2019, Vol. 23, p. 202-219.

166. *Bypassing renewable variability with a reversible solid oxide cell plant.* **Matthias Frank, Robert Deja, Roland Peters, Ludger Blum, Detlef Stolten.** s.l. : Applied Energy, 2018, Vol. 217, p. 101-112.

167. *A Cogeneration System Based on Solid Oxide and Proton Exchange Membrane Fuel Cells With Hybrid Storage for Off-Grid Applications.* **Francesco Baldi, Ligang Wang, Mar Pérez-Fortes, François Maréchal.** 139, s.l. : Frontiers in Energy Research, 2019, Vol. 6.

168. *SOFC Durability against Standby and Shutdown Cycling.* **M. Hanasaki, C. Uryu, T. Daio, T. Kawabata, Y. Tachikawa, S. M. Lyth, Y. Shiratori, S. Taniguchi, K. Sasaki.** 9, s.l. : Journal of The Electrochemical Society, 2014, Vol. 161, p. F850.

169. **Sasaki, Kazunari.** *Chapter 3 - The Impact of Fuels on Solid Oxide Fuel Cell Anode Lifetime: The Relationship Between Fuel Composition, Fuel Impurities, and Anode Lifetime and Reliability.* s.l. : Academic Press, 2017. Vol. 3.

170. *Transient operation of a solid oxide electrolysis cell.* **Floriane Petipas, Qingxi Fu, Annabelle Brisse, Chakib Bouallou.** 7, s.l. : Internation Journal of Hydrogen Energy, 2013, Vol. 38, p. 2957-2964.

171. *Extensive analysis of an SOC stack for mobile application in reversible mode under various operating conditions.* **Michael Preininger, Bernhard Stoeckl, Vanja Subotić, Christoph Hochenauer.** s.l. : Electrochimica Acta, 2019, Vol. 299, p. 692-707.

2. Tin-based anodes for lithium-ion batteries

SnO_2-based anodes are considered one of the most promising candidates among alloying and conversion-alloying materials as anode materials for next gen Li-ion batteries. This is due to its high theoretical capacity (i.e. 1494 mAh g^{-1}), environmental friendliness, natural abundance, and low cost (1; 2). SnO_2, as summarized in **Equations 10-11**, firstly react via a conversion mechanism giving a theoretical specific capacity of 711 mAh g^{-1}, and then via an alloying mechanism of Sn^0 with an associated specific capacity of 783 mAh g^{-1}. As a result, the overall theoretical specific capacity and volumetric specific capacity are 1494 mAh g^{-1} (4 times the value of graphite) and 10.383 Ah cm^{-3} (12.4 times the value of graphite), respectively (2). The theoretical specific capacity of SnO_2 is lower than Si (3579 mAh g^{-1} considering the phase $Li_{15}Si_4$) and Ge (1624 mAh g^{-1}). However, is higher than Sn (711 mAh g^{-1}) and transition metal oxides (500-1000 mAh g^{-1}). Furthermore, SnO_2 nanomaterials and nanocomposites can be synthesized by employing relatively low temperature methods while Si and Ge commonly require high temperature and expensive routes such as CVD (3), plasma synthesis (4), or electron beam evaporation (5). Thanks to its properties as well as its simple preparation, SnO_2 has been studied in various electrochemical energy storage applications (2; 6).

However, its practical application as anode material in commercial LIBs is still hindered by the specific capacity lower than the theoretical one, and the capacity decay upon cycling. The former can be attributed to several reasons i.e., (i) formation of large metal particles which hinder the kinetic of the conversion reaction and isolate itself from the Li_2O matrix (7), and (ii) larger energy barrier for the oxidation reaction compared to other transition metal oxides (7). This is mainly due to the larger atomic radius and lower temperature of recrystallization of Sn (T = 224 K) compared to other TMs (1). The latter can be attributed to the large volume expansion (≈ 300 %) which occurs during the alloying reaction of Sn. The prolonged volume expansion/contraction can lead to the active material particles detachment, loss of electrical contact, and eventually pulverization of the electrode. For these reasons, the synthesis of nanostructured SnO_2, along with caging it in active or inactive matrices, is of paramount importance to maintain a close contact between Sn and Li_2O and avoid Sn particle coarsening. Nanosizing SnO_2 shorten the Li^+ diffusion path, enhancing the reaction kinetic, and increase the free space to accommodate the volume expansion. These features reflect in improved electrode stability and rate capability. Morphologies such as 0D nanosphere (8), 1D nanowires (9; 10), nanotubes (11; 12) have already

shown remarkable improvements. However, the high specific surface area can lead to particles aggregation and Sn coarsening upon cycling, and thus loss of performances. For these reasons, a robust physical barrier must be used to avoid the coarsening of active material particles and maintain a close contact between Sn^0 and Li_2O. The containment matrices can be either active or inactive towards lithium and can be divided into carbonaceous materials, conductive polymers, and inorganic materials. The former, thanks to its chemical stability, mechanical properties, as well as high electronic conductivity can improve not only the cycling stability of SnO_2 but also its rate capability. This class includes amorphous carbon (13; 2), carbon nanotubes (14; 15), as well as graphene-based materials (16; 17). On the other hand, conductive polymer coatings can form a flexible barrier able to withstand the volume expansion while providing an electronic conducting path. The most employed polymers are polypyrrole (18), polyaniline (19), and the copolymer PEDOT:PSS (20). At last, the synthesis of SnO_2 nanocomposites with inorganic materials (commonly metals or metal oxides) can simultaneously alleviate the volume stresses and avoid Sn^0 particles coarsening. Metal oxides such as TiO_2 (21), Fe_2O_3 (22), and NiO (23) can also provide an additional specific capacity thanks to the conversion reaction, so that the overall specific capacity of the composite is higher compared to inactive matrices such as conductive polymers.

This chapter is divided in three sections according to the strategy adopted to stabilize the SnO_2-based anode. Specifically, in the first two sections the effect of the employment of an inorganic and a carbonaceous matrix is deeply studied in terms structural, morphological, and electrochemical characterization. In the last section, the effect of a tailored morphology is studied. All the nanocomposite materials have been structurally and morphologically characterized by FE-SEM, X-Ray Diffraction, and Raman Spectroscopy. TGA has also been employed to assess the carbon content in all the materials. Electrochemical characterization includes galvanostatic cycling with potential limitation (GCPL), cyclic voltammetry (CV), rate capability, potentiostatic electrochemical impedance spectroscopy (PEIS), and galvanostatic intermittent titration technique (GITT).

2.1 Experimental

All the nanocomposite materials presented in sections 2.2, 2.3, and 2.4 share the same experimental procedure; thus, all the details about structural, morphological, and electrochemical

characterizations are summarized in this section. Only the synthesis methods will be addressed specifically in each subsection.

2.1.1 Structural and morphological characterization

The structural characterization was pursued by Raman scattering and X-Ray Diffraction (XRD). Specifically, a Horiba iH320 Raman spectrometer equipped with a 532 nm laser source, and a Philips diffractometer equipped with a Cu-Kα source (λ=1.540 Å) were used for Raman spectroscopy and XRD, respectively. The morphological characterization was done by using a field-emission scanning electron microscope Zeiss Sigma series 300.

2.1.2 Thermal characterization

The carbon content in the composite materials was assessed by using a Perkin-Elmer STA6000 TGA-DTA, from r.t. up to 800 °C with a rate of 10 °C min^{-1} in oxidizing atmosphere.

2.1.3 Electrode processing

The electrode layers were prepared by doctor blade technique. All the slurries were prepared with the formulation of 70:20:10 of active material, Super C65 (Timcal C-Energy™) as conductive carbon additive, and polyacrylic acid (PAA, Sigma-Aldrich m.w. = 450000 g mol^{-1}) as binder, respectively. Firstly, the polymeric binder was dissolved in ethanol to obtain a 5 $\%_{ww}$ solution. In the meantime, active material and the conductive carbon additive were finely grounded in an agata mortar. The mixed powders were then added to the binder solution reaching a solid content of ca. 40 % and stirred overnight. Eventually, the slurries were casted onto copper foil (thickness = 10 μm) with a wet thickness of 150 μm. Electrode layer were than dried at 70 °C for 2h. Circular electrodes of Ø = 9mm were cut using an electrode puncher (EL-Cut, EL-CELL). Eventually, the electrodes were pressed at 4.7 tons cm^{-2}, weighted, and vacuum dried at 120 °C overnight. The average loading of active material was ≈ 1.5 mg cm^{-2}.

2.1.3 Electrochemical characterization

Three-electrode cells have been used for the electrochemical characterization employing the active material as working electrode, and Li metal as both counter and reference electrodes. 1 M $LiPF_6$ in EC:DMC (1:1 v:v) + 2 % VC was used as electrolyte, and Whatman GF/A glassfiber discs as separator. Swagelok-type cells were used for CV, GCPL, rate capability, and GITT. Prior any

electrochemical characterization, an open circuit voltage period of 12 h was used. Cyclic voltammetries were acquired from 50 $\mu V\ s^{-1}$ up to 500 $\mu V\ s^{-1}$ with 50 $\mu V\ s^{-1}$ increment steps. Galvanostatic cycling were performed by applying specific currents ranging from 50 mA g^{-1} up to 10 A g^{-1}. ECC-REF (EL-CELL) cells have been used for potentiostatic electrochemical impedance spectroscopy. Impedance spectra were acquired every 10^{th} cycle at selected bias potential by applying a sinusoidal voltage perturbation of $\Delta E = 5$ mV in the frequency domain 7 mHz < f < 200 kHz, and with 10 points per decade in logarithmic spacing. All the electrochemical measurements have been performed in the potential window 0.010 V < E < 3.000 V. All the potential values are referred to the Li^+/Li redox couple (-3.041 V vs SHE).

All the cell assembly procedures were carried out by using an Ar filled glovebox (Jacomex GP-Campus) with H_2O and O_2 < 1 ppm. All the electrochemical measurements have been performed on a VMP-3 multichannel galvanostat/potentiostat (BioLogic, France).

2.2 Synthesis and Characterization of TiO_2@SnO_2 Nanocomposite as Viable Anode for Lithium-Ion Batteries

2.2.1 Synthesis

SnO_2 nanopowder (Sigma-Aldrich, < 100 nm) were dispersed in isopropanol by ultrasonic treatment (50 W power; continuous mode) to achieve a homogeneous dispersion. Triton X-100 was added as capping agent (24) and a magnetic stirring was maintained for 2 h. Titanium (IV) isopropoxide (Sigma-Aldrich) was added and the temperature was raised to 80 °C. Eventually, aqueous ammonia solution (30% v/v) and ultrapure water were added dropwise to the solution, and the formation of a pale-yellow precipitate was observed. After the solvent evaporation overnight (T = 70 °C), the powder was treated in a tubular furnace at 600 °C for 4 h under Ar atmosphere (thermal gradient: 5 °C min^{-1}) to obtain Anatase crystal phase (25). The weight ratio between SnO_2 and TiO_2 is 3:1. The synthesis procedure is summarized in **Figure 2-1**.

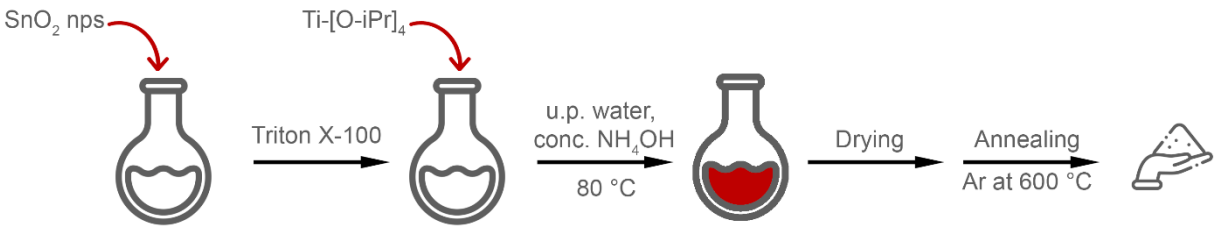

Figure 2-1. Schematic illustration of the synthesis of TiO_2@SnO_2

2.2.2 Results and discussion: structural, morphological, and thermal characterization

In **Figure 2-2**, the SEM micrographs of TiO_2@SnO_2, as well as commercial SnO_2 nanopowder are shown.

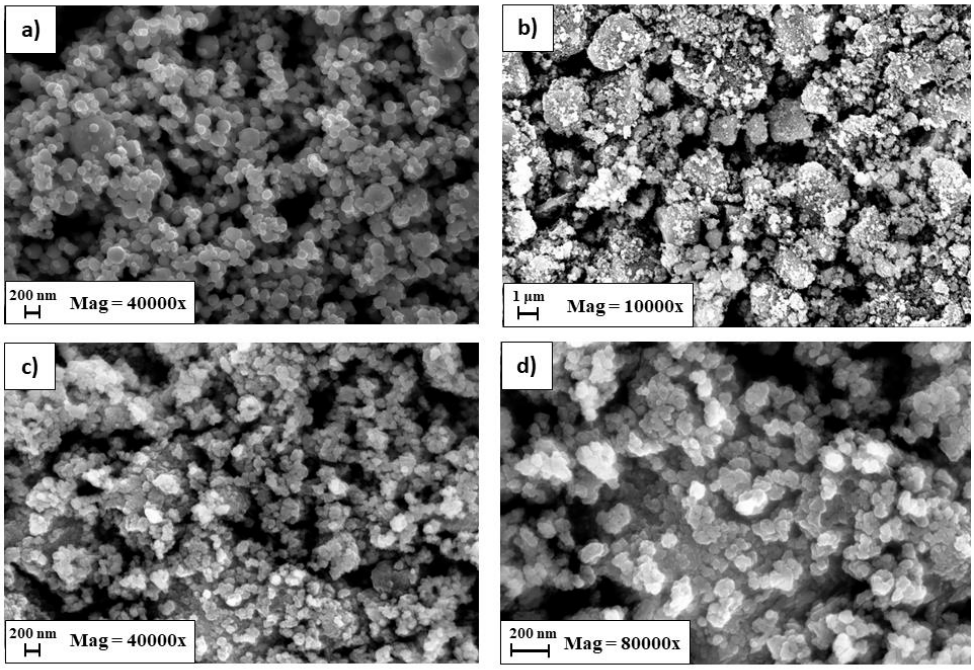

Figure 2-2. SEM micrographs of a) commercial SnO_2 nanopowder at 40000 x, and TiO_2@SnO_2 at b) 10000 x, c) 40000 x, and d) 80000 x

The morphology of commercial SnO_2 (**Figure 2-2a**) is characterized by spherical shape with a diameter ranging from 10 up to 100 nm. The composite (**Figure 2-2b-d**) is characterized by large aggregates probably due to magnetic stirring. However, at high magnifications the presence of the SnO_2 nanoparticles is confirmed, suggesting that their morphology was not modified, and the larger grains are probably TiO_2 crystals. The large particle size of TiO_2 can effectively sustain the volume stresses and avoid the agglomeration of Sn particles.

In **Figure 2-3**, the experimental diffractogram of TiO_2@SnO_2, as well as the reference cards of cassiterite SnO_2 and anatase TiO_2 are shown. The diffractogram of the composite reports a reflection pattern consistent with the rutile-type structure of cassiterite SnO_2 with space group $P4_2/mnm$ (JCPDS 41-1445). A small reflection at 25.23 ° can be indexed to the 101 set of planes of anatase TiO_2. No other reflections of anatase TiO_2 are detectable probably due to the lower amount of it in the composite as well as the broadened shape of the reflections due to the nanometer size of the powder. The average SnO_2 crystallite size was estimated as ≈ 18.08 nm by applying the Scherrer's equation (**Equation 13**), the main reflection 110 has been used for the calculation:

$$L = \frac{K\lambda}{\beta cos\theta} \qquad \textbf{Eq. 13}$$

Where L is the average crystallite size, K = 0.94, λ = 0.15418 nm (Cu Kα wavelength), β = peak broadening and θ = Bragg angle.

In **Figure 2-4**, the Raman spectra of the composite anode as well as the reference of cassiterite SnO_2 and anatase TiO_2 (taken form RUFF database) are shown. The Raman spectra of TiO_2@SnO_2 is consistent with the spectra of both cassiterite SnO_2 and anatase TiO_2. Specifically, the peaks located at 134 and 415 cm^{-1} can be assigned to E_g and B_{1g} mode of Anatase TiO_2 (26; 27), while the peaks located at 240 and 597 cm^{-1} can be assigned to the E_u - TO and A_{1g} mode of cassiterite SnO_2 (28).

Three peaks are clearly visible at 1337, 1583, and 2865 cm^{-1}, which are assigned to the D, G, and 2D mode of amorphous carbon, respectively. This phase is probably produced by thermal decomposition of the capping agent Triton X-100 under Ar.

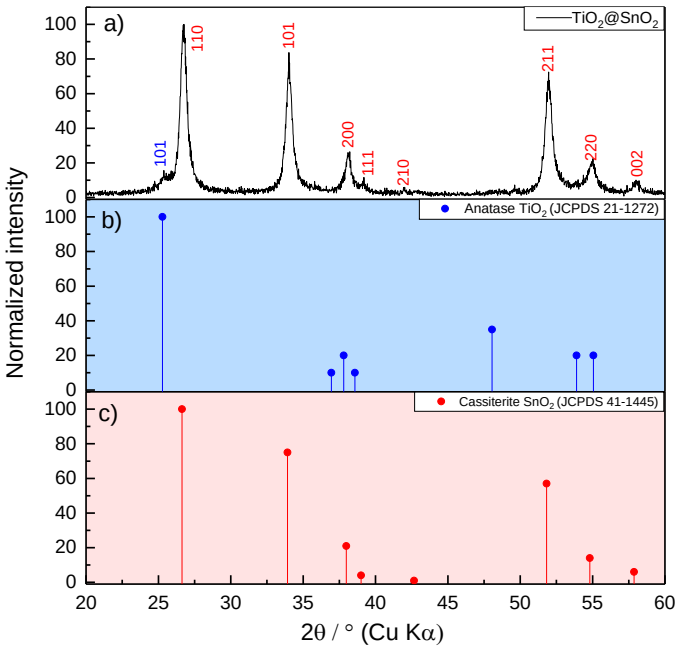

Figure 2-3. a) Experimental diffractogram of TiO_2@SnO_2. b) and c) reference cards of anatase TiO_2 and cassiterite SnO_2, respectively.

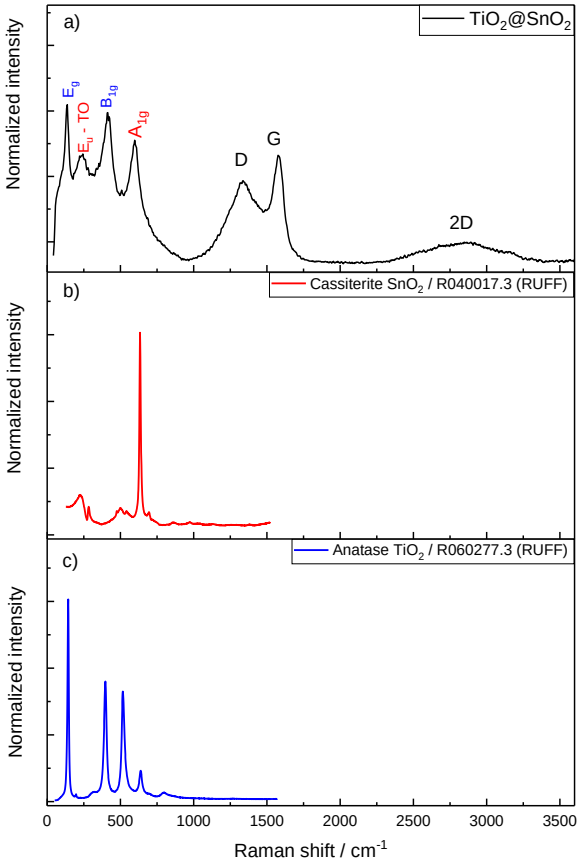

Figure 2-4. a) Raman spectra of TiO_2@SnO_2. b) and c) reference spectrum of cassiterite SnO_2 (RUFF ID R040017.3) and anatase TiO_2 (RUFF ID R060277.3), respectively.

In **Figure 2-5**, the TGA analysis of the nanocomposite material is shown.

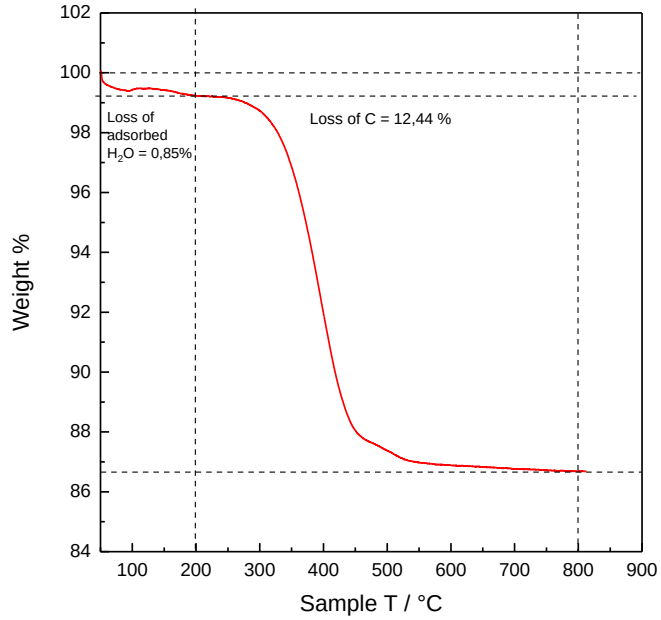

Figure 2-5. TGA of TiO_2@SnO_2 nanocomposite in oxidizing atmosphere

From r.t. up to 200 °C there is a small loss of weight of 0.85 % which can be ascribed to loss of adsorbed water. From 300 °C up to 500 °C the decomposition of amorphous carbon into CO_2 takes place, giving a loss of weight of 12.44 %. Thus, the formulation of the nanocomposite material can be calculated as 66:22:12 of SnO_2, TiO_2, and C, respectively.

2.2.3 Results and discussion: electrochemical characterization

In **Figure 2-6**, the cyclic voltammetry of TiO_2@SnO_2 obtained at 0.050 mV s^{-1} is reported. In the first cathodic scan the peak A at 1.75 V can be assigned to the lithium insertion into anatase TiO_2 lattice (29; 30; 31) according to **Equation 14**:

$$TiO_2 + xLi^+ + xe^- \leftrightarrow Li_xTiO_2 \qquad \textbf{Eq. 14}$$

Peak B located at 1.05 V is assigned to the reduction VC additive in the electrolyte, which polymerizes at the electrode surface giving a stable film made of poly alkyl Li-carbonate species (32). The sharp peak C at 0.85 V is due to the conversion reaction (33; 7; 2; 9), summarized in **Equation 15:**

$$SnO_2 + 4Li^+ + 4e^- \rightarrow Sn^0 + 2Li_2O \qquad \textbf{Eq. 15}$$

As mentioned in sections 1.1.1.1 and 2, this process is only partially reversible, indeed in the 2nd cycle the peak is almost not detectable. In this potential region, also the formation of a passivation layer due to decomposition of the electrolyte starts (34; 35).

Peak D correspond to the alloying reaction of Sn with Li (33; 7; 2; 9) (**Equation 16**):

$$Sn^0 + 4.4Li^+ + 4.4e^- \leftrightarrow Li_{4.4}Sn \qquad \textbf{Eq. 16}$$

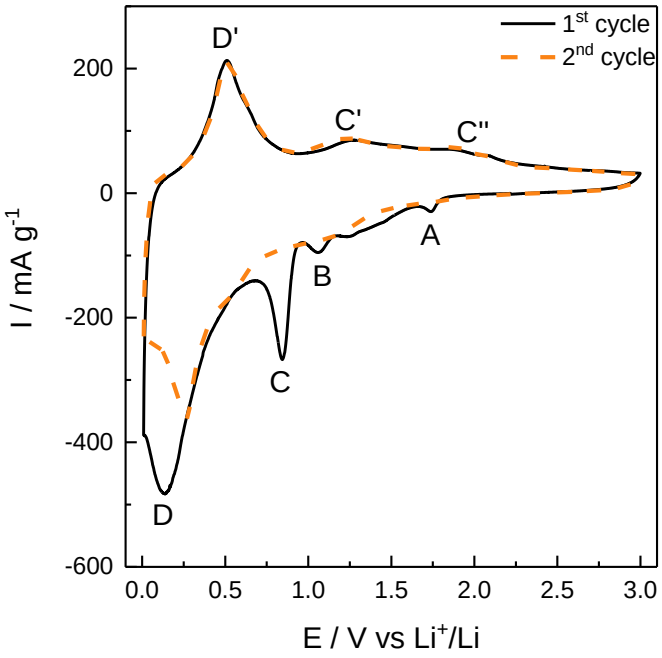

Figure 2-6. Cyclic voltammetry of TiO_2@SnO_2 obtained in the voltage window 0.010 < E < 3.000 V vs Li^+/Li with a scan rate of 0.05 V s^{-1}.

In the anodic scan, peak D' at 0.52 V is assigned to the reversible dealloying reaction, while the peaks C' and C'' located at 1.25 V and 1.94 V, respectively, suggest a partial oxidation of Sn to higher oxidation state (36). The peak of deinsertion of Li^+ from TiO_2 is not observed since is probably overlapped with peak C''. In the 2nd cycle the shape of the cyclic voltammogram is preserved apart from the peak C of the conversion reaction, which is replaced by a broad hump. Preliminary galvanostatic cycles were obtained by applying a specific current I_{spec} = 1000 mA g^{-1} with a constant voltage until the current reached a I_{CV} = 100 mA g^{-1}. The specific capacity values obtained are reported as a function of cycle number in **Figure 2-7**.

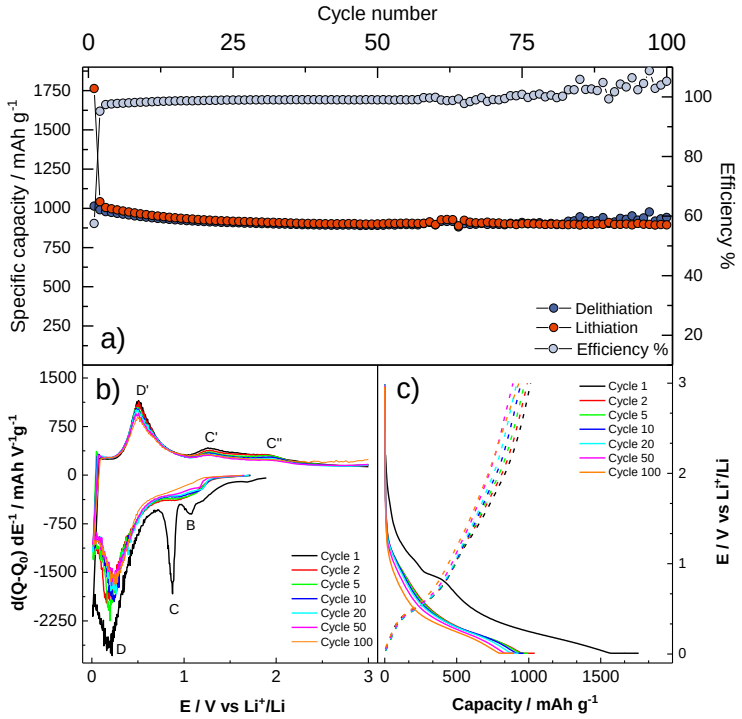

Figure 2-7. a) Specific capacity as a function of cycle number of TiO_2@SnO_2. Galvanostatic b) E vs. Q and c) dQ dE^{-1} vs. E profiles.

In the first lithiation/delithiation, a specific capacity of 1763 mAh g^{-1} and 1013 mAh g^{-1} was reached respectively, with an efficiency of 57,5 %. The low coulombic efficiency clearly reflects first cycle irreversible processes like SEI formation, and the conversion of SnO_2 to Sn^0. After a slight decrease in the first 10 cycles, the cells stabilize with an average specific capacity of Q_{100} = 908 mAh g^{-1} and an efficiency close to 100 %. The extracted galvanostatic E vs. Q profiles are shown in **Figure 2-7b**. In the first cycle there is a plateau at 0.88 V which can be ascribed to the conversion reaction of SnO_2, and a large slope reaching the lower cut-off voltage which can be ascribed to the alloying reaction of Sn with lithium. During delithiation, there are a quasi-plateau and a sloping line at 0.4 V and 1.2 V which can be ascribed to the dealloying reaction of $Li_{4.4}Sn$ phase and oxidation of Sn, respectively. From the 2nd lithiation forward the plateau due to the conversion reaction disappear leaving a sloping line. A large voltage hysteresis is evidenced, which is a common drawback for conversion and conversion-alloying materials. The differential galvanostatic dQ dE^{-1} vs. E profiles are in good agreement with the results obtained by CV. However, in the first lithiation the peak A associated to the Li^+ insertion into TiO_2 lattice was not detected.

In **Figure 2-8**, the voltage hysteresis is graphically demonstrated vs. a theoretical LFP cathode.

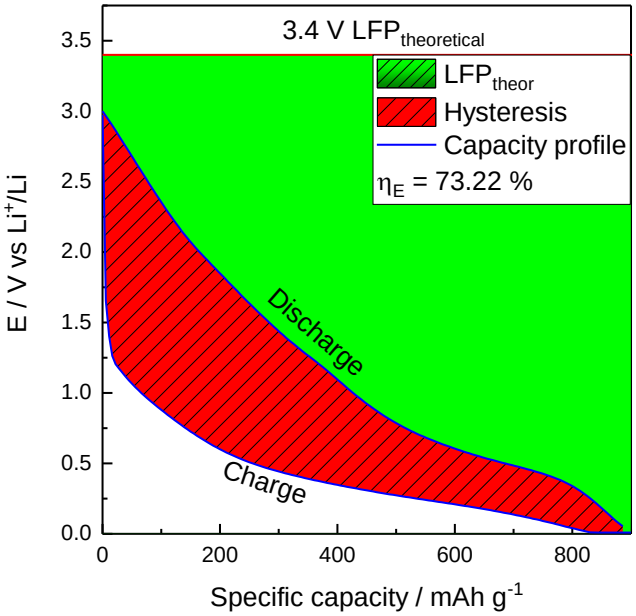

Figure 2-8. Voltage hysteresis at the 50th cycle calculated vs. a theoretical LFP cathode.

The voltage hysteresis was calculated by using the galvanostatic profile obtained at the 50th to be sure that all the irreversible processes have taken place and the specific capacity is stable. The energy efficiency was calculated vs. a theoretical LFP cathode. As is clearly depicted in **Figure 2-8**, there is a large gap (highlighted in red) between the "virtual" charge and discharge due to the hysteresis of the anode material. The energy efficiency was calculated according to **Equation 17**:

$$\eta_E = \eta_Q \times \eta_U = \eta_Q \frac{\bar{U}_{Discharge}}{\bar{U}_{Charge}} = \frac{\int_0^{Q_{fDis}} U(Q)dq}{\int_0^{Q_{fCh}} U(Q)dq} \qquad \textbf{Eq. 17}$$

Where η_E, η_Q and η_U are the energy, coulombic, and voltage efficiencies respectively. The terms $\bar{U}_{Discharge}$ and $\bar{U}_{Charge}$ refers to the average voltage of discharge and charge, respectively, while Q_f and Q_i refers to the initial and final amount of charge in the half-cycle. Thus, the calculated energy efficiency at the 50th cycle is η_E = 73.22 %, lower than LIBs employing the state-of-the-art graphite anode (37; 38). Afterwards, the effect of capacity limitation during delithiation on the energy efficiency was studied by performing galvanostatic cycles at I_{Spec} = 1000 mA g^{-1}, and capacity limited to 70 % of the obtained in **Figure 2-7** (Q_{Lim} = 700 mAh g^{-1}). The specific capacity vs. cycle number as well as the galvanostatic profiles vs. a theoretical LFP cathode are reported in **Figure 2-9**.

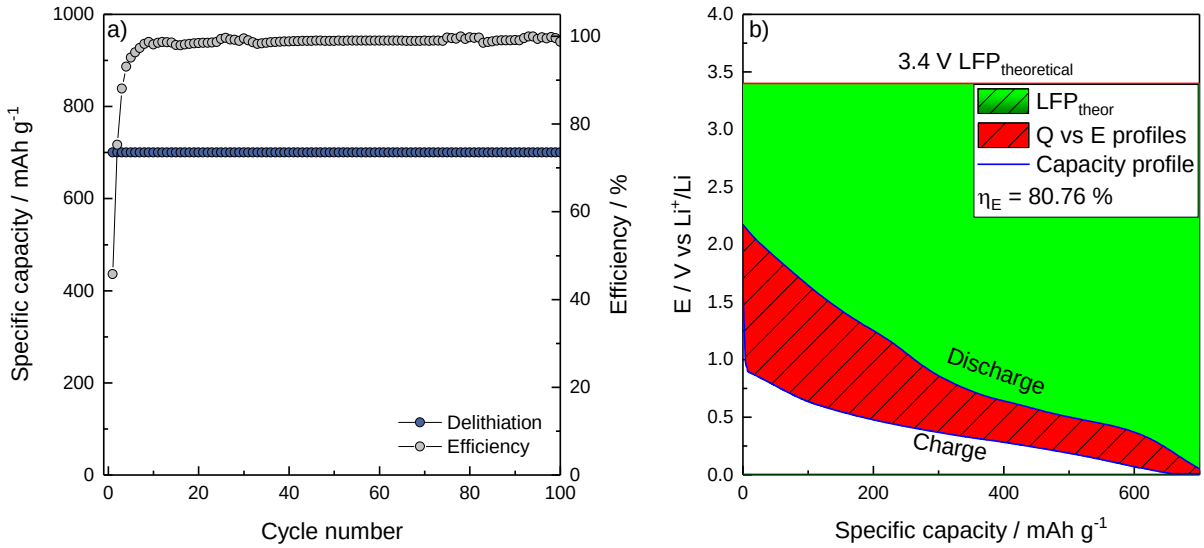

Figure 2-9. a) Galvanostatic cycles with capacity limitation Q_{Lim} = 700 mAh g^{-1}. b) Voltage hysteresis at the 50th cycle calculated vs. a theoretical LFP cathode.

In the first 10 cycles, the coulombic efficiency raises from 45.52 % in the first cycle reaching 99.12 % in the 10th cycles. This is due to the irreversible processes such as SEI formation and conversion reaction. Capacity limitation is a common strategy to further improve the energy efficiency of the full cell (39; 40; 41). In this case, by applying a capacity limitation of 70 % during delithiation (discharge of the "virtual" full cell), the anode reaction was limited mostly to the alloying reaction of Sn, thus the energy efficiency improved from 73.22 % to 80.76 %. Other strategies to improve the energy efficiency of conversion-alloying materials-based full cells could be applying a prelithiation or using a high-voltage cathode material (39). In the first case, the anode material will be partially lithiated, limiting Li loss due to irreversible processes such as SEI formation. Furthermore, the anode material will be already in the "alloying zone". In the second case, by using a high-voltage cathode the amount of stored energy (the green area in **Figure 2-8** and **Figure 2-9**) will be higher than using a low-voltage cathode such as LFP. However, due to time constraints these routes were not studied and will be subject for future works.

The rate capability of TiO_2@SnO_2 was assessed by applying specific currents ranging from 100 mA g^{-1} up to 2000 mA g^{-1} for 10 cycles. The obtained specific capacity values as well as galvanostatic E vs. Q and dQ dE^{-1} vs. E profiles are reported in **Figure 2-10**. The rate capability results are summarized in **Table 4**.

Remarkable specific capacities were obtained at all current rates, ranging from 707 mAh g^{-1} at 2000 mA g^{-1} to 1131 mAh g^{-1} at 100 mA g^{-1}. When the current was restored to 100 mA g^{-1}, a high

specific capacity of 939 mAh g^{-1} was recovered. However, at the low current rates 100 and 200 mA g^{-1}, the coulombic efficiency was about 97 %, while at 500 mA g^{-1} and the further cycles the coulombic efficiency stabilizes at 99 %.

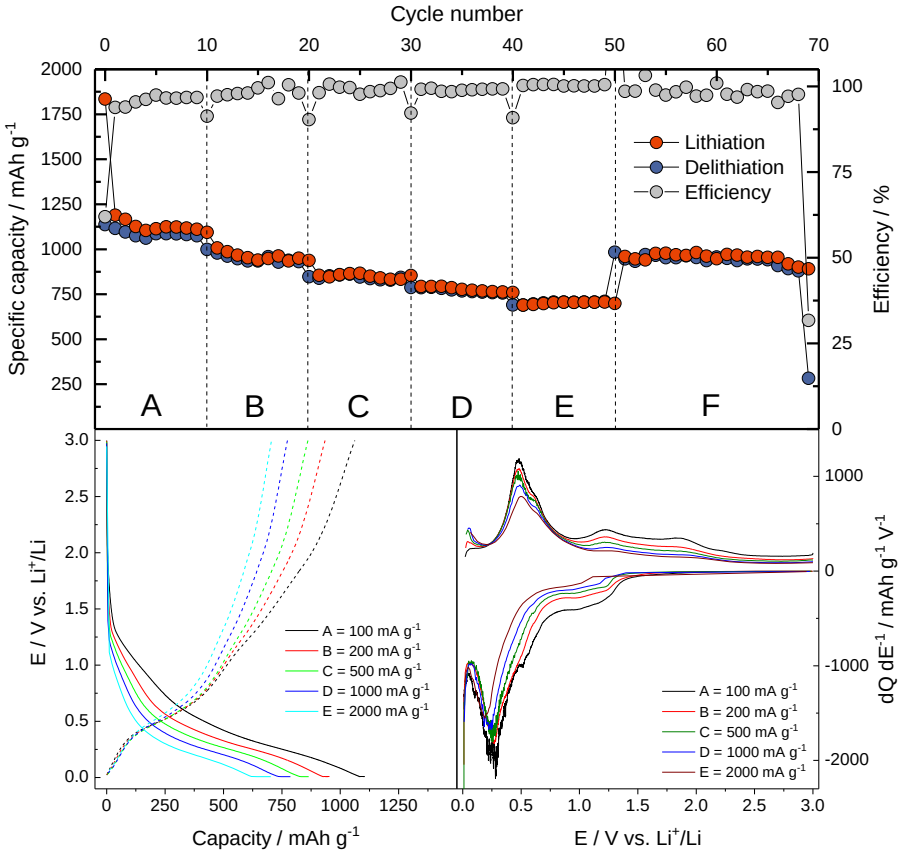

Figure 2-10. a) Specific capacity vs. cycle number. Galvanostatic b) E vs. Q and c) dQ dE^{-1} vs. E profiles. Specific current applied: A = 100 mA g^{-1}, B = 200 mA g^{-1}, C = 500 mA g^{-1}, D = 1000 mA g^{-1}, E = 2000 mA g^{-1}, and F = 100 mA g^{-1}.

E vs. Q and dQ dE^{-1} vs. E galvanostatic profiles were extracted to understand the current-controlled behavior of TiO_2@SnO_2 at different current rates. In both plots, the profiles preserve their shape even if the effect of polarization is visible. In the galvanostatic profile, the sloping line due to the alloying reaction at ≈ 0.6 V and the quasi-plateau at 0.4 V for the dealloying reaction are visible and in accordance with the previous results. In the differential dQ dE^{-1} vs. E profiles, both humps at 1.0 V during reduction and at 1.2 V and 1.9 V during oxidation almost disappears at higher current rates.

Table 4. Average specific lithiation capacity and coulombic efficiency as a function of the applied current.

Step	Current rate / mA g^{-1}	Average specific capacity / mAh g^{-1}	Average efficiency / %
A	100	1131	96.8
B	200	974	97.7
C	500	858	99.2
D	1000	786	99.0
E	2000	707	99.8
F	100	939	99.9

Electrochemical investigation of transport and interfacial properties

CV, GITT, and PEIS were used to investigate the transport and interfacial properties of TiO_2@SnO_2 electrodes. In **Figure 2-11**, the cyclic voltammetries acquired at different scan rates as well as the *I* vs. $\nu^{1/2}$ plot are reported.

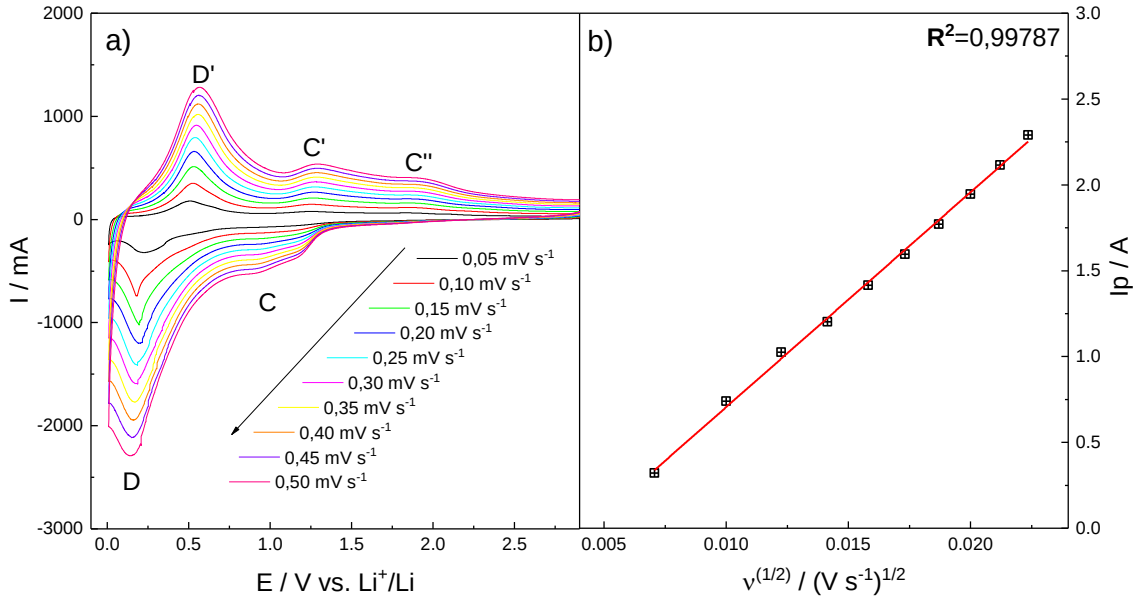

Figure 2-11. Cyclic voltammetries acquired at different scan rates. b) *I* vs. $\nu^{1/2}$ plot with linear fit.

As the scan rate increases, the exchanged current proportionally increases. In fact, by plotting the peak current (peak D has been used for the calculation) as a function of the square root of the scan rate, a linear relationship between them is observed. Indeed, by linear fitting the experimental data, a $R^2 = 0.99787$ is obtained, suggesting a diffusion-controlled behavior (42).

GITT was used for the calculation of the practical specific capacity as well as the Li^+ diffusion coefficient as a function of the electrode potential. The GITT curve as well as the D_{Li} vs. E curve are reported in **Figure 2-12**.

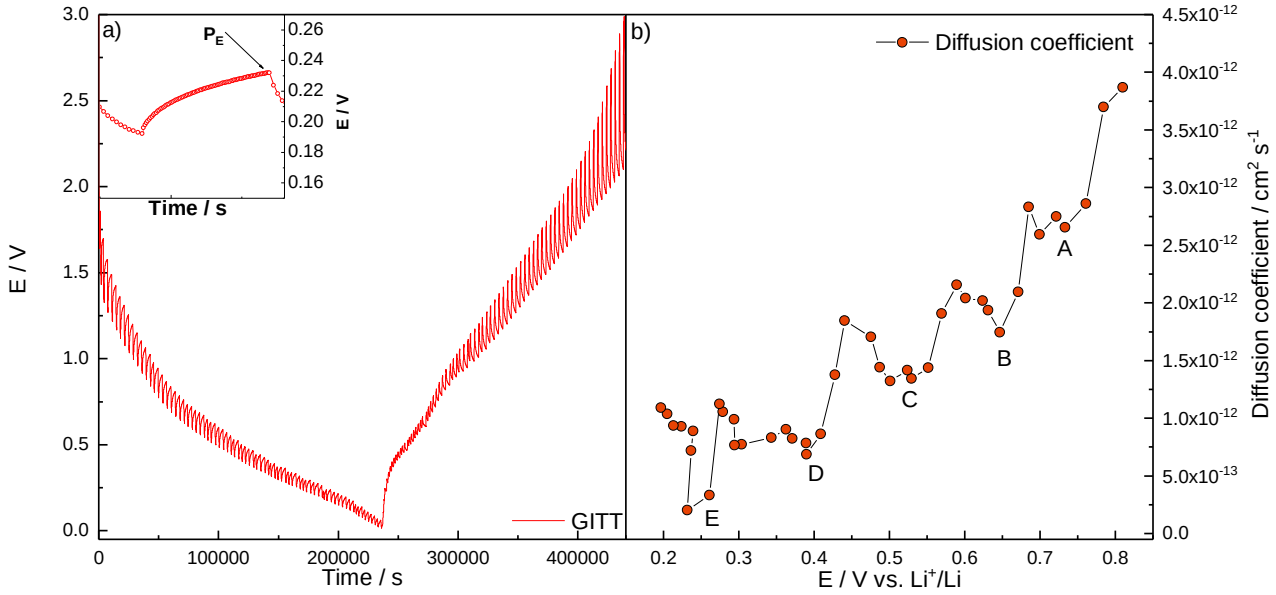

Figure 2-12. a) GITT curve and b) D_{Li} vs. E plot.

The electrode was cycled 4 times with a specific current I_{Spec} = 100 mA g^{-1} prior GITT measurement. For the titration experiment, a specific current I_{GITT} = 100 mA g^{-1} was applied for 10 minutes with a rest time of 1 h. In **Figure 2-12a**, the stepwise GITT curve as well as an inset showing a single titration step are reported. From the titration experiment an experimental specific capacity Q_{exp} = 1233 mAh g^{-1} was calculated. The titration was continued until potential 0.2 V was reached, in which the stoichiometry $Li_{4.4}Sn$ is formed. The lithium diffusion coefficient can be estimated by the **Equation 18** (43; 44):

$$D_{Li} = \frac{4}{\pi}\left(I\frac{V_m}{FS}\right)^2\left(\frac{dE}{d\delta}\Big/\frac{dE}{dt^{1/2}}\right)^2, \quad t \ll l^2/D_{Li} \qquad \textbf{Eq. 18}$$

Where I is the applied current, V_m is the molar volume of the active material, F Faraday constant (96485 C mol^{-1}), S electrode surface, $dE/d\delta$ the derivative of the potential according to δ (where $0 < \delta < 4.4$ in $Li_\delta Sn$), $dE/dt^{1/2}$ the derivative of the potential according to the square root of time. The calculated D_{Li} values fall in the range order between 10^{-13} to 10^{-12} cm^2 s^{-1}. As the potential decreases and the lithiation degree increases, the D_{Li} decreases with several local minima. These features

can be indexed to the three-phase equilibria introduced by Huggins in (45) between two different $Li_{\delta}Sn$ and $Li_{\delta+x}Sn$ phases, and the amorphous Li_2O matrix. All the minima potential as well as the phase compositions are summarized in **Table 5**.

Table 5. Summary of the local minima potential and corresponding three-phases equilibrium (45).

	Potential range Li^+/Li	$Li_{\delta}Sn$ Phases
A	0.76 – 0.70 V	Li_2O-Sn-$Li_{0.4}Sn$
B	0.65 V	Li_2O-$Li_{0.4}Sn$-$Li_{0.714}Sn$
C	0.55 V	Li_2O-$Li_{0.714}Sn$-$Li_{2.33}Sn$
D	0.49 V	Li_2O-$Li_{2.33}$-$Li_{2.6}Sn$
E	0.40 V	Li_2O-$Li_{2.6}Sn$-$Li_{3.5}Sn$
F	0.26 – 0.23 V	Li_2O-$Li_{3.5}Sn$-$Li_{4.4}Sn$

The electrode/electrolyte interface stability was studied by potentiostatic electrochemical impedance spectroscopy. Impedance spectra were acquired every 10^{th} cycle at the bias potential of E = 0.020 V. All the dispersion are characterized by the following features: (i) an intercept in the real axis, (ii) a small arc in the high-frequency region, (iii) an arc in the mid-frequency region, and (iv) a straight line in the low-frequency region. These features are commonly attributed to (i) migration of charges in the electrolyte, (ii) migration of Li^+ ions through the SEI layer, (iii) charge-transfer process and surface accumulation of charges in the active material, and (iv) diffusion of Li^+ ions in the active material (46). As the number of cycles increases, the overall impedance increases, especially in the medium-frequency region caused by the electrode/electrolyte interface worsening due to possible aggregation or electrode pulverization.

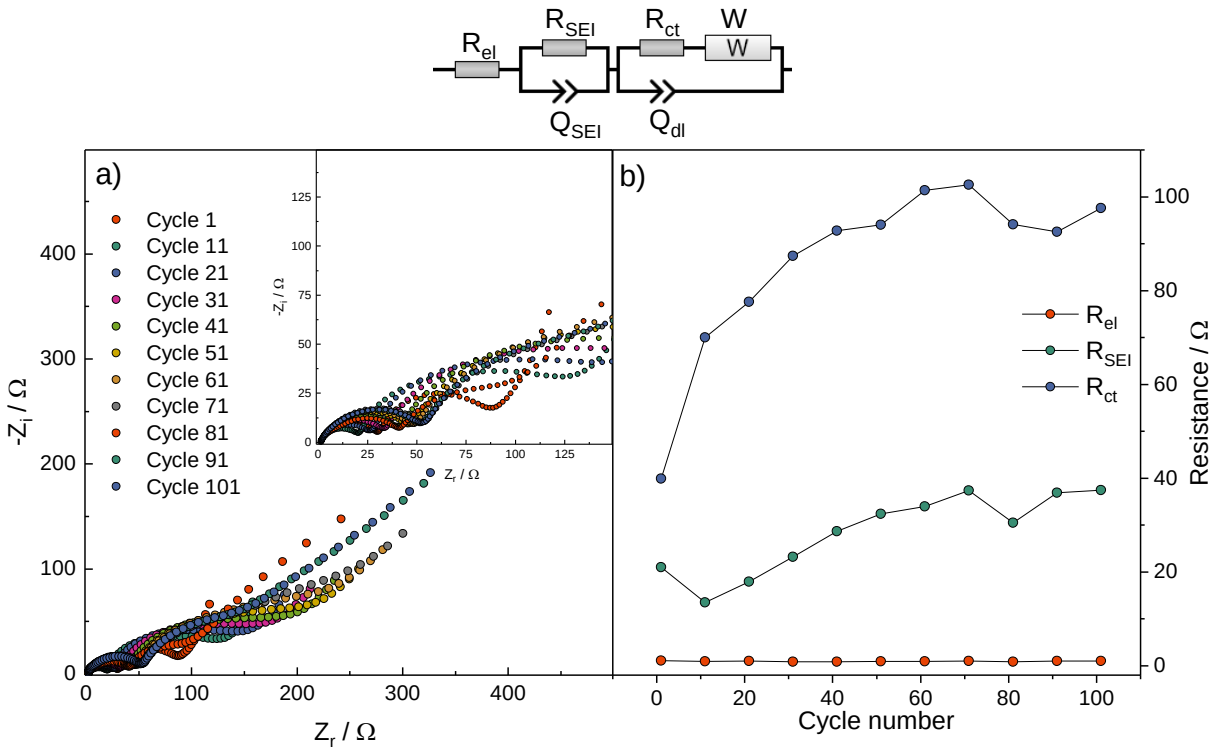

Figure 2-13. a) Nyquist plot acquired every 10th cycle and b) resistance values obtained by CNLS-fit.

In order to have an in-depth analysis, Relaxis 3 (rhd instruments, Germany) software was used for the mathematical fit of the acquired data. In this case, an equivalent circuit model consisting of $R_{el}(R_{SEI}C_{SEI})(R_{ct}C_{dl})W$ (Boukamp's notation (47)) was used, where R_{el} is the electrolyte resistance, R_{SEI} and C_{SEI} are the resistance and the capacitance of the passivation layer, R_{ct} and C_{dl} are the resistance correlated to the charge-transfer reaction and the double-layer capacitance, and W is the Warburg element used to describe the low-frequency polarization. All the capacitive elements were fitted by using a constant phase element (46) to consider roughness and electrode surface inhomogeneity. All the χ^2 obtained from the analysis were in the 10^{-5} order. The results of the CNLS fitting procedure are presented in **Figure 2-13b**. The resistance associated to the electrolyte does not change upon cycling, suggesting that no degradation of the electrolyte occurs. The resistances associated to the charge-transfer process and to the SEI layer increase upon cycling. The increase of the R_{ct} can be ascribed to the volume expansion/contraction of the active material upon cycling. Specifically, the resistance sharply increases in the first 40 cycles reaching a relative stabilization, suggesting that some structural reorganization occurs in the electrode. The increase of the R_{SEI} can be attributed to a breakage and re-formation of SEI due to the volume expansion/contraction of the active material.

2.2.4 Conclusions

A high-energy density composite anode material has been synthesized by sol-gel assisted method. The structural characterization revealed the presence of two different phases i.e., cassiterite SnO_2 and anatase TiO_2. Furthermore, the presence of 12.44 % of amorphous carbon was confirmed by both Raman spectroscopy and TGA. The SnO_2 nanopowder is characterized by a spherical shape with an average diameter of 18 nm. TiO_2 is present as larger grains in which SnO_2 nanoparticles are attached, suggesting a possible buffering effect. High specific capacities were obtained at different currents rates, ranging from 707 mAh g^{-1} at 2000 mA g^{-1} up to 1131 mAh g^{-1} at 100 mA g^{-1}. The investigation of transport properties by CV and GITT revealed a diffusion-controlled behavior. Furthermore, an experimental specific capacity of Q_{exp} = 1233 mAh g^{-1} was calculated. By calculating the D_{Li} from GITT measurements, the formation of three-phases equilibrium was exploited giving six local minima due to different degree of lithiation of Sn. The investigation of electrode-electrolyte interface revealed an increasing polarization related to the SEI breakage and re-formation as well as structural rearrangements of the active material.

2.3 Synthesis and Characterization of High-performance and Stability SnO_2/C Composite Anode for Li-ion Batteries

2.3.1 Synthesis

SnO_2/C was synthesized following a simple and fast procedure. Firstly, a certain amount of ACS sucrose (Sigma-Aldrich) was dissolved in ethanol. Then, commercial SnO_2 nanopowder (Sigma Aldrich, average particle size ≤ 100 nm) was dispersed into the above solution with the help of ultrasonic immersion stirrer (operated at 50 W, continuous mode), considering a final ratio of SnO_2:C 1:1. After 1 h the dispersion was heated at 70 °C until complete evaporation of the solvent. The obtained powder was ball-milled (Retsch S100 planetary ball mill) by using an agata jar and agata spheres of Ø = 10 mm (ball to powder weight ratio 10:1) at 400 rpm for 2 h. Eventually, the powder was collected and treated in a tubular furnace at 600 °C for 4 h under Ar atmosphere (thermal gradient: 5 °C min^{-1}) to obtain the amorphous carbon matrix. The synthesis procedure is summarized in **Figure 2-14**.

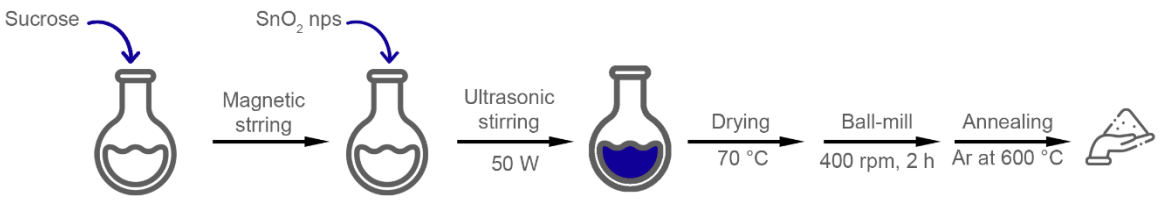

Figure 2-14. Schematic illustration of the synthesis of SnO_2/C.

2.3.2 Results and discussion: structural, morphological, and thermal characterization

The SEM micrographs of SnO_2/C are presented in **Figure 2-15**. At low magnification levels, the nanocomposite is characterized by large grains of ≈ 100 μm; however, with only secondary electrons is not possible to discern the exact morphology. For this reason, a micrograph at the same spot and magnification level was taken by using backscattered electrons. The large grains are characterized by a porous structure with embedded SnO_2 nanoparticles (assumption given by lighter spots on the grains). At higher magnification levels (40000 and 80000 x) the SnO_2 nanoparticles can be observed. They are characterized by a spherical shape with a diameter ranging from 10 up to 100 nm.

The structure of the nanocomposite material was characterized by both X-Ray Diffraction and Raman spectroscopy. The experimental diffractogram of SnO_2/C as well as the cassiterite SnO_2 reference card are shown in **Figure 2-16**. The reflections pattern of SnO_2/C clearly correspond to the rutile-type structure of cassiterite SnO_2 with a space group $P4_2/mnm$. An average crystallite size of ≈ 30 nm was estimated by applying Scherrer's equation (**Equation 13**). No signals of amorphous carbon were observed in the diffractogram. For this reason, Raman spectroscopy was employed to check the presence of carbonaceous materials. The Raman spectra of SnO_2/C is shown in **Figure 2-17**.

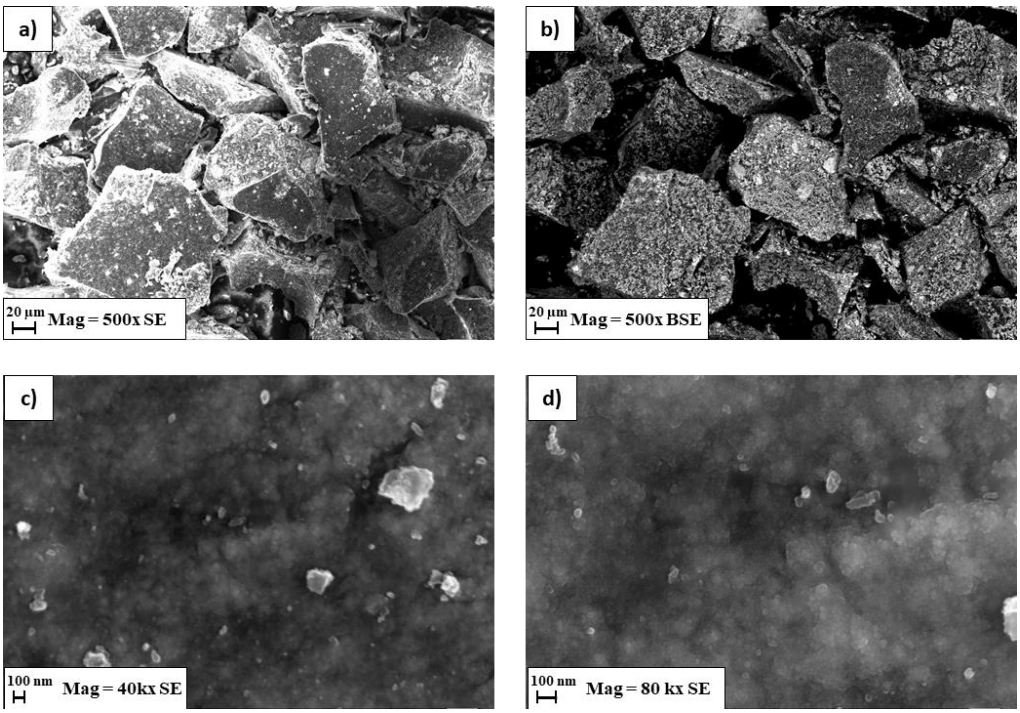

Figure 2-15. SEM micrographs of a) SnO_2/C nanopowder at 500 x with secondary electrons, at b) 500 x with backscattered electrons, c) 40000 x with secondary electrons, and d) 80000 x with secondary electrons.

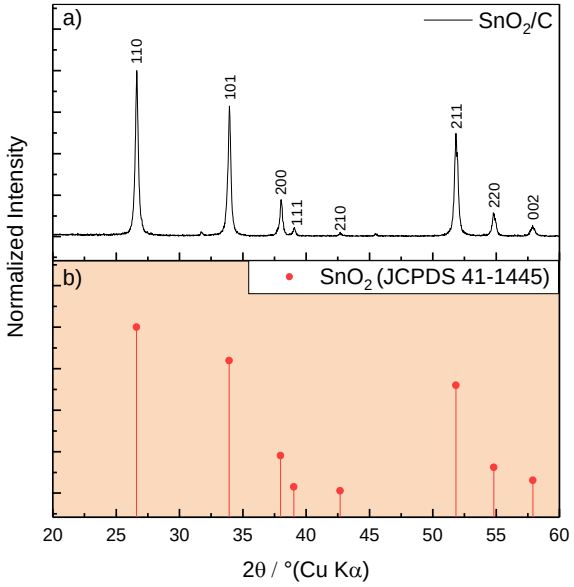

Figure 2-16. a) Experimental diffractogram of SnO_2/C. b) Reference card of cassiterite SnO_2.

The Raman spectrum of SnO_2/C is characterized by signals of both SnO_2 and amorphous carbon. Specifically, the four signals at 500, 623, 683, and 766 cm^{-1} can be ascribed to the A_{2u} $\nu_{(TO)}$, A_{1g}, A_{2u} $\nu_{(TO)}$, and B_{2g} modes of cassiterite SnO_2 (28). The two signals at 1351, and 1584 cm^{-1} can be assigned to the D and G bands of amorphous carbon, respectively.

The amount of C, and thus the ratio SnO_2:C was assessed by TGA in oxidizing atmosphere (**Figure 2-18**). The sample presented a weight loss from 400 up to 500 °C due to the decomposition of the carbon matrix into CO_2, giving a percentage of amorphous carbon of 44.04 %.

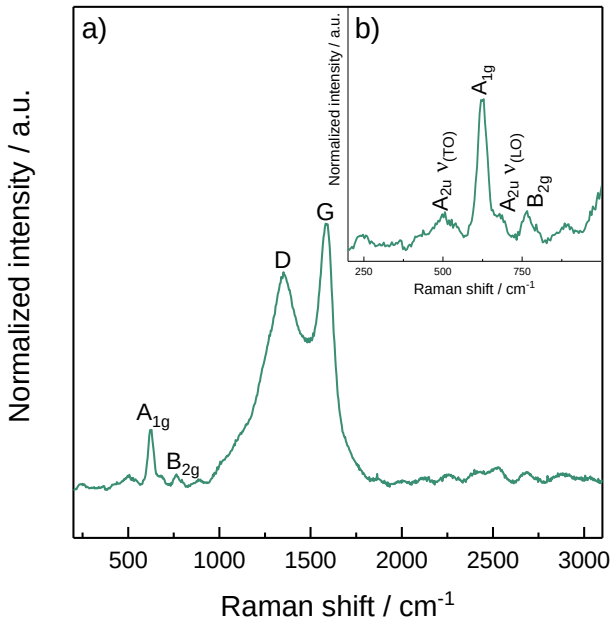

Figure 2-17.a) Raman spectra of SnO_2/C. b) Inset image of signals coming from SnO_2.

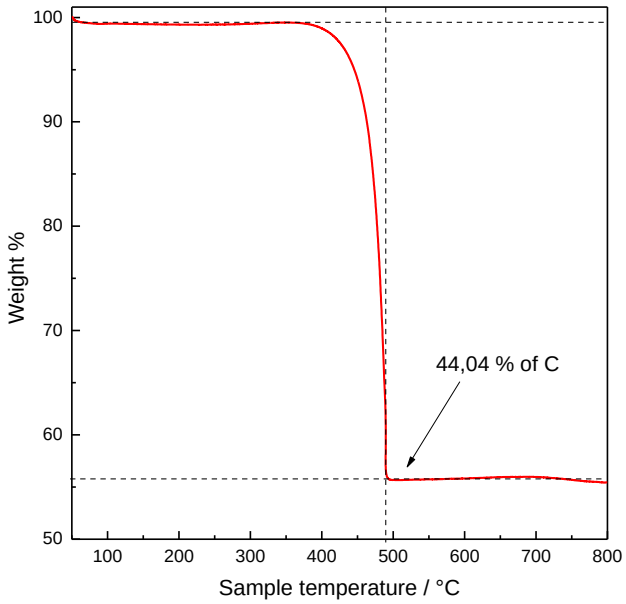

Figure 2-18. TGA of SnO_2/C composite.

2.3.3 Results and discussion: electrochemical characterization

In **Figure 2-19**, the cyclic voltammetry of SnO_2/C obtained at 0.100 mV s^{-1} is reported. In the first cathodic scan the peak A at 0.86 V can be assigned to the conversion reaction of SnO_2 as previously

described in **Equation 15** (33; 7; 2; 9). In the same potential region, the decomposition of the electrolyte leading to the formation of the SEI starts (34; 35). The peak of the conversion reaction is not as sharp as peak C of TiO_2@SnO_2 (**Figure 2-6**); this behavior can be explained by (i) the lower amount of SnO_2 in the composite, (ii) overlap with the intercalation of Li^+ into amorphous carbon, and (iii) overlap with the SEI formation. The peak B at 0.25 V can be assigned to the alloying reaction of Sn with lithium described in **Equation 16** (33; 7; 2; 9). During the first anodic scan, to peaks B' and B'' at 0.47 V and 0.64 V, respectively, can be assigned to the reversible dealloying reaction of different Li_xSn phases.

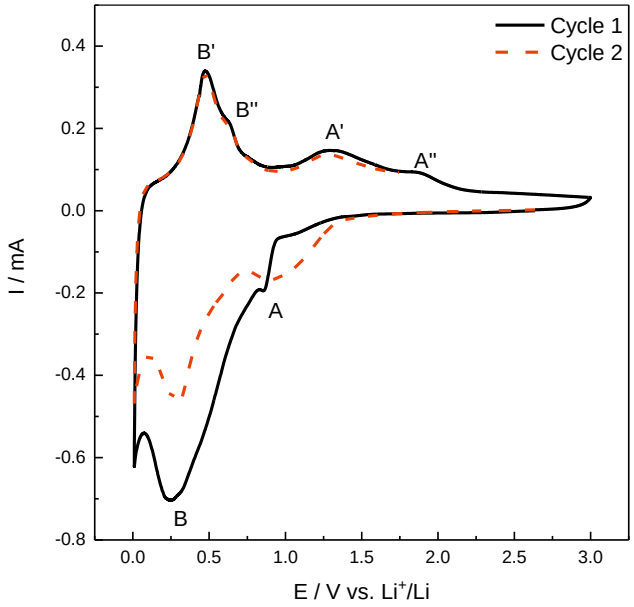

Figure 2-19. Cyclic voltammetry of SnO_2/C acquired on cycle 1 and 2 with a scan rate of 0.100 mV s^{-1}.

At higher potentials, the two peaks A' and A'' can be assigned to the partial oxidation of Sn to higher oxidation states (36). During the second scan, the shape of the voltammogram is preserved apart from peak A which is replaced by a broad hump.

Preliminary galvanostatic cycles were performed by applying a specific current I_{spec} = 500 mA g^{-1} in the potential window 0.010 < E< 3.000 V vs. Li^+/Li (**Figure 2-20**). A constant voltage period was applied during lithiation until the current reached I_{CV} = 50 mA g^{-1}.

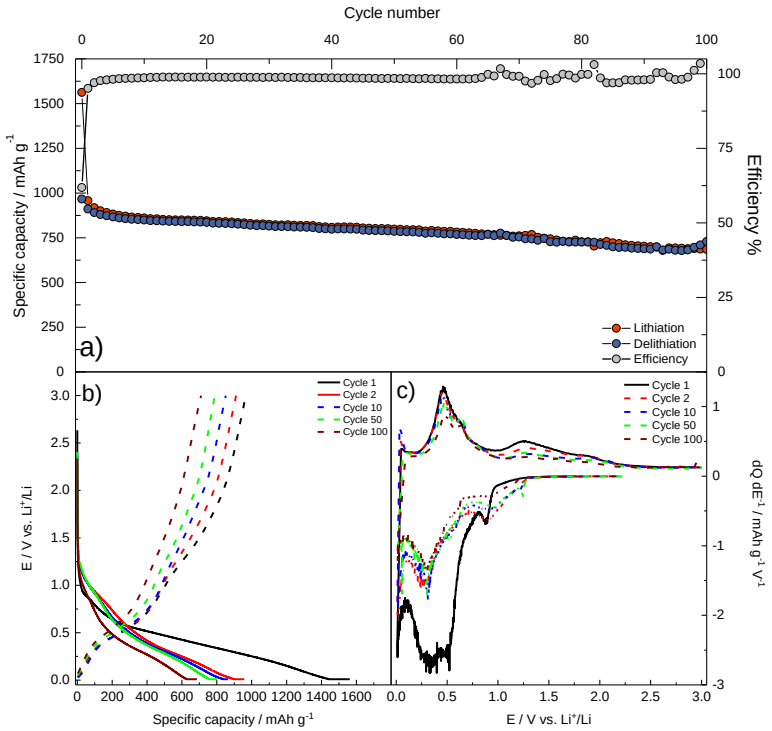

Figure 2-20. a) Specific capacity vs. cycle number of SnO_2/C. Galvanostatic b) E vs. Q and c) dQ dE^{-1} vs. E profiles.

During the 1st cycle, specific capacities of 1562 mAh g^{-1} and 966 mAh g^{-1} were measured for lithiation and delithiation, respectively, with a coulombic efficiency of η_Q = 62 %. A small capacity drop is present in the first 10 cycles probably due to structural rearrangements of the electrode material. Afterwards, an average specific capacity of 100 cycles Q_{100} = 798 mAh g^{-1} and a η_Q of almost 100 %. Looking at the galvanostatic E vs. Q profiles in **Figure 2-20b**, the voltage plateau at ≈ 0.90 V in the first lithiation can be assigned to the conversion reaction of SnO_2 with the formation of Sn metal and Li_2O matrix (33; 7; 2; 9). Then, a sloping line from ≈ 0.60 V down to the lower cut-off voltage can be assigned to the alloying reaction of Sn with lithium (33; 7; 2; 9). In the same potential region of the processes described above, the SEI formation and intercalation of Li^+ into amorphous carbon occur. During delithiation, two sloping lines are clearly visible i.e., at 0.4 V and 1.2 V assigned to the reversible dealloying reaction of Li_xSn and partial oxidation of Sn. Form the second cycle, the plateau at 0.9 V of the conversion reaction is replaced by a sloping line. The galvanostatic dQ dE^{-1} vs. E profiles clearly reflect the behavior observed by cyclic voltammetry. A large voltage hysteresis is clearly visible form the galvanostatic E vs. Q profiles, thus the energy efficiency η_E has been calculated in the 50th cycle vs. a theoretical LFP cathode (**Figure 2-21**).

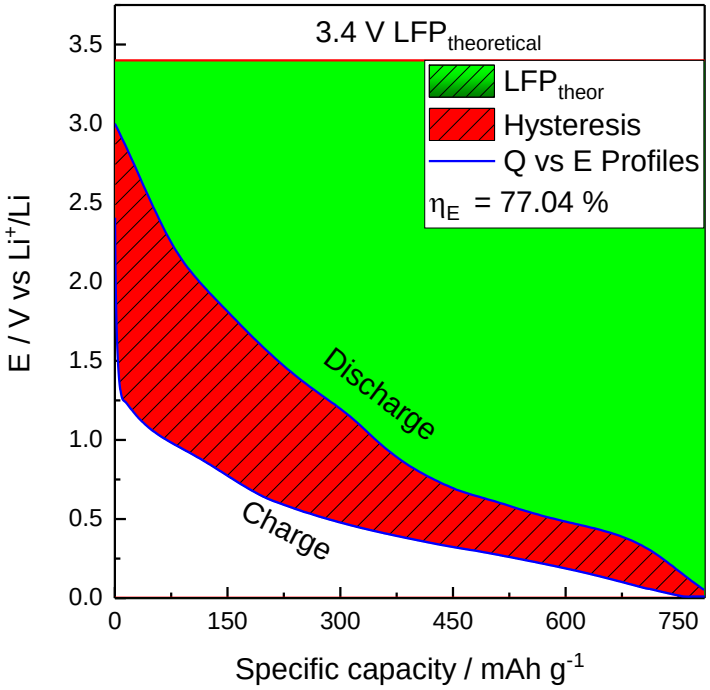

Figure 2-21. Graphical demonstration of the voltage hysteresis calculated at the 50th cycle vs. a theoretical LFP cathode.

A slightly higher energy efficiency η_E = 77.04 % than TiO_2@SnO_2 has been obtained. This feature can be ascribed to (i) the lower content of SnO_2 (from 66 % down to 56 %), and (ii) to the presence of amorphous carbon who has a slightly lower working potential compared to conversion materials. In **Figure 2-22**, the galvanostatic cycles with capacity limitation during delithiation as well as the voltage hysteresis profile are reported. By limiting the capacity to a 70 % of the one obtained in **Figure 2-20**, the storage mechanism is mostly limited to the alloying reaction. Indeed, a smaller voltage hysteresis, and thus a higher energy efficiency of 86.53 % was obtained.

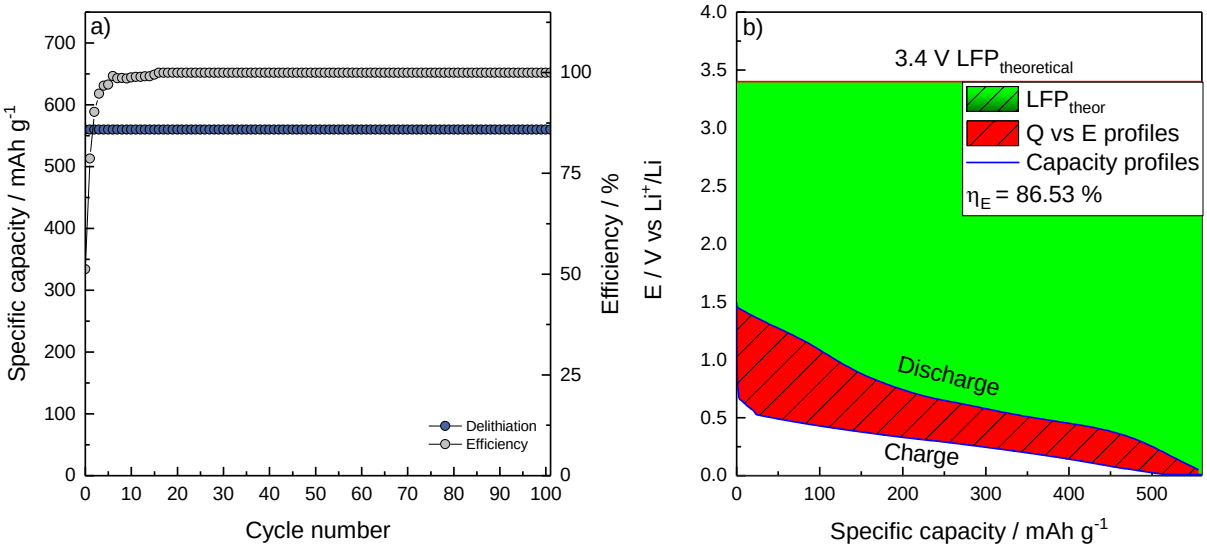

Figure 2-22. a) Galvanostatic cycles with capacity limitation Q_{Lim} = 560 mAh g^{-1}. b) Voltage hysteresis at the 50th cycle calculated vs. a theoretical LFP cathode.

The rate capability of SnO_2/C was assessed by galvanostatic cycling with specific current rates ranging from 50 up to 5000 mA g^{-1}. The obtained specific capacity values as well as galvanostatic E vs. Q and dQ dE^{-1} vs. E profiles are reported in **Figure 2-23**.

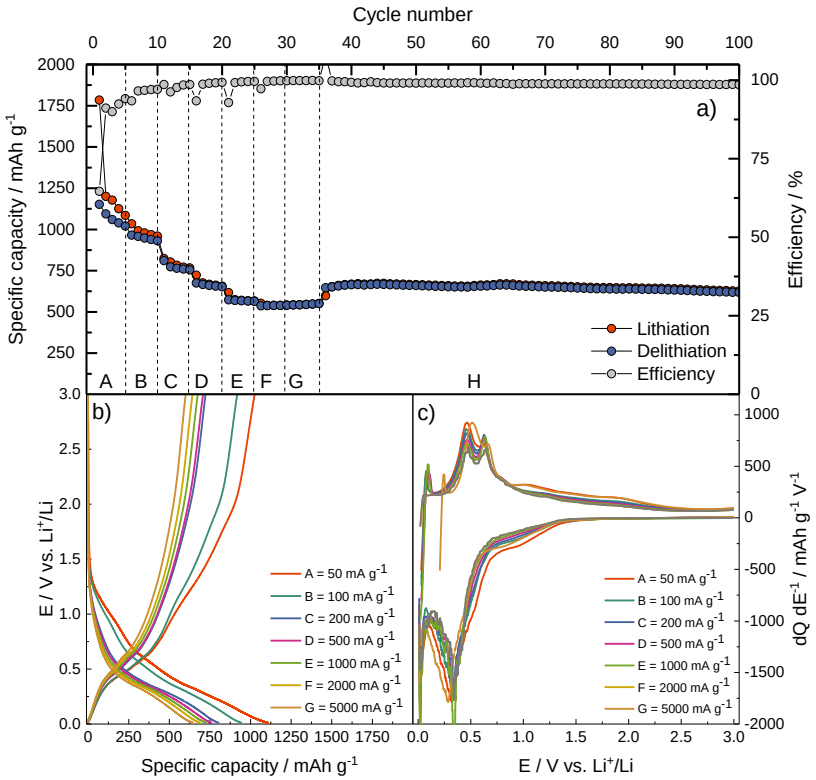

Figure 2-23. a) Specific capacity vs. cycle number. Galvanostatic b) E vs. Q and c) dQ dE^{-1} vs. E profiles. Specific current applied: A = 50 mA g^{-1}, B = 100 mA g^{-1}, C = 200 mA g^{-1}, D = 500 mA g^{-1}, E = 1000 mA g^{-1}, F = 2000 mA g^{-1}, G = 5000 mA g^{-1}, and H = 500 mA g^{-1}.

The rate capability results are summarized in **Table 6**.

Table 6. Average specific lithiation capacity and coulombic efficiency as a function of the applied current.

Step	Specific current / mA g^{-1}	Average lithiation specific capacity / mAh g^{-1}	Average coulombic efficiency / %
A	50	1146	92.1
B	100	986	96.8
C	200	789	98.1
D	500	676	98.3
E	1000	579	98.4

F	2000	542	99.2
G	5000	532	99.8
H	500	655	99.9

High specific capacities were obtained at all current rates, especially at the high current load of 5 A g^{-1} where the composite was able to deliver a specific capacity of 532 mAh g^{-1}. When the current was restored to 500 mA g^{-1}, the active material was able to retain an average specific capacity of 655 mAh g^{-1}. High average specific capacity values of 1146 and 986 mAh g^{-1} were also obtained at 50 and 100 mA g^{-1}, respectively. However, the associated coulombic efficiencies were 92.1 and 96.8 %, respectively, suggesting a poor reversibility of the lithiation reaction as well as concurrent parasitic reactions at the electrode/electrolyte interface. Galvanostatic E vs. Q and differential dQ dE^{-1} vs. E profiles were extracted in each current step to understand the current-controlled behaviour (**Figure 2-23b-c**). In both cases, as the current increases the profiles preserve their shapes. The two sloping lines observed in **Figure 2-20b** during lithiation at 1.2 and 0.4 V for the conversion reaction and alloying reaction are clearly visible, as well as the quasi-plateau at 0.5 V during delithiation due to the dealloying reaction. In the dQ dE^{-1} vs. E profiles, there is only a small effect of polarization, in which the alloying peak becomes smaller and shifts to lower potential, while the dealloying peak shifts to higher potentials.

Electrochemical investigation of transport and interfacial properties

CV, GITT, and PEIS were used to investigate the transport as well as interfacial properties of SnO_2/C electrodes. In **Figure 2-24**, the cyclic voltammetries acquired at different scan rates as well as the I_p vs. $\nu^{1/2}$ plot are reported. As the scan rate increases, the exchanged current proportionally increases. In fact, by plotting the peak current (peak B has been used for the calculation) as a function of the square root of the scan rate, a linear relationship between them is observed. Indeed, by linear fitting the experimental data, a $R^2 = 0.99798$ is obtained, suggesting a diffusion-controlled behavior (42).

GITT was performed in a similar way as for TiO_2@SnO_2. The SnO_2/C electrode was cycled 5 times at I_{Spec} = 50 mA g^{-1} prior the experiment. The titration was performed by applying a specific current of I_{GITT} = 50 mA g^{-1} for 10 min followed by an OCV period of 2 h.

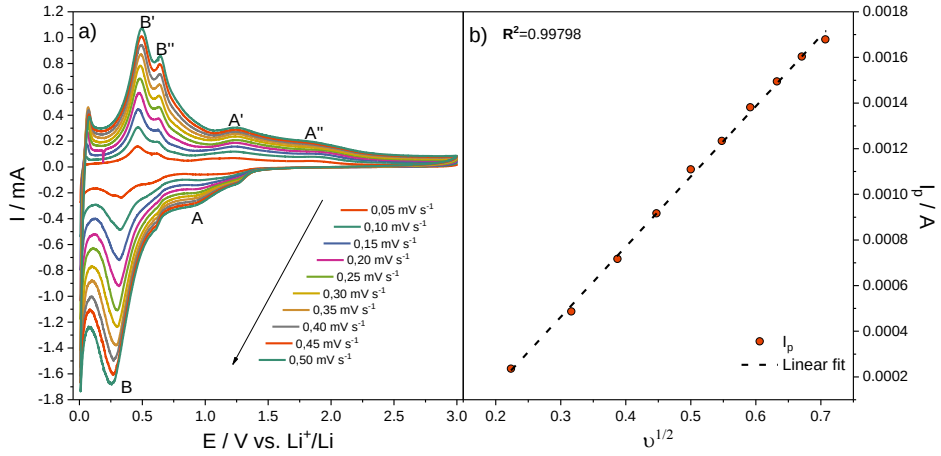

Figure 2-24. a) Cyclic voltammetries acquired at different scan rates. b) I_p vs. $\nu^{1/2}$ plot.

The GITT curve as well as the D_{Li} vs. E are reported in **Figure 2-25**.

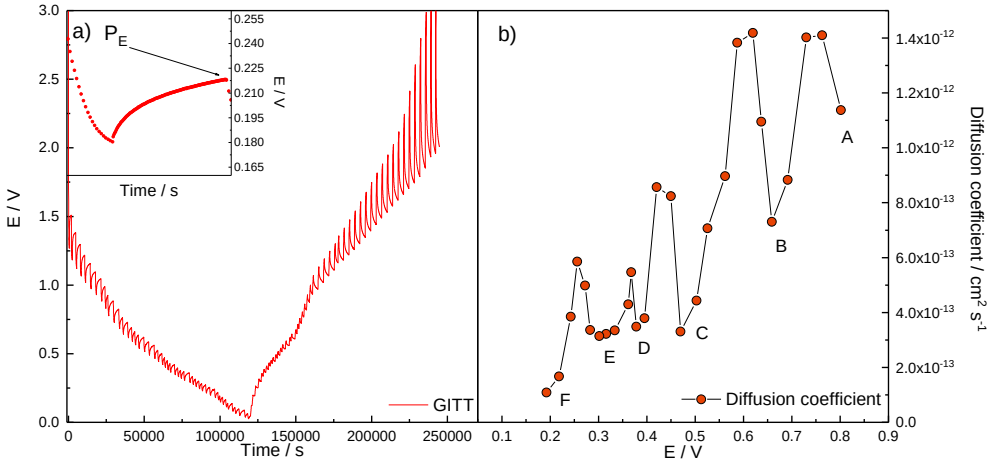

Figure 2-25. a) GITT curve of SnO_2/C electrode. b) D_{Li} vs. e plot.

From the titration experiment an experimental specific capacity Q_{exp} = 782 mAh g^{-1} was calculated. The titration was continued until reaching the voltage threshold of E = 0.2 V, in which the phase $Li_{4.4}Sn$ is formed. The D_{Li} was estimated using **Equation 18** as for TiO_2@SnO_2. The D_{Li} decreases with the increase of the lithiation degree with values in the order of 10^{-12} - 10^{-13} cm^2 s^{-1}. Six different local minima are observed as the previous SnO_2-based composite anode, representing the formation of different three-phases equilibrium (45). The potential range as well as the corresponding three-phases equilibrium are reported in **Table 7**.

Table 7. Summary of the local minima potential and corresponding three-phases equilibrium (45).

	Potential range Li^+/Li	Li_8Sn Phases
A	0.80 V	Li_2O-Sn-$Li_{0.4}Sn$
B	0.66 V	Li_2O-$Li_{0.4}Sn$-$Li_{0.714}Sn$
C	0.50 – 0.46 V	Li_2O-$Li_{0.714}Sn$-$Li_{2.33}Sn$
D	0.39 – 0.37 V	Li_2O-$Li_{2.33}$-$Li_{2.6}Sn$
E	0.33 – 0.28 V	Li_2O-$Li_{2.6}Sn$-$Li_{3.5}Sn$
F	0.2 V	Li_2O-$Li_{3.5}Sn$-$Li_{4.4}Sn$

The stability of the electrode/electrolyte interface was assessed by potentiostatic electrochemical impedance spectroscopy every 10th cycle at bias potential E = 0.180 V. The $-Z_{im}$ vs. Z_{re} complex plot as well as the fitted resistance parameter are reported in **Figure 2-26**.

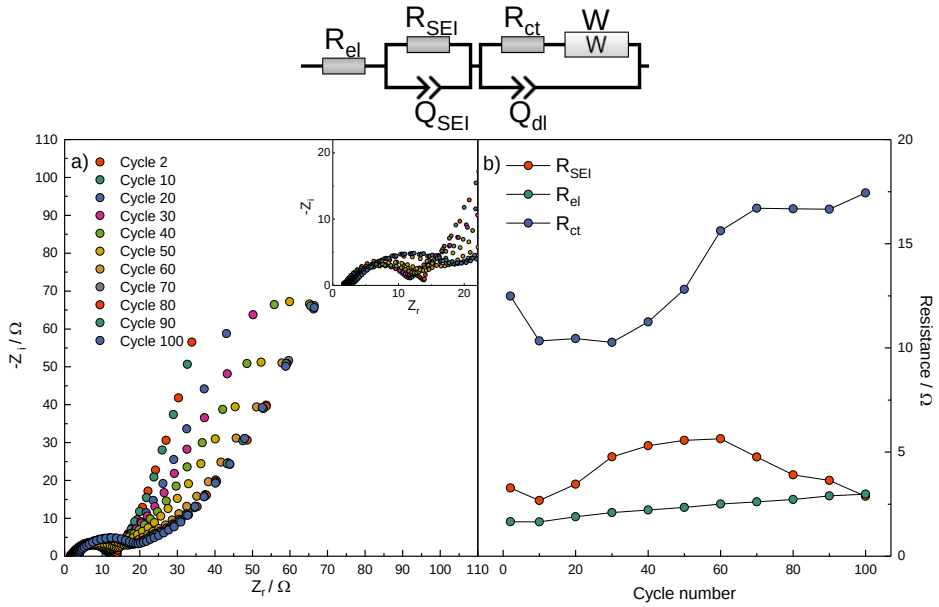

Figure 2-26. a) $-Z_{im}$ vs. Z_{re} complex plot acquired every 10th cycle. b) Fitted resistance parameters as a function of cycle number.

All the dispersions are characterized by (i) a straight line in the low-frequency range, (ii) a suppressed arc in the medium-frequency range, and (iii) an intercept in the real axis. These features are commonly accounted for (i) the diffusion of Li^+ ions into the active material, (ii) the charge transfer resistance as well as the electrochemical double layer, and (iii) migration of Li^+ ions in the electrolyte. A further feature i.e., the arc in the high-frequency region, commonly associated to the migration of Li^+ ions through the SEI layer, is probably overlapped with the arc related to the charge-transfer process. The impedance spectrums were CNLS-fitted by using

Relaxis 3 software (rhd instruments). An ECM consisting of $R_{el}(R_{SEI}C_{SEI})(R_{ct}C_{dl})W$ (Boukamp's notation (47)) was used, where R_{el} is the electrolyte resistance, R_{SEI} and C_{SEI} are the resistance and the capacitance of the passivation layer, R_{ct} and C_{dl} are the resistance correlated to the charge-transfer reaction and the double-layer capacitance, W is the Warburg element used to describe the low frequency polarization. All the capacitive elements were fitted by using a constant phase element (46) to consider roughness and electrode surface inhomogeneity. All the χ^2 obtained from the fitting procedure were in the 10^{-5} order. The results of the CNLS fitting procedure are presented in **Figure 2-26b**. The resistance associated to the electrolyte has a small increase upon cycling, suggesting a possible degradation of its components. The resistance associated to the SEI layer has a small increase between the 20th and the 80th cycle. This change can be explained by the structural rearrangement with the exposure of "fresh" surface of the active material in which the electrolyte can decompose. The resistance associated with the charge-transfer process increase upon cycling up to the 70th cycle, in which relatively stabilize. This behavior can be explained by the structural rearrangement of the active material as well as the unwanted coarsening of the Sn^0 particles.

2.3.4 Conclusions

A high-energy density composite anode material has been synthesized by simple method i.e., pyrolysis of sucrose. The structural characterization revealed the presence of two different phases i.e., cassiterite SnO_2 and amorphous carbon. TGA revealed a 44 % of C, as expected from the synthesis procedure. The SnO_2 nanopowder is characterized by a spherical shape with an average diameter of 30 nm. Amorphous carbon is present as larger grains in which SnO_2 nanoparticles are embedded, suggesting a possible buffering effect. High specific capacities were obtained at different currents rates, ranging from 532 mAh g^{-1} at 5000 mA g^{-1} up to 798 mAh g^{-1} at 500 mA g^{-1}. The investigation of transport properties by CV and GITT revealed a diffusion-controlled behavior. Furthermore, an experimental specific capacity of Q_{exp} = 782 mAh g^{-1} was calculated. By calculating the D_{Li} from GITT measurements, the formation of three-phases equilibrium was evidenced by six local minima due to different degrees of lithiation of Sn. The investigation of electrode-electrolyte interface revealed an increasing polarization related to the SEI breakage and re-formation as well as structural rearrangements of the active material.

2.4 Synthesis and Characterization of C/SnO_2 Nanorods as High-Performance Anode Material for Li-ion Batteries

2.4.1 Synthesis

SnO_2 nanorods have been synthesized by a modified polyol-mediated oligomerization of SnC_2O_4 nanowires (48; 49; 50). Briefly, 200 mL of ethylene glycol were heated at T = 160 °C. Afterwards, 2 g of ACS SnC_2O_4 and 1 g of Pluronic P123 were dissolved in EG. The solution was left at T = 160 °C for 12 h. Eventually, the powder was collected by centrifugation and thoroughly washed with u.p. H_2O and EtOH. The SnC_2O_4 was finally converted into SnO_2 by a thermal annealing in a tube furnace at 500 °C for 4 h (ramping rate = 1 °C min^{-1}, air flow 1 L min^{-1}).

The carbon composite was prepared by dehydration of sucrose in presence of H_2SO_4. SnO_2 nanorods were dispersed in a solution of sucrose in u.p. water (sucrose:SnO_2 ratio of 3:1). Then, 10 µL of conc. H_2SO_4 were added to the above solution and heated at T = 100 °C for 4 h. Eventually, the temperature was raised to T = 160 °C until the solution was evaporated. The powder was then collected, grounded, and treated in a tube furnace at T = 600 °C in Ar atmosphere (ramping rate = 1 °C min^{-1}, Ar flow 1 L min^{-1}). The synthesis procedure is summarized in **Figure 2-27**. For sake of clarity, the composite C/SnO_2 nanorods will be called "C/SnO_2NR".

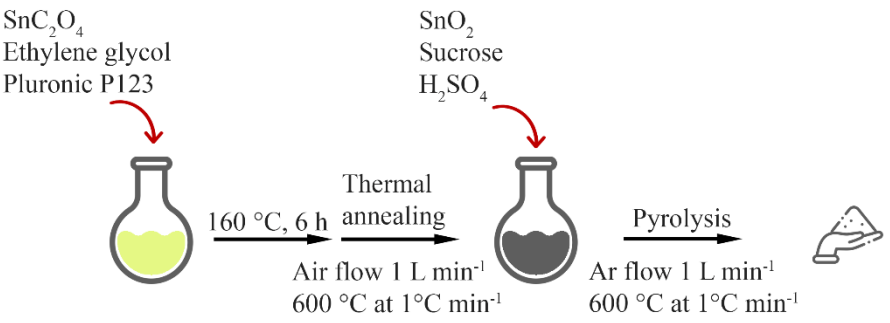

Figure 2-27. Schematic view of the synthesis of C/SnO_2NR.

2.4.2 Results and discussion: structural, morphological, and thermal characterization

The SEM micrographs of both SnO_2NR and C/ SnO_2NR are presented in **Figure 2-28**.

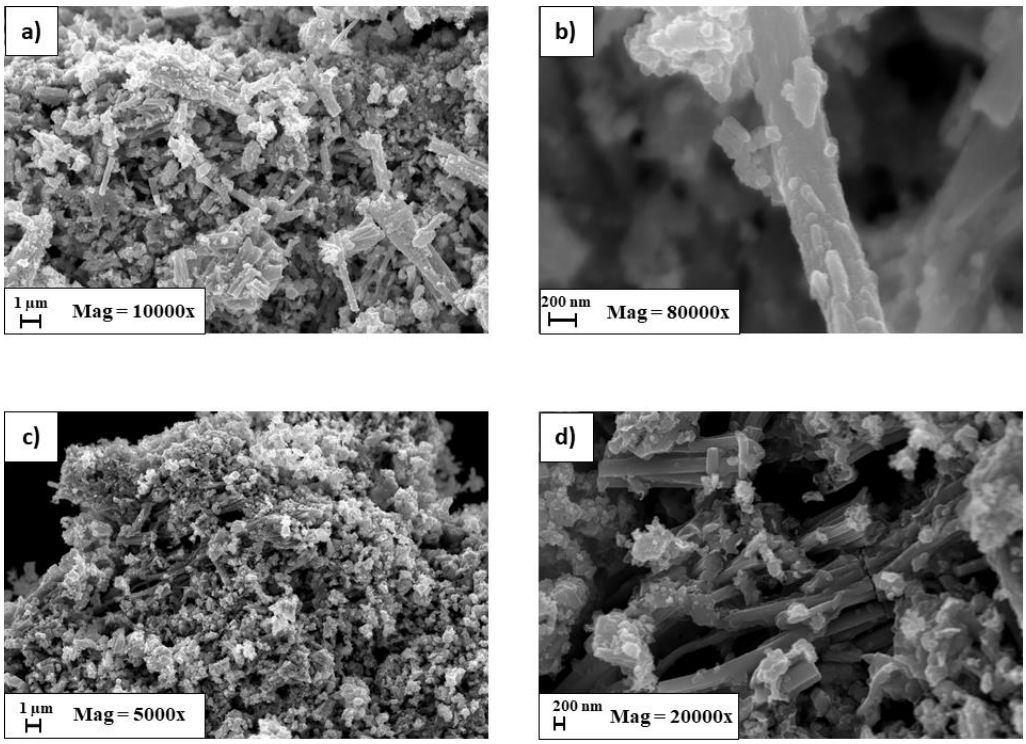

Figure 2-28. SEM micrographs of SnO_2NR at a) 10000x and b) 80000x, respectively. C/SnO_2NR micrographs at c) 5000x and d) 20000x, respectively.

The SnO_2NR are characterized by a rod-like morphology with uneven dimension. At a higher magnification level, the rods are composed by arranged SnO_2 nanoparticles with a diameter < 100 nm. The composite is characterized by rod-like SnO_2 surrounded by larger carbon grains. The synthesis method is adapted from the synthesis of SnC_2O_4 nanowires in (48; 49; 50), however a rod-like morphology was obtained. This is probably due to the thermal treatment for the conversion of SnC_2O_4 to SnO_2.

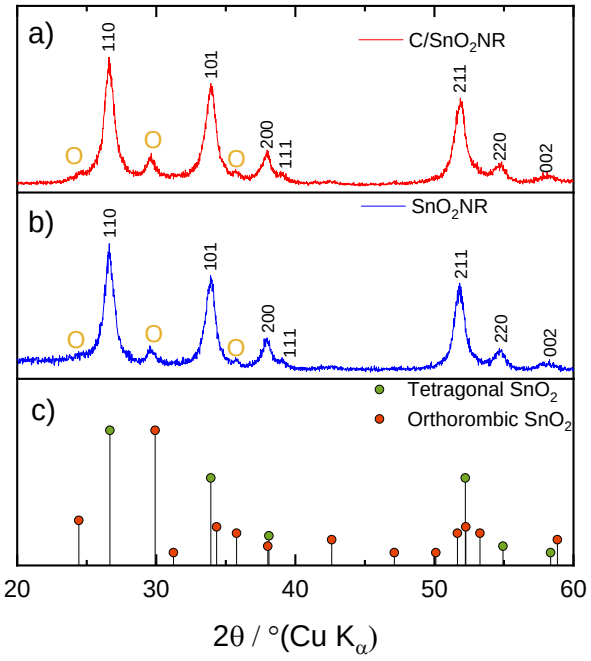

Figure 2-29. Experimental diffractogram of a) C/SnO_2NR and b) SnO_2NR. c) Reference diffractogram of tetragonal (cassiterite9 and orthorombic SnO_2

In **Figure 2-29**, the experimental diffractogram of both C/SnO_2NR and SnO_2NR are shown. In both cases, the main phase observed in the tetragonal cassiterite SnO_2 with space group $P4_2/mnm$. However, the presence of a second phase i.e., orthorhombic SnO_2 was also observed. No broad peak due to the presence of amorphous carbon was observed in the C/SnO_2NR diffractogram. By applying Scherrer's equation (**Equation 13**) an average crystallite size of 11.22 and 9.37 nm was calculated for SnO_2NR and C/SnO_2NR, respectively.

The Raman spectrum of C/SnO_2NR (**Figure 2-30**) is characterized by signals of both SnO_2 and amorphous carbon. Specifically, the four signals at 500, 623, 683, and 766 cm^{-1} can be ascribed to the A_{2u} $\nu_{(TO)}$, A_{1g}, A_{2u} $\nu_{(TO)}$, and B_{2g} modes of cassiterite SnO_2 (28). The three signals at 1351, 1584, and 2894 cm^{-1} can be assigned to the D, G and 2D bands of amorphous carbon, respectively.

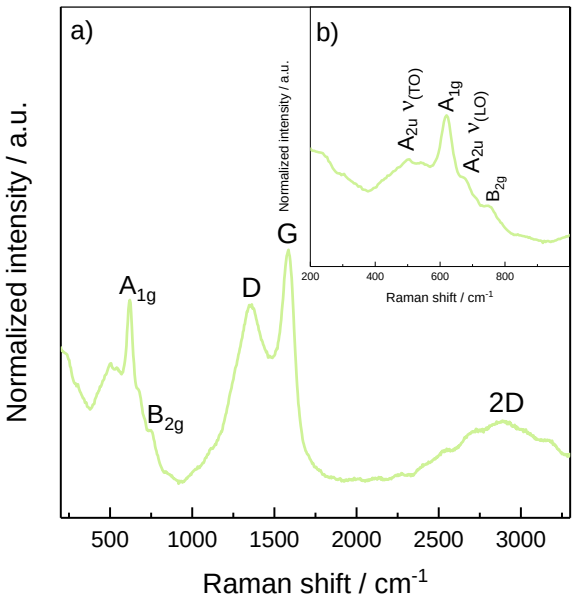

Figure 2-30. a) Raman spectra of C/SnO_2NR. b) Inset image of signals coming from SnO_2.

The amount of amorphous carbon in C/SnO_2NR was assessed with TGA in oxidising atmosphere (**Figure 2-31**).

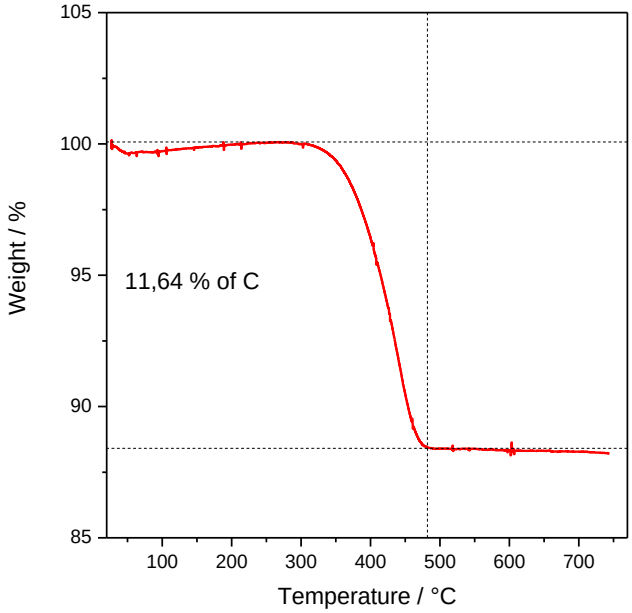

Figure 2-31. TGA of C/SnO_2NR in oxidising atmosphere at 10 °C min^{-1}.

The composite has a weight drop starting from 300 °C up to 500 °C, due to the decomposition of carbon into CO_2. The amount of amorphous carbon was assessed as 11.64 %, thus the SnO_2:C ratio can be calculated as 88:12.

2.4.3 Results and discussion: electrochemical characterization

In **Figure 2-32**, the cyclic voltammetry of C/SnO_2NR obtained at 0.100 mV s^{-1} is reported. In the first cathodic scan, the sharp peak A at 0.8 V can be assigned to the conversion reaction of SnO_2 (33; 7; 2; 9). In the same potential region, the SEI formation is triggered (34; 35). At lower potentials, the broad peaks B_1 and B_2 located at 0.5 and 0.2 V, respectively, can be assigned to the formation of different Li_xSn phases (33; 7; 2; 9). In the anodic scan, the peak B' at 0.51 V can be assigned to the reversible dealloying reaction, while the broad peaks A' and A'' at 1.27 and 1.87 V can be assigned to the partial oxidation of Sn^0 to its higher oxidation states (36). In the second cathodic scan, the sharp peak A at 0.8 V is replaced by a smaller and broader peak, suggesting a poor reversibility of the conversion reaction.

Preliminary galvanostatic cycles were performed by applying a specific current I_{spec} = 1000 mA g^{-1} in the potential window 0.010 < E< 3.000 V vs. Li^+/Li (**Figure 2-33**). A constant voltage period was applied during lithiation until the current reached I_{CV} = 100 mA g^{-1}.

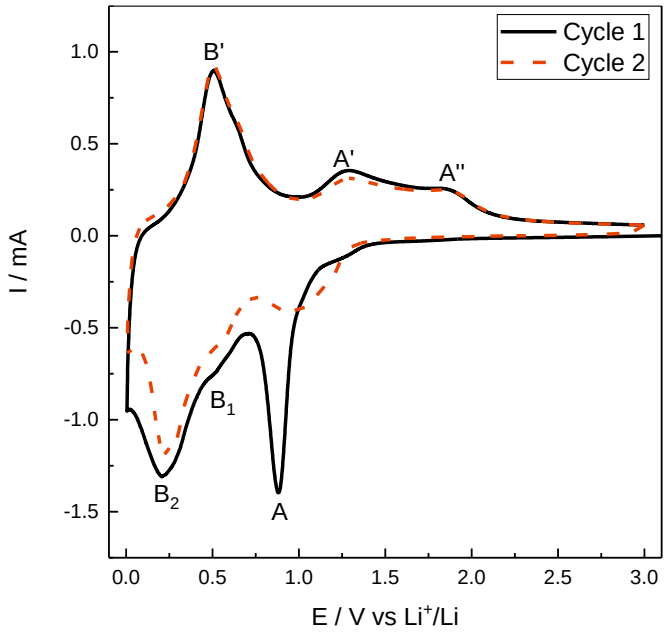

Figure 2-32. Cyclic voltammetry of C/SnO_2NR acquired at 100 μV s^{-1} during the first two cycles.

During the 1st cycle, specific capacities of 1744 mAh g^{-1} and 1137 mAh g^{-1} were measured for lithiation and delithiation, respectively, with a coulombic efficiency of η_Q = 65 %. The low coulombic efficiency clearly reflects first cycle irreversible processes like SEI formation, and the conversion of SnO_2 to Sn^0.

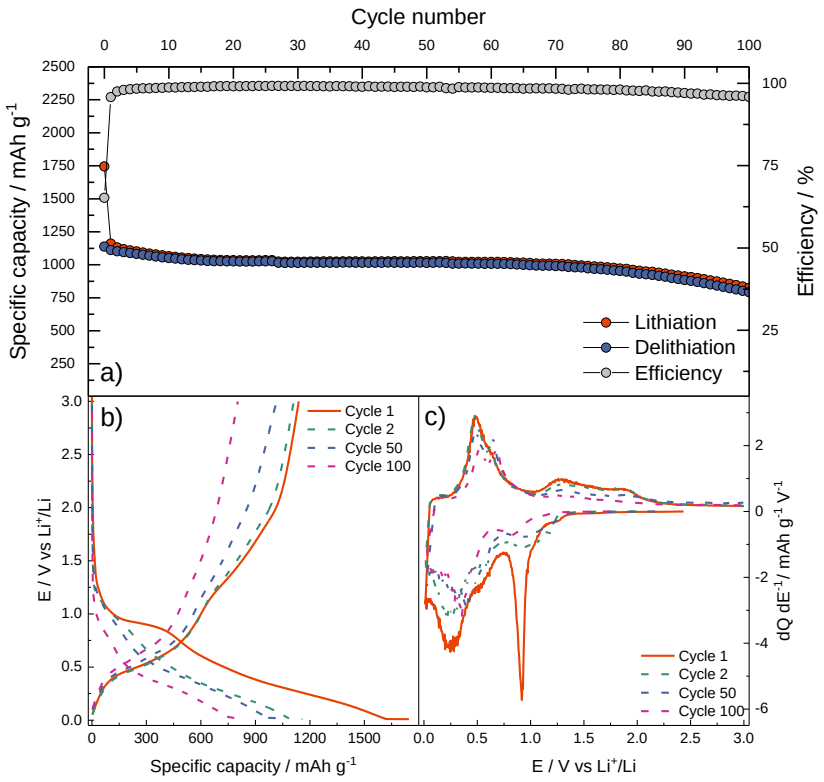

Figure 2-33. a) Specific capacity vs. cycle number of C/SnO_2NR. Galvanostatic b) E vs Q and c) dQ dE^{-1} vs. E profiles.

The specific capacity is stable in the first 70th cycles with an efficiency close to 100 %. However, after the 70th cycle, a capacity drop as well as a decrease of the coulombic efficiency were observed. The average specific capacity 100 cycle is Q_{100} = 1007 mAh g^{-1}. The extracted galvanostatic E vs. Q profiles are shown in **Figure 2-33b**. In the first lithiation, the plateau at E = 0.8 V and the following sloping line can be assigned to the conversion reaction of SnO_2 to Sn^0, and the alloying reaction, respectively (33; 7; 2; 9). Three features were observed during delithiation i.e., a quasi-plateau at E = 0.5 V due to the reversible dealloying reaction, and two sloping lines at E = 1.26 V and E = 1.9 V which can be assigned to the oxidation of Sn^0 to its higher oxidation states (36). In the further lithiation profiles, the plateau at E = 0.8 V was not observed and is replaced by a sloping line. The differential galvanostatic profiles dQ dE^{-1} vs. E shown in **Figure 2-33c**, confirm the results obtained from cyclic voltammetry measurements. A large voltage hysteresis is clearly visible form the galvanostatic E vs. Q profiles, thus the energy efficiency η_E has been calculated in the 50th cycle vs. a theoretical LFP cathode (**Figure 2-34**). As for the previous SnO_2-based anode materials, the energy efficiency without any capacity limitation is around 75 %. For this reason, a capacity limitation during delithiation (70 % of the obtained capacity in **Figure 2-33**, Q_{lim} = 700 mAh g^{-1}) was applied. The capacity vs. cycle number as well as the voltage hysteresis at the 50th

cycle are shown in **Figure 2-35**. By limiting the storage mechanism mostly to the alloying reaction, thus mostly avoiding the voltage hysteresis of the conversion reaction, a higher energy efficiency η_E = 86.04 % was obtained.

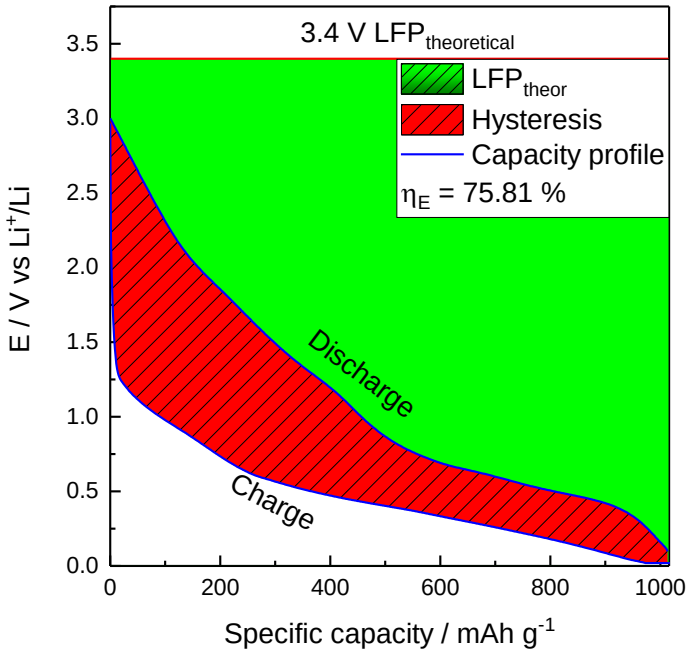

Figure 2-34. Voltage hysteresis curve of C/SnO_2NR calculated vs. a theoretical LFP cathode.

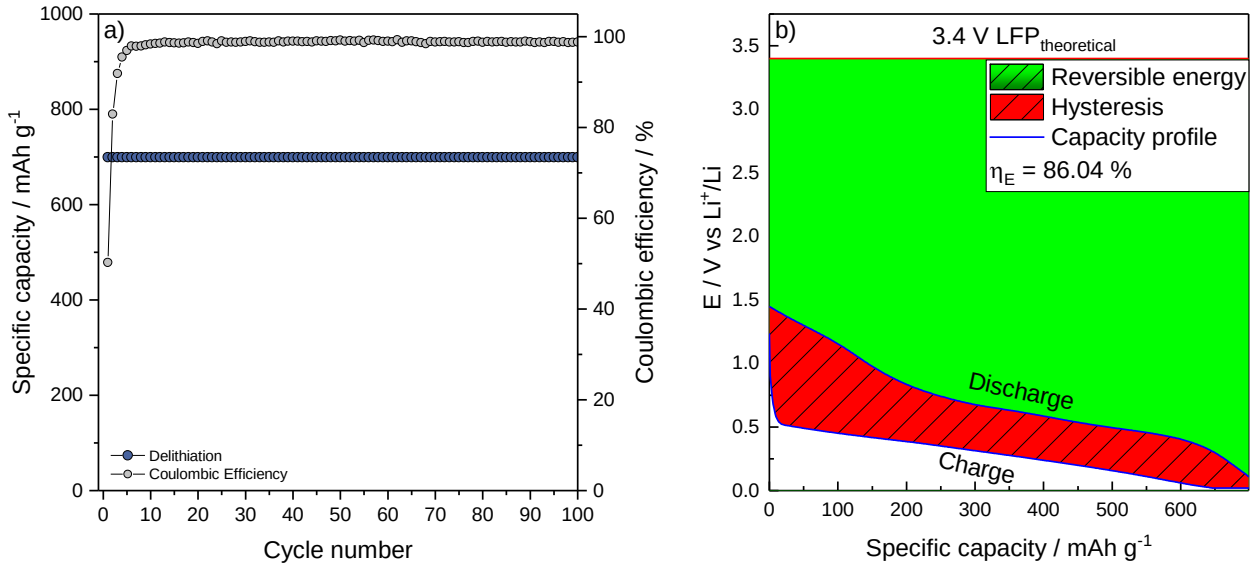

Figure 2-35. a) Galvanostatic cycles with capacity limitation Q_{Lim} = 700 mAh g^{-1}. b) Voltage hysteresis at the 50th cycle calculated vs. a theoretical LFP cathode.

The rate capability was assessed by applying different specific currents ranging from 100 mA g^{-1} up to 10 A g^{-1}. The obtained specific capacity as well as the extracted galvanostatic E vs. Q and dQ dE^{-1} vs. E profiles are shown in **Figure 2-36**. The obtained results are summarized in **Table 8**. Good specific capacities were obtained at all current rates, especially at the high current load of

10 A g^{-1} where a specific capacity of 393 mAh g^{-1} was retained. When the current was restored to 1000 mA g^{-1}, the active material was able to retain an average specific capacity of 763 mAh g^{-1}. High average specific capacity values of 1222 and 1049 mAh g^{-1} were also obtained at 100 and 200 mA g^{-1}, respectively. However, the associated coulombic efficiencies were 93.6 and 97.6 %, respectively, suggesting a poor reversibility of the lithiation reaction as well as concurrent parasitic reactions at the electrode/electrolyte interface. Galvanostatic E vs. Q and differential dQ dE^{-1} vs. E profiles were extracted in each current step to understand the current-controlled behaviour (**Figure 2-36b-c**).

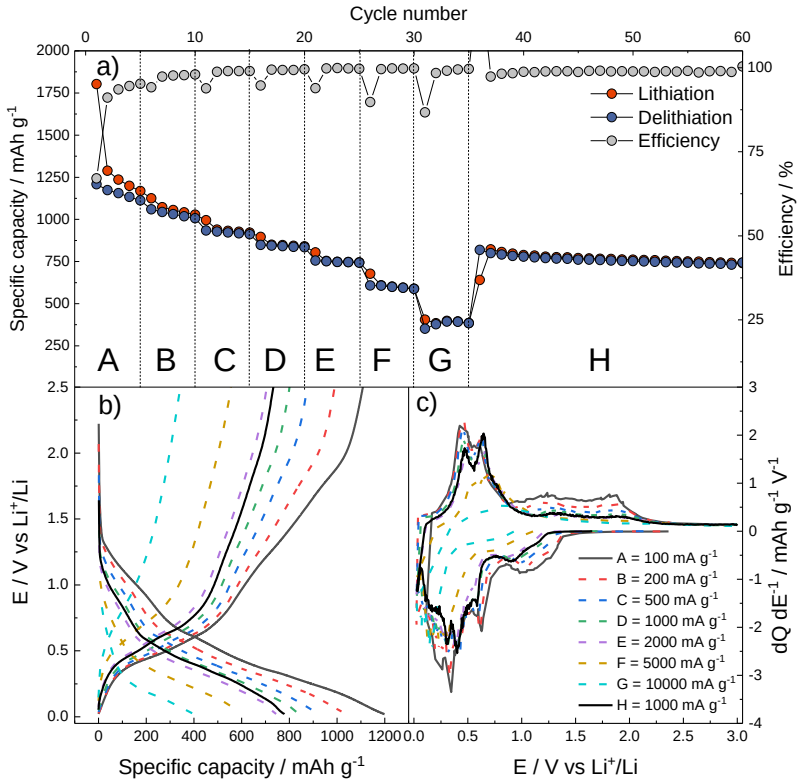

Figure 2-36. a) Rate capability of C/SnO_2NR. Extracted galvanostatic b) E vs. Q and c) dQ dE^{-1} vs. E profiles.

In both cases, as the current increases the profiles preserve their shapes at the exception of step G (10 A g^{-1}). The two sloping lines observed in **Figure 2-33b** during lithiation at 1.2 and 0.4 V for the conversion reaction and alloying reaction are clearly visible, as well as the quasi-plateau at 0.5 V during delithiation due to the dealloying reaction. In the case of step G (10 A g^{-1}) the effect of the polarization of the electrode is clearly visible. Indeed, by observing the extracted galvanostatic dQ dE^{-1} vs. E profile, the conversion reaction peak is almost not visible while the alloying peak shifts at lower potential.

Table 8. Summarized results of the rate capability test of C/SnO_2NR.

Step	Specific current / mA g^{-1}	Average lithiation specific capacity / mAh g^{-1}	Average coulombic efficiency / %
A	100	1222	93.6
B	200	1049	97.6
C	500	929	98.9
D	1000	844	99.3
E	2000	748	99.7
F	5000	598	99.7
G	10000	393	99.1
H	1000	763	99.1

Electrochemical investigation of transport and interfacial properties

CV, GITT, and PEIS were used to investigate the transport as well as interfacial properties of C/SnO_2NR electrodes. In **Figure 2-37**, the cyclic voltammetries acquired at different scan rates as well as the I_p vs. $\nu^{1/2}$ are reported.

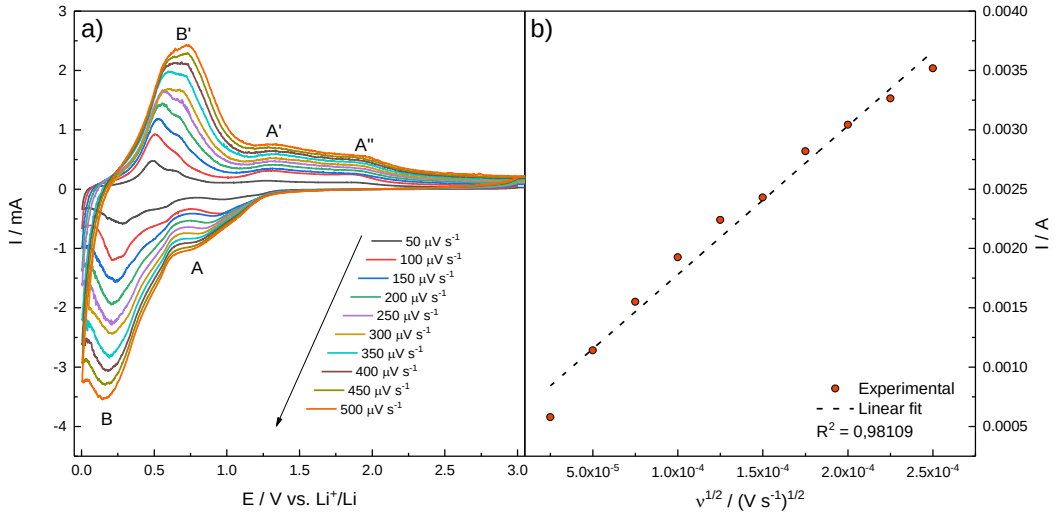

Figure 2-37. a) Cyclic voltammetries acquired at different scan rates. b) I_p vs. $\nu^{1/2}$ plot with linear fit.

As the scan rates increases, the shape and the peaks intensity proportionally increase. Indeed, by plotting the peak current (the alloying peak B has been considered for the calculation) as a

function of the square root of the scan rate, a linear behavior was found ($R^2 = 0.98109$). This feature can be translated in a diffusion-controlled behavior for the alloying reaction (42).

GITT was performed in a similar way as TiO_2@SnO_2 and SnO_2/C. The electrode was cycled 5 times with a specific current I_{Spec} = 50 mA g^{-1} before conducting the titration experiment. The titration was pursued by applying a specific current I_{GITT} = 50 mA g^{-1} for 10 min followed by a rest of t_{rest} = 3 h. The GITT curve as well as the calculated D_{Li} as a function of the potential are reported in **Figure 2-38**.

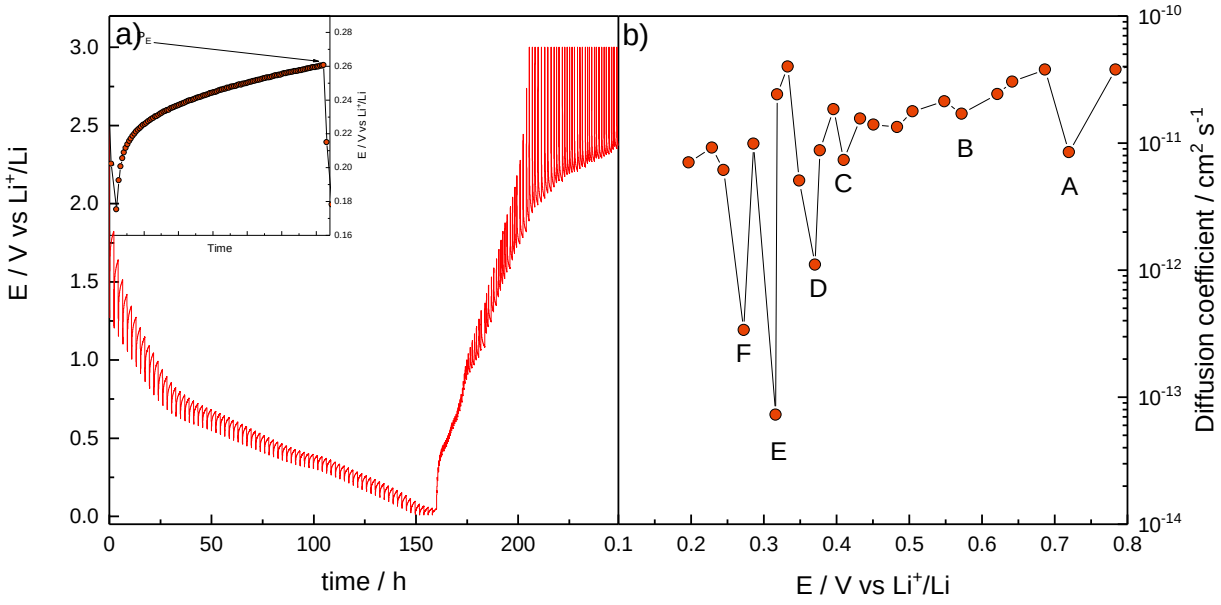

Figure 2-38. a) GITT curve of C/SnO_2NR. b) Calculated D_{Li} as a function of the potential.

From the titration experiment an experimental specific capacity Q_{exp} = 1289 mAh g^{-1} was calculated. The titration was continued until reaching the voltage threshold of E = 0.2 V, in which the phase $Li_{4.4}Sn$ is formed. The D_{Li} was estimated using **Equation 18**. The D_{Li} decreases with the increase of the lithiation degree with values in the order of 10^{-11} - 10^{-13} cm^2 s^{-1}. Six different local minima are observed as the previous SnO_2-based composite anodes, representing the formation of different three-phase equilibria (45). The potential ranges as well as the corresponding three-phases equilibria are reported in **Table 9**.

Table 9. Summary of the local minima potential and corresponding three-phases equilibrium (45).

	Potential range Li^+/Li	$Li_\delta Sn$ Phases
A	0.72 V	Li_2O-Sn-$Li_{0.4}Sn$
B	0.57 V	Li_2O-$Li_{0.4}Sn$-$Li_{0.714}Sn$
C	0.41 V	Li_2O-$Li_{0.714}Sn$-$Li_{2.33}Sn$
D	0.37 V	Li_2O-$Li_{2.33}$-$Li_{2.6}Sn$
E	0.32 V	Li_2O-$Li_{2.6}Sn$-$Li_{3.5}Sn$
F	0.27 V	Li_2O-$Li_{3.5}Sn$-$Li_{4.4}Sn$

The stability of the electrode/electrolyte interface was assessed by PEIS every 10th cycles at the bias potential of E = 0.180 V. The $-Z_{im}$ vs. Z_{re} complex plot as well as the fitted resistance parameter are reported in **Figure 2-39**. All the dispersions are characterized by three common features i.e., (i) a shift in the real axis, (ii) two overlapped semicircles in the high- medium- frequency region, and (iii) a straight line in the low frequency region. These features are commonly ascribed to (i) the migration of charges through the electrolyte, (ii) the migration of charges through the passivation layer and the charge-transfer process, and (iii) the diffusion of Li^+ ions in the active material.

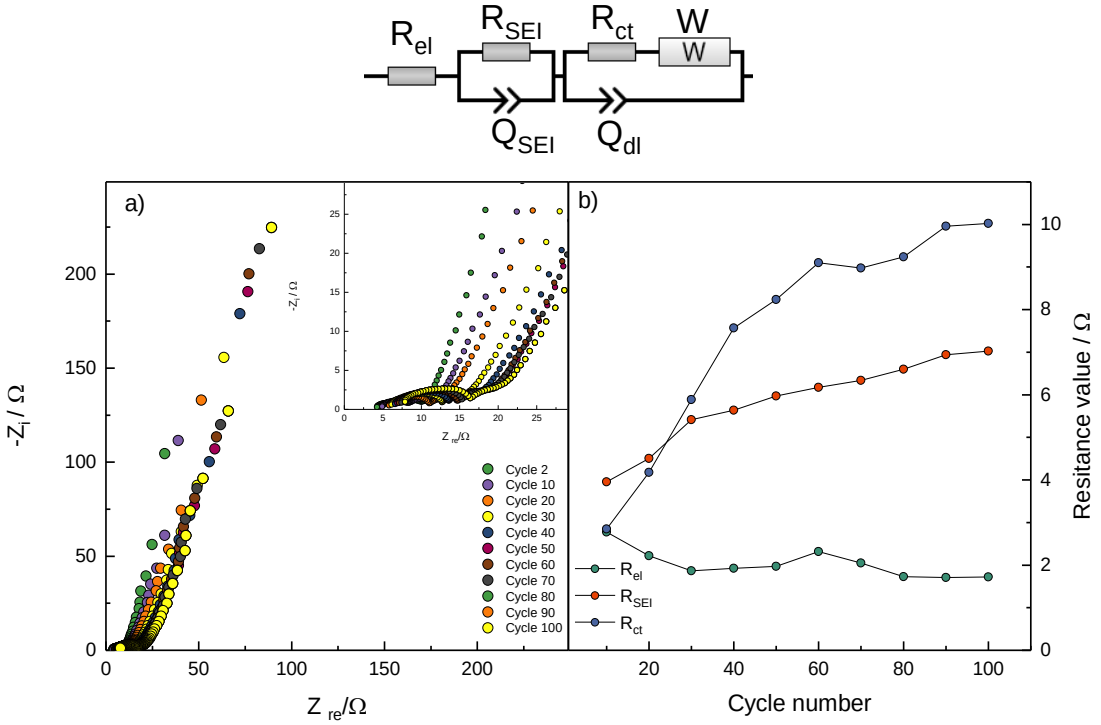

Figure 2-39. a) $-Z_{im}$ vs. Z_{re} complex plot acquired every 10th cycle. b) Fitted resistance parameters as a function of cycle number.

The impedance spectra were CNLS-fitted by using Relaxis 3 software (rhd instruments). An ECM consisting of $R_{el}(R_{SEI}C_{SEI})(R_{ct}C_{dl})W$ (Boukamp's notation (47)) was used, where R_{el} is the electrolyte resistance, R_{SEI} and C_{SEI} are the resistance and the capacitance of the passivation layer, R_{ct} and C_{dl} are the resistance correlated to the charge-transfer reaction and the double-layer capacitance, W is the Warburg element used to describe the low frequency polarization. All the capacitive elements were fitted by using a constant phase element (46) to consider roughness and electrode surface inhomogeneity. All the χ^2 obtained from the fitting procedure were in the 10^{-5} order. The results of the CNLS fitting procedure are presented in **Figure 2-39b**. The resistance associated to the electrolyte does not show any significant changes upon cycling, suggesting that its chemical composition as well as the physico-chemical properties were not subjected to changes upon cycling. The resistance associated to the passivation layer and to the charge-transfer process increase upon cycling. This behavior can be explained by the remarkable structural changes of active material occurring upon cycling which can lead to (i) agglomeration of Sn particles towards the surface of the electrode, (ii) loss of electrical contact, and (iii) increase of the thickness of the passivation layer.

2.4.4 Conclusions

A high-energy density composite anode material has been synthesized by polyol-mediated oligomerization of SnC_2O_4. The structural characterization revealed the presence of two different phases i.e., cassiterite SnO_2 and amorphous carbon. TGA revealed a 12 % of C, as expected from the synthesis procedure. The SnO_2 is characterized by spherical nanoparticles arranged with a rod architecture. Amorphous carbon is present as larger grains above the surface of SnO_2 nanorods. High specific capacities were obtained at different currents rates, ranging from 393 mAh g^{-1} at 10 A g^{-1} up to 1222 mAh g^{-1} at 100 mA g^{-1}. The investigation of transport properties by CV and GITT revealed a diffusion-controlled behavior. Furthermore, an experimental specific capacity of Q_{exp} = 1289 mAh g^{-1} was calculated. By calculating the D_{Li} from GITT measurements, the formation of three-phase equilibria was exploited giving six local minima due to different degree of lithiation of Sn. The investigation of electrode-electrolyte interface revealed an increasing polarization related to the SEI breakage and re-formation as well as structural rearrangements of the active material.

2.5 Chapter summary

Three different SnO_2-based anode materials with different stabilizing matrices and morphologies have been synthesized and characterized. The effect of an active anatase-TiO_2 matrix, an inactive amorphous carbon matrix, and an improved morphology has been investigated. Concerning the specific capacity, and thus the energy density, the C/SnO_2NR has shown the highest specific capacity in 100 cycles, with a Q_{100} = 1007 mAh g^{-1} (**Figure 2-40**).

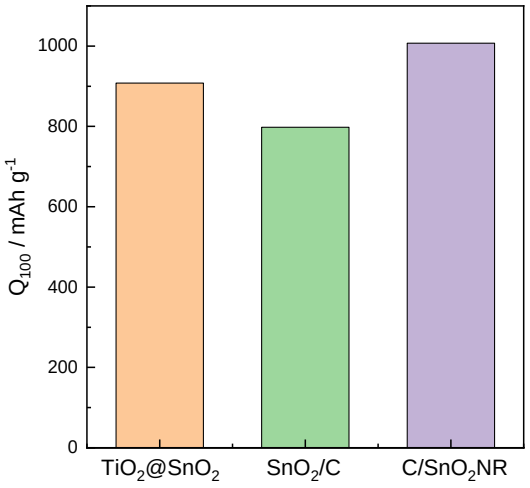

Figure 2-40. Comparison of the obtained Q_{100} for the three SnO_2-based anode materials.

As regards the rate performance, both TiO_2@SnO_2 and C/SnO_2 have shown the best capacity retention under high current rates (**Figure 2-41**).

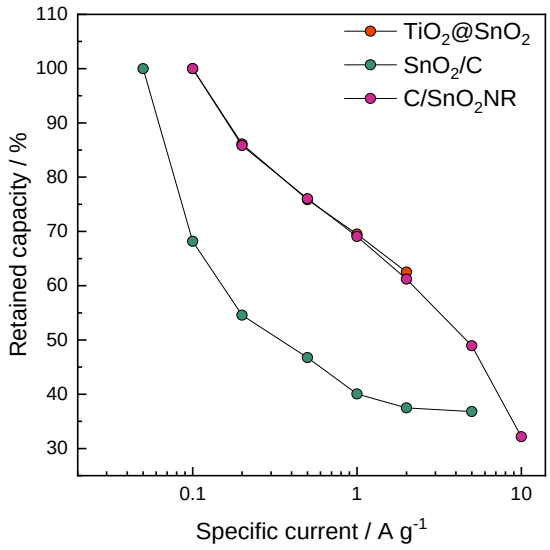

Figure 2-41. Comparison of the rate performances of the three SnO_2-based anode materials.

In terms of energy efficiency, versus a theoretical LFP cathode, SnO_2/C has the highest energy efficiency (77.04 % without capacity limitation, 86.53 % with capacity limitation), obtaining the A^+ label according to the European Union Energy label (**Figure 2-42**). These findings confirms that SnO_2 can be a suitable, green, and especially versatile candidate anode material for the next generation of Li-ion batteries, with tailored performances according to the end-user application.

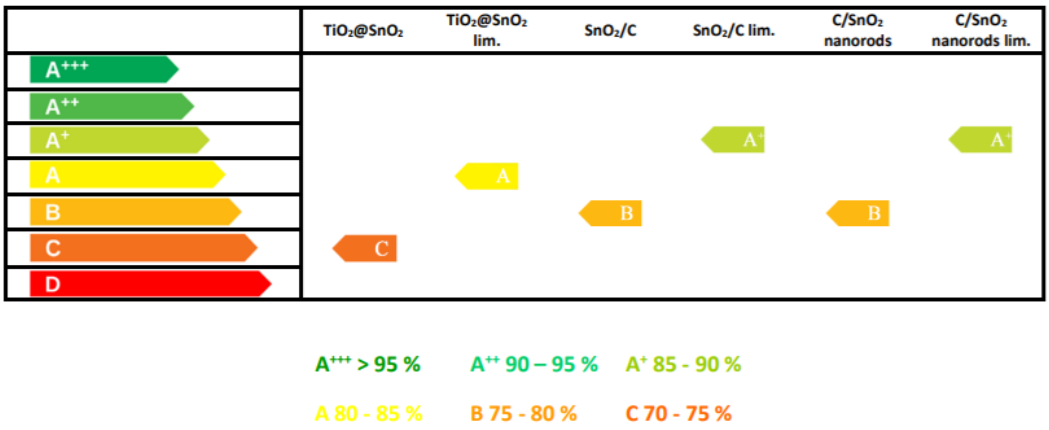

Figure 2-42. Classification of the energy efficiency of the three SnO_2-based anode material with and without capacity limitation according to the European Union Energy label (51).

References

1. **N. N. Greenwood, A. Earnshaw.** *Chemistry of the Elements.* s.l. : Butterworth-Heinemann, 1997. 9780750633659.

2. *SnO2 as Advanced Anode of Alkali-Ion Batteries: Inhibiting Sn Coarsening by Crafting Robust Physical Barriers, Void Boundaries, and Heterophase Interfaces for Superior Electrochemical Reaction Reversibility.* **Shiqiang Zhao, Christopher D. Sewell, Ruiping Liu, Songru Jia, Zewei Wang, Yanjie He, Kunjie Yuan, Huile Jin, Shun Wang, Xueqin Liu, Zhiqun Lin.** 6, s.l. : Advanced Energy Materials, 2019, Vol. 10, p. 1902657.

3. *Large-Scale Production of a Silicon Nanowire/Graphite Composites Anode via the CVD Method for High-Performance Lithium-Ion Batteries.* **Bei Liu, Peng Huang, Zhiyong Xie, Qizhong Huang.** 3, s.l. : Energy & Fuels, 2021, Vol. 35, p. 2758-2765.

4. *Scalable synthesis of highly dispersed silicon nanospheres by RF thermal plasma and their use as anode materials for high-performance Li-ion batteries.* **Guolin Hou, Benli Cheng, Yuebin Cao, Mingshui Yao, Fei Ding, Peng Hu, Fangli Yuan.** 35, s.l. : Journal of Materials Chemistry A, 2015, Vol. 3, p. 18136-18145.

5. *Porous silicon thin films as anodes for lithium ion batteries deposited by co-evaporation of silicon and zinc.* **Stefan Saager, Bert Scheffel, Olaf Zywitzki, Thomas Modes, Markus Piwko, Susanne Doerfler, Holger Althues, Christoph Metzner.** s.l. : Surface and Coatings Technology, 2019, Vol. 358, p. 586-593.

6. *SnO2-Based Nanomaterials: Synthesis and Application inLithium-Ion Batteries and Supercapacitors.* **Qinqin Zhao, Lisha Ma, Qiang Zhang, Chenggang Wang, Xijin Xu.** s.l. : Journal of Nanomaterials, 2014, Vol. 2015.

7. *Dramatically enhanced reversibility of Li2Oin SnO2-based electrodes: the effect of nanostructure on high initial reversible capacity.* **Renzong Hu, Dongchang Chen, Gordon Waller, Yunpeng Ouyang, Yu Chen, Bote Zhao, Ben Rainwater, Chenghao Yang, Min Zhu, Meilin Liu.** s.l. : Energy & Environmental Science, 2016, Vol. 9, p. 595-603.

8. *Polymer-Templated Formation of Polydopamine-Coated SnO2 Nanocrystals: Anodes for Cyclable Lithium-Ion Batteries.* **Beibei Jiang, Yanjie He, Bo Li, Shiqiang Zhao, Shun Wang, Yan-Bing He, Zhiqun Lin.** 7, s.l. : Angewandte Chemie International Edition, 2017, Vol. 56, p. 1869-1872.

9. *Hybrid Tin Oxide Nanowires as Stable and High Capacity Anodes for Li-Ion Batteries.* **Praveen Meduri, Chandrashekhar Pendyala, Vivekanand Kumar, Gamini U. Sumanasekera, Mahendra K. Sunkara.** 2, s.l. : Nano Letters, 2009, Vol. 9, p. 612-616.

10. *Preparation and Electrochemical Properties of SnO2 Nanowires for Application in Lithium-Ion Batteries.* **Min-Sik Park, Guo-Xiu Wang, Yong-Mook Kang, David Wexler, Shi-Xue Dou, Hua-Kun Liu.** 5, s.l. : Angewandte Chemie International Edition, 2007, Vol. 46, p. 750-753.

11. *In Situ Growth of Mesoporous SnO2 on Multiwalled Carbon Nanotubes: A Novel Composite with Porous-Tube Structure as Anode for Lithium Batteries.* **Z. Wen, Q. Wang, Q. Zhang, J. Li.** 15, s.l. : Advanced Functional Materials, 2007, Vol. 17, p. 2772-2778.

12. *Facile synthesis of the SnO2@OCNTs(open-tips carbon nano tubes) composite with superior cyclability for Li-ion batteries.* **Ji Yu, Yuan Xia.** s.l. : Electrochimica Acta, 2014, Vol. 147, p. 720-725.

13. *The preparation of double-void-space SnO2/carbon composite as high-capacity anode materials for lithium-ion batteries.* **Wenchao Wang, Penghui Li, Yanbao Fu, Xiaohua Ma.** s.l. : Journal of Power Sources, 2013, Vol. 238, p. 464-468.

14. *The fast filling of nano-SnO2 in CNTs by vacuum absorption: a new approach to realize cyclic durable anodes for lithium ion batteries.* **Renzong Hu, Wei Sun, Hui Liu, Meiqin Zeng, Min Zhu.** 23, s.l. : Nanoscale, 2013, Vol. 5, p. 11971-11979.

15. *Sn-SnO2 hybrid nanoclusters embedded in carbon nanotubes with enhanced electrochemical performance for advanced lithium ion batteries.* **Li Sun, Haochen Si, Yuanxing Zhang, Yan Shi, Ke Wang, Jingang Liu, Yihe Zhang.** s.l. : journal of Power Sources, 2019, Vol. 415, p. 126-135.

16. *Enhancing the Lithium Storage Performance of Graphene/SnO2 Nanorods by a Carbon-Riveting Strategy.* **Xianghong Liu, Tiantian Ma, Li Sun, Yongshan Xu, Jun Zhang, Nicola Pinna.** 8, s.l. : ChemSusChem, 2018, Vol. 11, p. 1321-1327.

17. *Dually Fixed SnO2 Nanoparticles on Graphene Nanosheets by Polyaniline Coating for Superior Lithium Storage.* **Yanfeng Dong, Zongbin Zhao, Zhiyu Wang, Yang Liu, Xuzhen Wang, Jieshan Qiu.** 4, s.l. : ACS Applied Materials & Interfaces, 2015, Vol. 7, p. 2444-2451.

18. *Fully Reversible Conversion between SnO2 and Sn in SWNTs@SnO2@PPy Coaxial Nanocable As High Performance Anode Material for Lithium Ion Batteries.* **Yi Zhao, Jiaxin Li, Ning Wang, Chuxin Wu, Guofa Dong, Lunhui Guan.** 35, s.l. : The Journal of Physical Chemistry C, 2012, Vol. 116, p. 18612-18617.

19. *SnO2@PANI Core–Shell Nanorod Arrays on 3D Graphite Foam: A High-Performance Integrated Electrode for Lithium-Ion Batteries.* **Feng Zhang, Chengkai Yang, Xin Gao, Shuai Chen, Yiran Hu, Huanqin Guan, Yurong Ma, Jin ZhangOrcid, Henghui Zhou, Limin Qi.**

20. *Core-Shell Structure of SnO2@C/PEDOT : PSS Microspheres with Dual Protection Layers for Enhanced Lithium Storage Performance.* **Hui Li, Bao Zhang, Xing Ou, Qijie Zhou, Chunhui Wang, Chunli Peng, Jiafeng Zhang.** 8, s.l. : ChemElectroChem, 2019, Vol. 6, p. 2182-2188.

21. *Fabrication of three-dimensional carbon coating for SnO2/TiO2 hybrid anode material of lithium-ion batteries.* **Qinghua Tian, Jingbin Yan, Li Yang, Jizhang Chen.** s.l. : Electrochimica Acta, 2018, Vol. 282, p. 38-47.

22. *SnO2/Fe2O3 hybrid nanofibers as high performance anodes for lithium-ion batteries.* **Feng Zan, Nawishta Jabeen, Wen Xiong, Ahmad Hussain, Yadong Wang, Hui Xia.** s.l. : Nanotechnology, 2020, Vol. 31, p. 185402.

23. *SnO2–NiO–C nanocomposite as a high capacity anode material for lithium-ion batteries.* **Mohd Faiz Hassan, M. M. Rahman, Zaiping Guo, Zhixin Chenc, Huakun Liu.** 43, s.l. : Journal of Materials Chemistry, 2010, Vol. 20, p. 9707-9712.

24. *Triton Facilitated Spherical TiO2 Nanoparticles and Their Advantage in a Dye-Sensitized Solar Cell.* **N. A. Al-Omair, S. M. Reda, F. M. Al-Hajri.** 2, s.l. : Advances in Materials Physics and Chemistry, 2014, Vol. 4, p. 29-32.

25. *Effect of annealing temperature of titanium dioxide thin films on structural and electrical properties.* **A. S. Bakri, M. Z. Sahdan, F. Adriyanto, N. A. Raship, N. D. M. Said, S. A. Abdullah, M. S. Rahim.** 1, s.l. : AIP Conference Proceedings, 2017, Vol. 1788.

26. *Structure sensitive photocatalytic reduction of nitroarenes over TiO2.* **Swapna Challagulla, Kartick Tarafder, Ramakrishnan Ganesan, Sounak Roy.** 8783, s.l. : Scientific Reports, 2017, Vol. 7.

27. *Raman spectra of titanium dioxide (anatase, rutile) with identified oxygen isotopes (16, 17, 18).* **Otakar Frank, Marketa Zukalova, Barbora Laskova, Jenö Kürti, János Koltai, Ladislav Kavan.** 42, s.l. : Physical Chemistry Chemical Physics, 2012, Vol. 14, p. 14567-14572.

28. *The complete Raman spectrum of nanometric SnO2 particles.* **A. Die´guez, A. Romano-Rodrı´guez, A. Vila, J. R. Morante.** s.l. : The Journal of Chemical Physics, 2001, Vol. 90, p. 1550-1557.

29. *Large Impact of Particles Size on Insertion Reactions. A Case for Anatase LixTiO2.* **Marnix Wagemaker, Wouter J. H. Borghols, Fokko M. Mulder.** 14, s.l. : Journal of The American Chemical Society, 2007, Vol. 129, p. 4323-4327.

30. *Current Advances in TiO2-Based Nanostructure Electrodes for High Performance Lithium Ion Batteries.* **Mahmoud Madian, Alexander Eychmüller, Lars Giebeler.** 7, s.l. : Batteries, 2018, Vol. 4.

31. *Multiple Li Positions inside Oxygen Octahedra in Lithiated TiO2 Anatase.* **Marnix Wagemaker, Gordon J. Kearley, Ad A. van Well, Hannu Mutka, Fokko M. Mulder.** 3, s.l. : Journal of American Chemical Society, 2003, Vol. 125, p. 840-848.

32. *Electrolyte additives for lithium ion battery electrodes: progress and perspectives.* **Atetegeb Meazah Haregewoin, Aselefech Sorsa Wotango,Bing-Joe Hwang.** 6, s.l. : Energy & Environmental Science, 2016, Vol. 9, p. 1955-1988.

33. *Tin oxide-based anodes for both lithium-ion and sodium-ion batteries.* **Kebede, mesfin A.** s.l. : Current Opinion in Electrochemistry, 2020, Vol. 21, p. 182-187.

34. *Studies of Lithium Intercalation into Carbons Using Nonaqueous Electrochemical Cells.* **Rosamaria Fong, ulrich von Sacken, J. R. Dahn.** 7, s.l. : Journal of The Electrochemical Society, 1990, Vol. 137, p. 2009-2013.

35. *Review—SEI: Past, Present and Future.* **E. Peled, S. Menkin.** s.l. : journal of The Electrochemical Society, 2017, Vol. 164, p. A1703.

36. *SnO2 Model Electrode Cycled in Li-Ion Battery Reveals the Formation of Li2SnO3 and Li8SnO6 Phases through Conversion Reactions.* **Giulio Ferraresi, Claire Villevieille, Izabela Czekaj, Michael Horisberger, Petr Novák, Mario El Kazzi.** 10, s.l. : ACS Applied Materials & Interfaces, 2018, Vol. 10, p. 8712-8720.

37. *Progress in electrical energy storage system: A critical review.* **Haisheng Chena, Thang Ngoc Cong, Wei Yang, Chunqing Tan, Yongliang Li, Yulong Ding.** 3, s.l. : Progress in Natural Science, 2009, Vol. 19, p. 291-312.

38. *Best Practice: Performance and Cost Evaluation of Lithium Ion Battery Active Materials with Special Emphasis on Energy Efficiency.* **Paul Meister, Haiping Jia, Jie Li, Richard Kloepsch, Martin Winter, Tobias Placke.** 20, s.l. : Chemistry of Materials, 2016, Vol. 28, p. 7203-7217.

39. *Revisiting the energy efficiency and (potential) full-cell performance of lithium-ion batteries employing conversion/alloying-type negative electrodes.* **Jakob Asenbauer, Alberto Varzi, Stefano Passerini, Dominic Bresser.** s.l. : journal of Power Sources, 2020, Vol. 473, p. 228583.

40. *Fe-doped SnO2 nanoparticles as new high capacity anode material for secondary lithium-ion batteries.* **Franziska Mueller, Dominic Bresser, Venkata Sai Kiran Chakravadhanula, Stefano Passerini.** s.l. : Journal of Power Sources, 2015, Vol. 299, p. 398-402.

41. *Carbon Coated ZnFe2O4 Nanoparticles for Advanced Lithium-Ion Anodes.* **Dominic Bresser, Elie Paillard, Richard Kloepsch, Steffen Krueger, Martin Fiedler, René Schmitz, Dietmar Baither, Martin Winter, Stefano Passerini.** 4, s.l. : Advanced Energy Materials, 2012, Vol. 3, p. 513-523.

42. **Allen J. Bard, Larry R. Faulkner.** *Electrochemical Methods: Fundamentals and Applications.* 2000.

43. *Li-ion diffusion behavior in Sn, SnO and SnO2 thin films studied by galvanostatic intermittent titration technique.* **J. Xie, N. Imanishi, A. Hirano, Y. Takeda, O. Yamamoto, X. B. Zhao, G. S. Cao.** 35-36, s.l. : Solid State Ionics, 2010, Vol. 181, p. 1611-1615.

44. *Determination of the Kinetic Parameters of Mixed-Conducting Electrodes and Application to the System Li3Sb.* **W. Weppner, R. A. Huggins.** s.l. : journal of the Electrochemical Society, 1977, Vol. 124, p. 1569.

45. *Alloy negative electrodes for lithium batteries formed in-situ from oxides.* **Huggins, R. A.** s.l. : Ionics, 1997, Vol. 3, p. 245-255.

46. **Evgenij Barsoukov, J. Ross Macdonald.** *Impedance Spectroscopy: Theory, Experiment, and Applications.* s.l. : john Wiley & Sons, 2005.

47. *A Nonlinear Least Squares Fit procedure for analysis of immittance data of electrochemical systems.* **Boukamp, Bernard A.** 1, s.l. : Solid State ionics, 1986, Vol. 20, p. 31-44.

48. *Growth mechanism of SnC2H4O2 nanowires prepared by the polyol process as SnO2 precursor nanowires.* **Dongkook Park, Man Sig Lee.** 6, s.l. : RSC Advances, 2019, Vol. 9, p. 3203-3207.

49. *Ethylene glycol-mediated synthesis of metal oxidenanowires.* **Xuchuan Jiang, Yuliang Wang, Thurston Herricks, Younan Xia.** 4, s.l. : Journal of Materials Chemistry, 2004, Vol. 14, p. 695-703.

50. *A Solution-Phase, Precursor Route to Polycrystalline SnO2 Nanowires That Can Be Used for Gas Sensing under Ambient Conditions.* **Yuliang Wang, Xuchuan Jiang, Younan Xia.** 52, s.l. : Journal of The American Chemical Society, 2003, Vol. 125, p. 16176-16177.

51. **European Union Energy Label. [Online] https://ec.europa.eu/info/energy-climate-change-environment/standards-tools-and-labels/products-labelling-rules-and-requirements/energy-label-and-ecodesign/about_en.**

3. Iron oxide-based anode for LIBs and NIBs

Iron oxides have attracted a lot of interest in both LIBs and NIBs systems thanks to their high theoretical specific capacity (ranging from 744 mAh g^{-1} for FeO (1) up to 1007 mAh g^{-1} for Fe_2O_3 (2)) as well as their cost, nontoxicity, and abundancy (3). However, the poor capacity retention due to the continuous structural rearrangement given by the conversion reaction must be overcome to ensure its practical application in commercial LIBs and NIBs. Common strategies involve the preparation of nanostructured materials and/or nanocomposite materials. Nanostructured materials have the advantages of higher rate performances and higher stability upon cycling given by the higher specific surface areas, the shorter diffusion path, and the smaller volume changes. Morphologies such as 0D nanoparticles (4), nanotubes (5), and chain-like particles (6) have shown remarkable improvements.

The preparation of nanocomposite materials with an active or inactive matrix can effectively alleviate the volume stresses occurring during cycling. Carbon-based materials are one of the mostly used buffering matrices thanks to their remarkable electronic conductivity and low cost (7). Graphene has already been studied as active material thanks to its high electronic conductivity, reliable mechanical properties, and high aspect ratio (8; 9; 10). However, its use in ESSs is still questioned by drawbacks such as high cost and trends to restack to form amorphous carbon, and eventually graphite (11). Nevertheless, its use in nanocomposite formulation can buffer the volume changes and improve the mechanical instability of the electrode. Furthermore, the overall electrode conductivity may be enhanced. For these reasons, graphene has already been used as containment matrix for conversion and conversion-alloying materials for both LIBs and NIBs systems (12). Nevertheless, some drawbacks regarding the synthesis of Fe_3O_4/graphene-based composite materials need to be overcome. In most case, hydrothermal and high temperature calcinations are used which can hinder the scale-up of the synthesis process (13).

3.1 Experimental

3.1.1 Synthesis of Fe_3O_4 nanoparticles and Fe_3O_4@rGO

The synthesis procedure is summarized in **Figure 3-1**.

A base-promoted coprecipitation was used for the synthesis of pristine Fe_3O_4 nanoparticles. Briefly, stoichiometric amounts of $FeCl_2 \cdot 4H_2O$ and $FeCl_3 \cdot 6H_2O$ were dissolved in 40 mL of demineralized water. 100 mL of 10 % NH_4OH solution were added to the precursor solution

giving a black precipitate. The solution was heated and stirred until reaching 80 °C. Afterwards, further 30 mL of concentrated NH_4OH were added and left to react for 8 h. The obtained black precipitate was recovered and thoroughly washed with ultrapure water, acetone, and ethanol. Eventually, the powder was vacuum dried at 50 °C.

A sonochemical approach was used for the embedding of Fe_3O_4 nanoparticles into reduced graphene oxide. 200 mg of graphene oxide (C:O ratio of 5:4.3 from Nanoinnova technologies SL) were dispersed in 150 mL of ultrapure water and sonicated for 1 h. Then, 500 mg of pristine Fe_3O_4 nanoparticles were added to the above dispersion under magnetic stirring and sonicated again for 1 h. Afterwards, 10 mL of hydrazine hydrate was added to the solution to reduce graphene oxide. An ice bath was used to control the heat of the reaction. The dispersion was further sonicated for 2 h. Eventually, the composite material was vacuum filtered with Millipore filtering system (0.2 μm GTTP), thoroughly washed with ethanol, and vacuum dried at 50 °C.

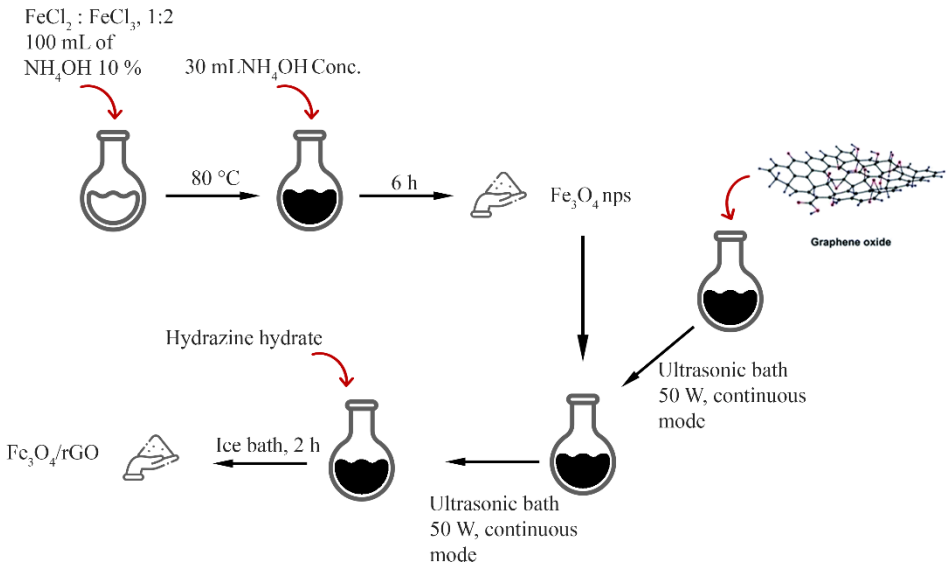

Figure 3-1. Synthesis procedure of Fe_3O_4/rGO.

3.1.2 Structural and morphological characterization

The structural characterization was pursued by Raman scattering and X-Ray Diffraction (XRD). Specifically, a Horiba iH320 Raman spectrometer equipped with a 532 nm laser source, and a Philipps diffractometer equipped with a Cu-Kα source (λ=1.540 Å) were used for Raman spectroscopy and XRD, respectively. The morphological characterization was done by using a field-emission scanning electron microscope Zeiss Sigma series 300.

3.1.3 Thermal characterization

The rGO content in the composite material was assessed by using a Perkin-Elmer STA6000 TGA-DTA, from r.t. up to 800 °C with a rate of 10 °C min^{-1} in oxidizing atmosphere

3.1.4 Electrode processing

The electrode layers were prepared by doctor blade technique. All the slurries were prepared with the formulation of 70:20:10 of active material, Super C65 (Timcal C-Energy™) as conductive carbon additive, and polyacrylic acid (PAA, Sigma-Aldrich m.w. = 450000 g mol^{-1}) as binder, respectively. Firstly, the polymeric binder was dissolved in ethanol to obtain a 5 $\%_{ww}$ solution. In the meantime, active material and the conductive carbon additive were finely grounded in an agata mortar. The mixed powders were then added to the binder solution reaching a solid content of ca. 40 % and stirred overnight. Eventually, the slurries were casted onto copper foil (thickness = 10 μm) with a wet thickness of 150 μm. Electrode layer were than dried at 70 °C for 2h. Circular electrodes of Ø = 9mm were cut using an electrode puncher (EL-Cut, EL-CELL). Eventually, the electrodes were pressed at 4.7 tons cm^{-2}, weighted, and vacuum dried at 120 °C overnight. The average loading of active material was ≈ 1-1.5 mg cm^{-2}.

3.1.5 Electrochemical characterization

Three-electrode cells have been used for the electrochemical characterization employing the active material as working electrode, and Li or Na metal as both counter and reference electrodes. 1 M $LiPF_6$ in EC:DMC (1:1 v:v) + 2 % VC and 1 M $NaClO_4$ in EC:PC (1:1 v:v) were used as electrolyte in LIB and NIB configuration, respectively. Whatman GF/A glassfiber discs were as separator. Swagelok-type cells were used for CV, GCPL, rate capability. Prior any electrochemical characterization, an open circuit voltage period of 12 h was used. Cyclic voltammetries were acquired from 50 μV s^{-1} up to 500 μV s^{-1} with 50 μV s^{-1} increment steps. Galvanostatic cycling were performed by applying specific currents ranging from 50 mA g^{-1} up to 10 A g^{-1}. ECC-REF (EL-CELL) cells have been used for potentiostatic electrochemical impedance spectroscopy. Impedance spectra were acquired every 10^{th} cycle at selected bias potential by applying a sinusoidal voltage perturbation of ΔE = 5 mV in the frequency domain 7 mHz < f < 200 kHz, and with 10 points per decade in logarithmic spacing. All the electrochemical measurements have

been performed in the potential window 0.010 V < E < 3.000 V. All the potential values are referred to the Li^+/Li redox couple (-3.041 V vs SHE) or Na^+/Na redox couple (-2.710 vs SHE).

Ex-situ Raman measurements have been performed on samples which had been brought to selected states of charge (SOC) during the first cycle, by galvanostatic discharge/charge at 500 mA g^{-1} followed by 6h-constant voltage step to ensure electrode equilibration. Subsequently, the cells were disassembled in glove-box under Ar atmosphere, then washed three times with dimethyl carbonate (anhydrous DMC, Sigma-Aldrich) to remove electrolyte components which could interfere with the Raman analysis, and finally put between two microscope slides sealed with epoxy resin.

All the cell assembly/disassembly procedures were carried out by using an Ar filled glovebox (Jacomex GP-Campus) with H_2O and O_2 < 1 ppm. All the electrochemical measurements have been performed on a VMP-3 multichannel galvanostat/potentiostat (BioLogic, France).

3.2 Results and discussion: structural and morphological characterization

The SEM micrographs of Fe_3O_4 nanoparticles as well as the composite Fe_3O_4/rGO are shown in **Figure 3-2**. The morphology of pristine Fe_3O_4 is characterized by large aggregates probably due to magnetic stirring. However, at high magnification levels spherical particles with a diameter ranging from 5 to 10 nm can be visually estimated.

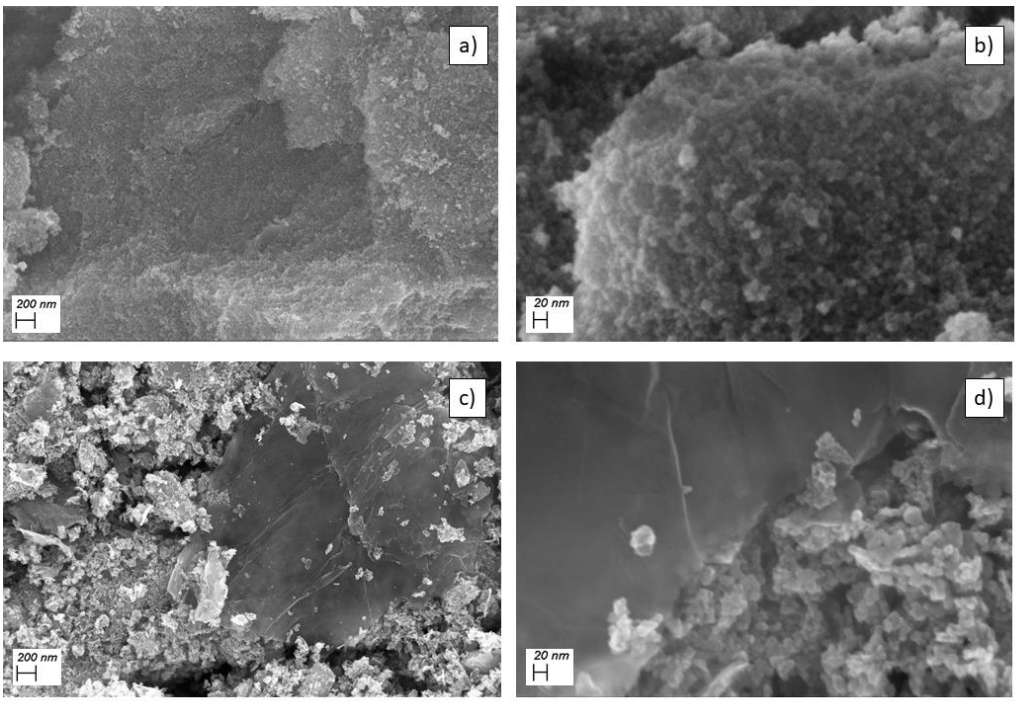

Figure 3-2. SEM micrographs of Fe_3O_4 nanoparticles at a) 40000X and b) 275000X. SEM micrographs of Fe_3O_4/rGO at a) 40000X and b) 275000X.

Regarding the composite material (**Figure 3-2c-d**), the nanoparticles appear to be aggregated in even larger clusters. However, at high magnification levels (**Figure 3-2d**) the effective embedding of Fe_3O_4 nanoparticles is confirmed.

The Raman spectra of Fe_3O_4, rGO, and Fe_3O_4/rGO are shown in **Figure 3-3a-c**.

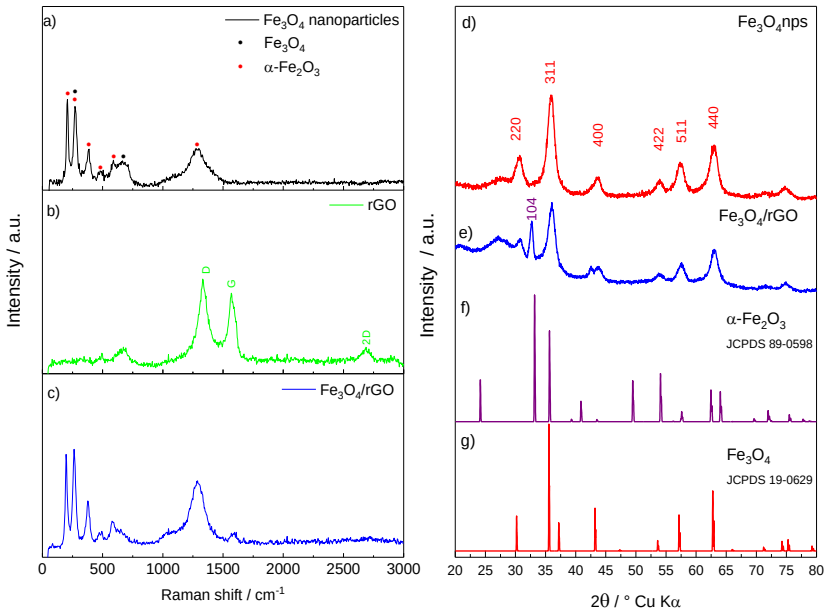

Figure 3-3. Raman spectra of a) Fe_3O_4 nanoparticles, b) rGO, and c) Fe_3O_4/rGO. Experimental diffractogram of d) Fe_3O_4 nanoparticles, and e) Fe_3O_4/rGO. Reference XRD cards of f) α-Fe_2O_3, and g) Fe_3O_4.

The observed Raman pattern of pristine Fe_3O_4 is consistent with the Raman spectrum of both hematite (α-Fe_2O_3) and magnetite (Fe_3O_4) (14; 15; 16). The peaks labelled in red and located at 229 cm^{-1}, 414 cm^{-1}, 484 cm^{-1}, 615 cm^{-1}, and 1288 cm^{-1} can be indexed to the A_{1g}, E_g, A_{1g}, E_g, and $2E_u$ modes of α-Fe_2O_3. The peak labeled in black located at 667 cm^{-1} can be indexed to the A_{1g} mode of Fe_3O_4 (14; 15; 16). The peak located at 271 cm^{-1} can be ascribed to an overlapping of the E_g and T_{1g} modes of α-Fe_2O_3 and Fe_3O_4, respectively. The Raman pattern of rGO (**Figure 3-3b**) clearly shows the three characteristic peaks of carbonaceous material (17). Specifically, the D- and G-band located at 1302 cm^{-1} and 1581 cm^{-1} confirm the recovery of sp^2 carbon pattern with defects (17). The high I_D/I_G ratio (≈1.31) suggest a high number of structural defects on rGO surface. The Raman spectrum of Fe_3O_4/rGO (**Figure 3-3c**) retained all the features observed for pristine Fe_3O_4 nanoparticles and rGO, suggesting that the embedding relies only by electrostatic interactions without any chemical modifications. In **Figure 3-3d**, the experimental diffractogram of pristine Fe_3O_4 nanoparticles is reported. The reflections pattern can be ascribed to the spinel Fe_3O_4 with space group Fd-3m (JCPDS 19-0629). The broad shape of the peaks suggests a small crystallite size which was estimated to be $L \approx 5.65$ nm by applying the Scherrer's equation (**Equation 13**, reflection 311 has been used for the calculation). Concerning the Fe_3O_4/rGO composite, the experimental diffractogram preserved the reflections pattern observed with Fe_3O_4 nanoparticles. However, a further reflection corresponding to the *104* set of planes of α-Fe_2O_3 with space group R-3c has been identified (JCPDS 89-0598). A crystallite size $L \approx 5.80$ nm was calculated from the Scherrer's equation for the Fe_3O_4 phase in the composite, suggesting no coarsening of the particles after the embedding of Fe_3O_4 into the rGO matrix. The broad peak at $2\theta = 26°$ in the XRD of the composite can be indexed to the amorphous carbon rGO phase.

The rGO content was assessed by thermogravimetric analysis in oxidizing atmosphere (**Figure 3-4**).

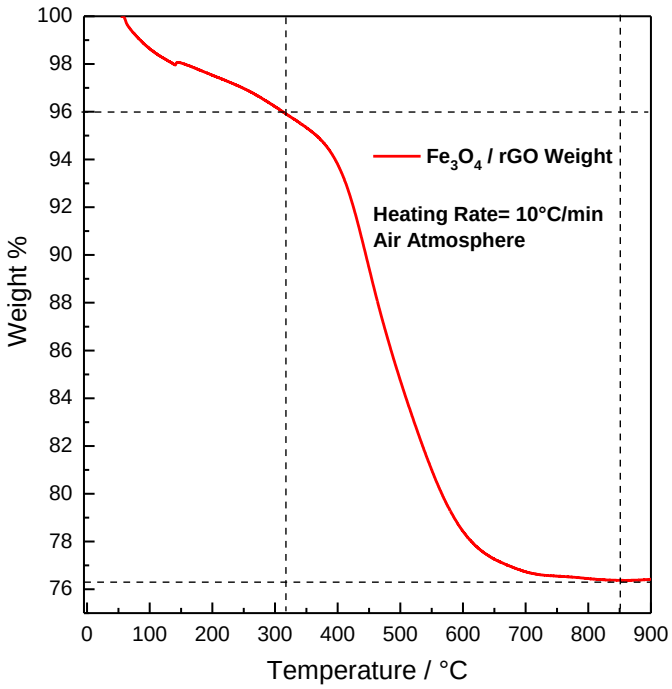

Figure 3-4. TGA curve of Fe_3O_4/rGO composite in oxidising atmosphere.

Two features with different slope have been evidenced: (i) from r.t. up to 300 °C there is a small weight drop due to the loss of adsorbed water, and (ii) a large weight drop at T > 400 °C due to the decomposition of rGO into CO_2. Thus, the Fe_3O_4:rGO ratio has been calculated as 79:21. The theoretical capacity was thus calculated as 881 mAh g^{-1}, considering the theoretical capacity of Fe_3O_4 (924 mAh g^{-1}) and graphene (744 mAh g^{-1}).

3.3 Results and discussion: electrochemical characterization in LIBs

In **Figure 3-5**, the cyclic voltammetry of Fe_3O_4/rGO obtained at 100 μV s^{-1} is reported. In the first cathodic scan three features can be observed i.e., a small hump at 1.5 V denoted as *, and two peaks at 1.05 V (B) and at 0.75 V (A). The broad hump at 1.5 V has also been observed for other transition metal oxides (18) and can be ascribed to irreversible interfacial properties occurring only on the first reduction. Peak B, as proposed by Thackeray et al (19), can be ascribed to the Li^+ ions intercalation into the spinel Fe_3O_4 (**Equation 19**).

$$Fe_3O_4 + 2Li^+ + 2e^- \rightarrow Li_2Fe_3O_4 \qquad \textbf{Eq. 19}$$

Peak A can be indexed to the reduction of Fe^{3+} to Fe^0 according to **Equation 20**.

$$Li_2Fe_3O_4 + 6Li^+ + 6e^- \rightarrow 3Fe + 4Li_2O$$ **Eq. 20**

In the same potential region, the formation of the passivation layer towards the electrode surface occurs.

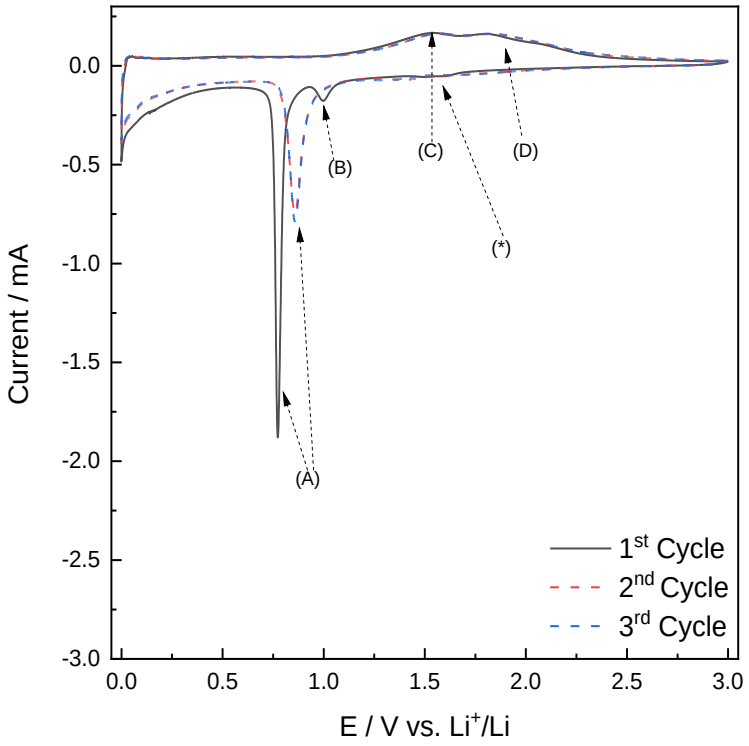

Figure 3-5. Cyclic voltammetry of Fe_3O_4/rGO obtained at 100 μV s^{-1}.

During the anodic scan, two broad peaks at 1.57 V and 1.89 V can be ascribed to the oxidation of Fe^0 to Fe^{2+} and Fe^{2+} to Fe^{3+}, respectively. During the cathodic scan in the subsequent cycles, peak B disappear and peak shift to a higher potential E = 0.8 V.

In **Figure 3-6a**, the galvanostatic cycling of Fe_3O_4/rGO at 1C-rate (881 mAh g^{-1}) are reported.

In the first cycle, specific capacities of 1634 and 1186 mAh g^{-1} during lithiation and delithiation were obtained, respectively, with a corresponding coulombic efficiency of 72 %. In the first 40 cycles, specific capacity values higher than 1000 mAh g^{-1} were obtained. Specific capacities higher than the theoretical one have already been encountered for conversion materials by several authors and can be ascribed to several phenomenon. Two main hypotheses have been proposed, i.e.: (i) interfacial Li storage (20) and (ii) reversible Li storage due to the reversible formation/dissolution of carbonates and semicarbonates (21) in the external layers of SEI, commonly described as "gel-type" layer (22). Upon long-term cycling, the specific capacity drops at 700 mAh g^{-1} at the 100th cycle, with a coulombic efficiency close to 100 %. The galvanostatic E

vs. Q profiles in **Figure 3-6b** reveals a small plateau at E = 1.02 V, and a larger one at E = 0.81 V in the first cycle. These two plateaus can be indexed to the Li^+ insertion into Fe_3O_4 and the conversion reaction, respectively. During delithiation, two slopping plateaus at E = 1.54 V and E = 1.83 V can be indexed to the oxidation of Fe. During the second lithiation, the small plateau at E = 1.02 V disappear and only a large plateau is visible at E = 0.89 V due to the conversion reaction. These features are clearly reflected in the galvanostatic dQ dE^{-1} vs. E plot in **Figure 3-6c**, in which two peaks at E = 1.02 V and E = 0.81 V were observed in the first lithiation, while two peaks, due to the oxidation of Fe, were observed during delithiation at E = 1.54 V and E = 1.83 V. In **Figure 3-7**, the galvanostatic cycling at 2C- (1848 mAh g^{-1}) and 4C-rate (3696 mAh g^{-1}) are reported.

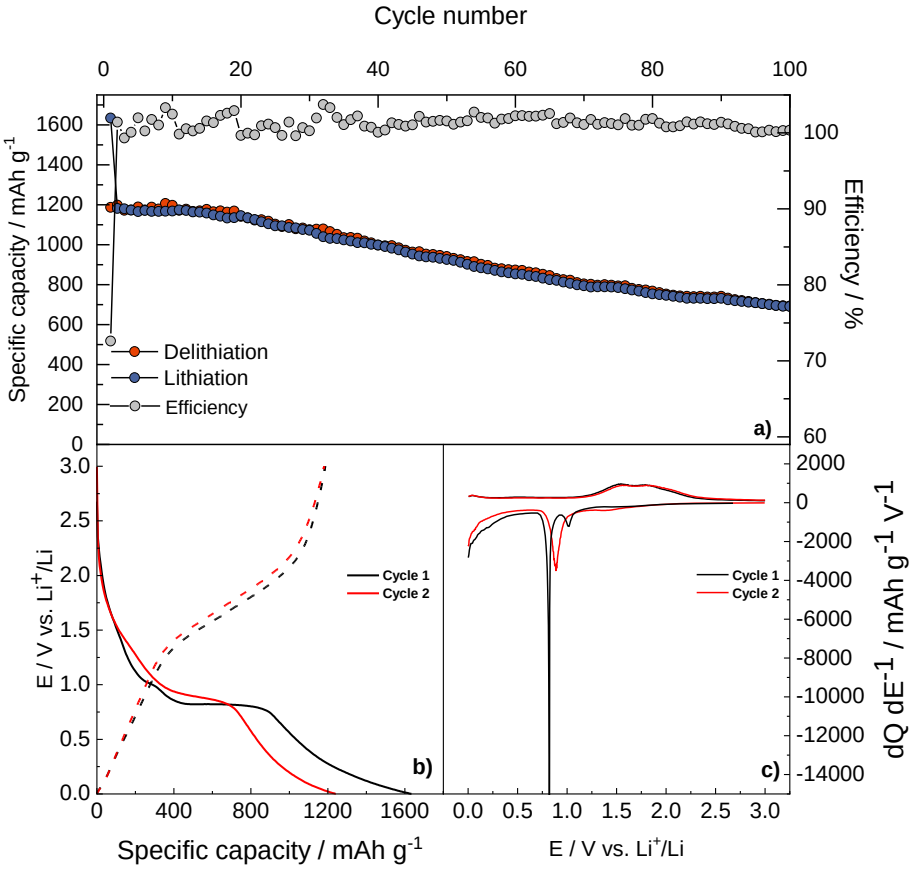

Figure 3-6. a) Specific capacity of Fe_3O_4/rGO as a function of cycle number. Galvanostatic b) E vs. Q and c) dQ dE^{-1} vs. E profiles.

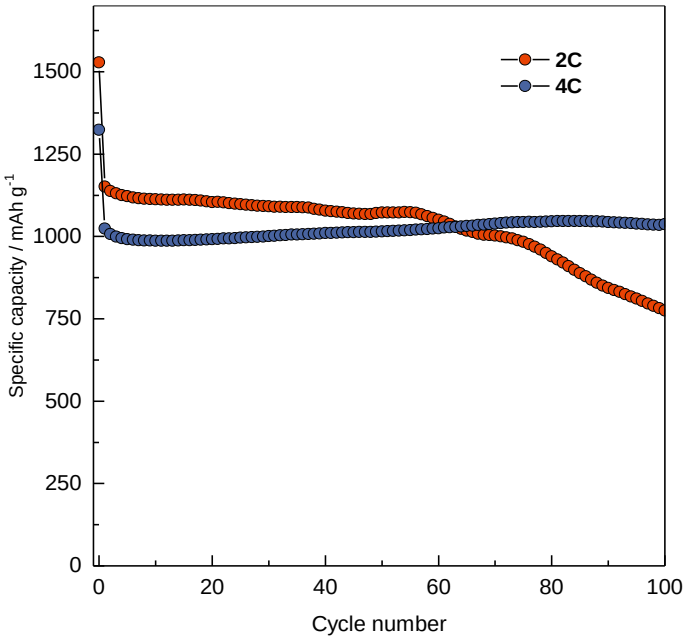

Figure 3-7. Galvanostatic cycling of Fe_3O_4/rGO at 2C- (1848 mAh g^{-1}) and 4C-rate (3696 mAh g^{-1}).

In both cases, the material shows a high specific capacity and an improved stability upon cycling. This behavior can be explained by both the electronic conductivity of reduced graphene oxide as well as the small particle size of Fe_3O_4. At 2C-rate, the material was able to deliver a specific capacity higher than 1100 mAh g^{-1} for the first 50 cycles, for then decreasing at around 700 mAh g^{-1} at the 100th cycle probably due to a mechanical collapse of the electrode structure. At 4C-rate, specific capacities of 1393 and 993 mAh g^{-1} were obtained during the first lithiation and delithiation, respectively. The material was able to deliver an average specific capacity of 980 mAh g^{-1} during 100 cycles with an efficiency close to 100 %. The stability upon cycling remarkably improved, suggesting that the Fe_3O_4/rGO works better at high current rates.

This behavior was also confirmed by the rate capability test, by cycling Fe_3O_4/rGO in the current range from C/10 (88.1 mAh g^{-1}) up to 10C (8810 mAh g^{-1}). The rate capability test is shown in **Figure 3-8**, and summarized in **Table 10**.

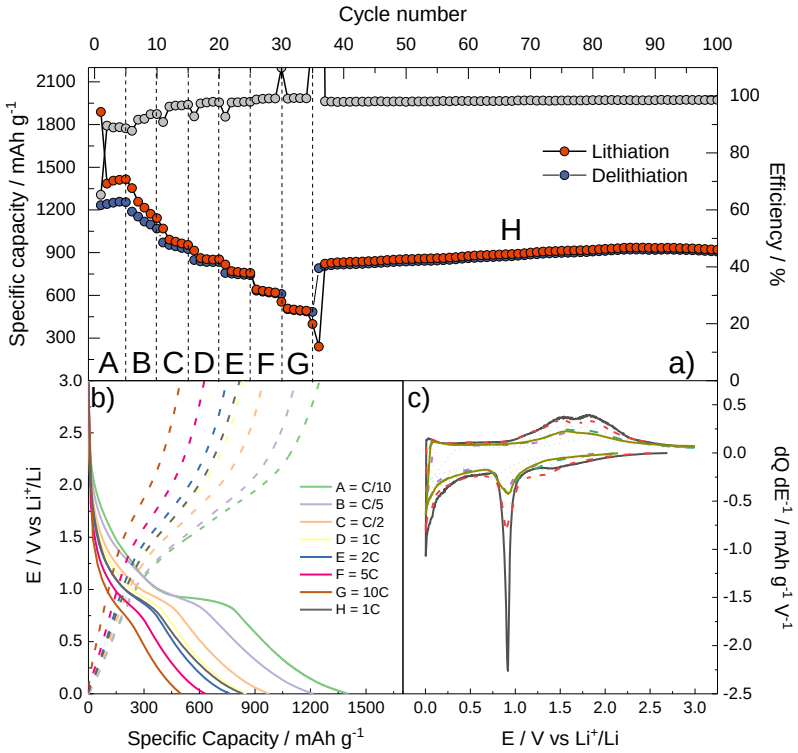

Figure 3-8. a) Rate capability test of Fe_3O_4/rGO. b) E vs. Q galvanostatic profiles extracted at the different scan rates. c) dQ dE^{-1} vs. E profiles extracted at the different current rates.

Table 10. Summarized results of the rate capability test of Fe_3O_4/rGO.

	C-rate	Capacity / mAh g^{-1}	Efficiency / %
A	**C/10**	1253	88.6
B	**C/5**	1069	93.6
C	**C/2**	925	96.4
D	**1C**	834	97.7
E	**2C**	742	98.0
F	**5C**	610	99.1
G	**10C**	484	99.2
H	**1C**	874	99.6

The rate capability test confirms that the Li storage behavior of Fe_3O_4/rGO is greatly affected by the current rate and is more stable at high C-rate. Indeed, up to C/2 a large irreversible capacity, as well as a capacity decay is observed. As the C-rate increases, the irreversibility decreases with a coulombic efficiency approaching 100 %. This behavior can be tentatively explained by parasitic irreversible processes concurrent to the storage mechanism, which can lead to a possible decomposition of the electrode material. The irreversible processes as well as the SEI formation at low C-rates are enhanced by the high specific surface area of reduced graphene oxide. On the

other hand, by cycling at high C-rates the electrochemical storage processes become predominant, and the performances of the electrode are very stable.

Thanks to the small particles size of Fe_3O_4, as well as the electronic conductivity of rGO, a high specific capacity of 484 mAh g^{-1} was retained at 10C. When the current rate was restored to 1C, an average specific capacity of ≈ 900 mAh g^{-1} was retained. The small increase in capacity during the final long-term cycling can be ascribed to structural rearrangements of the active material as well as the increased wetting by the electrolyte, which increase the number of active sites for Li storage.

The Li exchange kinetics was studied by potentiostatic electrochemical impedance spectroscopy, with regard to the role played by the rGO matrix. For this reason, the impedance response of both electrodes made with pristine Fe_3O_4 and Fe_3O_4/rGO was studied as a function of the cycle number. In **Figure 3-9**, the Nyquist plot of both Fe_3O_4 and Fe_3O_4/rGO as well as the fitted resistance value are reported.

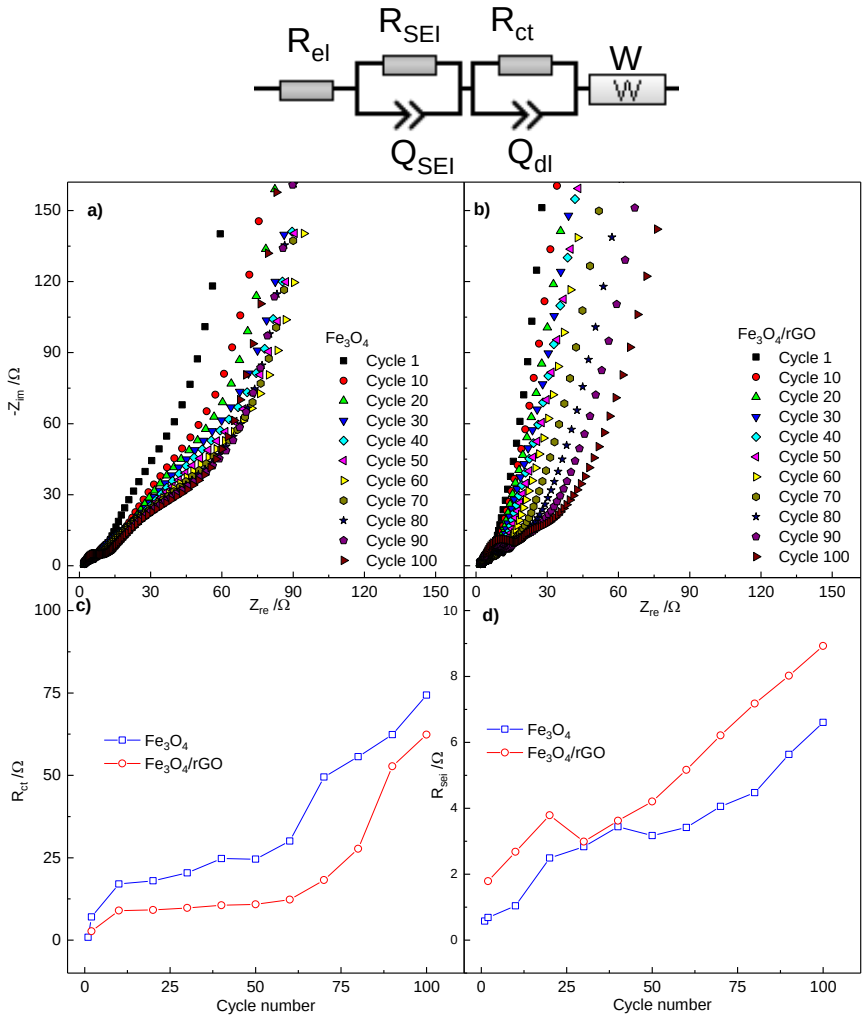

Figure 3-9. Nyquist plot of a) pristine Fe_3O_4 and b) Fe_3O_4/rGO. c) Fitted charge-transfer resistance and d) fitted passivation layer resistance.

The impedance responses were acquired at the bias potential E = 0.75 V in the first cycle and E = 0.90 V for the further cycles, corresponding to the peak A in **Figure 3-5**. All the dispersions are characterized by four common features i.e., (i) a positive shift in the real axis, (ii) a small semicircle in the high-frequency region, (iii) a larger semicircle in the medium-frequency region, and (iv) a low frequency polarization visualized as a straight line. These features, which are typical for a Li-ion battery anode, can be ascribed to (i) the electrolyte resistance, (ii) the migration of Li^+ ions through the passivation layer with a corresponding accumulation of charges on its surface, (iii) the charge-transfer reaction couple to the formation of a charged double-layer, and (iv) Li diffusion in the active material. In both materials, the overall impedance increases upon cycling manly due to structural rearrangements. The main contribution to this growth is given by the medium-frequency arc, which can be caused by structural rearrangements of the active material,

electronic contact loss, and large inter-particle resistance. When comparing the dispersion of the two materials, Fe_3O_4/rGO had a more limited growth compared to the pristine Fe_3O_4 nanoparticles. However, the high-frequency arc of Fe_3O_4/rGO had a larger growth compared to the parent material, which can be explained by the larger specific surface area of rGO exposed to the passivation process in the first cycles.

The dispersion have been fitted by CNLS-fit procedure using Boukamp's software EQVCRT (23) by using the equivalent circuit $R_{el}(R_{SEI}C_{SEI})(R_{ct}C_{dl})W$ (written in Boukamp's notation) (23). R_{el}, R_{SEI}, C_{SEI}, R_{ct}, C_{dl}, and W are the electrolyte resistance, the resistance of the passivation layer, the capacitance of the passivation layer, the charge-transfer resistance, the double layer capacitance, and the Warburg diffusion, respectively. All the pure capacitor elements have been substituted by a constant phase element to consider the inhomogeneities and roughness of the electrode (24). The calculated resistance values of R_{ct} and R_{SEI} are reported in **Figure 3-9c-d**, respectively. In both cases, the obtained resistance values increase upon cycling. However, the composite Fe_3O_4/rGO has a lower R_{ct} given by the improved electronic conductivity due to the rGO matrix. On the other hand, the R_{SEI} of Fe_3O_4/rGO is larger compared to the parent material, which can be explained by the large specific surface area of rGO.

3.4 Results and discussion: electrochemical characterization in NIBs

The cyclic voltammetry of Fe_3O_4/rGO in Na-ion battery configuration is reported in **Figure 3-10**.

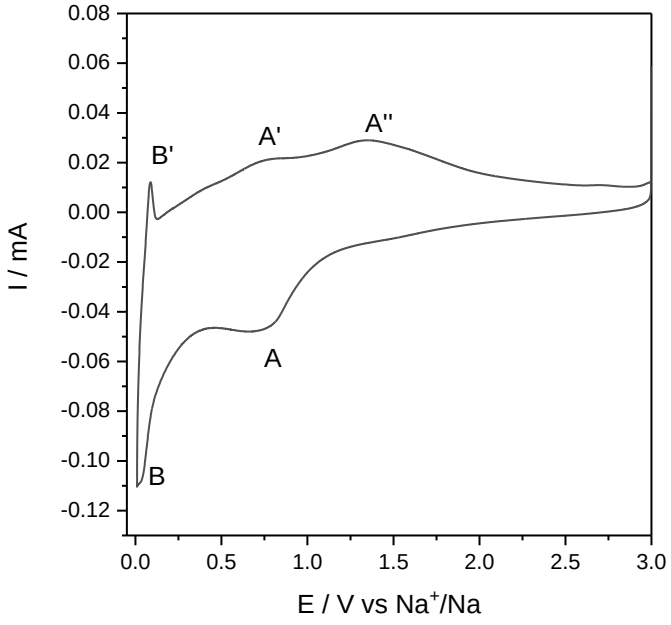

Figure 3-10. Cyclic voltammetry of Fe_3O_4/rGO in NIB configuration.

In the first cathodic scan, two main features are evidenced i.e., a broad peak labeled as (A) at E = 0.80 V, which can be assigned to the conversion reaction of Fe_3O_4 (**Equation 21**) (25; 26), and a sharp peak labeled as (B) at low potential which can be attributed to a Na^+ storage into rGO (**Equation 22**) (27).

$$Fe_3O_4 + 8Na^+ + 8e^- \rightarrow 4Na_2O + 3Fe \qquad \textbf{Eq. 21}$$

$$rGO + xNa^+ + xe^- \rightarrow Na_xrGO \qquad \textbf{Eq. 22}$$

Furthermore, part of the activity assigned to peak (A) can be indexed to the reduction of the electrolyte and formation of the passivation layer, which is triggered at E < 0.8 V in Na-ion batteries (28). During the oxidation scan, three features are evidenced i.e., a sharp peak labeled as (B') at low potential indexed to the removal of Na^+ ions from rGO matrix, and a couple of broad peaks labeled as (A') and (A'') at E > 0.80 V which can be attributed to the oxidation of Fe to Fe^{2+} and from Fe^{2+} to Fe^{3+}, respectively.

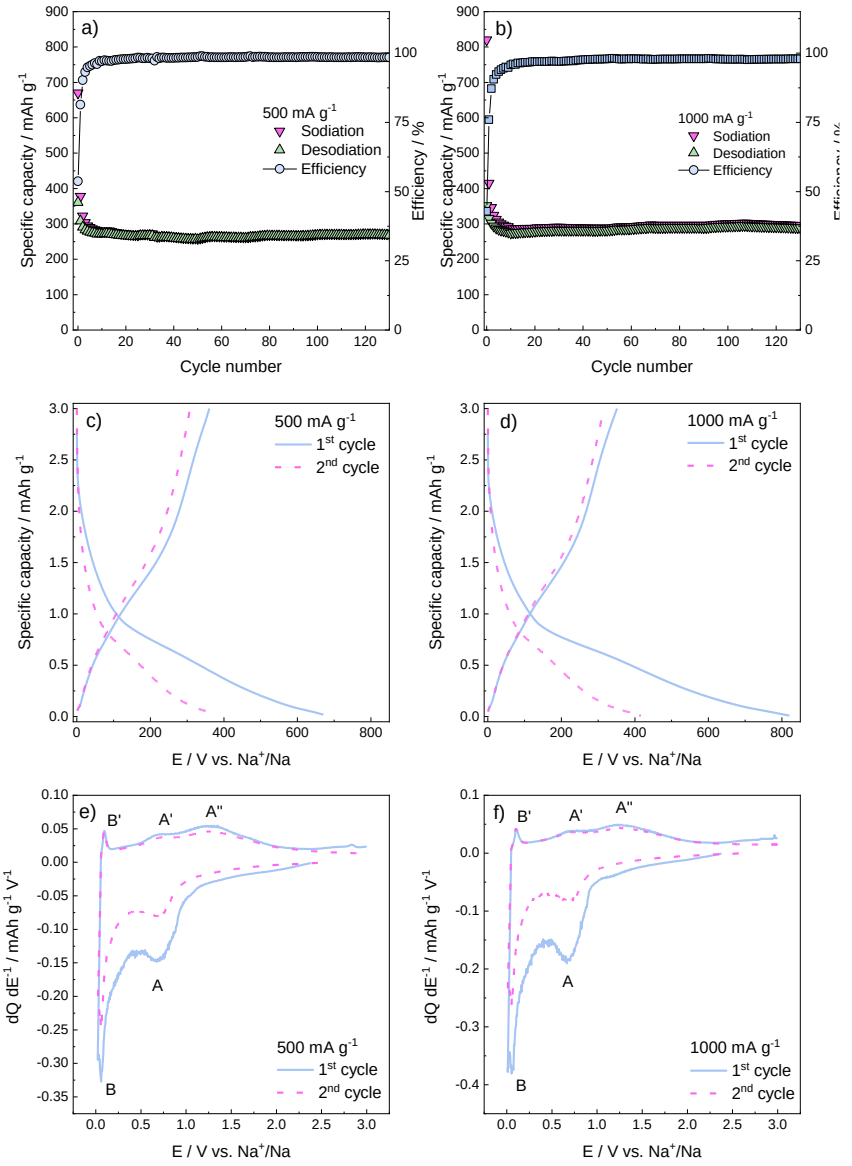

Figure 3-11. Specific capacity values and coulombic efficiency values obtained at a) 500 mA g^{-1} and b) 1000 mA g^{-1}. Galvanostatic E vs. Q profiles at c) 500 mA g^{-1} and d) 1000 mA g^{-1}. Differential dQ dE^{-1} vs. E plot obtained at e) 500 mA g^{-1} and f) 1000 mA g^{-1}.

The Na-storage capability of Fe_3O_4/rGO was assessed by galvanostatic cycling at the current rates of I_{Spec} = 500 mA g^{-1} and I_{Spec} = 1000 mA g^{-1}. The specific capacity values, as well as the coulombic efficiencies at 500 and 1000 mA g^{-1} are reported in **Figure 3-11a-b**.

At both applied currents, there is a capacity decay in the initial cycles which can be indexed to the irreversible SEI formation as well as the partially irreversible Fe_3O_4 conversion reaction. Indeed, a large irreversibility was assessed in the first cycle at both conditions, with coulombic efficiencies values of 53.75 % and 42.85 % for 500 and 1000 mA g^{-1}, respectively. The irreversibilities progressively decrease upon cycling, in which the specific capacity stabilizes at ≈

300 mAh g^{-1} in both cases. The E vs. Q galvanostatic profiles (**Figure 3-11c-d**) confirm the first-cycle irreversibility of the electrodes. No clear plateaus are evidenced by the sodiation/desodiation profiles of the first two cycles, suggesting that completion of the several phase transitions, related to the (de)conversion processes, is kinetically hindered. Looking at the differential dQ dE^{-1} vs. E plots, a large capacity contribution in the first cycle is given in the same potential region of peak A, while in the following desodiation step the electrodes did not yield the same amount of charge. This behavior confirms that the irreversibilities are mainly due to the irreversible SEI formation as well as the partially irreversible conversion reaction of Fe_3O_4.

The behavior of Fe_3O_4/rGO at different current rates was assessed by applying a rate capability protocol. In this regards, specific current of 100, 200, 500, 1000, 2000, and 5000 mA g^{-1} were applied to the electrode for 5 cycles. Eventually, a specific current of 1000 mA g^{-1} was applied to assess the capacity retention of the active material. The rate capability results are shown in **Figure 3-12**, and summarized in **Table 11**.

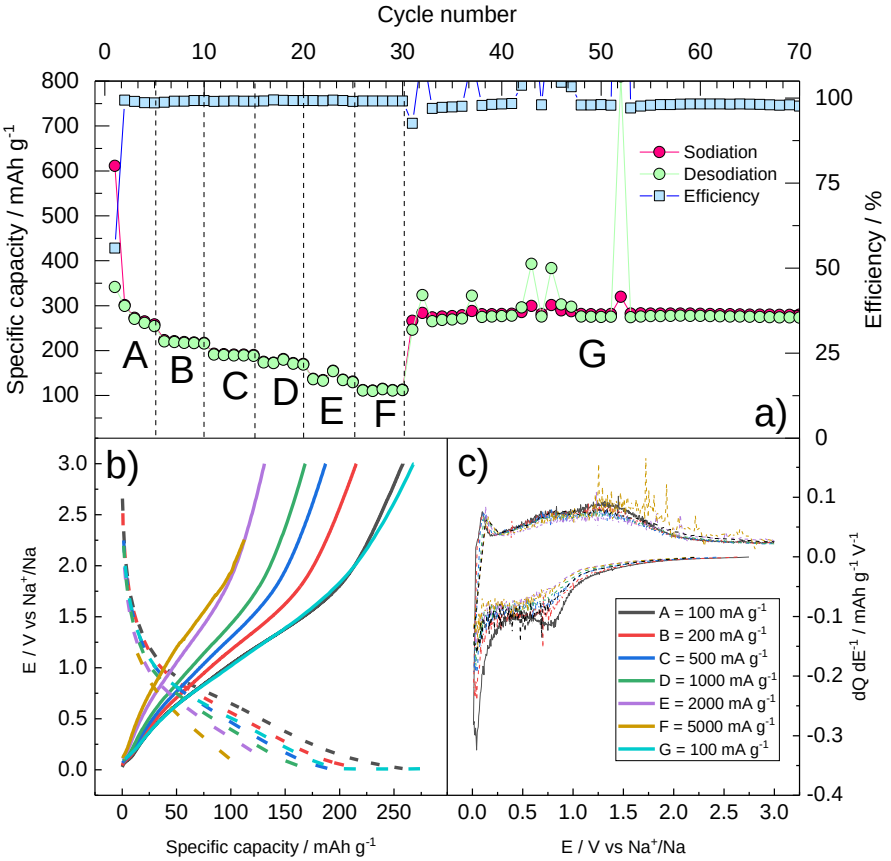

Figure 3-12. a) Rate capability test of Fe_3O_4/rGO. b) E vs. Q galvanostatic profiles at different current rates. c) dQ dE^{-1} vs. E profiles at different current rates.

Table 11. Summarized results of the rate capability test of Fe_3O_4/rGO with Na.

	C-rate / mA g^{-1}	Capacity / mAh g^{-1}	Efficiency / %
A	100	274	98.88
B	200	220	99.08
C	500	191	99.07
D	1000	174	99.27
E	2000	138	99.21
F	5000	112	99.11
G	100	280	99.66

The rate performance tests confirm that the active material can withstand high current rates. As expected, as the current rate increases, the specific capacity decreases. Nevertheless, a capacity retention of 50 and 40 %, respect to the initial capacity obtained at 100 mA g^{-1}, was observed at 2000 and 5000 mA g^{-1}, respectively. When the current is restored to the initial value of 100 mA g^{-1}, a stable capacity of ≈ 280 mAh g^{-1} was observed. However, some cycles exhibit capacity spikes during desodiation which are probably due to the breakage of the passivation layer, and thus release of Na^+ ions which are plated back to the counter electrode. This is a common behavior for anode material in Na-ion batteries, due to the instability of the passivation layer (29).

Electrochemical investigation of transport and interfacial properties

The investigation of transport and interfacial properties of Fe_3O_4/rGO with Na was assessed by cyclic voltammetry at different scan rates, potentiostatic electrochemical impedance spectroscopy, and Ex-situ Raman spectroscopy. The cyclic voltammetries at different scan rates are reported in **Figure 3-13**.

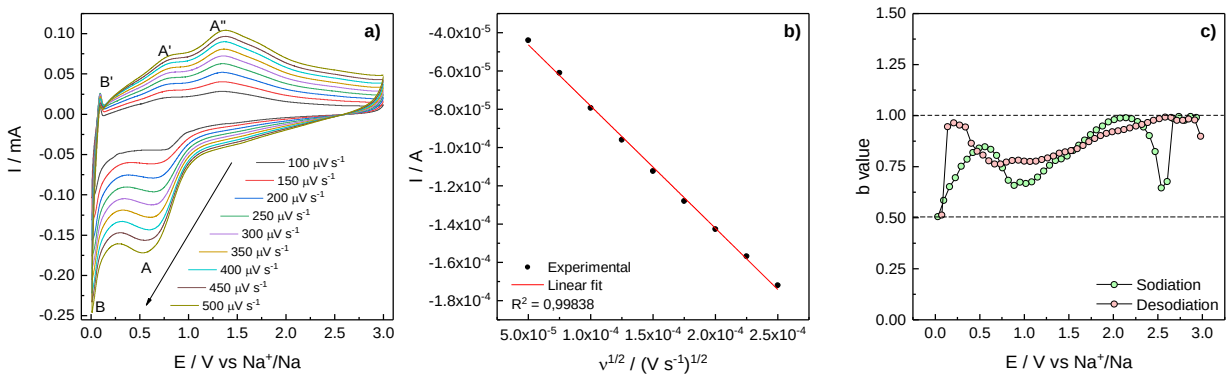

Figure 3-13. a) Cyclic voltammetries at different scan rates. b) I vs. $\nu^{1/2}$ and its linear fit. c) Calculated b-value from power-law as a function of the electrode potential.

As expected, as the scan rate increases the peaks area and intensity increase. Indeed, a linear relationship between the peak current I_P and the square root of the scan rate $\nu^{1/2}$ was found (R^2 = 0.99838), which suggest that the storage of Na^+ ions occur with a diffusion-controlled behavior. However, if both capacitive current i_{Cap} and faradaic current i_{Far} are considered, the measured current at each potential step can be approximated by the empirical relationship in **Equation 23**, known as power-law (30; 31; 32).

$$i(v) = i_{Cap} + i_{Far} = av^b \qquad \textbf{Eq. 23}$$

Where i_v is the measured current, while a and b are adjustable dimensionless parameters. The b-value can be calculated as the slope in the log i vs. log v plot (**Equation 24**).

$$\log i(v) = \log a + b \log v \qquad \textbf{Eq. 24}$$

When b = 0.5 the process is purely faradaic and controlled by solid-state diffusion, while when b = 1 the process is purely capacitive. Intermediates values of b are commonly assigned to pseudocapacitive behaviors, or as in this case, to redox pseudocapacitive behaviors i.e., adsorption of charge to the electrode material surface accompanied by a fast faradaic reaction (33).

In **Figure 3-13c**, the calculated b-value as a function of the electrode potential is reported. At potential values close to the reduction peaks A and B observed in cyclic voltammetry (**Figure 3-10**), the b-value approaches 0.5, consistent with a pure faradaic process. At E values far from the mentioned peaks, the b-value approaches 1, suggesting a storage of charge on the surface of the electrode material. During desodiation, in the potential region of the oxidation peaks A′ and A′′, the b parameter assumes the intermediate value of 0.75, suggesting that the release of Na^+ ions is redox pseudocapacitive process.

To further characterize the kinetics of the storage process, impedance spectra were acquired over the bias potential E = 0.5 V every 10th cycle. The Nyquist plot as well as the fitted resistance parameters are shown in **Figure 3-14**.

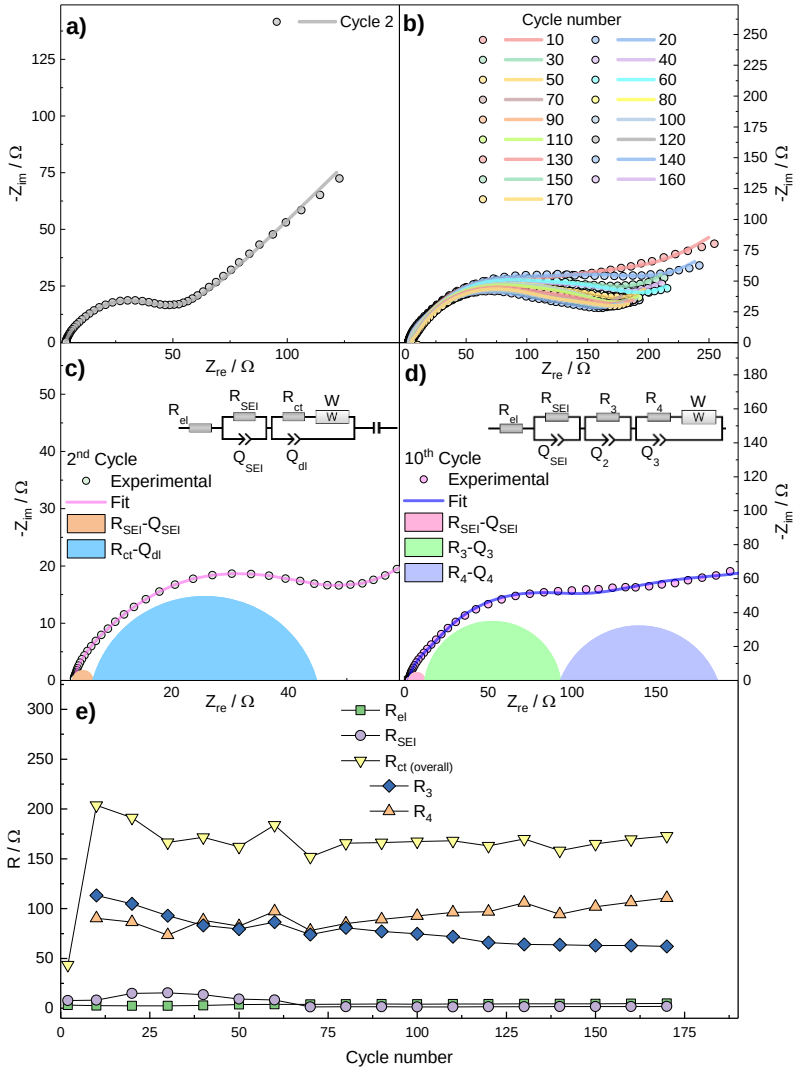

Figure 3-14. Nyquist plot of a) the 2nd cycle and b) of the further cycles. Equivalent circuit models and graphical fir of c) the 2nd cycles and d) of the 10th cycle. e) Fitted resistance parameters as a function of cycle number.

The Nyquist plot of the 2nd cycle is characterized by a positive shift in the real axis, a large, suppressed arc in the medium-frequency region, and a low-frequency polarization represented as a straight line. The Nyquist plot was analyzed by the Equivalent Circuit method (23) and the fitting parameters have been calculated by CNLLS-fit using Relaxis 3 software (rhd instruments). The shift in the real axis, describing the migration of charges through the electrolyte, can be modelled as a pure resistive element R_{el}. The medium-frequency arc, describing the migration of Na^+ ions through the passivation layer as well as the charge-transfer process, can be modelled by two resistive elements R_{SEI} and R_{ct}, respectively. Coupled to them, there are two capacitor element C_{SEI} and C_{dl}, which describe the accumulation of charges at the surface of the passivation layer, and the electrical double-layer capacitance, respectively. Finally, the low-frequency polarization, describing the semi-infinite diffusion to a blocking electrode, can be modelled by using a

Warburg element in series with a capacitor C_i. The equivalent circuit used for fitting is $R_{el}(R_{SEI}C_{SEI})([R_{ct}W]C_{dl})C_i$, written in Boukamp's notation (23). During the fitting procedure, all the capacitor elements have been replaced by constant phase element to consider electrode inhomogeneities and roughness (24). The impedance response after the 2nd cycle was subjected to a drastic change. This event, as well as the specific capacity lower than the theoretical one can be explained by the formation of large cluster of Na_2O during the conversion reaction, which act as transport barrier. This behavior has already been encountered for SnO_2-based electrodes in Na-ion battery configuration, in which specific capacities way lower than the theoretical one were observed, and ascribed to the formation of large clusters of Na_2O (34). Therefore, the ac-dispersions of the 10th cycle and onwards have been fitted by deconvoluting the ($R_{ct}C_{dl}$) arc into two (R_3C_3) and (R_4C_4) features, resulting into the equivalent circuit $R_{el}(R_{SEI}C_{SEI})(R_3C_3)([R_4W]C_4)C_i$. The deconvolution of the 2nd and 10th cycle, as well as the used equivalent circuit model are shown in **Figure 3-14c-d**. The fitted resistance parameter R_{el}, R_{SEI}, and R_{ct} from the ECM in **Figure 3-14c** for the 2nd cycle, as well as R_3 and R_4 obtained with fitting from the 10th cycle onwards with the ECM in **Figure 3-14d** are reported in **Figure 3-14e**. For the cycles other than the 2nd, R_{ct} represents the sum of R_3 and R_4.

As expected, R_{el} is practically stable upon cycling. R_{SEI} shows a small increase in the initial cycles, which can be assigned to the breakage and subsequent reformation of the passivation layer in the initial cycles. This phenomenon confirms the irreversible capacity, and thus the low coulombic efficiency, observed in the initial cycles in **Figure 3-11a**. After the 30th cycle, R_{SEI} values decrease reaching a relative stabilization. This feature can be tentatively explained by the anisotropic growth of the SEI layer upon cycling. In the case of R_{ct}, the overall resistance increases after the 2nd due to the aforementioned formation of large Na_2O clusters during the conversion reaction.

The reversibility of Na storage in the active material was assessed by ex-situ Raman spectroscopy at selected potential values in the first sodiation/desodiation. The points highlighted in red in **Figure 3-15a**, represents the following conditions during sodiation: (i) fresh electrode before the conversion reaction of Fe_3O_4 and formation of the SEI (E = 1.5 V); (ii) initial stages of the conversion reaction and formation of the passivation layer (E = 0.72 V); (iii) complete formation of the passivation layer and initial stages of Na-C processes (E = 0.25 V); (iv) electrode fully sodiated (E = 0.02 V). The points highlighted in blue in **Figure 3-15a**, represents the following conditions during desodiation: (v) electrode after the release of most of Na by C matrix (E = 0.12 V); (vi) intermediate stages of Fe oxidation (E = 0.81 V); (vii) final stages of Fe oxidation (E = 1.4

V); (viii) electrode fully desodiated (E = 3 V). All the spectra contains the D and G band due to the presence of rGO and SuperC65 in the electrode. In the spectra from (i) to (iii) in the first sodiation, the peak at 667 cm^{-1} can be assigned to the A_{1g} mode of Fe_3O_4. Compared to the Raman spectra in **Figure 3-3a&c**, no signals of α-Fe_2O_3 are clearly discernible (only a glimpse of the E_u mode of α-Fe_2O_3 is visible and overlapped with the D-band of amorphous carbon). This can be ascribed to the sealing of the electrode in glovebox under Ar atmosphere, so that no laser-induced oxidation of Fe^{2+} to Fe^{3+} occurs. This feature suggests that the observed signal of α-Fe_2O_3 which were observed in **Figure 3-3a&c**, were actually due to the oxidation induced by the laser irradiation under air atmosphere.

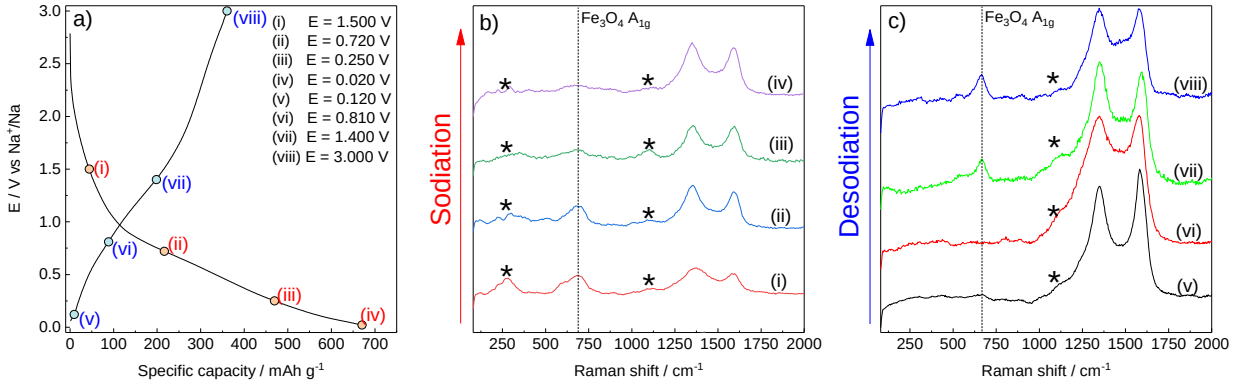

Figure 3-15. a) E vs. Q galvanostatic profile with highlighted points in which Raman spectra were acquired. b) Raman spectra acquired during sodiation. c) Raman spectra acquired during desodiation.

As the sodiation proceeds, the intensity of the A_{1g} peak of Fe_3O_4 decreases leaving a small hump at point (iv) in which the electrode is fully sodiated (E = 0.02 V). This result confirms that the conversion reaction of Fe_3O_4 to Fe occurs. However, the A_{1g} peak is still present, suggesting that the conversion reaction does not go to completion. Indeed, an experimental specific capacity lower than the theoretical one was observed upon cycling. This behavior can be tentatively explained by the formation of large Na_2O clusters, as hypothesized with EIS, which by acting as transport barriers also limits the sodiation of the active material. The two constant peaks located at 250 cm^{-1} and 1000 cm^{-1} (labelled as *) can be indexed to both inorganic SEI components such as Na_2CO_3 or organic alkyl carbonates (35; 36; 37; 38). Specifically, the band located at 1100 cm^{-1} can be ascribed to the stretching ν C-O-C bonds in alkyl carbonates.

During desodiation, an opposite trend was observed. Indeed, from point (vii) to (viii), the intensity of the A_{1g} peak progressively increases. This feature confirms that the oxidation of Fe to

Fe^{2+} and Fe^{3+} occurs, and thus the reversibility of the conversion reaction which leads back to Fe_3O_4.

3.5 Conclusion

It was demonstrated that Fe_3O_4 nanoparticles, synthesized by a green and facile method, are a suitable anode material for both Li- and Na-ion batteries. When composite electrodes, with high Fe_3O_4 loading (Fe_3O_4:rGO 80:20) are cycled in Li half-cells, specific capacities in the order of 1000 mAh g^{-1} are obtained. Furthermore, excellent capacity retention was obtained at high current rates, with specific capacities in the order of 500 mAh g^{-1} at 10C. The EIS meauraments confirm that its outstanding performances with Li are given by the embedding of Fe_3O_4 nanoparticles into the rGO matrix, resulting in a lower charge-transfer polarization.

When cycled in Na half-cells, stable specific capacities of ≈ 300 mAh g^{-1}, with an excellent capacity retention at high rates of 50 and 40 % at the current of 2 and 5 A g^{-1}, respectively. The investigation of transport properties done by cyclic voltammetries at different scan rate highlights that the storage of Na^+ ions during sodiation occurs mainly by a Faradaic process, while on sodiation the material behaves as a redox pseudocapacitive material. EIS measurements evidenced the formation of a new interface given by the formation of large Na_2O clusters. Ex-situ Raman spectroscopy proved that the conversion reaction does not go to completion upon sodiation; however, the Fe nanoparticles are reversibly oxidized back to Fe_3O_4 during desodiation.

These findings, together with the easiness of the synthesis procedure, suggest that the composite Fe_3O_4 is a suitable green, sustainable, and reliable candidate anode material for both Li- and Na-ion batteries.

References

1. *FeO/C anode materials of high capacity and cycle stability for lithium-ion batteries synthesized by carbothermal reduction.* **Mingxia Gao, Pei Zhou, Peng Wang, Junhua Wang, Chu Liang, Jialei Zhang, Yongfeng Liu.** s.l. : Journal of Alloyis and Compounds, 20113, Vol. 565, p. 97-103.

2. *α-Fe2O3 nanoplates with superior electrochemical performance for lithium-ion batteries.* **Li Xiu, Yuhui Tian, Tiefeng Liu, Henan Li, Jingxia Qiu, Sheng Li, Huaming Li, Shouqi Yuan, Shanqing Zhang.** 2, s.l. : Green Energy & Environment, 2018, Vol. 3, p. 156-162.

3. **N. N. Greenwood, A. Earnshaw.** *Chemistry of the Elements.* s.l. : Butterworth-Heinemann, 1997. 9780750633659.

4. *3D Porous γ-Fe2O3@C Nanocomposite as High-Performance Anode Material of Na-Ion Batteries.* **Ning Zhang, Xiaopeng Han, Yongchang Liu, Xiaofei Hu, Qing Zhao, Jun Chen.** 5, s.l. : Advanced Energy Materials, 2014, Vol. 5, p. 1401123.

5. *Highly Efficient Sodium Storage in Iron Oxide Nanotube Arrays Enabled by Built-In Electric Field.* **Jiangfeng Ni, Menglei Sun, Liang Li.** 41, s.l. : Advanced Materials, 2019, Vol. 31, p. 1902603.

6. *Magnetic Field Facilitated Resilient Chain-like Fe3O4/C/Red P with Superior Sodium Storage Performance.* **Guohui Qin, Jingying Duan, Yuchen Yang, Fusheng Liu.** 7, s.l. : ACS Applied Materials & Interfaces, 2018, Vol. 10, p. 6441-6452.

7. *A review of carbon materials and their composites with alloy metals for sodium ion battery anodes.* **Muhammad-Sadeeq Balogun, Yang Luo, Weitao Qiu, Peng Liu, Yexiang Tong.** s.l. : Carbon, 2016, Vol. 98, p. 162-178.

8. *Superior Thermal Conductivity of Single-Layer Graphene.* **Alexander A. Balandin, Suchismita Ghosh, Wenzhong Bao, Irene Calizo, Desalegne Teweldebrhan† Feng Miao, and Chun Ning Lau.** 3, s.l. : Nano Letters, 2008, Vol. 8, p. 902-907.

9. *Electrical conductivity of compacts of graphene, multi-wall carbon nanotubes, carbon black, and graphite powder.* **Bernardo Marinho, Marcos Ghislandi, Evgeniy Tkalya, Cor E. Koning, Gijsbertus de With.** s.l. : Powder Technology, 2012, Vol. 221, p. 351-358.

10. *Mechanical properties of graphene and graphene-based nanocomposites.* **Dimitrios G. Papageorgiou, Ian A.Kinloch, Robert J.Young.** s.l. : Progress in Material Science, 2017, Vol. 90, p. 75-127.

11. *The role of graphene for electrochemical energy storage.* **Rinaldo Raccichini, Alberto varzi, Stefano Passerini, Bruno Scrosati.** s.l. : Nature Materials, 2015, Vol. 14, p. 271-279.

12. *Metal oxide/graphene composite anode materials for sodium-ion batteries.* **Lei Wang, Zengxi Wei, Minglei Mao, Hongxia Wang, Yutao Li, Jianmin Ma.** s.l. : energy Storage Materials, 2019, Vol. 16, p. 434-454.

13. *A facile synthesis of Fe3O4 nanoparticles/graphene for high-performance lithium/sodium-ion batteries.* **Yanqing Fu, Qiliang Wei, Xianyou Wang, Gaixia Zhang, Hongbo Shu, Xiukang Yang, Ana C. Tavares, Shuhui Sun.** 20, s.l. : RSC Advances, 2016, Vol. 6, p. 16624-16633.

14. *An Eco-Friendly Means of Biosynthesis of Superparamagnetic Magnetite Nanoparticles via Marine Polymer.* **Yen Pin Yew, Kamyar Shameli, Mikio Miyake, Nurul Bahiyah Bt Ahmad Khairudin, Shaza Eva Bt Mohamad, Hirofumi Hara, Mariam Firdhaus Bt Mad Nordin, Kar Xin Lee.** 6, s.l. : IEEE Transactions on Nanotechnology, 2017, Vol. 16, p. 1047-1052.

15. *Nano magnetite decorated multiwalled carbon nanotubes: a robust nanomaterial for enhanced carbon dioxide adsorption.* **Ashish Kumar Mishra, Sundara Ramaprabhu.** 3, s.l. : Energy & Environmental Science, 2011, Vol. 4, p. 889-895.

16. *Vibrational Spectroscopic Characterization of Hematite, Maghemite, and Magnetite Thin Films Produced by Vapor Deposition.* **Aaron M. Jubb, Heather C. Allen.** 10, s.l. : ACS Applied Materials & Interfaces, 2010, Vol. 2, p. 2804-2812.

17. *Raman spectroscopy of graphene-based materials and its applications in related devices.* **Jiang-Bin Wu, Miao-Ling Lin, Xin Cong, He-Nan Liu, Ping-Heng Tan.** 5, s.l. : Chemical Society Reviews, 2018, Vol. 47, p. 1822-1873.

18. *Highly reversible Co3O4/graphene hybrid anode for lithium rechargeable batteries.* **Haegyeom Kim, Dong-Hwa Seo, Sung-Wook Kim, Jongsoon Kim, Kisuk Kang.** 1, s.l. : Carbon, 2011, Vol. 49, p. 326-332.

19. *Spinel electrodes for lithium batteries - A Review.* **M. M. Thackeray, L. A. Picciotto, A. de Kock, P. J. Johnson, V. A. Nicholas, K. T. Adendorff.** 1, s.l. : Journal of Power Sources, 1987, Vol. 21, p. 1-8.

20. *Combined XRD, EXAFS, and Mössbauer Studies of the Reduction by Lithium of α Fe2 O 3 with Various Particle Sizes.* **D. Larcher, D. Bonnin, R. Cortes, I. Rivals, L. Personnaz, J.-M. Tarascon.** 12, s.l. : Journal of The Electrochemical Society, 2003, Vol. 150, p. A1643.

21. *On the Origin of the Extra Electrochemical Capacity Displayed by MO/Li Cells at Low Potential.* **S. Laruelle, S. Grugeon, P. Poizot, M. Dollé, L. Dupont, J-M. Tarascon.** s.l. : Journal of The Electrochemical Society, 2002, Vol. 149, p. A627.

22. *Mass Spectrometry Investigations on Electrolyte Degradation Products for the Development of Nanocomposite Electrodes in Lithium Ion Batteries.* **Laurent Gireaud, Sylvie Grugeon, Serge Pilard, Pierre Guenot, Jean-Marie Tarascon, and Stephane Laruelle.** 11, s.l. : Analytical Chemistry , 2006, Vol. 78, p. 3688-3698.

23. *A Nonlinear Least Squares Fit procedure for analysis of immittance data of electrochemical systems.* **Boukamp, Bernard A.** 1, s.l. : Solid State ionics, 1986, Vol. 20, p. 31-44.

24. **Evgenij Barsoukov, J. Ross Macdonald.** *Impedance Spectroscopy: Theory, Experiment, and Applications.* s.l. : john Wiley & Sons, 2005.

25. *High capacity and low cost spinel Fe3O4 for the Na-ion battery negative electrode materials.* **P. Ramesh Kumar, Young Hwa Jung, K. Kamala Bharathi, Chek Hai Lim, Do Kyung Kim.** s.l. : Electrochimica Acta, 2014, Vol. 146, p. 503510.

26. *A sustainable iron-based sodium ion battery of porous carbon-Fe3O4/Na2FeP2O7 with high performance.* **Jun Ming, Hai Ming, Wenjing Yang, Won-Jin Kwak, Jin-Bum Park, Junwei Zheng, Yang-Kook sun.** s.l. : RSC Advances, 2015, Vol. 5, p. 8793-8800.

27. *Reduced graphene oxide with superior cycling stability and rate capability for sodium storage.* **Yun-Xiao Wang, Shu-Lei Chou, Hua-Kun Liu, Shi-Xue Dou.** s.l. : Carbon, 2013, Vol. 57, p. 202-208.

28. *Review—SEI: Past, Present and Future.* **E. Peled, S. Menkin.** s.l. : journal of The Electrochemical Society, 2017, Vol. 164, p. A1703.

29. *Composition and Evolution of the Solid-Electrolyte Interphase in Na2Ti3O7 Electrodes for Na-Ion Batteries: XPS and Auger Parameter Analysis.* **Miguel A. Muñoz-Marquez, Maider Zarrabeitia, Elizabeth Castillo-Martinez, Aitor Eguia-Barrio, Teofilo Rojo, Montse Casas-Cabanas.** s.l. : ACS Applied Materials & Interfaces, 2015, Vol. 7, p. 7801-7808.

30. *Advanced Energy Storage Devices: Basic Principles, Analytical Methods, and Rational Materials Design.* **Jilei Liu, Jin Wang, Chaohe Xu, Hao Jiang, Chunzhong Li, Lili Zhang, Jianyi Lin, Ze Xiang Shen.** 1, s.l. : Advanced Science, 2017, Vol. 5, p. 1700322.

31. *Electrochemical Kinetic Study of LiFePO4 Using Cavity Microelectrode.* **J. Come, P.-L. Taberna, S. Hamelet, C. Masquelier, P. Simon.** s.l. : Journal of The Electrochemical Society, 2011, Vol. 158, p. A1090.

32. *Pseudocapacitive Contributions to Electrochemical Energy Storage in TiO2 (Anatase) Nanoparticles.* **John Wang, Julien Polleux, James Lim, Bruce Dunn.** 40, s.l. : The Journal of Physical Chemistry, 2007, Vol. 111, p. 14925-14931.

33. *Definitions of Pseudocapacitive Materials: A Brief Review.* **Yuqi Jiang, Jinping Liu.** 1, s.l. : Energy & Environmental Materials, 2019, Vol. 2, p. 30-37.

34. *Difference in Electrochemical Mechanism of SnO2 Conversion in Lithium-Ion and Sodium-Ion Batteries: Combined in Operando and Ex Situ XAS Investigations.* **Ditty Dixon, Marta Ávila, Helmut Ehrenberg, Aiswarya Bhaskar.** 6, s.l. : ACS Omega, 2019, Vol. 4, p. 9731-9738.

35. *Raman and Infrared Spectral Studies of Anhydrous Li2CO3 and Na2CO3.* **M. H. Brooker, John B. Bates.** s.l. : Journal of Chemical Physics, 1971, Vol. 11, p. 4788.

36. *In Situ Raman Spectroscopy on Silicon Nanowire Anodes Integrated in Lithium Ion Batteries.* **Andreas Krause, Olga Tkacheva, Ahmad Omar, Ulrike Langklotz, Lars Giebeler, Susanne Dorfler, ¨ 5 F. Fauth,6 Thomas Mikolajick,1,2 and Walter M. Weber.** s.l. : journal of The Electrochemical Society, 2019, Vol. 166, p. A5378-A5385.

37. *Unraveling the Nanoscale Heterogeneity of Solid Electrolyte Interphase Using Tip-Enhanced Raman Spectroscopy.* **Jagjit Nanda, Guang Yang, Tingzheng Hou, Dmitry N. Voylov, Xin Li, Rose E. Ruther, Michael Naguib, Kristin Persson, Gabriel M.Veith, Alexei P.Sokolov.** 8, s.l. : Joule, 2019, Vol. 3, p. 2001-2019.

38. *An In Situ Raman-Electrochemical Investigation of Carbon Steel Corrosion in Na2CO3/NaHCO3, Na2SO4, and NaCl Solutions.* **C. T. Lee, M. S. Odziemkowski, D. W. Shoesmith.** s.l. : Journal of The Electrochemical Society, 2006, Vol. 153, p. B33.

4. Electrochemical Characterization of Commercial Anode-Supported Solid Oxide Fuel Cells

As mentioned in section **1.2.2**, SOFCs offer several advantages respect to other fuel-cell types i.e., highest H_2-to-power efficiency, modularity without losing efficiency (from 1 kW up to 1 MW), and possibility to work in reversible mode (fuel cell – electrolyzer) coupled to a renewable energy system (1; 2; 3; 4; 5). However, their use under real operating conditions intrinsically implies temperature and load variations, as well as impurities in the feeding gases (6; 7; 8; 9). These unwanted conditions can lead to several degradation pathways on the three main components of the cell i.e., the anode, the cathode, and the electrolyte. In **Table 12**, the main degradation phenomena occurring in the three components of SOFCs are summarized.

Table 12. Summary of the main degradation phenomena occurring in the three main components of a SOFC.

Fuel electrode	Air electrode	Electrolyte
Coarsening and oxidation of Ni catalyst (10)	Chromium poisoning (11)	Crystal phase change
Crack formation	Crystal phase change	Delamination at the electrode/electrolyte interface
Carbon deposition Sulfur poisoning (12)		

According to recent literature reports, operation as electrolyzer may cause even harsher damages to the SOFC materials (13). To reach a widespread commercialization, properties such as lifetime, cost, and maintenance must be optimized.

Three possible strategies can be investigated to improve the aforementioned properties i.e., (i) development of new high-performance and resilient materials, (ii) optimization of operating conditions, and (iii) operando measuraments for the assessment of the SoH of the cell and detection of degradation phenomena in the early stage.

Operando measurements in SOFCs

Performance losses are a macroscopic effect of degradation phenomena. A precise assessments of performance losses can be done by polarization measurements. However, they are not able to provide any information regarding the single-process and the cause of it. Several spectroscopic and electrochemical techniques are available to monitor the SoH of SOFCs in detail. With former, techniques such as Raman (14; 15), Electron microscopy (16; 17), and X-Ray based (18), such as X-Ray diffraction and X-Ray absorption can provide the perfect picture of what is occurring inside the cell. However, their implementation is hindered by the difficulty to implement the system while the cell is running, and the complexity and cost of the instrument itself. On the other hand, electrochemical characterizations such as Electrochemical Impedance Spectroscopy (EIS) can be applied while the cell is running without any complex setup. EIS is a non-destructive technique able to distinguish polarization losses given by reaction kinetics, mass transport, and ohmic features. In SOFCs, the impedance response is determined by material properties (grain size, porosity, layer thickness, morphology, etc.) and operating conditions (working temperature, current density, fuel composition and flow, air flow and composition). EIS has already proven to be able to detect chromium- (19),and sulfur-induced poisoning phenomena (20), and even degradation of the electrode microstructure (21).

This chapter can be divided into two sections: (i) the identification of polarization losses and establishment of a meaningful electrochemical model, and (ii) validation of the obtained model. In the former, an extended experimental campaign in which EIS spectra were acquired at different operating conditions i.e., working temperature, current density, fuel flow and composition was pursued. In the latter, the electrochemical model obtained in the first phase has been validated by applying an a *priori* known stress agent. Further details will be given in the next sections.

EIS measurement in SOFCs

Usually, EIS responses are approximated by complex non-linear least square (CNLS) fit by using a proper equivalent circuit model (ECM). Common circuital elements are resistors (R), capacitors (C), constant phase elements (Q), inductors (L), Warburg-based diffusion elements (W), or a series/parallel combination of them. However, finding a proper ECM requires *a priori* knowledge of the system under study. Furthermore, processes having relaxation times close each other are often overlapped in the Nyquist plots, and thus are not distinguishable. Therefore, multiple

ECMs, having different physio-chemical meanings, can fit the same ac-dispersion with the same quality. To facilitate the monitoring of the EIS response, as well as the creation of a meaningful electrochemical model, ac-responses can be deconvoluted according to their relaxation time with a technique called distribution of relaxation time (DRT). Since the EIS response is affected by both operating conditions and material properties, the DRT function can provide in detail information about each single physicochemical process. Therefore, by using the DRT output it is possible to build a meaningful ECM.

Distribution of relaxation times

Distribution of relaxation time is a function which is used to transform a frequency dispersion in the τ-domain (22). DRT has already been used for the electrochemical characterization of SOFC, by the pioneristic work of the group of Ivers-Tiffée (23), Li-ion batteries (24), and solar cells (25; 26). In SOFC, the measurements of each peak position and area under different operating condition can provide useful information about the transport, and interfacial properties of the cell itself (23).

The transformation into the τ-domain is defined by **Equation 25**:

$$Z(\omega_i) = R_\infty + R_p \int_0^\infty \frac{\gamma(\tau)}{1+j\omega_i\tau} d\tau \qquad \textbf{Eq. 25}$$

Where Z(ω) is the impedance response, R_∞ is the high-frequency resistance (intercept in the real axis in Nyquist plot), R_P is the polarization resistance, and γ(τ) is the distribution function of relaxation time.

Since γ(τ) is a normalized function (**Equation 26**):

$$\int_0^\infty \gamma(\tau) d\tau = 1 \qquad \textbf{Eq. 26}$$

Unfortunately, **Equation 25** is a Fredholm integral of the first kind and its inversion is an "ill-posed problem" i.e., its solving can lead to many possible solutions. Several routes are available to approximate the distribution function such as: Fourier-transform (27; 28), Tikhonov regularization (29; 30; 31), Maximum entropy (32; 33), and multiple (RQ) fit (34; 28). In the Fourier-transform method, a window function must be applied which can have significant effect

on the shape of the DRT. In the case of Tikhonov regularization and maximum entropy, the adjustment of a "special" parameter is mandatory to avoid under- or overestimation of the impedance spectra. Common ways to display impedance spectra are Nyquist or Bode plot. However, it is impossible to distinguish two individual processes with time constants or frequency very similar.

In **Figure 4-1**, there is an example of how DRT can help to understand the physical processes hiding behind an ac-dispersion. A (R_1C_1)(R_2C_2) circuit with close time constants $\tau_2 = 2\ \tau_1$, is represented as a single arc in the Nyquist plot. However, its DRT deconvolution can highlight two different time constants.

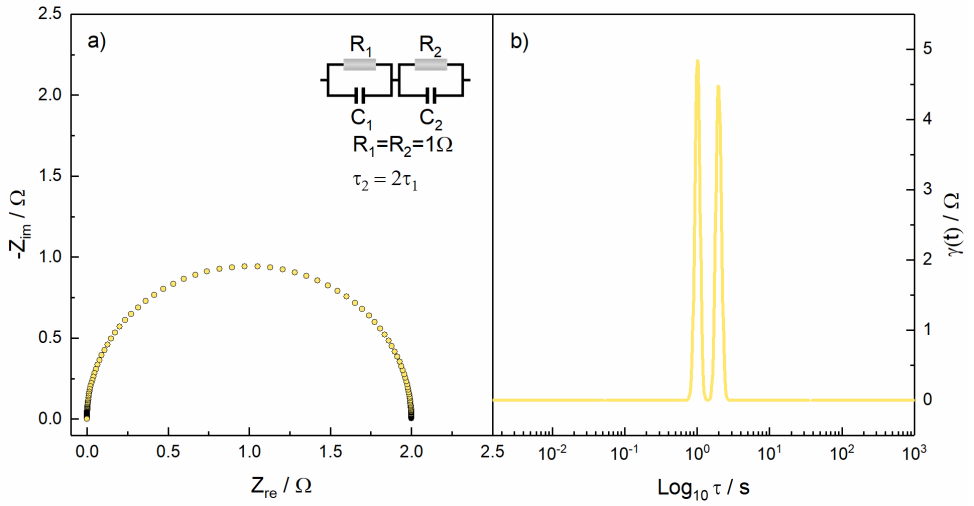

Figure 4-1. a) Nyquist plot of an (R_1C_1)(R_2C_2) circuit with $\tau_2 = 2\tau_1$. b) DRT computation of the ac-dispersion.

In a more complex system, such as a SOFC, DRT deconvolution can reveal several time constants which are greatly affected by the operating conditions. In **Figure 4-2**, there is an example of an impedance response of a SOFC operated at T = 800°C, fuel electrode flowrate = 200 mL min^{-1} H_2, air electrode flowrate = 300 mL min^{-1} air.

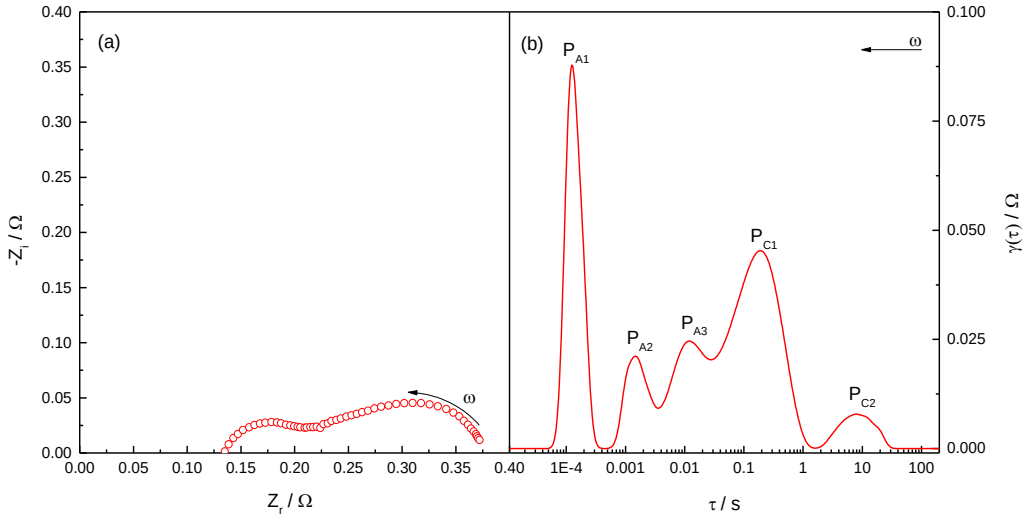

Figure 4-2. a) Impedance response of a SOFC operated at T = 800 °C, FE = 200 mL min^{-1} H_2, AE = 300 mL min^{-1} air. b) DRT deconvolution of the obtained DRT plot with $\lambda = 10^{-3}$.

In this case, the Nyquist plot is characterized by a smaller high-frequency arc and larger arc in the medium-/low-frequency region. However, by DRT (regularization parameter $\lambda = 10^{-3}$) it was possible to highlight at least 5 different time constants.

In this work, an extended experimental campaign in which EIS spectra were acquired at different temperatures (640 < T < 820 °C with 20 °C steps), fuel flow rates(150 ± 50 mL min^{-1}), fuel compositions (100 % H_2, 50 % H_2, and 25 % H_2 balanced with N_2), and current densities (0 < i < 1500 mA cm^{-2}).

4.1 Identification of Polarization Losses in Solid Oxide Fuel Cell by means of Electrochemical Impedance Spectroscopy and Distribution of Relaxation Time

4.1.1 Experimental

Materials

Experiments have been conducted on a commercial planar NiYSZ/8YSZ/GDC-LSCF cell with active surface area of 1 cm^2. In **Figure 4-3**, the cell used for the characterization is presented. The fuel electrode consists of a cermet of NiO (reduced to Ni after the start-up of the cell) with yttria-doped zirconia (8% yttria, 8YSZ). The air electrode is a mixed ionic-electronic conductor belonging to the family of lanthanum strontium cobalt ferrites $La_xSr_{1-x}Co_yFe_{1-y}O_{3-\delta}$ (LSCF). The structural support is given by the NiYSZ cermet fuel electrode (Ø = 28 mm) in which the 8YSZ

electrolyte is sintered. The LSCF air electrode is screen-printed on the fuel electrode-electrolyte assembly. An interlayer of gadolinium-doped ceria (GDC) is interposed between the electrolyte and the air electrode.

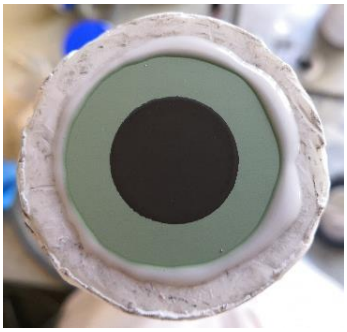

Figure 4-3. SOFC used for the impedance characterization. Large green circle is the fuel electrode support made of NiO/8YSZ (reduced to Ni after the start-up of the cell). The black circle with a surface area of 1 cm^2 is the GDC-LSCF air electrode.

The experimental setup is summarized in **Figure 4-4**.

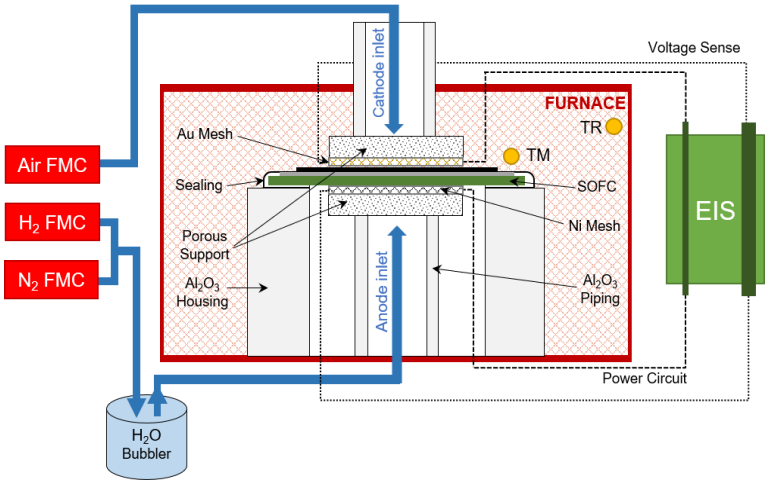

Figure 4-4. Schematic of the experimental setup.

The cell was placed in a corundum housing sealed with Schott G018-311, a glass paste compatible with the thermal expansion of SOFC. The assembly was placed in an electric furnace with a temperature measurement given by two k-thermocouples. The fuel electrode was fed with technical purity H_2 and N_2, with supply control given by Vögtlin Red-y Smart digital flow meter controller. The fuel is humidified by a water bubbler. Ni and Au meshes with 99.999 % purities have been used for the electrical contact in the air and fuel electrode, respectively.

Electrochemical characterization

All the electrochemical characterizations have been performed by using a SP-240 galvanostat/potentiostat from Bio-Logic. Polarization curves were acquired in potentiostatic mode by applying a voltage ramp of -40 mV min^{-1} from OCV to 0.7 V, and a voltage ramp of 40 mV min^{-1} from 0.7 V back to OCV. EIS spectra were acquired in galvanostatic mode (GEIS) in the frequency range 200 kHz < f < 50 mHz. GEIS spectra were acquired at different points in the polarization curve (from OCV up to 1.5 A cm^{-2}) by applying a current sinusoidal perturbation of $\pm$20 mA. Any impedance data elaboration has been performed by using the software Relaxis 3 from rhd instruments. A $\lambda = 10^{-3}$ has been chosen as proper DRT regularization parameter to avoid under- and overestimation of the impedance spectra. The inductive feature present in the high-frequency region has been cut prior the DRT computation. CNLS-fit has been pursued, after finding the proper ECM, until reaching $\chi^2 \approx 10^{-7}$.

Experimental campaign

An extended experimental campaign has been pursued to isolate the single physicochemical processes occurring in the cell. Therefore, the effect of several operating parameters has been studied, by using a centered-body approach i.e., varying systematically, one by one, a few significant user-defined parameters. The parameters in the test matrix are: temperature (660 < T < 820 °C), current density (OCV < i < 1.5 A cm^{-2}), fuel flowrate ($Q_{Fuel} = \pm$ 150 mL min^{-1}), and fuel composition (from pH_2 = 1 to 0.5 and 0.25, balanced with N_2). The air electrode was constantly fed with atmospheric air with pO_2 = 0.21.

The experimental campaign is summarized in **Table 13**.

Table 13. Summary of the extended experimental campaign conditions. On top there are the temperature dependent experiments. On the bottom there are the remaining EIS mapping experiments.

T-dependent experiments					
Temperature /°C	Anode Total Flowrate /mL min^{-1}	Anode Composition H_2:N_2 /%vol, dry basis	Anode humidification /%vol, wet basis	Cathode Total Flowrate /mL min^{-1}	Cathode composition O_2:N_2 /%vol, dry basis
660 – 680 – 700 – 720 – 740 – 760 – 780 – 800 – 820	150	100:0	3%	300	21:79

EIS mapping experiments					
Temperature /°C	Anode Total Flowrate /mL min^{-1}	Anode Composition H_2:N_2 /%vol, dry basis	Anode humidification /%vol, wet basis	Cathode Total Flowrate /mL min^{-1}	Cathode composition O_2:N_2 /%vol, dry basis
800	200 **150** 100	**100:0**	3%	**300**	21:79
	200 **150** 100	50:50			
	200 **150** 100	25:75			
775	200 **150** 100	**100:0**			
	200 **150** 100	50:50			
	200 **150** 100	25:75			
750	200 **150** 100	**100:0**			
	200 **150** 100	50:50			
	200 **150** 100	25:75			

4.1.2 Results and discussion

Preliminary assessment

As mentioned, the DRT function is greatly affected by the regularization parameter λ: too large values of λ will lead to an underestimation of the function with smoothening of the peaks, while a too small λ will lead to an overestimation of the function with the creation of artifact peaks.

An example of how the DRT function shape is affected by the λ values is reported in **Figure 4-5**.

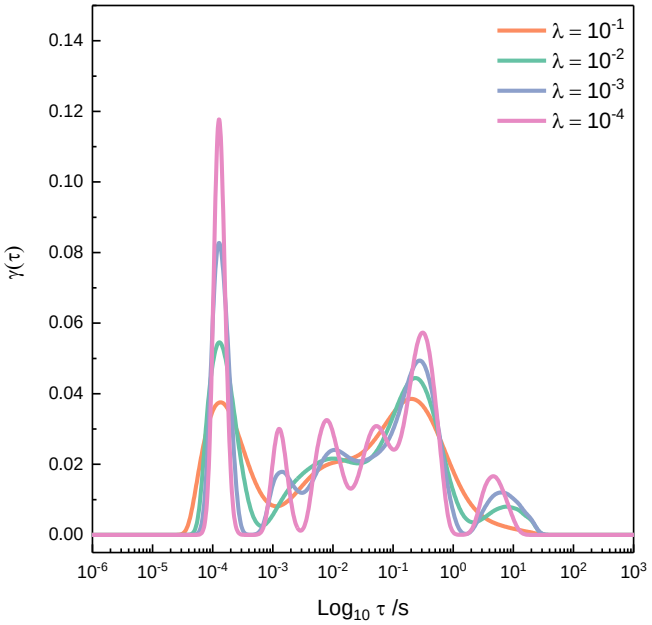

Figure 4-5. Comparison of the shape of the DRT function with different regularization parameters.

At $\lambda = 10^{-1}$, the function is characterized by 4 peaks with two of them being overlapped. On the other hand, at $\lambda = 10^{-4}$ the shape is characterized by 6 sharp peaks. Choosing the proper λ values is crucial for the correct estimation of the polarization losses occurring inside a SOFC. Our strategy to assess the proper λ value was to calculate the DRT function with different λ. Nyquist plots were then reconstructed from the obtained DRT and, at last, residuals from the DRT-reconstructed Nyquist and the experimental Nyquist were calculated. The residuals for $\lambda = 10^{-1}$, 10^{-2}, 10^{-3}, 10^{-4}, as well as the sum square residuals vs. λ are reported in **Figure 4-6**.

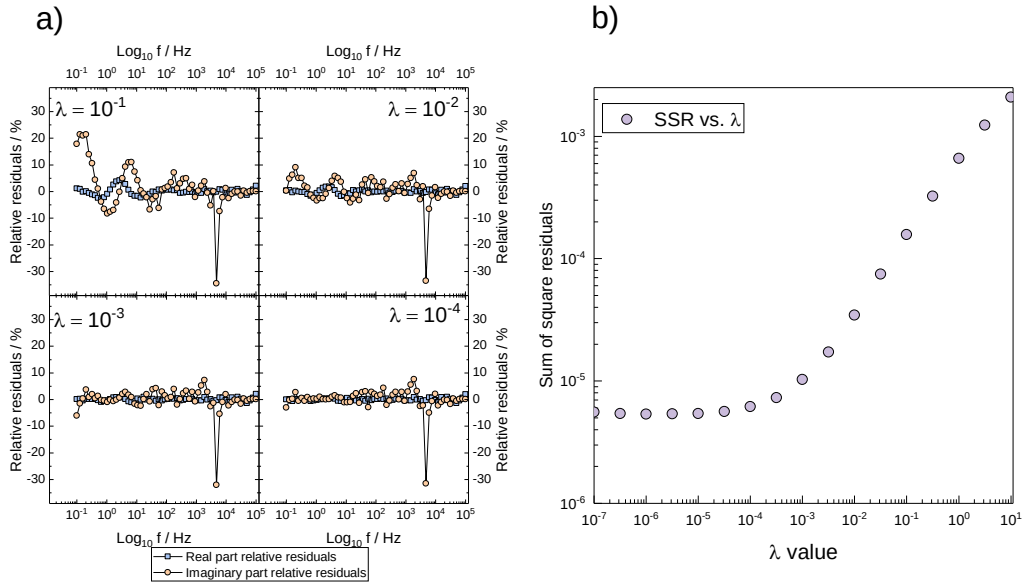

Figure 4-6. a) Residuals calculated from DRT-reconstructed Nyquist vs. experimental Nyquist at different λ values. b) Sum of square residuals at different λ values.

For $\lambda > 10^{-3}$, large residual values on the imaginary part were observed. The relative residuals decrease with the decrease of the adopted λ. No further improvements were detected at $\lambda < 10^{-3}$. Looking at the sum of square residuals vs. λ plot in **Figure 4-6b**, the SSR decreases with the decrease of the regularization parameter reaching an asymptote at $\lambda < 10^{-3}$. For this reason, a $\lambda = 10^{-3}$ was chose for the DRT computation of all EIS responses, since going lower will not improve the SSR and residuals with the risk of creating artifact peaks.

Effect of temperature

In **Figure 4-7**, the EIS responses acquired at different temperatures (FE = 150 mL min^{-1} H_2, AE = 300 mL min^{-1} air) and their DRT are shown.

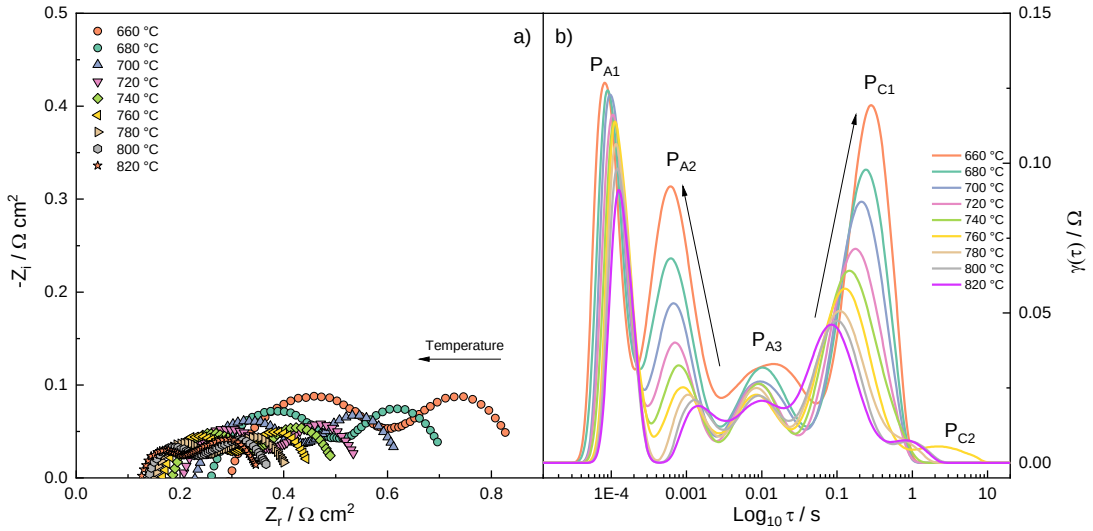

Figure 4-7. a) Nyquist plot acquired in the temperature range 660 < T < 820 °C (20 °C steps). b) DRT of the acquired EIS responses. i = OCV, FE = 150 mL min^{-1} H_2, and AE = 300 mL min^{-1} air.

As expected, the overall impedance decreases with the increase of temperature and the intercept with the real axis becomes smaller. In the DRT plot, all the peaks are affected by the temperature change. However, two peaks, namely P_{A2} and P_{C1}, have a high dependency on the temperature change, while the peaks P_{A1}, P_{A3}, and P_{C2} show a negligible change. This behavior suggests that P_{A2} and P_{C1} are electrochemical reactions which are usually thermally activated (35). Thus, it is reasonable to assume that P_{A2} and P_{C1} are charge-transfer processes while the remaining peaks are associated to transport phenomena.

Effect of current density

The second parameter explored was the current density from OCV < i < 1.5 A cm^{-2}. The EIS responses at different current densities as well as different T and fuel compositions are shown in **Figure 4-8**. Looking at the Nyquist plot in **Figure 4-8a**, as the current density increases the overall impedance decreases, however it is not possible to discern what is occurring inside the cell. In the DRT computation, **Figure 4-8b**, all the peaks intensities decrease with the increase of the current density. Notably, two couples of peaks start merging as the current load increases (P_{A2} with P_{A3} and P_{C1} with P_{C2}). A possible reason to this behavior is that at high current rates, the diffusion is the rate-determining step. In a similar way as it occurs in the polarization curve, in which the high-current end is called "mass-transport region", the reactants are quickly consumed at the electrode interface and the overall rate of the reaction is determined by the supply of the reactants

i.e., diffusion processes. By that, it is reasonable to assume that both consumption and transport phenomena are occurring in the same time scale.

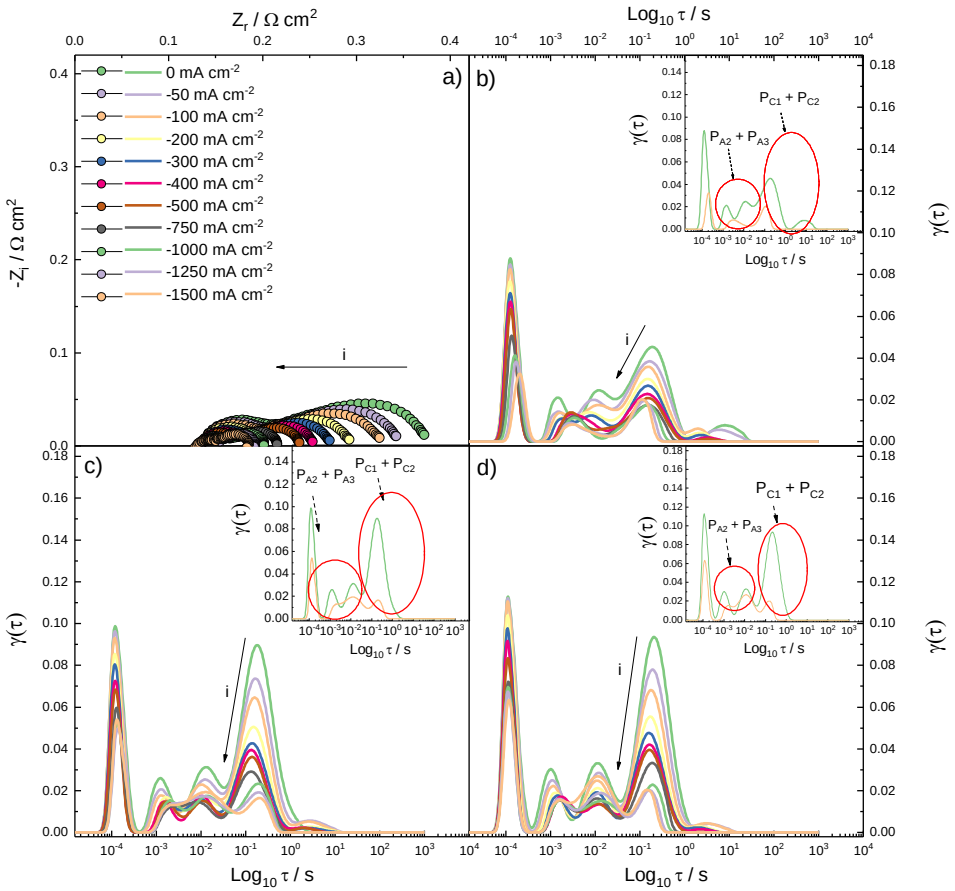

Figure 4-8. a) Nyquist plot acquired at different current densities. Operating conditions T = 800 °C, FE = 200 mL min^{-1} H_2, AE = 300 mL min^{-1}. b) Corresponding DRT plot of a). c) DRT plot at different current densities. Operating conditions T = 775 °C, FE = 200 mL min^{-1} H_2:N_2 25:75, AE = 300 mL min^{-1}. d) DRT plot at different current densities. Operating conditions T = 750 °C, FE = 200 mL min^{-1} H_2:N_2 25:75, AE = 300 mL min^{-1}.

This behavior was also encountered in other experiments at different T and fuel compositions, suggesting that it is strictly connected by the applied current density. Indeed, in the DRT plots in **Figure 4-8c-d** (T = 775 °C, FE = 200 mL min^{-1} H_2:N_2 25:75; T = 750 °C, FE = 200 mL min^{-1} H_2:N_2 25:75), the two couples of peaks overlap in the same way encountered at T = 800 °C, FE = 200 mL min^{-1} H_2.

Effect of fuel electrode feeding: total flow and composition

To understand the impedance response at different fuel electrode feedings, experiments at different fuel compositions from 100 %$_{vol}$ down to 25 %$_{vol}$ (balanced with N_2), different fuel flows Q_{fuel} = 150±50 mL min^{-1}, and different temperatures T = 775±25 °C were carried out. In **Figure 4-9**,

the DRT spectra in which the peaks P_{A2} and P_{A3} start overlapping are reported, according to the operating temperature, fuel flow, and composition. At T = 800 °C, the two peaks start overlapping at a current density i = 400 mA cm^{-2}, with no changes in their intensities. However, with a fuel composition as low as pH_2 = 0.25, P_{A3} slightly shifts to higher relaxation times (lower frequencies). At T = 775 °C, the two peaks start merging at higher current densities, especially at low fuel flow and composition. Indeed, the P_{A2} and P_{A3} start overlapping at the higher current density i = 1000 mA cm^{-2} at T = 775 °C, pH_2 = 0.25, and fuel flow of 150 and 100 mL min^{-1}, compared to the i = 400 mA cm^{-2} seen in the experimental dataset at T = 800 °C.

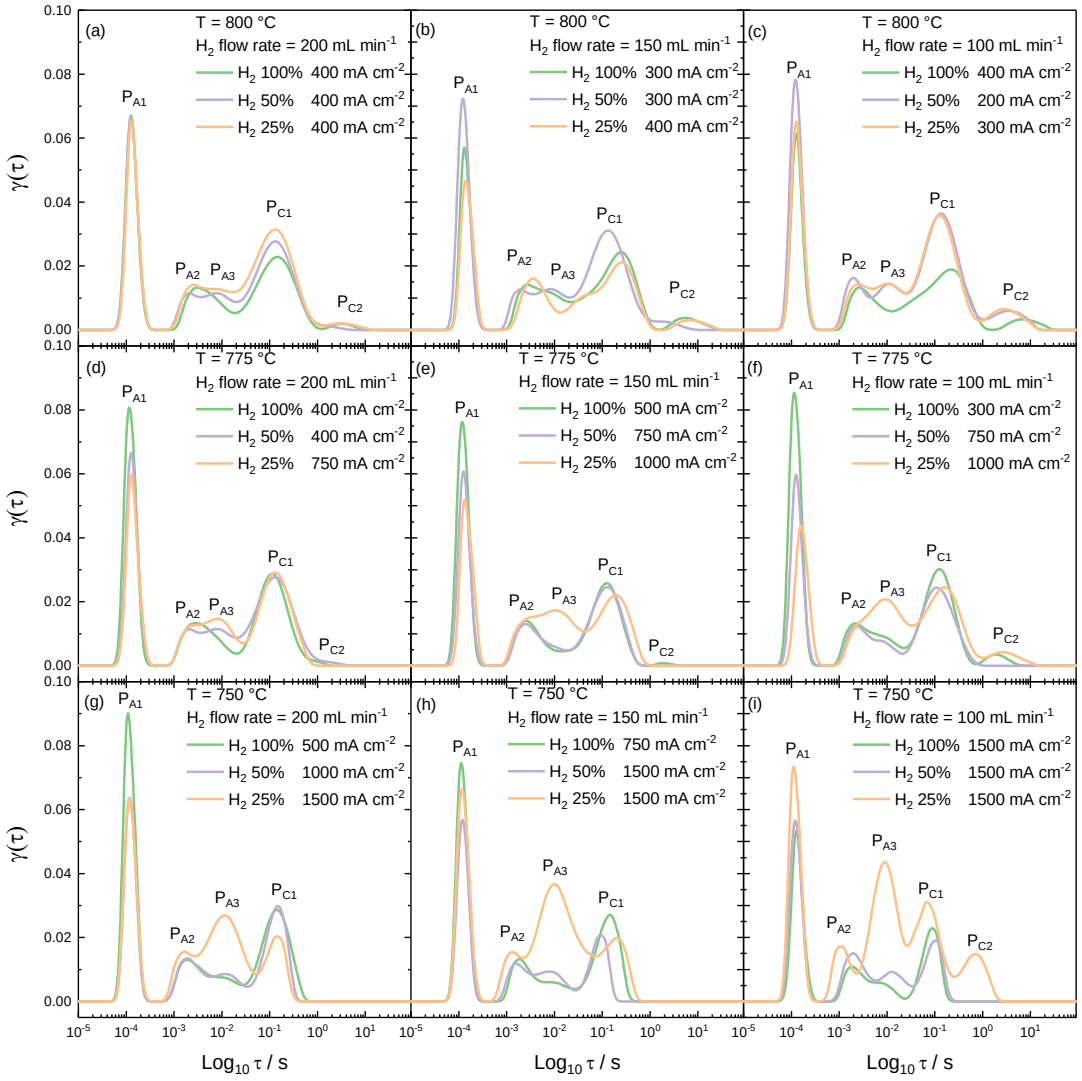

Figure 4-9. DRT spectra in which P_{A2} and P_{A3} start overlapping. a) T = 800 °C, FE = 200 mL min^{-1}. b) T = 800 °C, FE = 150 mL min^{-1}. c) T = 800 °C, FE = 100 mL min^{-1}. d) T = 775 °C, FE = 200 mL min^{-1}. e) T = 775 °C, FE = 150 mL min^{-1}. f) T = 775 °C, FE = 100 mL min^{-1}. g) T = 750 °C, FE = 200 mL min^{-1}. h) T = 750 °C, FE = 150 mL min^{-1}. i) T = 750 °C, FE = 100 mL min^{-1}. The green, purple, and orange line stands for pH_2 = 1, 0.5, and 0.25, respectively. AE = 300 mL min^{-1} air for all the experiments.

A similar behavior was observed also at T = 750 °C in which even at i = 1500 mA cm^{-2} the two peaks did not overlap. Furthermore, the intensity of P_{A3} progressively increases as the fuel flow decreases at pH_2 = 0.25. Since P_{A3} was the most affected peak by the fuel electrode feeding conditions, it was assigned to the fuel transport process in the fuel electrode. Furthermore, as seen in the temperature effect and current density effect sections, P_{A2} is a charge-transfer process strictly connected with P_{A3}. Therefore, the charge-transfer process P_{A2} was assigned to the Hydrogen Oxidation Reaction (HOR) at the triple-phase boundary. On the other hand, the peak P_{A1} did not show any dependence to the fuel electrode feeding. A similar behavior was observed in (36), in which a high-frequency polarization was independent by the pH_2 and pH_2O in the fuel. For this reason, P_{A1} was assigned as the oxygen transport in the fuel electrode. The two remaining peaks P_{C1} and P_{C2} were assigned to the Oxygen Reduction Reaction (ORR) and to the Oxygen surface exchange and diffusion in the air electrode, respectively.

Equivalent circuit model analysis

The equivalent circuit model is created according to the experimental results obtained with the previous DRT analysis. The proposed ECM is composed by 7 elements and shown in **Figure 4-10**. The charge-transfer processes (P_{A2}-HOR and P_{C1}-ORR) have been modelled by two (RQ) parallel ($R_{A2}Q_{A2}$) and ($R_{C1}Q_{C1}$). A finite-length Warburg was used to model the gas-diffusion in the fuel electrode (P_{A3}) (35), while a Gerischer element was used for modelling the Oxygen surface exchange and diffusion in the air electrode (P_{C2}) (37; 38). An (RQ) has been used for modelling the peak P_{A1} assigned to the oxygen transport in the fuel electrode. At last, a pure resistive element R_0 has been used for the electrolyte resistance in series with an inductor needed to model the high-frequency inductive feature due to electrical wiring and cell geometry.

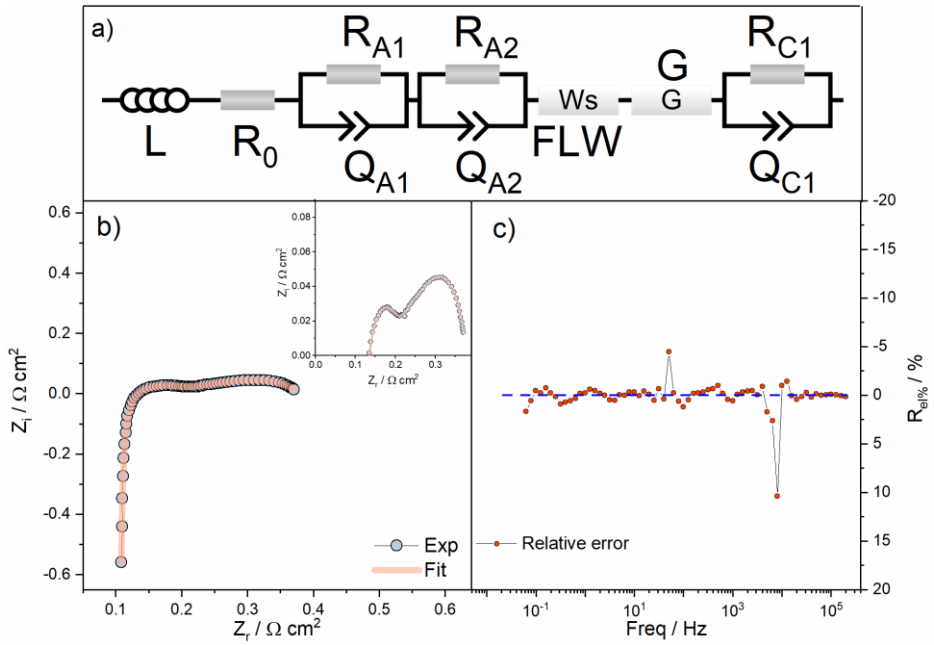

Figure 4-10. a) Proposed ECM $LR_0(R_{A1}Q_{A1})(R_{A2}Q_{A2})W_{FLW}G(R_{C1}Q_{C1})$. b) Experimental and fit Nyquist plot at T = 800 °C, FE = 200 mL min^{-1} H_2, AE = 300 mL min^{-1} air. c) Residual analysis.

Thus, the experimental data have been fitted with the ECM $LR_0(R_{A1}Q_{A1})(R_{A2}Q_{A2})W_{FLW}G(R_{C1}Q_{C1})$, in Boukamp's notation (39), by using Relaxis3 software from rhd instruments. The fit procedure was done until reaching a $\chi^2 = 10^{-6}$. The values of the resistance parameters vs. the fuel flow and composition are shown in **Figure 4-11**. As expected, since the specimen is an anode-supported cell, which implies a higher thickness of the fuel electrode, the resistance parameters associated to the fuel electrode are higher than the one for the air electrode. The resistances R_0 and R_{C1} have a constant behavior with small fluctuation as the fuel flow and composition change. The resistance R_{A1} (oxygen transport in the fuel electrode) has a small decrease as the pH_2 increases. The resistance R_{A2} (associated to the HOR) drastically decreases with the increase of pH_2, suggesting that, as expected, the HOR is affected by the supply of the fuel.

In **Figure 4-12**, the ln(1/R) vs. 1000/T plot is reported. The fitted resistance parameters R_{A1}, R_{A2}, and R_{C1} have a linear relationship with the operating temperature and have been fitted with an Arrhenius relation. An activation energy E_a = 1.36 eV, and E_a = 1.41 eV have been calculated for the oxygen transport in the fuel electrode and the HOR, respectively. These values are in good agreement with the literature reports (37; 38; 35). Only the E_a related to the ORR has a slightly lower value (E_a = 0.80 eV) compared to the literature reports, probably due to different air electrode chemistry and feeding conditions.

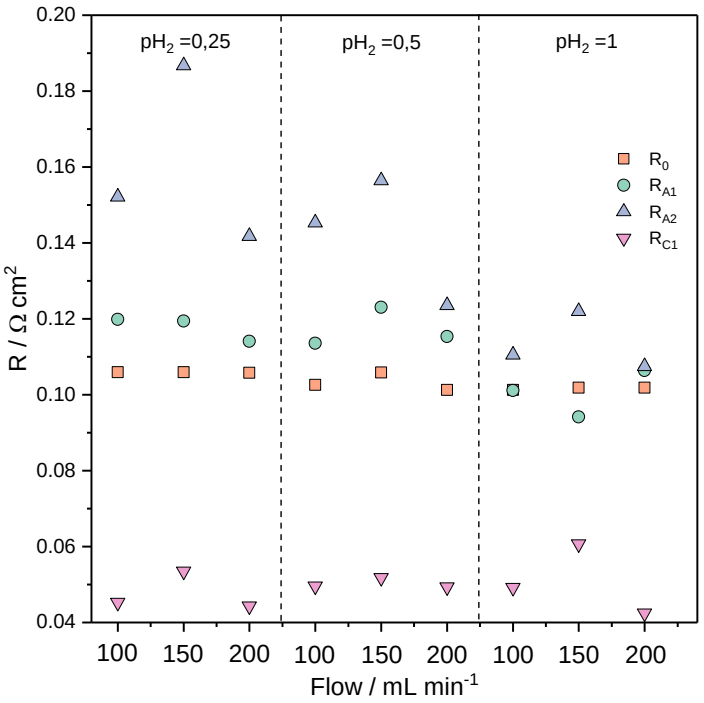

Figure 4-11. Values of the resistance parameters R_0, R_{A1}, R_{A2}, and R_{C1} vs. the fuel flow and composition.

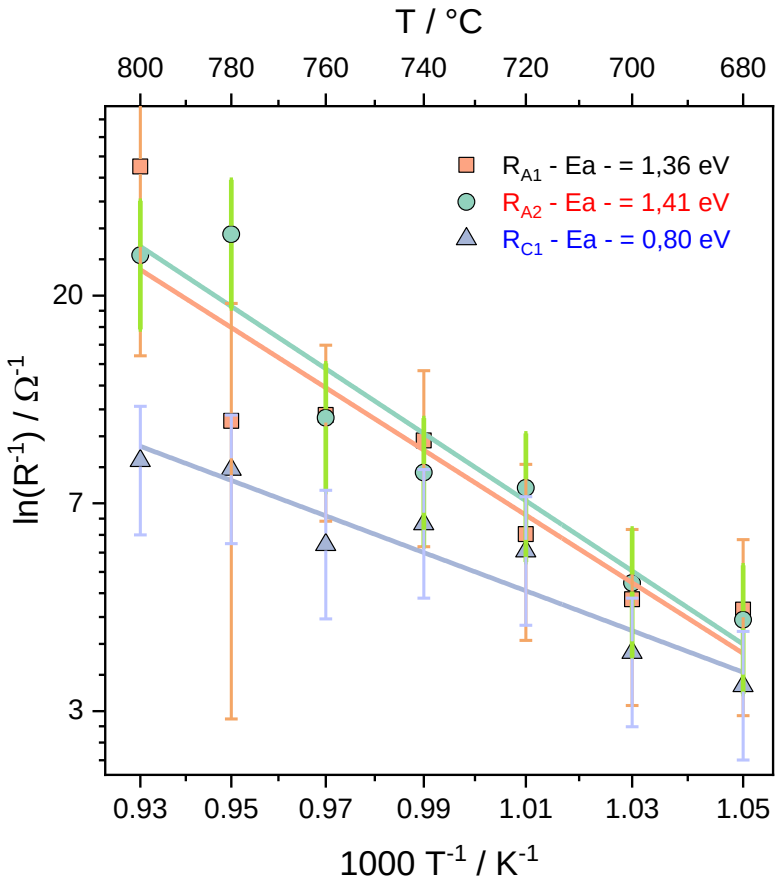

Figure 4-12. $\ln(R^{-1})$ vs. 1000/T plot with linear fir of R_{A1}, R_{A2}, and R_{C1}

4.1.3 Conclusions

This section presents a methodology to assess the different losses occurring in a Solid Oxide Cell operated in fuel cell mode by varying the operating temperature, the current density, and both fuel composition and flow. The electrochemical characterization relies on electrochemical impedance spectroscopy and its elaboration done by distribution of relaxation times, and complex nonlinear least square fit. Five different time constants have been exploited by this procedure which, thanks to the extended experimental campaign, allowed the elaboration of the equivalent circuit model $LR_0(R_{A1}Q_{A1})(R_{A2}Q_{A2})W_{FLW}G(R_{C1}Q_{C1})$. Two time constants, P_{A2} and P_{C1}, have been assigned to the charge-transfer processes HOR and ORR, respectively, and fitted with two (RQ) parallels. The gas-diffusion in the fuel electrode has been modeled by using a finite-length Warburg element, while a Gerischer element has been used to model the Oxygen surface exchange and diffusion in the air electrode. The impedance response has been analyzed at different current densities, which highlights that under high polarization, some time constants are not anymore resolved and overlap, due to the limitation of the supply of the reactants. To provide a proper nondestructive, operando diagnosis tool, the electrochemical model has been validated by applying *a priori* known stress agent. The methodology, as well as the results of the validation test will be discussed in **Section 4.2**.

4.2 Electrochemical Impedance Spectroscopy as Early Diagnosis Tool for Solid Oxide Fuel Cells

4.2.1 Experimental

Materials

The experiments were carried out on a planar two-electrode cell, with a surface area of 1 cm^2. The cell composition and geometric features are the same as in **Section 4.1**. The cell is sealed in a corundum housing by using Schott G018-311 paste. The experimental set-up is the same used in **Section 4.1**. Electrical measurements have been performed by using a Keysight DAQ system (accuracy 0.0004%). The operation of the cell is managed by using a Lab-view software developed in-house. All the impedance measurements have been performed by using a galvanostat/potentiostat Bio-Logic Sp-240.

Methods

The test conditions are summarized in **Table 14**. The current and voltage of the cell are constantly measured during all the tests.

Table 14. Summary of the test protocol adopted. Legend: X = volume composition [%$_{vol\ dry\ basis}$], Q = volume flow rate [mL min^{-1}], T = temperature [K].

TEST	Fuel Electrode		Air Electrode			Operating Settings	Duration
ID	X	Q	x	Q	T	Load	hours
Start-up	100% N_2	50	21% O_2 + 79% N_2	300	RT[1] →1073	OC	16 h
Reduction	100% N_2 →100% H_2	150	21% O_2 + 79% N_2	300	1073	OC	1.5 h
Stabilization	100% H_2	150	21% O_2 + 79% N_2	300	1073	Constant j=250 mA/cm^2	100 h
Begin Ref	25% H_2 + 75% N_2	200	21% O_2 + 79% N_2	300	1048	i-V: OC→ 0.7 V EIS: 0, 100, 250, 500, 750 mA/cm^2	30 min 1 h
Stress (repeated)	25% H_2 + 75% N_2	200	21% O_2 + 79% N_2	300	1048	Constant j=1500 mA/cm^2 EIS: 0, 100, 250, 500 mA/cm^2	4 h 30 min
End Point	25% H_2 + 75% N_2	200	21% O_2 + 79% N_2	300	1048	i-V: OC→ 0.7 V EIS: 0, 100, 250, 500, 750 mA/cm^2	30 min 1 h
Shut down	5% H_2 + 95% N_2	100	100% N_2	100	1073→ RT	OC	c.a. 12 h

The test phases are described below:

1. Start-up: The sealing paste is cured according to the producer instructions with a temperature ramp of 1 K min^{-1}. During this phase, the fuel electrode is fed with nitrogen and the air electrode with air. Once 1073 K are reached, the NiO catalyst reduction begins.
2. Reduction: The nitrogen on the fuel electrode is gradually substituted with H_2 reduce Ni^{2+} to Ni.
3. Stabilization: The cell is kept at 1073 K for at least 100 h. A mild current load of 250 mA cm^{-2} is set.
4. Begin reference: The temperature is set at T = 775 K. The fuel electrode is fed with a mixture of H2 (50 mL min^{-1}) and N2 (150 mL min^{-1}). The air electrode is fed with air (300 mL min^{-1}). Polarization curve and impedance measurement are used as reference characterization before the stress test. The i-V curve is acquired in potentiostatic mode, varying the potential from Open Circuit (OC) to 0.7 V with a rate of -40 mV min-1 and

back with a rate of 40 mV min-1. Impedance responses are acquired in galvanostatic mode within the frequency range 100 mHz < f < 100 kHz, with 10 points per decade logarithmically spaced. A perturbation of ± 20 mA over the current densities of 0, 100, 250, 500, and 750 mA cm^{-2}.

5. Stress test: The cell temperature, as well as the air/fuel compositions and flows are the same of the reference characterization. The cell is continuously operated at a current density of i = 1.5 A cm^{-2} for time intervals of 4 hours. After each interval, the cell is brought back to OC and impedance measurement are acquired. The GEIS settings are the same of the reference characterization. The impedance responses have been acquired over the current densities 0, 250, and 500 mA cm^{-2}. This process is repeated until the cell reaches the voltage value E = 0.6 V.
6. End point: The final characterization is performed in the same condition and with the same settings as in the reference characterization.
7. Shut down: The cell is disconnected from the electric load. Eventually, the cell is cooled down to room temperature with a decreasing rate of -1 K min^{-1}, fuel electrode is fed with H_2:N_2 5:95 (100 mL min^{-1}), and air electrode is fed with N_2 (100 mL min^{-1}).

Cell morphological and structural characterization

After the test, the exhausted SOFC specimen is extracted from the experimental setup for the morphological and structural characterization. Both cell face and section are morphologically characterized by using a FE-SEM Zeiss Sigma Series 300. Raman spectra were acquired by using a Horiba iH320 spectrometer with a 532 nm laser source. A new cell from the manufacturer and a new cell after the reduction of NiO have been analyzed as reference materials.

Impedance data elaboration

The DRT has been done by using Tikhonov regularization with a regularization parameter λ = 10^{-3}. The inductive feature in the high-frequency region has been cut prior DRT calculation. All the impedance data processing has been done by using Relaxis3 software for rhd instruments.

4.2.2 Results and discussion

Stress test

The stress test lasted until the cell reached the voltage threshold of E = 0.6 V, which occurred after 32 hours (after the 8th interval of 4 h). In **Figure 4-13**, the polarization curve before and after the stress test are reported. There is small gap between the two polarization curves, which increases in the high current density region of the curve. However, as discussed in the introduction, it is not possible to discern what occurred inside the cell.

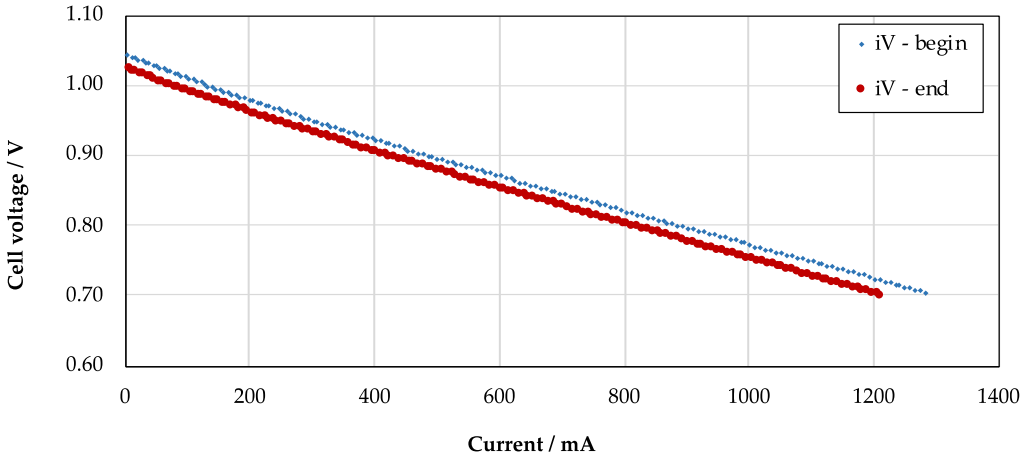

Figure 4-13. Polarization curves before and after the stress test. Blue = i-V curve prior the stress test. Red = i-V curve after the stress test.

In **Figure 4-14**, the E vs. time curve of the stress test is reported.

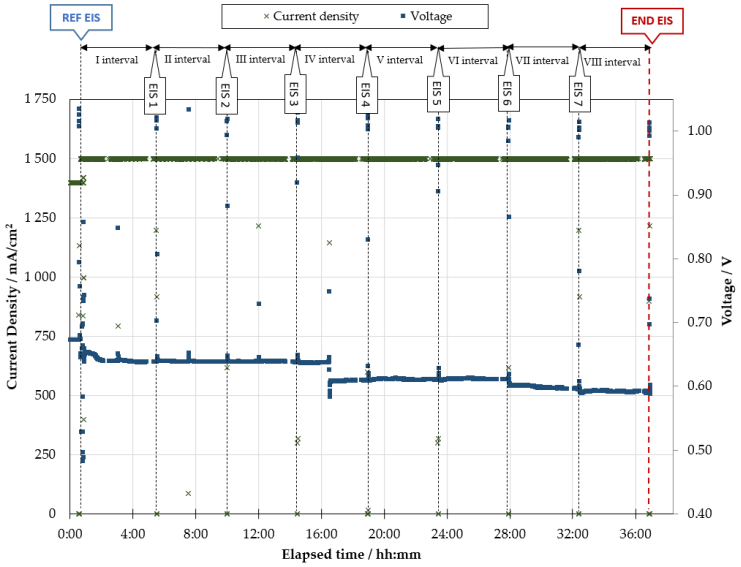

Figure 4-14. E vs. time curve during the stress test.

In the first three 4h-intervals, the cell was stable with an average potential value of E = 0.643 V. During the IV interval, a sudden voltage drop of -30 mV occurred. The cell remained stable during the V and VI interval, then the voltage gradually decreased during the VII and VIII intervals, eventually reaching the voltage threshold of 0.60 V.

Diagnosis investigation

Figure 4-15 reports an example of the impedance responses acquired at three checkpoints during the stress test.

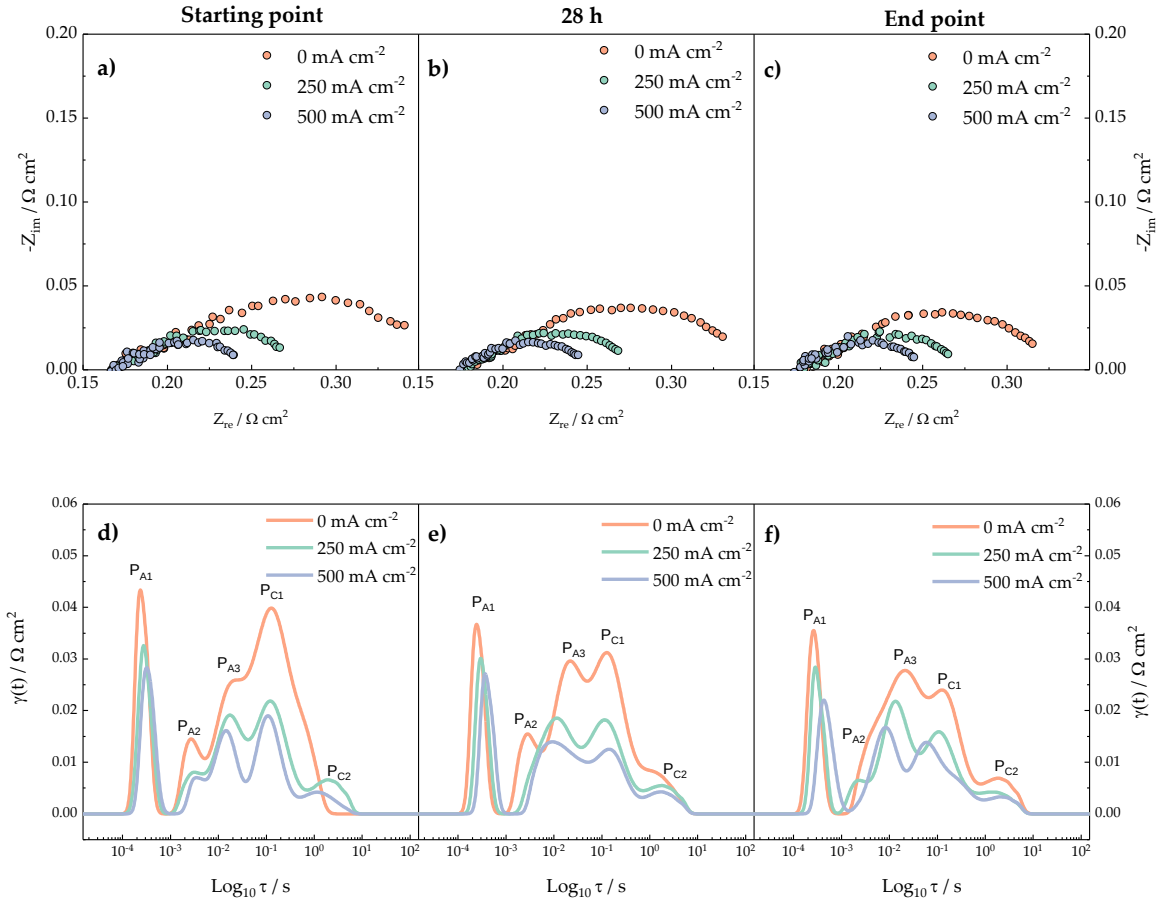

Figure 4-15. Nyquist plots acquired a) before the stress test, b) during the stress test at 28 h, and c) after the stress test. DRT plots acquired d) before the stress test, e) during the stress test at 28 h, and f) after the stress test. Orange = 0 mA cm^{-2}. Green = 250 mA cm^{-2}. Blue = 500 mA cm^{-2}.

Looking at the Nyquist plots, as the applied current density increases the shape is preserved and the overall impedance decreases. Interestingly, as the stress test proceeds, the overall impedance becomes slightly smaller. In the DRT plots, as the current density increases the intensities of all peaks decreases. Furthermore, while the stress test goes forward, some peaks areas and relaxation

times change, especially two anode-related peaks P_{A2} and P_{A3} (HOR and gas diffusion in the fuel electrode). To have a better understanding, the DRT plots have been fitted with a Gaussian function (**Equation 27**) to monitor the changes in the peaks area (impedance related to the peak) and centre point (relaxation time).

$$y = y_0 \frac{A}{w\sqrt{\frac{\pi}{2}}} e^{\frac{-2(x-x_c)^2}{w^2}} \qquad \textbf{Eq. 27}$$

Where A, w, y_0 and x_c stand for the area, the width, the minimum height, and the centre point of each peak, respectively. The DRT plots have been fitted until reaching a $\chi^2 = 10^{-9}$. An example of a fitted DRT plot is given in **Figure 4-16**.

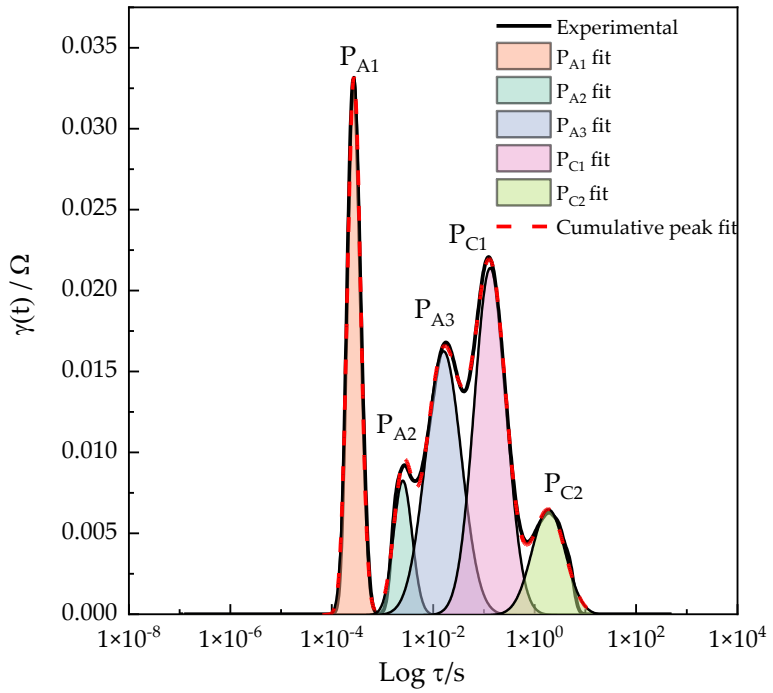

Figure 4-16. Example of a fitted DRT plot with a Gaussian function.

Figure 4-17a reports the relaxation times and area of the DRT peaks acquired at 250 mA cm^{-2}. In all the peaks, a small fluctuation of the relaxation time was evidenced. This behavior can be due to the data acquisition as well as the elaboration within the experimental error. In a macroscopic view, two fuel electrode-related peaks, P_{A2} and P_{A3}, had a sudden change in both area and relaxation time at t ≈ 16 h. This feature agrees with the sudden voltage drop observed in the E vs. t plot in **Figure 4-14**, in which a voltage drop of -30 mV occurred in the IV interval. P_{A2} area and

relaxation time increased, suggesting that somehow the HOR kinetics started worsening, giving a higher contribution in the overall impedance. In the case of P_{A3}, the area increased until 16 h, for then decreasing as the test proceeded. P_{A1} had only a very small decrease in area after few hours of the experiment. Concerning the air electrode peaks, P_{C2} (Oxygen surface exchange and diffusion) was practically constant along the experiment, while P_{C1} had a sudden decrease in the area at 16 h, for then going back to its original values. A similar behavior was also observed for the measurements acquired at 500 mA cm^{-2} (**Figure 4-17b**). However, the changes in peaks areas and relaxation times are less appreciable since the overall impedance is decreased due to the increased current density. The peak P_{A1} had a similar behavior as in **Figure 4-17a**, with a small change after few hours the experiment started. In the case of P_{A2} and P_{A3}, their relaxation time was almost constant during the stress test, while their area was subjected to changes. In the case of the air electrode peaks, P_{C2} was practically constant while P_{C1} had small fluctuation during the test. This behavior can be explained by the HOR and ORR interrelation.

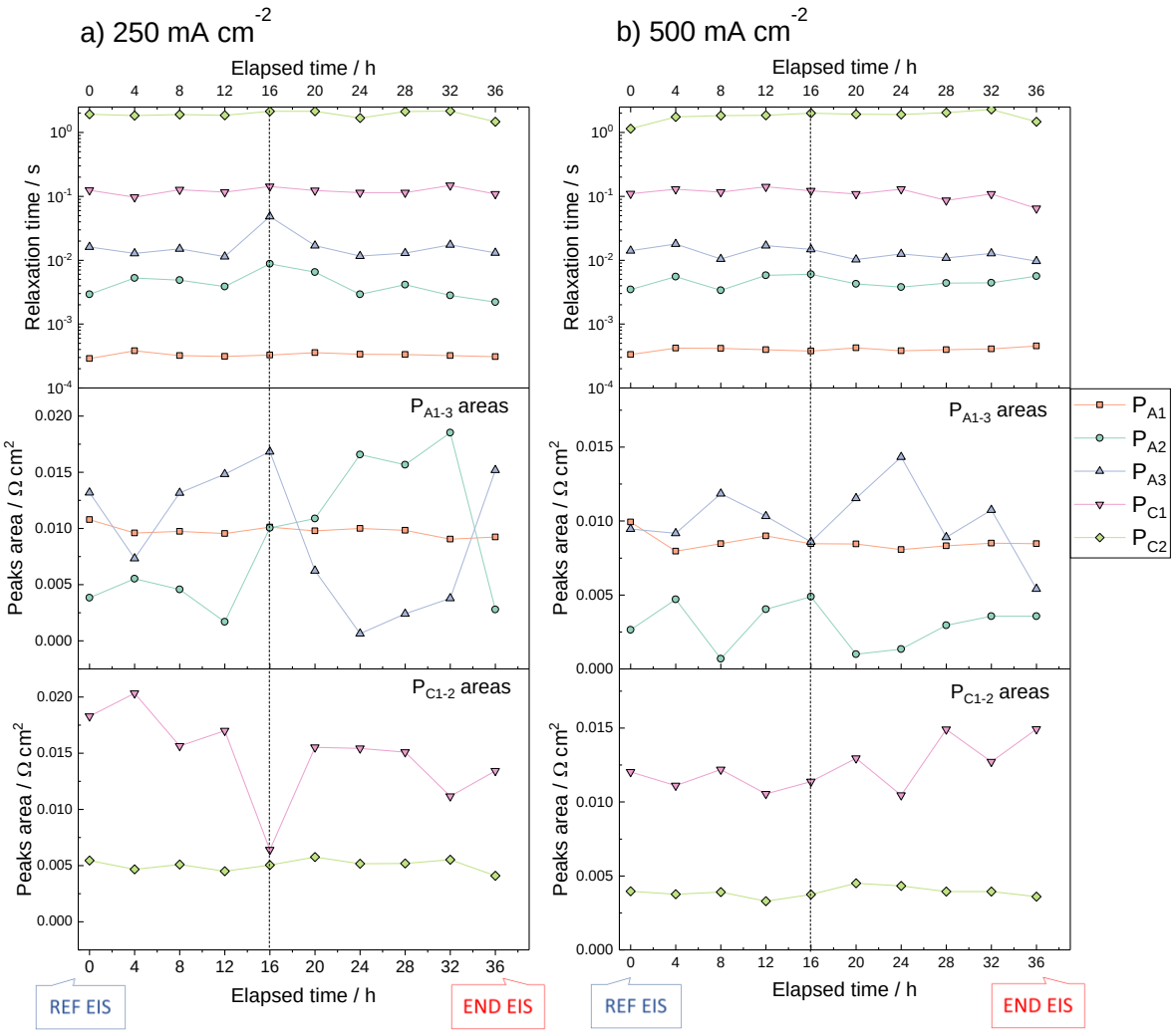

Figure 4-17. Relaxation times and areas of the DRT peaks vs. elapsed time of the stress test at a) 250 mA cm^{-2} and b) 500 mA cm^{-2}.

Diagnosis validation

The validation of the diagnostic tool was achieved by the *post-mortem* characterization of the exhausted SOFC specimen. The cell who underwent the stress test was extracted from the testing apparatus and characterized by FE-SEM and Raman spectroscopy. In **Figure 4-18**, the micrographs of both section and fuel electrode face of the exhausted specimen are reported. A fresh-reduced cell was also characterized for comparison. The section images are characterized by three different layers which are, from the left, the fuel electrode, the electrolyte, and the air electrode. The fuel electrode faces are characterized by two types of particles which, by elemental mapping, have been recognized as the Ni catalyst and the 8YSZ electrolyte. In both section and face micrographs there are no signs of delamination at the electrode-electrolyte interface, nor noticeable signs of the Ni catalyst particle coarsening. However, by calculating the distribution

of the Ni catalyst particle size (ImageJ has been used for the measurement), a small variation was detected (**Figure 4-19**).

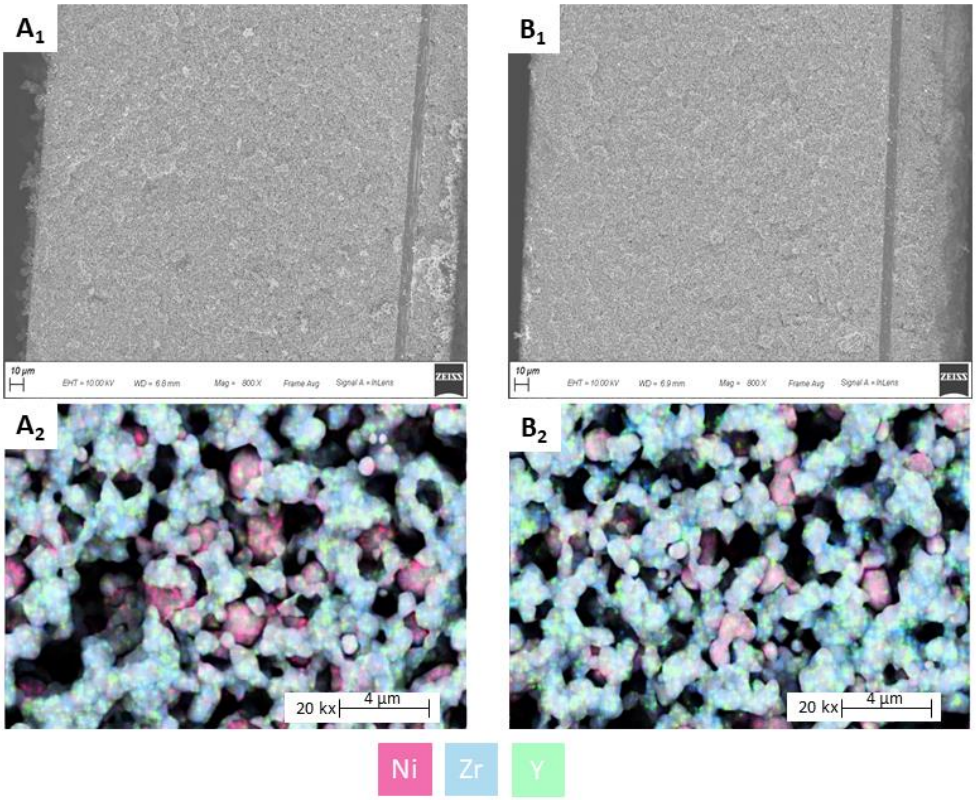

Figure 4-18. FE-SEM micrographs of both section and fuel electrode face of fresh-reduced cell (A_1 & A_2) and exhausted specimen (B_1 & B_2).

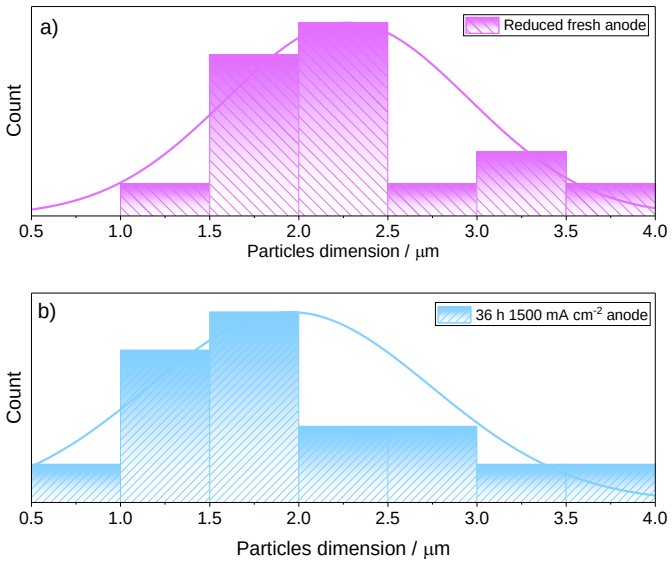

Figure 4-19. Distribution of the Ni catalyst particle size of a) fresh-reduced cell and b) exhausted specimen.

To have a better insight, the microstructure of the fuel electrode was characterized by Raman spectroscopy (**Figure 4-20**). The fresh cell presented all the characteristic peaks of YSZ and NiO. Indeed, the signals at 157, 271, 33, 474, and 650 cm^{-1} (labelled as Δ) can be assigned to the tetragonal ZrO_2 (40). At a Raman shift higher than 700 cm^{-1} there are four peaks which can be assigned to NiO. Specifically, the signals at 730, 906, 1090, and at 1500 cm^{-1} can be assigned to the two-phonon 2nd order transverse optical mode (Ni_{2P}), the two-phonon transverse optical mode + longitudinal mode (Ni_{2P}), the two-phonon 2nd order longitudinal optical mode, and two-magnon mode, respectively (41; 42). No signals of the one-phonon modes were observed, probably because were overlapped bby the scattering of YSZ. During the start-up of the cell, the NiO catalyst is reduced to Ni. Indeed, all the peaks related to NiO scattering are no more visible, suggesting a complete reduction of NiO to Ni. To study the microstructure of exhausted specimen, Raman spectra were acquired both at the centre and on the side of the fuel electrode. The signals related to tetragonal ZrO_2 are still visible. However, two peaks which were at 474 cm^{-1} and 650 cm^{-1}, shifted to 478 cm^{-1} and 640 cm^{-1}, respectively. A new set of signals appeared from 190 up to 730 cm^{-1}. Specifically, the peaks at 190, 380, 570, and 730 cm^{-1} were assigned to the zone-boundary phonon mode, one-phonon transverse optical mode, one-phonon longitudinal mode, and two-phonon 2nd order transverse optical mode of NiO. The intensity of the one-phonon mode is higher compared to the fresh cell because of the defect-rich surface of the catalyst particle, which is reasonable after the stress test (41). On the other hand, the two-phonon modes of NiO (>700 cm^{-1}) could be weak due to two factors, i.e.: (i) the surface layer is amorphous, (ii) there are adsorbate species such as water and oxygen on the surface of the particles (42). At last, the absence of the two-magnon peak at 1500 cm^{-1} can be due to the laser-induced heating above the Néel temperature, and thus destruction of magnetic ordering (42).

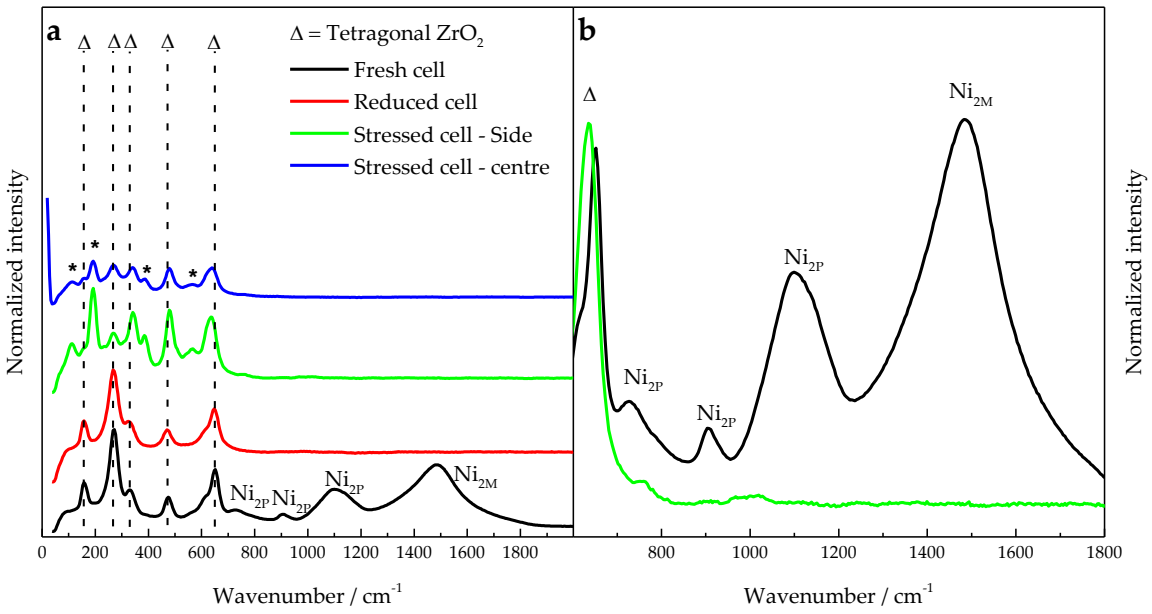

Figure 4-20. a) Raman spectra of stressed cell at both centre and side. The spectra of a fresh cell and fresh reduced cell have been included for comparison. b) Comparison between fresh and stressed cell from 600 up to 1800 cm^{-1}.

4.2.3 Conclusions

In this methodology, *a priori* known stress agent was applied, along with a constant monitoring of the impedance response of the SOFC specimen. The experiment was stopped after 36 h because the cell reached the voltage threshold of E = 0.6 V. The comprehensive analysis of the evolution of DRT peaks (both centre and area) confirmed the effect of the stress test. Furthermore, two peaks were the most affected by the stress test i.e., PA_2 and PA3, HOR and gas diffusion in the fuel electrode, respectively. The post-mortem morphological characterization did not evidence any sign of delamination at the electrode/electrolyte interface, nor catalyst particle coarsening. However, the microstructural analysis done by Raman spectroscopy confirmed the presence of an amorphous layer of NiO on the surface of the Ni catalyst. Thanks to the electrochemical model, as well as the non-destructive impedance analysis, it was possible to detect a degradation phenomenon in the early stage, right before the cell was irreversibly damaged.

References

1. *Efficient hydrogen production for industry and electricity storage via high-temperature electrolysis.* **Oliver Posdziech, Konstantin Schwarze, Jörg Brabandt.** 35, s.l. : International Journal of Hydrogen Energy, 2019, Vol. 44, p. 19089-19101.

2. *Application of solid oxide fuel cell technology for power generation—A review.* **Arnab Choudhury, H. Chandra, A. Arora.** s.l. : Renewable and Sustainable Energy Reviews, 2013, Vol. 20, p. 430-442.

3. **Ali Keçebaş, Muhammet Kayfeci, Mutlucan Bayat.** Chapter 9 - Electrochemical hydrogen generation. *Solar Hydrogen Production: Processes, Systems and Technologies.* s.l. : Academic Press, 2019.

4. *Multiscale Modeling for Reversible Solid Oxide Cell Operation.* **Fiammetta Rita Bianchi, Arianna Baldinelli, Linda Barelli, Giovanni Cinti, Emilio Audasso, Barbara Bosio.** s.l. : Energies, 2020, Vol. 13.

5. *Bypassing renewable variability with a reversible solid oxide cell plant.* **Matthias Frank, Robert Deja, Roland Peters, Ludger Blum, Detlef Stolten.** s.l. : Applied Energy, 2018, Vol. 217, p. 101-112.

6. *Long-term tests of a Jülich planar short stack with reversible solid oxide cells in both fuel cell and electrolysis modes.* **Van Nhu Nguyen, Qingping Fang, Ute Packbier, Ludger Blum.** 11, s.l. : International Journlao f Hydrogen Energy, 2013, Vol. 38, p. 4281-4290.

7. *SOFC Durability against Standby and Shutdown Cycling.* **M. Hanasaki, C. Uryu, T. Daio, T. Kawabata, Y. Tachikawa, S. M. Lyth, Y. Shiratori, S. Taniguchi, K. Sasaki.** 9, s.l. : Journal of The Electrochemical Society, 2014, Vol. 161, p. F850-F860.

8. **Samuel J.Cooper, Nigel P.Brandon.** Chapter 1 - An Introduction to Solid Oxide Fuel Cell Materials, Technology and Applications. *Solid Oxide Fuel Cell Lifetime and Reliability.* s.l. : Academic Press, 2017, p. 1-18.

9. *Transient operation of a solid oxide electrolysis cell.* **Floriane Petipas, Qingxi Fu, Annabelle Brisse, Chakib Bouallou.** 7, s.l. : Internation Journal of Hydrogen Energy, 2013, Vol. 38, p. 2957-2964.

10. *Oxidation stages of Ni electrodes in solid oxide fuel cell environments.* **Farid El Gabaly, Kevin F. McCarty, Hendrik Bluhm, Anthony H. McDaniel.** s.l. : Physical Chemistry Chemical Physics, 2013, Vol. 15, p. 8334-8341.

11. *Effect of cathode and electrolyte transport properties on chromium poisoning in solid oxide fuel cells.* **Fergus, Jeffrey W.** 16, s.l. : International Journal of Hydrogen Energy, 2007, Vol. 32, p. 3664-3671.

12. *H2S Poisoning of Solid Oxide Fuel Cells.* **K. Sasaki, K. Susuki, A. Iyoshi, M. Uchimura, N. Imamura, H. Kusaba, Y. Teraoka, H. Fuchino, K. Tsujimoto, Y. Uchida.** s.l. : Journal of The Electrochemical Society, 2006, Vol. 153, p. A2023.

13. *Transient operation of a solid oxide electrolysis cell.* **Floriane Petipas, Qingxi Fu, Annabelle Brisse, Chakib Bouallou.** 7, s.l. : Internation Journal of Hydrogen Energy, 2013, Vol. 38, p. 2957-2964.

14. *High-temperature surface enhanced Raman spectroscopy for in situ study of solid oxide fuel cell materials.* **Xiaxi Li, Jung-Pil Lee, Kevin S. Blinn, Dongchang Chen, Seungmin Yoo, Bin Kang, Lawrence A. Bottomley, Mostafa A. El-Sayed, Soojin Park, Meilin Liu.** 1, s.l. : Energy & Enrivonmental Science, 2014, Vol. 7, p. 306-310.

15. *In Situ and Surface-Enhanced Raman Spectroscopy Study of Electrode Materials in Solid Oxide Fuel Cells.* **Xiaxi Li, Kevin Blinn, Dongchang Chen, Meilin Liu.** s.l. : Electrochemical Energy Reviews, 2018, Vol. 1, p. 433-459.

16. *In Situ Transmission Electron Microscopy on Energy-Related Catalysis.* **Sooyeon Hwang, Xiaobo Chen, Guangwen Zhou, Dong Su.** 11, s.l. : Advanced Energy Materials, 2019, Vol. 10, p. 1902105.

17. *Atomic Resolution Imaging of Nanoscale Chemical Expansion in PrxCe1−xO2−δ during In Situ Heating.* **Jessica G. Swallow, Ja Kyung Lee, Thomas Defferriere, Gareth M. Hughes, Shilpa N. Raja, Harry L. Tuller, Jamie H. Warner, Krystyn J. Van Vliet.** 2, s.l. : ACS Nano, 2018, Vol. 12, p. 1359-1372.

18. *n situ and operando characterisation techniques for solid oxide electrochemical cells: recent advances.* **Alexander Stangl, David Muñoz-Rojas, Mónica Burriel.** 1, s.l. : Journal of Physics Energy, 2020, Vol. 3, p. 012001.

19. *Degradation of anode supported cell (ASC) performance by Cr-poisoning.* **Michael Kornely, Anita Neumann, Norbert H. Menzler, André Leonide, André Weber, Ellen Ivers-Tiffée.** 17, s.l. : Journal of Power Sources, 2011, Vol. 196, p. 7203-7208.

20. *Electrochemical Analysis of Sulfur-Poisoning in Anode Supported SOFCs Fuelled with a Model Reformate.* **A. Kromp, S. Dierickx, A. Leonide, A. Weber, E. Ivers-Tiffée.** s.l. : Journal of The Electrochemical Society, 2012, Vol. 159, p. B597.

21. *Degradation evaluation by distribution of relaxation times analysis for microtubular solid oxide fuel cells.* **Hirofumi Sumi, Hiroyuki Shimada, Yuki Yamaguchi, Toshiaki Yamaguchi, Yoshinobu Fujishiro.** s.l. : Electrochimica Acta, 2020, Vol. 339, p. 135913.

22. *Analysis of Electrochemical Impedance Spectroscopy Data Using the Distribution of Relaxation Times: A Bayesian and Hierarchical Bayesian Approach.* **Francesco Ciucci, Chi Chen.** s.l. : Electrochimica Acta, 2015, Vol. 167, p. 439-454.

23. *How the distribution of relaxation times enhances complex equivalent circuit models for fuel cells.* **Sebastian Dierickx, André Weber, Ellen Ivers-Tiffée.** s.l. : Electrochimica Acta, 2020, Vol. 355, p. 136764.

24. *Determination of the Distribution of Relaxation Times by Means of Pulse Evaluation for Offline and Online Diagnosis of Lithium-Ion Batteries.* **Erik Goldammer, Julia Kowal.** 2, s.l. : Batteries, 2021, Vol. 7.

25. *Impedance Spectroscopy for Emerging Photovoltaics.* **Hauff, Elizabeth von.** 18, s.l. : Journal of Physical Chemistry C, 2019, Vol. 123, p. 11329-11346.

26. *Exploring Transport Behavior in Hybrid Perovskites Solar Cells via Machine Learning Analysis of Environmental-Dependent Impedance Spectroscopy.* **Dohyung Kim, Eric S. Muckley, Nicole Creange, Ting Hei Wan, Myung Hyun Ann, Emanuele Quattrocchi, Rama K. Vasudevan, Jong H. Kim, Francesco Ciucci, Ilia N. Ivanov, Sergei V. Kalinin, Mahshid Ahmadi.** 15, s.l. : Advanced Science, 2021, Vol. 8, p. 2002510.

27. *Deconvolution of electrochemical impedance spectra for the identification of electrode reaction mechanisms in solid oxide fuel cells.* **H. Schichlein, A. C. Muller, M. Voigts, A. Krugel, E. Ivers-Tiffée.** s.l. : Journal of Applied Electrochemistry, 2002, Vol. 32, p. 875-882.

28. *Fourier transform distribution function of relaxation times; application and limitations.* **Boukamp, Bernard A.** s.l. : Electrochimica Acta, 2015, Vol. 154, p. 35-46.

29. *Optimal Regularization in Distribution of Relaxation Times applied to Electrochemical Impedance Spectroscopy: Ridge and Lasso Regression Methods - A Theoretical and Experimental Study.* **Mattia Saccoccio, Ting Hei Wan, Chi Chen, Francesco Ciucci.** s.l. : Electrochimica Acta, 2014, Vol. 147, p. 470-482.

30. *Influence of the Discretization Methods on the Distribution of Relaxation Times Deconvolution: Implementing Radial Basis Functions with DRTtools.* **Ting Hei Wan, Mattia Saccoccio, Chi Chen, Francesco Ciucci.** s.l. : Electrochimica Acta, 2015, Vol. 184, p. 483-499.

31. *Combined Deconvolution and CNLS Fitting Approach Applied on the Impedance Response of Technical Ni/8YSZ Cermet Electrodes.* **V. Sonn, A. Leonide, E. Ivers-Tiffée.** s.l. : Journal of The Electrochemical Society, 2008, Vol. 155, p. B675.

32. *Maximum entropy in impedance spectroscopy of non-inductive systems.* **Hörlin, Tom.** 1-2, s.l. : Solid State Ionics, 1993, Vol. 67, p. 85-96.

33. *Deconvolution and maximum entropy in impedance spectroscopy of noninductive systems.* **Hörlin, Tom.** 3-4, s.l. : Solid State Ionics, 1998, Vol. 107, p. 241-253.

34. *Analysis and Application of Distribution of Relaxation Times in Solid State Ionics.* **Bernard A. Boukamp, Auréelie Rolle.** s.l. : Solid State ionics, 2017, Vol. 302, p. 12-18.

35. *Evaluation and Modeling of the Cell Resistance in Anode-Supported Solid Oxide Fuel Cells.* **A. Leonide, V. Sonn, A. Weber, E. Ivers-Tiffée.** s.l. : Journal of The Electrochemical Society, 2007, Vol. 155, p. B36.

36. *Hydrogen oxidation kinetics at Ni – Zr0.9Sc0.1O1.95 anode: Influence of the difference of potential in the dense part of the double electric layer.* **D. A. Osinkin, B. L. Kuzin.** s.l. : Electrochimica Acta, 2018, Vol. 282, p. 128-136.

37. *Impedance of SOFC electrodes: A review and a comprehensive case study on the impedance of LSM:YSZ cathodes.* **Jimmi Nielsen, Johan Hjelm.** s.l. : Electrochimica Acta, 2014, Vol. 115, p. 31-45.

38. *Electrode Kinetics of Porous Mixed-Conducting Oxygen Electrodes.* **S. B. Adler, J. A. Lane, B. C. H. Steele.** s.l. : Journal of The Electrochemical Society, 1996, Vol. 143, p. 3554.

39. *A Nonlinear Least Squares Fit procedure for analysis of immittance data of electrochemical systems.* **Boukamp, Bernard A.** 1, s.l. : Solid State ionics, 1986, Vol. 20, p. 31-44.

40. *Influence of crystal structure of nanosized ZrO2 on photocatalytic degradation of methyl orange.* **Sulaiman N. Basahel, Tarek T. Ali, Mohamed Mokhtar, Katabathini Narasimharao.** 73, s.l. : Nanoscale Researche Letters, 2015, Vol. 10.

41. *Raman scattering in nanosized nickel oxide NiO.* **N. Mironova-Ulmane, A. Kuzmin, I. Steins, J. Grabis, I. Sildos, M. Pärs.** s.l. : Journal oh Physics: Conference Series, 2007, Vol. 93, p. 012039.

42. *Performance Optimization of Cermet SOFC anodes: An Evaluation of Nanostructured NiO.* **Ilya Burmistrov, Dmitrii Agarkov, Ilya Tartakovskii, VLadislav Kharton, Sergey Bredikhin.** 1, s.l. : ECS Transactions, 2015, Vol. 68, p. 1265-1274.

5. General conclusions

In this work, the interfacial and transport properties of electrochemical energy storage and conversion systems have been studied. Regarding EESs, three viable anode materials based on SnO_2 have been studied for Li-ion batteries, according to the different stabilizing strategies adopted. A further composite material based on Fe_3O_4 has been synthesized and characterized as a sustainable and high-performance anode material for Na-ion batteries. All the materials have been characterized in terms of structure, morphology, and electrochemical performance. Then, interfacial and transport properties have been studied by means of cyclic voltammetry at different scan rates, galvanostatic intermittent titration technique (GITT), and potentiostatic electrochemical impedance spectroscopy (PEIS). Ex-situ Raman spectroscopy has been applied to the Fe_3O_4-based anode material to check the reversibility of the conversion reaction.

Concerning EECs, an extended experimental campaign based on EIS has been carried out on a commercial Solid Oxide Fuel Cell to develop a meaningful equivalent circuit model for the SoH assessment of the cell. Then, the model has been validated by applying an *a priori* known stress agent and post-mortem analysis.

The electrochemical performance of SnO_2-based anode materials has been stabilized by applying three different strategies, i.e.: (i) use of inorganic active matrix (TiO_2, TiO_2@SnO_2), (ii) use of carbonaceous active matrix (C, SnO_2/C), and (iii) use of a tailored morphology (nanorod SnO_2, C/SnO_2NR). In terms of electrochemical performance, TiO_2@SnO_2 and C/SnO_2NR have shown the highest retained capacity during the rate capability tests, with the latter having the highest average specific capacity in 100 cycles Q_{100} = 1007 mAh g^{-1}. Regarding the energy efficiency, C/SnO_2 is the most efficient vs. a $LiFePO_4$ cathode, with estimated η_E values being 86.53 % and 77.04 % with and without capacity limitation, respectively. In all three materials, the cyclic voltammetries acquired at increasing scan rates highlights a linear relationship between the peak current of the alloying reaction vs. the $\nu^{1/2}$, suggesting a diffusion-controlled behavior. A similar behavior for all the three materials was observed with the galvanostatic intermittent titration technique, characterized by a decreasing Li^+ diffusion coefficient as the lithiation proceed. Six different local minima were observed on the D_{Li} vs. E curves which can be indexed to the formation of the three-phases equilibria Li_2O-$Li_\alpha Sn$-$Li_{\alpha+\beta}Sn$. The material C/SnO_2NR has shown the highest D_{Li} among the SnO_2-anode materials thanks to its tailored morphology (nanorods made of hierarchically assembled 10 nm nanoparticles). The CNLS-fit of EIS data revealed a

growth of the resistances associated with the charge-transfer process and migration of Li^+ through the SEI layer, suggesting structural rearrangements of the electrode upon cycling, and exposure of fresh active material surface towards electrolyte reduction. These findings confirms that SnO_2 can be a suitable, green, and especially versatile candidate anode material for the next generation of Li-ion batteries, with tailored performances according to the end-user application.

Regarding the Fe_3O_4-based anode material, it was demonstrated that the Fe_3O_4 nanoparticles, synthesized by a green and facile method, stabilized with reduced graphene oxide are a suitable candidate anode material for both Li- and Na-ion batteries. Despite the low amount of rGO, the composite material showed remarkably improved cycling stability with specific capacity in the range order of 1000 mAh g^{-1} in Li-half cells. Furthermore, an excellent capacity retention was observed during the rate capability test with a retained capacity of ≈ 50 % at 10 C-rate. The EIS measurements confirm that its outstanding performances with Li are given by the embedding of Fe_3O_4 nanoparticles into the rGO matrix, resulting in a lower charge-transfer polarization. When cycled in Na half-cells, stable specific capacities of ≈ 300 mAh g^{-1}, with an excellent capacity retention at high rates of 50 and 40 % at the current of 2 and 5 A g^{-1}, respectively. The investigation of transport properties given by cyclic voltammetries at different scan rates highlights a linear relationship between the peak current of the conversion reaction vs. $\nu^{1/2}$, suggesting a faradaic behavior. However, by calculating the b-value of the Power law, it was observed a redox pseudocapacitive behavior, i.e.: the simultaneous adsorption of charges onto the active material surface and a fast faradaic reaction. EIS analysis highlighted the presence of a further interface which is probably given by the formation of large Na_2O clusters acting as transport barriers. At last, *ex-situ* Raman spectroscopy demonstrated the reversibility of the conversion reaction despite the incomplete reduction of Fe_3O_4 during the sodiation.

In the last section, a methodology to assess the polarization losses in a Solid Oxide Cell operated in Fuel Cell mode is presented. By acquiring EIS spectra within an extended experimental campaign, in which different working temperatures, current densities, fuel flows and compositions were used, it was possible to observe at least 5 different time constants. The peaks P_{A2} and P_{C1}, have been assigned to the charge-transfer processes HOR and ORR, respectively. The peaks P_{A3} and P_{C1} have been assigned to the gas diffusion in the anode support layer and oxygen surface exchange coupled to O^{2-} diffusion in the cathode, respectively. The peak P_{A1} has been assigned to the transport of O^{2-} by 8YSZ in the anode layer. An equivalent circuit model $LR_0(R_{A1}Q_{A1})(R_{A2}Q_{A2})W_{FLW}G(R_{C1}Q_{C1})$ (written in Boukamp's notation) has been elaborated for the

CNLS-fit. The model was then validated by applying an *a priori* known stress agent, along with a constant monitoring of the EIS response during the stress test. The comprehensive analysis of the evolution of DRT peaks (both center and area) confirmed the effect of the stress test. Furthermore, two peaks were the most affected by the stress test i.e., P_{A2} and P_{A3}, HOR and gas diffusion in the anode support layer, respectively. The *post-mortem* morphological characterization did not evidence any sign of delamination at the electrode/electrolyte interface, nor catalyst particle coarsening. However, the microstructural analysis done by Raman spectroscopy confirmed the presence of an amorphous layer of NiO on the surface of the Ni catalyst. Thanks to the electrochemical model, as well as the non-destructive impedance analysis, it was possible to detect a degradation phenomenon in the early stage, right before the cell was irreversibly damaged.

In summary, electrochemical impedance spectroscopy, analyzed by equivalent circuit method and distribution function of relaxation times, has been proven to be a reliable tool for the assessment of the interfacial phenomena, of the SoH and thus, the ageing of electrode materials and electrochemical system under study. On EESs, EIS measurements upon cycling allowed the quantification of the degradation of active material, solid electrolyte interphase, and electrolyte. In the case of Fe_3O_4/rGO, it allowed to detect a further interface probably due to the formation of large Na_2O clusters. On EECs, thanks to "deconvolution" analysis by DRT, it allowed the creation of a meaningful equivalent circuit model based on the evolution of the impedance response at different operating conditions. When applied as *operando* diagnosis tool, it was able to detect degradation in the early stage, without the need to stop the cell or perform any destructive measurement.